Modelling and dynamic analyses of TLP-type floating wind turbine

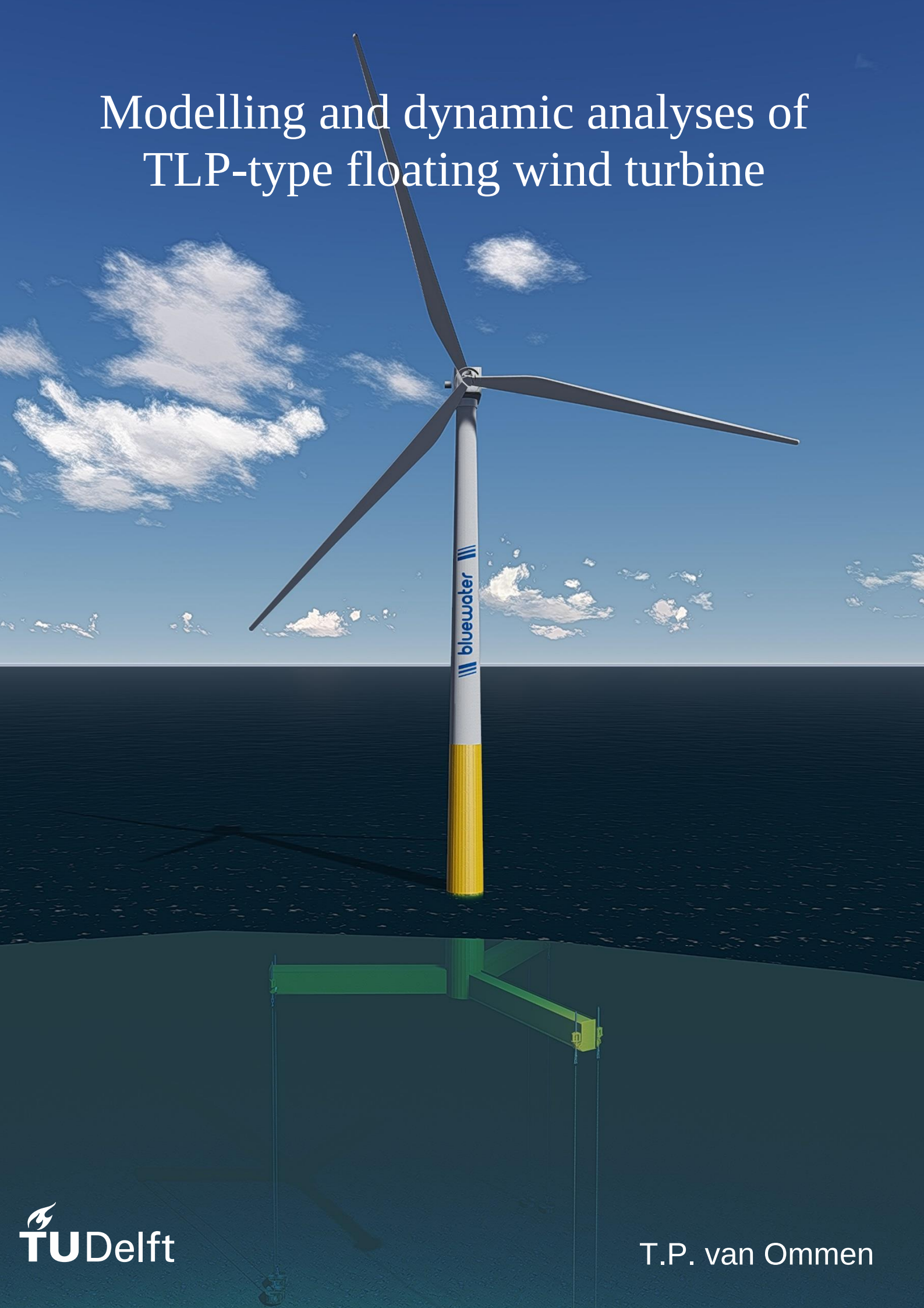

TU Delft

T.P. van Ommen

Modelling and dynamic analyses of TLP-type floating wind turbine

By

T.P. van Ommen

in partial fulfilment of the requirements for the degree of

Master of Science

in Offshore and Dredging Engineering

at the Delft University of Technology,

to be defended publicly on Thursday, December 06, 2018 at 14:30 PM

Supervisor:	Prof. dr. ir. M.L. Kaminski,	TU Delft
Thesis committee:	Ir. P.S. van Lieshout,	TU Delft
	Dr. Ir. P.Th.L.M van Woerkom,	TU Delft
	Ir. E. van Vliet,	Bluewater Energy Services
	Ir. L.B. de Vries,	Ketelbink / Bluewater Energy Services

TU Delft

ACKNOWLEDGEMENTS

During my adventure of graduation, I have been helped by many helpful and kind people. I would like to express my gratitude to all my colleagues of Bluewater Energy Services for their assistance and providing a very interesting graduation topic. However, special thanks to my supervisors from Bluewater, Eelco van Vliet and Leo de Vries, for their time to answer question, their broad knowledge and reviewing my report. I would also like to thank Clemens van der Nat from Bluewater for reviewing my report.

Additionally, I would like to thank my supervisor and also committee chairman Mirek Kaminski for answering my questions during the progress meetings, and the other committee members, Paula van Lieshout and Paul van Woerkom, for the assistance during the last months of my graduation.

Furthermore, I would like to thank my fellow students of the Master Offshore & Dredging engineering, special thanks to my friend and fellow student Ho-Seung Seo for the great collaboration in many courses of my study, during the last two years.

Finally, I would like to express my profound gratitude to the most important people in my life, my parents and brothers, for their unconditional support.

ABSTRACT

Fixed support structures for offshore wind turbines are commonly used for shallow water (till 45 meters). In many countries shallow-waters are rare. Floating support structures may be the solution for these areas. Many concepts have been developed but three concepts have been analyzed (spar, semi-submergible and the tension leg platform (TLP)) in the literature. This study focuses on the TLP, which has the lowest weight of these concepts but the dynamic system is complex and has significant more risk than the other support structures, for example the risk of resonance of structural elements.

The structural integrity of the total structure is important for the tension leg platform wind turbine (TLPWT). This study investigates the modelling techniques of the flexible TLPWT, with the aim to model the dynamics of floating wind turbine correctly. An Aero-hydro-elastic-servo model is implemented in Matlab, which includes aerodynamics of the wind turbine, hydrodynamic loads on the floating structure and mooring system, the flexibility of the total structure and the control system of the wind turbine. This model solves the equation of motion with the Houbolt numerical time integration method. In addition, the validity of the model is confirmed by validation using an Orcaflex model. The model is used to analyze the effect of the gyroscopic moments and the non-harmonic periodic load oscillations on the motion responses.

Steel structures are vulnerable to cyclic loading. Small cracks may initiate and grow in the structure, this is called fatigue. Fatigue is stress driven and resonance drives stresses. The fatigue performance can be improved by avoiding resonance of structural elements. A method has been developed to find a design with the natural frequencies outside the wind, wave and passing blade frequencies. The method consists of two algorithms, mode tracking algorithm and the selection algorithm. The method is used for a North-Sea site and the result of this an improved design, which has the natural frequencies outside the frequencies where wave and wind have energy. This design has better dynamic characteristics, which indicate better fatigue performance, in comparison of the reference TLPWT, which is predominantly designed to prevent slack tendons. The approach has shown to be successful but the method can only assist in the preliminary design phase of a TLPWT for any given site.

CONTENTS

NOMENCLATURE

MATRIX

Symbol	Definition	Symbol	Definition
$\boldsymbol{C}$	Damping matrix	$\boldsymbol{H}$	Circulatory stiffness
$\boldsymbol{G}$	Gyroscopic matrix	$\boldsymbol{K}$	Stiffness matrix
$\boldsymbol{M}$	Mass matrix	$\boldsymbol{T}$	Transformation matrix

SYMBOLS

Symbol	Definition	Symbol	Definition
A	Area	a	Acceleration structure
C	Coefficient	D	Diameter
d	depth	F	Force
f	frequency	f	Force per unit length
g	Gravity acceleration	H	Transfer function
h	Time step	I	Mass moment of inertia
k	Wave number	L	Momentum
l	Lift force per unit length	P	Power
p	pressure	p	Design parameter
R	Radius rotor blade	r	radius
S	Spectrum	T	period
t	Time	u	Environmental velocity
v	Velocity TLPWT	x	Displacement TLPWT

GREEK

Symbol	Definition	Symbol	Definition
α	Angle of attack	β	Numerical parameter
γ	Numerical parameter	γ	Peak enhancement factor
ε	Error	ε	strain
ζ	Wave amplitude	θ	Numerical parameter
θ	Flow angle	θ	Pitch angle
η	Surface elevation	κ	Shear correction factor

λ	Eigenvalue	λ	Wave length
μ	Direction	ν	Poisson ratio
ξ	Damping ratio	ρ	Density
Φ	Velocity potential	σ	Standard deviation
ϕ	Phase angle	Ψ	Mode shape
Ω	Rotational speed disk	ω	Angular velocity

SUBSCRIPTS AND SUPERSCRIPTS

Symbol	Definition	Symbol	Definition
$\star_a$	Added mass	$\star_d$	drag
$\star_e$	Element matrix	$\star_l$	lift
$\underset{\star}{\rightarrow}$	vector	$\dot{\star}$	Derivative with respect to time
$\star^T$	transpose	$\star^H$	Complex conjugate

ABBREVIATIONS

Symbol	Definition	Symbol	Definition
BFWT	Bottom Founded Wind Turbine	EoM	Equation of Motion
FLS	Fatigue limit state	FPO	Floating Production Offloading
FPSO	Floating Production Storage Offloading	FWT	Floating Wind Turbine
MAC	Modal assurance criterion	MSL	Mean Sea Level
PI	Proportional and Integral	ODE	Ordinary Differential Equation
RMSE	Root Mean Square Error	RNA	Rotor Nacelle Assembly
SPM	Single Point Mooring	TLP	Tension Leg Platform
TLPWT	Tension Leg Platform Wind Turbine	TSR	Tip-speed ratio
ULS	Ultimate limit state		

DEFINITIONS OF FLOATING WIND TURBINE

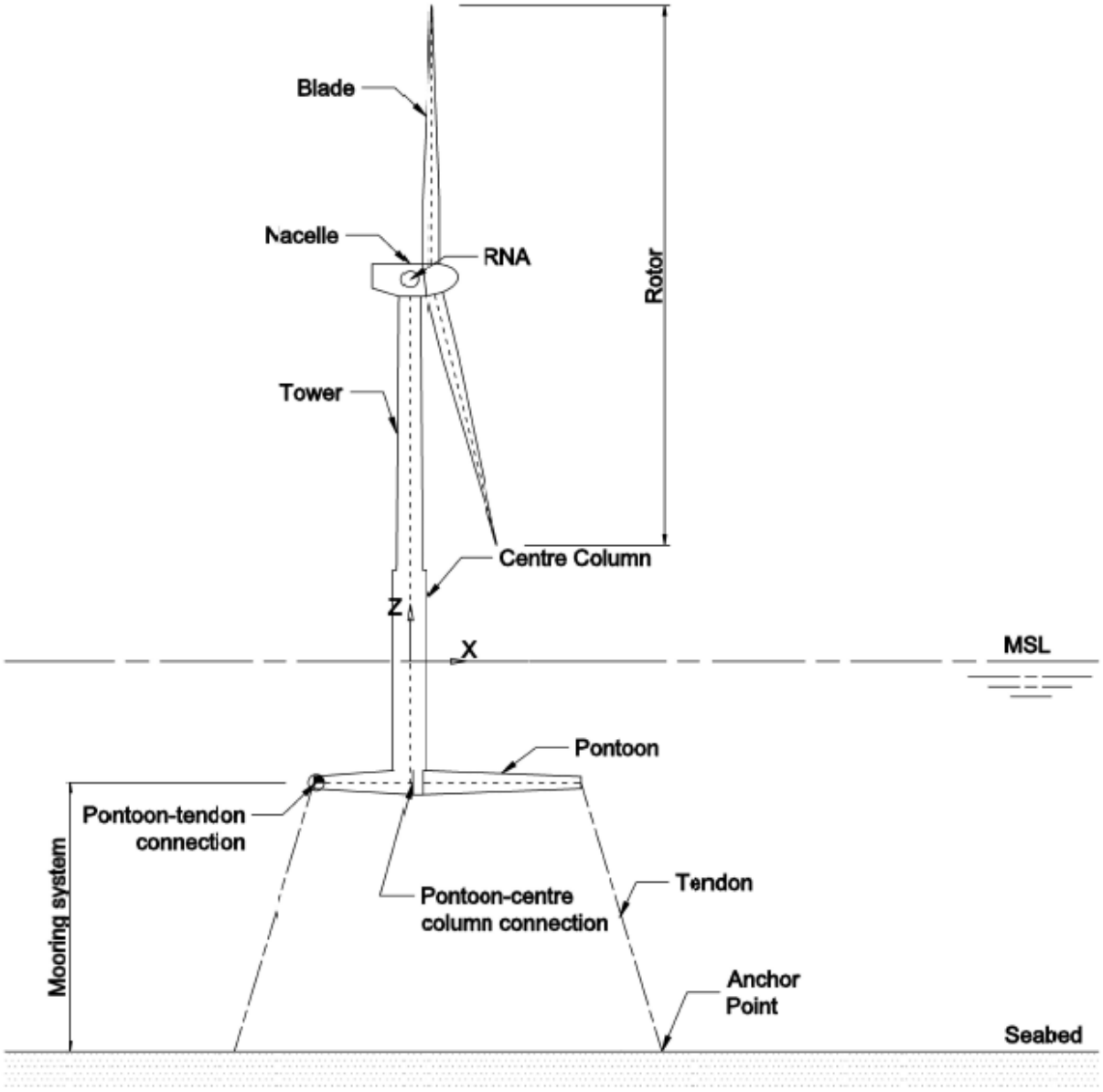

This page is intentionally left blank

1 INTRODUCTION

1.1 BACKGROUND

Fixed support structures for offshore wind turbines are commonly used for shallow water, till a water depth of approximately 45 meter. In the United States, China, Scotland and many other countries shallow-water areas are rare. For these countries floating support structures may be a solution to expanding offshore wind in deeper waters [1]. Different floating offshore wind turbine (FOWT) concepts are developed, but three main concepts have been investigated, namely the spar (see Figure 1-1, a), semi-submersible (see Figure 1-1, b) and tension leg platform (TLP) (see Figure 1-1, c) concepts. The floating principle for these concepts are in other existing offshore oil and gas applications.

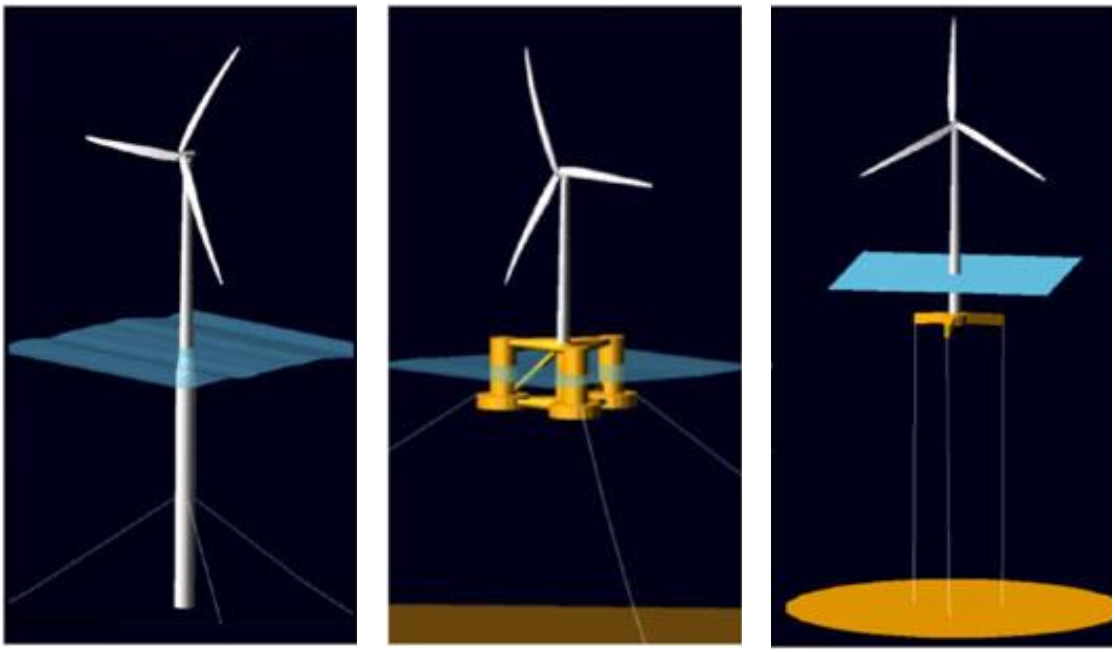

(a) *(b)* *(c)*

Figure 1-1: Floating wind turbine concepts [2]

The difference between these concepts is the way how they stabilize. The spar is ballast stabilized, the semi-submersible is buoyancy stabilized and the TLP is mooring stabilized. The spar concept is used in the Hywind windfarm [3], worlds first floating offshore wind farm. For stability requirements, the draft of the spar should be larger than the hug height. The hug height is the distance from the mean water level (MWL) till the rotor height. This makes the spar applicable for larger water depths. However, a major challenge of this concept is the pitch motion. Large pitch motion can affect the gyroscopic stability of the hull [4]. The semi-submersible is a promising concept and lighter than the spar concept. For maximal performance, active ballast systems should be used to compensate for the change wind speed and direction [4]. The TLP is stiffer in heave, roll and pitch motion in comparison to the other concepts. This results in a lower natural period [5], typically outside the frequencies where waves have energy. A summary of the concepts is given in Table 1-1.

Table 1-1: Qualitative assessment [6] of offshore wind turbine platform classes: + advantages, 0 neutral - disadvantage

	TLP	*Spar*	*Semi-submergible*
Stability	Mooring	Ballast	Buoyancy
Natural periods	+	0	-
Coupled motions	+	0	-
Wave sensitivity	0	+	-
Turbine weight	0	-	+
Moorings	+	-	-
Anchors	-	+	+

1.1.1 Tension-Leg-Platform Concept

The TLP has the lowest weight of all three concepts and is expected to result in a better cost-effective design. The TLP concept has many similarities with the mini-TLP, used for the offshore oil and gas industry. A mini-TLP is a single surface-piercing column structure (Figure 1-2, b). The mini-TLP is designed for deep-water applications, especially for smaller oil and gas fields [7]. The structure consists of a tower and three legs, supported by six tendons. A tendon can be made of chains, steel wire or synthetic lines. Other than the mini-TLP, which is designed to minimize the heave motion to allow the application of steel catenary riser, the tension leg platform wind turbine (TLPWT) is designed to avoid resonance of the waves, wind and passing blade frequencies of the wind turbine [4].

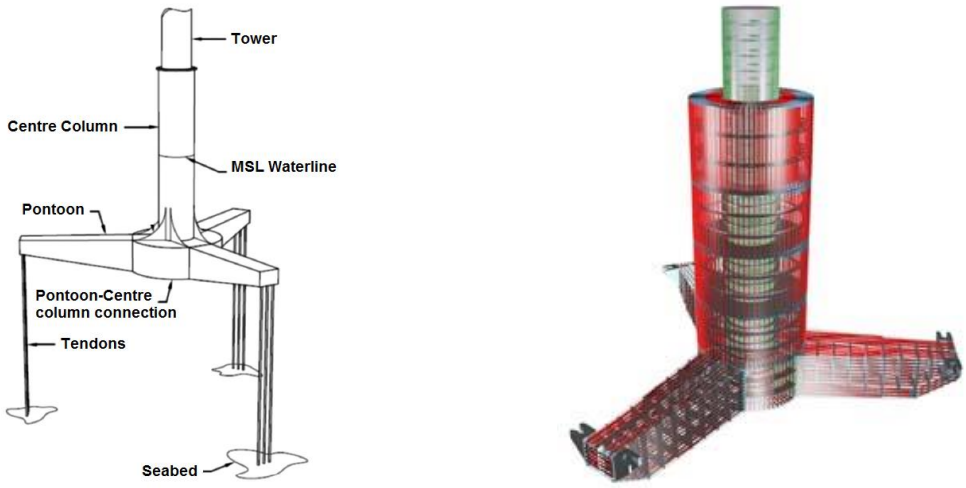

Figure 1-2: (a) Tension leg turbine platform concept [4]. (b) SeaStar mini-TLP [7].

The dynamic system of the TLPWT is complex. Tracy [8] investigated the motions of the TLPWT in time domain simulations. This study showed that high pitch motions can lead to slack tendons and snap loads. Snap loads are shock loads on the mooring lines due to a slack wire becoming taut caused by large wave- and wind-induced motions. Slack tendons can result in total failure of the TLPWT. A slack tendon should be avoided under all conditions. In extreme cases, the TLPWT can be confronted with 50% higher loads than a fixed offshore wind turbine. The simulations of Tracy's also show the possibility of a number of resonance excitation of the TLP. The design of a TLPWT has significant more risk to encounter resonance in structural elements than the other support structures. However, if a successful design can be developed for offshore wind turbines, than the design is a light-weight and cost-effective offshore foundation, which can be used for a large range of water depths [9].

The study of Tracy's shows the possibility of resonance excitations of the TLPWT, but also time simulations of Bluewater show resonance excitations. Figure 1-3 gives an example of resonance motions of the wind turbine tower. The TLPWT with natural period of the tower bending mode equal to the wave peak period (blue) shows large motion amplitude in comparison of the TLPWT with the natural period of the tower bending mode lower than the wave peak period.

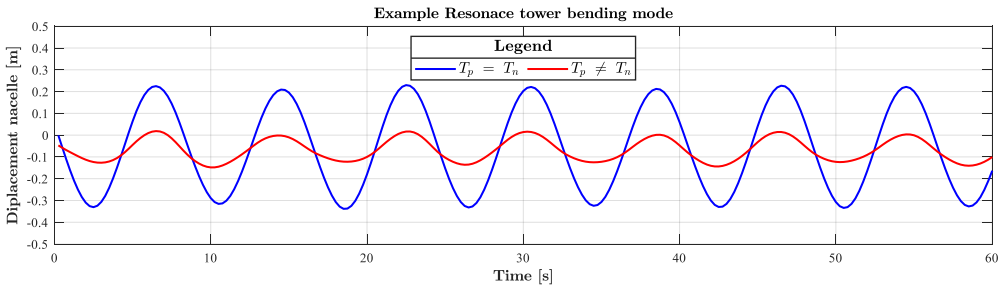

Figure 1-3: Example resonance

The dynamic properties of a TLP are shown in the list below [9].

- A TLP structure is unstable and is depending on the mooring lines, which provide the stability of the system.
- The tendons of the TLP limit the motions. In case of a large motion, the TLP will also have a displacement in vertical plane.
- Low stiffness in surge and sway directions, but high stiffness in heave. The high stiffness is provided by the pretension and the high mooring stiffness.

1.2 WINDFLO

Bluewater Energy Services, hereafter called Bluewater, is a company, which is specialized in designing and operating Floating Production Storages and Offloading (FPSO) tankers, Floating Production and Offloading (FPO) and Single Point Mooring (SPM) systems for the oil and gas industry. Currently Bluewater investigates the floating wind energy market and started the WindFlo project in 2017, to develop a TLP-type floating wind turbine concept. The WindFlo concept is a three legged TLP-type support structure. The TLPWT is the lightest TLPWT in the market and includes innovative solutions for the mooring system and anchoring. The TLPWT has three rectangular shaped pontoons with each two tendons. A cylindrical shaped centre column connects the wind turbine tower and the pontoons. The WindFlo concept has no active systems. The TLPWT is suitable for water depths, deeper than 60 to 80 meters, depending on the wave conditions of the offshore site.

(a) *(b)*

Figure 1-4: WindFlo wind turbine concept illustrations

1.3 PROBLEM STATEMENTS

1.3.1 Statement 1: Resonating motions of structural elements

A cost competitive floating wind structure has to operate for at least 25 years in a harsh environment. The aerodynamic and hydrodynamic loads acting on the TLPWT are oscillating loads. It is known that steel structures are vulnerable for cyclic loads. Small cracks may initiate and grow in the structure. This phenomena is called fatigue. Fatigue is defined as the damage accumulation due to the oscillating stress and strains in the material [10]. A fatigue assessment should be performed to prove the fatigue life of at least 25 years is assured. Possible fatigue damage growth over time can be computed with a spectral fatigue analysis or time domain fatigue analysis. Spectral fatigue analysis can only be used for linear dynamical systems. However, the TLPWT is a nonlinear dynamical system, which means that a time-consuming time domain fatigue analysis needs to be performed.

In the design phase of the TLPWT many design iteration are needed, to optimize the design. Linearization of the equation of motion may help to reduce the computation time and cost. Kim [11] proposed an innovative method to analyze the fatigue of a floating wind turbine. The transfer function of the combined wave and wind forces is approximated by artificial neural networks. Salih [12] investigated several methods to linearize the equation of motion for a TLPWT, using a rigid-body model to compute the fatigue damage. Salih successfully developed a method to predict the fatigue damage of a rigid TLPWT, but many research questions are still unanswered, especially if the structure can be assumed to be rigid.

The dynamic interaction of the fluctuating loads and the moving structure is complex, for example the interaction of the wind- and wave response cannot be ignored. Engineering practice shows that the effect of cyclic loading can be reduced significantly by avoiding the resonating motions or providing sufficient damping in the system. This can be illustrated by the dynamic amplification factor (DAF), which is defined as the ratio between the dynamic response and the quasi-static response. Figure 1-5 gives the DAF for a single degree-of-freedom dynamic system, showing the impact upon the DAF for difference damping ratios.

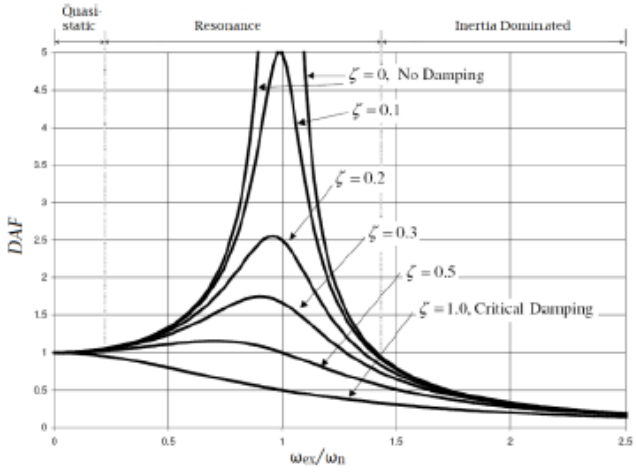

Figure 1-5: Dynamic amplification factor

1.3.2 Statement 2: Absence of elastic model

Adequate computation model to quantify the motions of a TLPWT including its own deformations is required. This model needs to meet the requirements of modelling structural damping, hydrodynamics, aerodynamics, flexibility of the structure and the control system of the wind turbine. This model needs to capture the complex dynamic system of the TLPWT, for example the wave- and

wind coupling. Two commonly used time domain programs are coupled: FAST-Orcaflex, but this coupling only works for rigid models in Orcaflex. Orcaflex [13] is a commercial software package, developed by Orcina, for dynamic analysis of marine systems. FAST [14] is an open-source software package, developed by National Renewable Energy Laboratory (NREL), for simulating the coupled dynamic response of wind turbine. In this situation, Orcaflex is used to compute the hydrodynamic loading and the mooring line responses of the TLPWT and FAST is used to compute the blade responses and the aerodynamic loading. The Fast-Orcaflex coupling is highly time consuming because the response of the wind turbine defines the time step size that is used to the complete system

The equation of motion (EoM) is a very stiff ordinary differential (ODE) equation due to the large differences in stiffness. It may be expected that the MATLAB build-in first-order ODE-solvers become numerical instable. Non-physical oscillations may be visible in the time simulations or the entire simulation is blown up. Several numerical time integration methods will be investigated and a numerical time integration method will be studied of that perform time simulation which take the flexibility of the total structure into account.

1.4 GOALS OF THIS THESIS

The fatigue lifetime of the structure is key dependent of the number of oscillations and the stress amplitudes. The number of oscillations is depending on the force frequencies and these are site dependent. The stress amplitudes are depending on the force amplitude, frequency and geometry of the structure. The stress amplitudes can be reduced by avoiding resonance of structural members. Therefore, the aim of this study is to automate the design exploration and find a good starting point to design a TLPWT with the critical natural frequencies outside the frequency spectrum of the environmental loads and wind turbine as well.

In order to find design parameters for a TLPWT with the critical natural frequencies outside the frequency spectrum, first the critical natural frequencies are identified. Secondly, the influence of the gyroscopic effect and the nonlinear stiffness on the natural frequencies are investigated. Finally, the dynamical system is analyzed to identify the frequency spectrum of the environmental loads and passing blade frequencies, which may be different for a floating offshore wind turbine.

The main research question can be formulated as:
‘’Given a site, how to achieve a primary design in the tender phase of a TLP-type floating wind turbine with the critical frequencies outside the loading frequencies?’’

1.5 SCOPE OF WORK

First, in order to quantify the natural frequencies of the TLPWT and for computing the motion responses of a TLPWT, an aero-hydro-elastic-servo model has to be developed. The focus of this model is correctly describe the interaction of the floating support structure, the mooring system and the wind turbine. The Aero-hydro-elastic-servo model includes the aerodynamics of the wind turbine (aero), the hydrodynamics and hydrostatics loads (hydro), the elasticity of the floating support structure, tendons and wind turbine tower (elastic) and the control system of the wind turbine (servo).

The current study does not include the wind turbine blade responses. The wind turbine is modelled as a rigid actuator disk. Blade response is especially of interest for the blade-nacelle and the nacelle-tower connection, but is expected to have limited impact on the pontoon-tower connection, due to the large flexible tower. The control system is modelled as a closed-form linear control system based on the NREL control system. A more advanced control system can be incorporated in further studies.

The NREL control system may not be suitable for a floating wind turbine, but investigating the control system for floating wind turbine is outside the scope of this study.

Bluewater has developed a wind turbine external function for their time simulations. This function models the aerodynamics loads of the wind turbine, tower shadow effect and the control system of the wind turbine. This function is included in the Matlab model.

This study investigates four hydrodynamic models (First-order hydromechanics, second-order hydromechanics, third-order hydromechanics and Morison equation) to compute the hydrodynamic loads. The model uses the Morison equation, which is suitable for slender structures where diffraction can be neglected. This assumption is not investigated in this study, but a study of Bluewater shows that diffraction can be neglected [15].

It is well known that third-order wave loads are important for structures when the wave-amplitudes have the same magnitude as the cross-sectional dimensions, the structure a has surface-piercing column and has natural periods between 1 and 5 seconds [16]. The responses of these loads are called ringing vibrations and are observed in full-scale TLPs used in the oil and gas industry. The TLPWT complies these criteria, depending on the offshore site ringing loads may be important. However, these loads are omitted in this study, but ringing responses should be investigated in further studies.

1.6 Thesis Outline

Chapter 2: Theoretical Review

A theoretical background of wind turbine dynamics, wind turbine loads computation methods, hydromechanics models, environmental modelling, nonlinear dynamics and numerical time integration methods are investigated in this chapter.

Chapter 3: Development of Aero-Hydro-Elastic-Servo model

This chapter explains the aerodynamics, structural, hydrodynamic and the servo model. This chapter is finalized with validation of the Aero-hydro-elastic-servo model. The Aero-Hydro-Elastic-Servo model is validated with Orcaflex. Orcaflex is multiple times used for floating wind turbines studies.

Chapter 4: Dynamical analysis

In this chapter the effects of the rotating blades on the natural periods and motions are investigated, including the effect of the nonlinearities on the natural periods and non-harmonic periodic loads of wind turbines are investigated.

Chapter 5: Development and application of the algorithms

The design process is automated. Two algorithms are developed to track the natural frequencies and select a good starting point. In addition, a design case is performed on the reference TLPWT for a North-Sea site to verify and to possible improve the design of the TLPWT from a resonance point of view.

Chapter 6: Conclusions and Recommendations

From the applications results conclusions are drawn about the algorithms, finalized by recommendations for further research, improvements for the model and improvements of the algorithms.

2 THEORETICAL REVIEW

2.1 INTRODUCTION

The following chapter focuses on the underlying principles of the wind turbine dynamics, including typical phenomena of wind turbine like passing blade frequencies, gyroscopic moment, aerodynamic damping and the control system. Also this chapter focuses on the commonly accepted modelling techniques for the environment, computation methods of aerodynamics loads, hydrodynamics models and the modelling techniques of mooring system. In addition, the fundamentals of numerical time integration methods are explained in detail and investigated. Last, the numerical analysis techniques of nonlinear and linear dynamics are investigated and explained.

2.2 WIND TURBINE

The wind turbine is the most important part of the TLPWT. Firstly, the principles of the wind turbine are explained. The dynamics of the wind turbine should be correct implemented in the model and the typical phenomena of the wind turbine are investigated with respect to the fatigue lifetime of the TLPWT. The following phenomena of the wind turbine are investigated:

- Passing blade frequencies
- Gyroscopic moments
- Aerodynamic damping
- Control system

2.2.1 Principles of wind turbine

A wind turbine converts kinetic energy of the wind into electric energy. The total power in the wind can be determined with equation (2-1). By removing kinetic energy from the wind, the wind speed will decrease, but only the air mass of the wind that is passing the rotor disk. The air mass that slows down will stay separated from the air mass that did not pass the rotor disk. A boundary layer can be drawn, which is illustrated in Figure 2-1. By assuming that atmospheric pressure remains constant, then the area of the air flow upstream should increase to accommodate the slower moving air [17]. The area increases because the continuity of mass flow remains constant.

$$P_{wind} = \frac{1}{2}\rho_{air} A_d u_{wind}^3 \tag{2-1}$$

P_{wind} Power wind
u_{wind} Wind speed
ρ_{air} Density air
A_d Area rotor disk

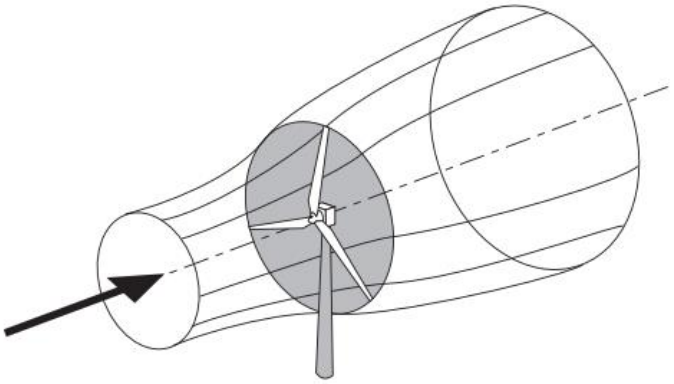

Figure 2-1: Energy extracting stream-tube of a wind turbine [17]

The presence of the wind turbine causes the wind speed to drop. In addition, the wind that is approaching the rotor disk is already slower than the free-stream wind. After passing the rotor disk, there is a pressure drop. At a certain distance behind the wind turbine, the pressure reaches the atmospheric pressure to satisfy equilibrium. To reach equilibrium static pressure rises, which is caused by a decrease in velocity (see Figure 2-2). Thus a loss of kinetic energy of the wind [17]. The total power that is produced by the rotor disk can be calculated by equation (2-2).

$$P_{produce} = \frac{1}{4}\rho_a A_d (u_1^2 - u_2^2)(u_1 + u_2) \quad (2\text{-}2)$$

$P_{produce}$	Power production	ρ_{air}	Density air
u	Wind speed	A_d	Area rotor disk

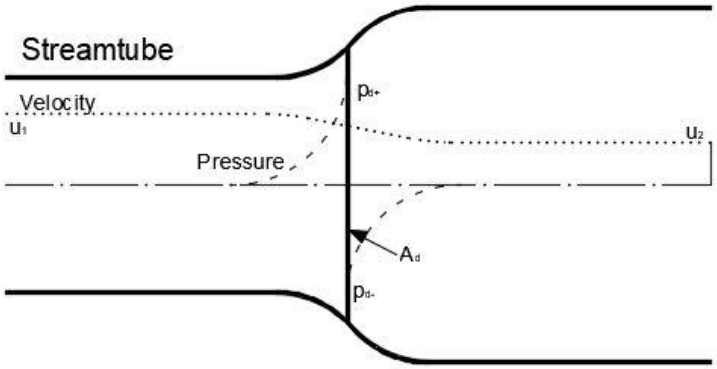

Figure 2-2: Energy extracting actuator disk and streamtube

The theory of a rotor disk only explains how kinetic energy from the wind is converted to rotor energy in an ideal situation. The fundamental difference with the reality is that the actual power depends on the aerodynamic lift and drag forces [18]. Aerodynamic lift and drag forces are caused by air flow crossing the blades. The physical explanation of the reaction force is that the streamline curves around the wind turbine blade. The pressure far from the blade is equal to the atmospheric pressure. Thus, a pressure difference is present between the fore and aft of the blade. Integrating of the pressure around the blade gives a reaction force, the orthogonal component is the lift force and the parallel component the drag force (Figure 2-3). The lift/drag-ratio of the blade is a key indicator for the aerodynamic efficiency. However, the drag force for a wind turbine blade is very low [19].

The free-stream velocity is defined as the wind speed infinitely far away from the wind turbine when the wind turbine is kept as referential and thus the free-stream velocity is the vector sum of the angular velocity of the blade and the wind velocity. The angle between the airfoil chord and the free-stream velocity is the aerodynamics angle of attack. As explained above, the lift force is perpendicular and the drag force is parallel to free-stream velocity. The lift force can be resolved in the plane of the rotation. The tangential component, L_{torque} (Figure 2-3, b), constitutes the driving torque of the rotor and the normal components, $L_{thrust,}$ (Figure 2-3, b), are the thrust force of the wind turbine. The torque on the wind turbine drives the generator of the wind turbine [19]. The drive train of a wind turbine that converts the rotational energy into electricity is outside the scope of this thesis, but can be found in many books, for example [19].

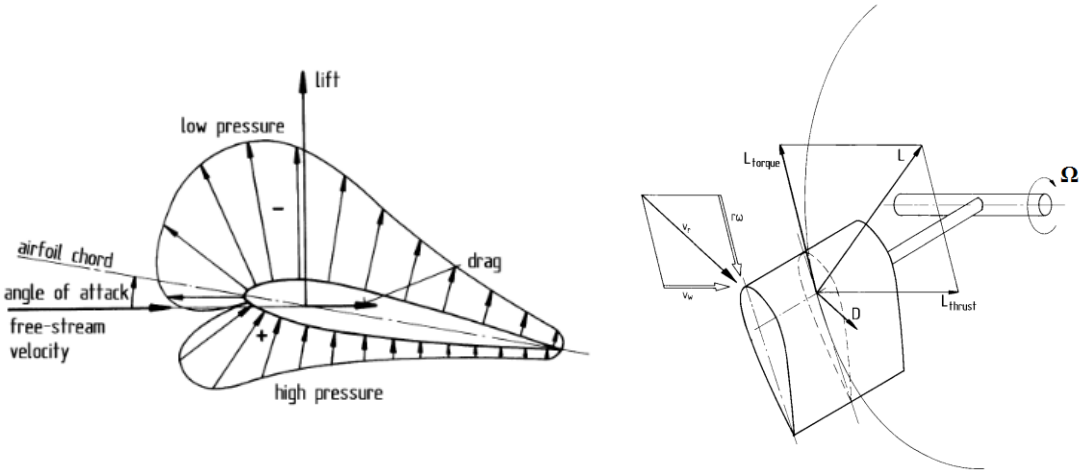

(a) *(b)*

Figure 2-3: (a) Pressures around a rotor blade [19] (b) Velocities and aerodynamic forces acting on a turbine blade – like rotor [19]

2.2.2 Passing blade frequencies

The thrust force variations are due to wind turbulence and non-harmonic periodic processes. These non-harmonic periodic processes are mainly due to the tower shadow effect and the wind shear effect. These processes occur even in wind without wind turbulence and can be approximated by a Fourier series [20]. The thrust force oscillations are for a three bladed wind turbine the 3P and it multiples. The passing blade frequencies are important for the power quality, control system and fatigue life of the blades [21]. The power output of the wind turbine fluctuates at a frequency thrice that of the rotational speed of the rotor [22]. The influence of passing blade frequencies on power and the thrust force is depending on the control region, especially when blade-pitch controller is active [22]. Also the control system can be used to avoid resonance of the tower bending modes caused by the passing blade frequencies.

2.2.2.1 Tower shadow effect

The tower shadow effect is the dynamic interaction between the tower and the blades. The tower shadow effect for downwind turbines is larger than for upwind wind turbines. For upwind wind turbines the wind velocity decreases close to the tower. The lower velocity is due to the reflection of the wind through the tower. Due to the lower wind speed, the trust force is slightly lower. The oscillations in the thrust force due to the tower shadow effect are important for the fatigue assessment of the wind turbine [23].

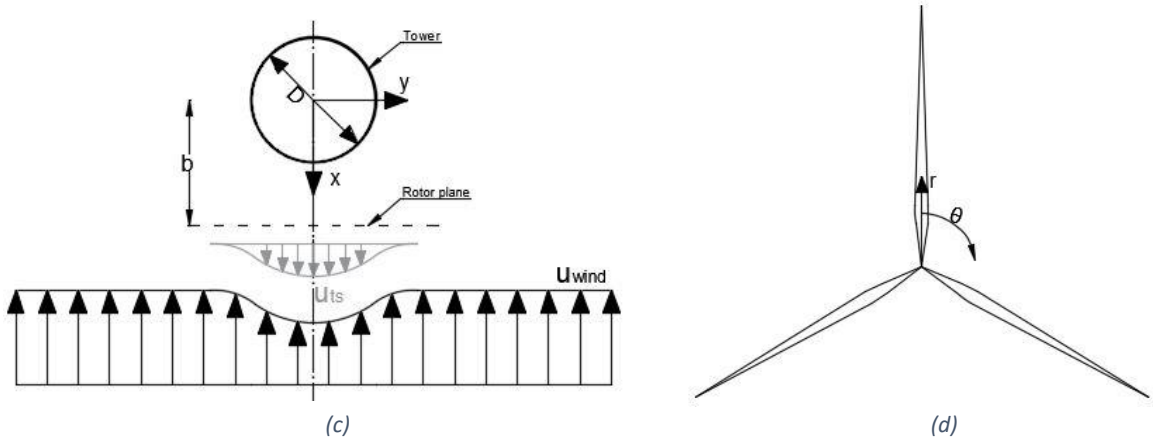

(c) *(d)*

Figure 2-4: (a) Velocity of the wind in the vicinity of the tower (b) Geometric of the equation

The tower shadow effect for wind turbines occurs even at constant wind speed. The most common method to model the tower shadow effect is to use a doublet [24]. A doublet is a potential flow element. Superposing the stream function of the doublet and the uniform flow, the equation of the reflected wind can be derived and is expressed by the equation (2-3) and the definitions are given in Figure 2-4.

$$u_{ts} = u_{wind}\left(\left(\frac{D}{2}\right)^2 \frac{(r\sin\theta)^2 - b^2}{b^2 + (r\sin\theta)^2}\right) \tag{2-3}$$

u_{ts}	Tower shadow wind velocity	u_{wind}	Wind velocity
D	Diameter tower	r	radius
θ	Azimuth of wind turbine blade	b	Distance tower and rotor plane

The tower shadow effect has two important parameters. The distance from the blade to the centre of the tower (b in Figure 2-4) and the diameter of the tower (D, in Figure 2-4). Decreasing b, the influence of presence of the tower increases, meaning that the redirected wind velocity is higher. Figure 2-5 shows the influence of the presences of the tower.

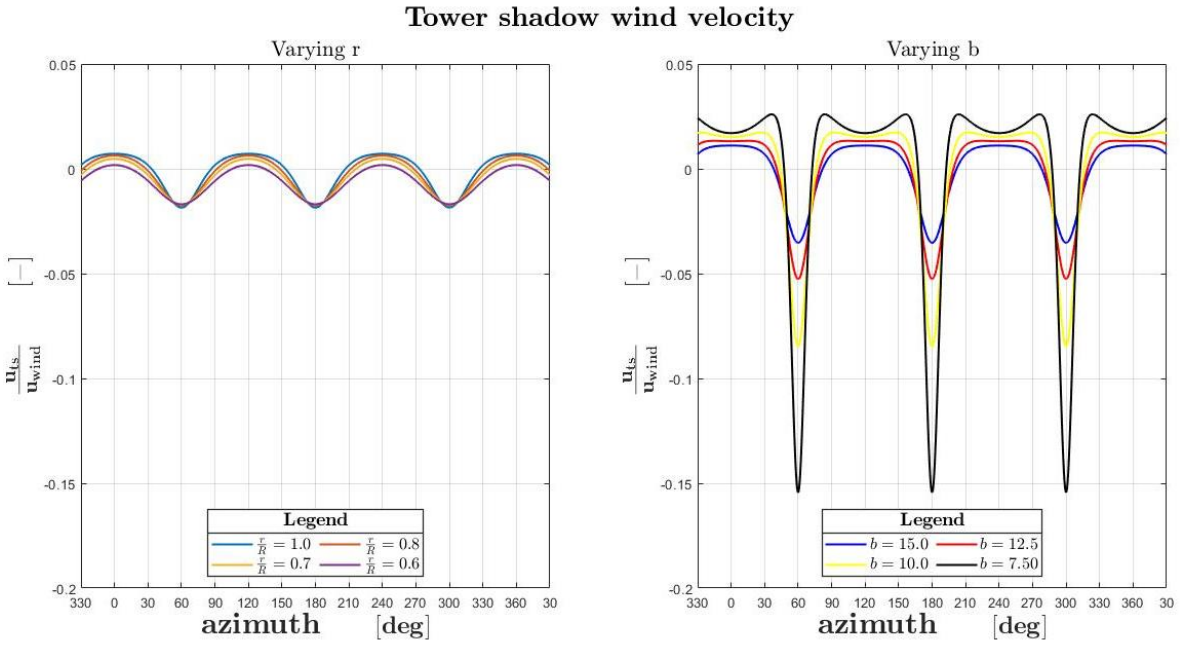

(a) *(b)*

Figure 2-5: (a) Dimensionless U_{ts} with varying r (b) Dimensionless U_{ts} with varying b

2.2.2.2 Wind shear effect

The main wind speed increases with height, this is called the shear effect. The rotating blades encounter different wind conditions through a complete cycle. For example, a blade rotating upwards would encounter higher wind speed than a blade rotating downwards (see Figure 2-6). During each complete cycle, the thrust force is oscillating with the same number of blades. The influence of the wind shear effect on the thrust force is depending on the tower height and the wind shear profile.

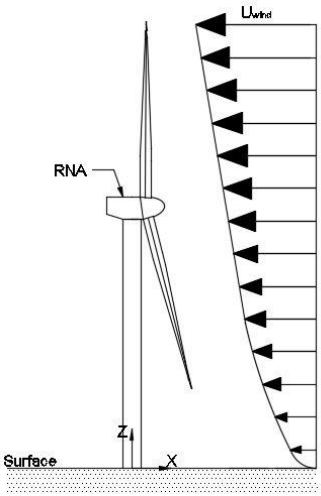

Figure 2-6: Schematic of blade and wind shear [25]

2.2.2.3 Conclusions

The tower shadow effect and the wind shear effect are the main source of the non-harmonic periodic loads, which oscillations are in 3P and its multiples. The influence of these periodic oscillations are important for the fatigue life of the wind turbine blades, but the effect of these periodic oscillations on the motion response of the RNA and the pontoon-centre column connection (PC-connection) are investigated in chapter 4 of this study.

2.2.3 Gyroscopic effect

When a rotating structure is subjected to a rotation perpendicular to the plane of a rotation, then the structure experiences gyroscopic effects. The motions involved are very complex and are difficult to analyze. The gyroscopic effect takes place in every system where there is a rotating mass part and it is defined as follows by Shilovskii [26]: ‘’Any couple, apparently tending to incline the axis of rotation body in a given direction, actually causes an inclination of the axis in the plane perpendicular to that given direction’’.

Instead of a fixed rotation axis system, a rotation axis system is used that is moving with the rotating structure. When the rotating structure is rotating with a constant angular velocity, then the angular moment is constant. The angular moment is a vector quantity, because it has a direction and a magnitude. The magnitude of the angular momentum is equal to equation (2-4) and the direction of the angular momentum is perpendicular to the angular velocity.

$$\vec{L} = \boldsymbol{J}\vec{\Omega} \tag{2-4}$$

$$\boldsymbol{J} = \begin{bmatrix} I_{xx} & I_{xy} & I_{xz} \\ I_{yx} & I_{yy} & I_{yz} \\ I_{zx} & I_{zy} & I_{zz} \end{bmatrix}$$

L Angular momentum Ω Angular velocity

$\boldsymbol{J}$ Inertia tensor

If an external moment is working on the system and results into a change of motion, the direction and the magnitude of the angular moment change. The change of angular momentum is equivalent to the angular impulse caused by the change in orientation. The change of angular momentum is a torque. The derivative with respect to time of a rotating structure with respect to a fixed axis system consist two parts, the angular acceleration of the structure and the correction term of the rotating reference frame. These equations are also known as Euler rotation equations of a rigid body (equation (2-5)). The last term in the equation is known as the gyroscopic moment.

$$\frac{\partial \vec{L}}{\partial t} = \frac{\partial \boldsymbol{J}\Omega}{\partial t} + \Omega \times \boldsymbol{J}\Omega \tag{2-5}$$

L	Angular momentum	Ω	Angular velocity
$\boldsymbol{J}$	Inertia tensor		

Under some circumstances, the floating wind turbine is effected by gyroscopic moments. There are two motions of the wind turbine that generate a gyroscopic moment; a yaw motion and a pitch motion. For the first motion, the gyroscopic moment occurs when the rotating blades are moved into the direction of the wind or the floating wind turbine is rotating around the z-axis. For the second motion, the TLPWT is tilting upwards and downwards or the tower is bending around the y-axis [26].

The angular velocity of the wind turbine and the angular velocities of the floating support structure are uncoupled. The angular velocity of the wind turbine is constant, the angular momentum vector changes only due to rotation of the floating support structure. Filling in equation (2-5) gives equation (2-6). With this equation is concluded that a rotation of the floating support structure around the z-axis gives a moment around the y-axis and vice versa [20].

$$\frac{\partial \vec{L}}{\partial t} = \frac{\partial \boldsymbol{J}\Omega_{\mathrm{w}}}{\partial t} + \Omega_{\mathrm{w}} \times \boldsymbol{J}\Omega_{TLP} = \Omega_{w}\begin{bmatrix} 0 \\ -J_z\dot{\theta}_z \\ J_y\dot{\theta}_y \end{bmatrix} \tag{2-6}$$

$$\Omega_w = [\Omega \quad 0 \quad 0]^T$$

$$\Omega_{TLP} = \begin{bmatrix} \dot{\theta}_x & \dot{\theta}_y & \dot{\theta}_z \end{bmatrix}^T$$

L	Angular momentum	Ω_{w}	Angular velocity wind turbine
$\boldsymbol{J}$	Inertia tensor	Ω_{TLP}	Angular velocity TLP
$\dot{\theta}_i$	Angular velocity in direction i		

For a three blade wind turbine the inertia tensor is constant and diagonal, also the inertia is the same in the symmetry plane ($I_{yy} = I_{zz}$). Therefore, the gyroscopic moments are written as matrix equation, as (2-7).

$$M_{gyro} = \Omega_w \begin{bmatrix} 0 & 0 & 0 \\ 0 & 0 & I \\ 0 & -I & 0 \end{bmatrix} \begin{bmatrix} \dot{\theta}_x \\ \dot{\theta}_y \\ \dot{\theta}_z \end{bmatrix} \tag{2-7}$$

Ω_w	Angular velocity wind turbine blades
I	Mass moment of inertia rotor
$\dot{\theta}_i$	Angular velocity TLP in direction i

The wind turbine is following the motions of the nacelle-tower connection. A gyroscopic moment is generated perpendicular to plane of rotation. For a fixed offshore wind turbine the gyroscopic moments are small, and can be neglected. The yaw motions and pitch motions of a FWT are much larger than the motions of BFWT, therefore the gyroscopic moments may be relevant for the motion responses of the TLPWT. The effect of the gyroscopic moment is further investigated in chapter 4 of this study.

2.2.4 Aerodynamic damping

The interaction of the blades and the airflow cannot be neglected. The aerodynamic forces and moments depend on the relative velocity with respect to the structure, especially for flexible structures like wind turbines blades. The structural motions affect the airflow and in general this lead to a reduction of the aerodynamic moments and forces. This effect is called damping because the force and moment reduction is related to the velocity term in the equation of motion [27].

The aerodynamic forces and moments are depending on the angle of attack of the wind flow and variation in this angle can reduce or increase the aerodynamic forces. The aerodynamic forces can increase with the structural response, the increase of the forces is called negative damping. This means that the flow supplies energy to the system [28]. The aerodynamics are coupled with the surge and pitch motions of the floating support structure. Those motions are the most dominant motions with respect to the yaw and heave motions of the system, because the moments in yaw-direction and forces in heave-direction are smaller [29]. The aerodynamic damping reduces the aerodynamic forces. The aerodynamic damping is higher than the hydrodynamic damping, more pronounced for high winds.

2.2.5 Control system

The control system of the wind turbine includes of multiple control systems. The primary function of the control system is to ensure that the wind turbine operates at preferred settings. The control system maximizes the power production within the constraints of the grid power input capability, prevent extreme loads, minimizes fatigue damage and ensure safe operations.

The control system of the wind turbine can be split in the safety control system, the supervisory control system and the power control system. The safety control system checks if the power control and supervisory control are working correctly. The safety control system activates when the power control and supervisory control are failing. The system works independent of the power control system and supervisory control system. If a failure is detected, the braking action of the generator is used to assist the shutdown of the wind turbine in a safe manner [17].

The supervisory control system manages the wind turbine between the different operation stages. The operations stages are the stand-by, start-up, power production, shutdown stage. The switch from an operation state to another operation state is divided into stages. The supervisory control checks for each stage if it is successfully completed. The supervisory controller shuts the wind turbine down if a stage is not completed in a certain time or if a fault is detected [17].

2.2.5.1 Power control system

The power control system controls the blade-pitch controller, variable-speed controller and the yaw controller. The blade-pitch controller controls the pitch of the blade in order to control the power output. However, changing the pitch angle of the blade takes time, the change is typically in the order of a degree per second. The variable-speed controller controls the generator torque, the generator torque can change with a negligible decay. The yaw controller keeps the nacelle aligned with the wind direction [30].

The variable-speed controller and blade-pitch controller are independent control loops. The variable-speed controller uses the generator speed to calculate generator speed error and the generator speed demand. The blade-pitch controller also uses the generator speed to calculate a blade-pitch error and a blade-pitch demand. The yaw controller uses the wind direction to calculate a nacelle-yaw-error and calculates a nacelle-yaw demand. The demands are used to update the yaw angle of the nacelle, pitch angle of the blades and the rotational speed of the wind turbine to control the aerodynamic torque, which constitutes the generator [17]. When the wind speed varies close to the rated speed, it is possible that both control systems are active and the controllers are conflicting. However, this is outside the scope of this study.

The power controller operates in 6 wind speed regions. Region 1 spans the operation between startup and the cut-in wind speed. The cut-in wind speed is defined as the wind speed when the generator is turned on and the wind turbine starts producing power. Region 2 uses the variable-speed controller to maximize the power production. The blade pitch angle is kept constant and the rotor speed varies. The goal of the variable-speed controller is to keep the tip speed ratio optimal. Region 1.5 is the transition region between region 1 and region 2. Region 3 is the constant power region, by adjusting the blade pitch angle it becomes possible to have a constant energy production. In region 3, the control system reduces the thrust when there is an increased wind velocity. Region 2.5 is the transition region between region 2 and region 3. Region 4 is the last region and is the cut-out region. The wind speeds are above the cut-out wind speed [31].

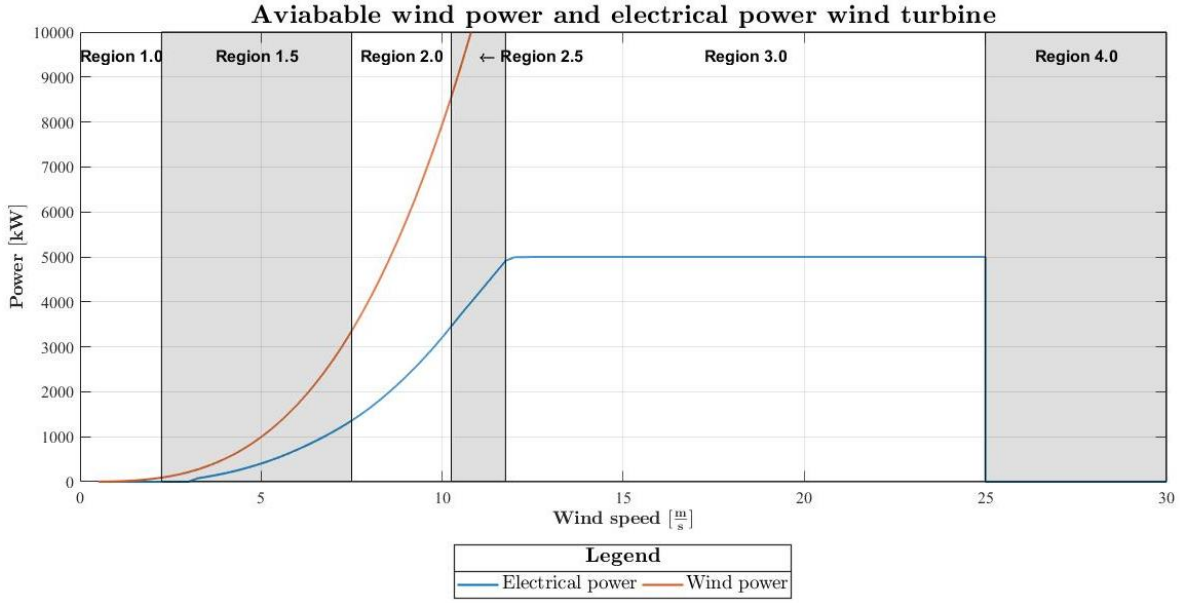

Figure 2-7: Steady-state rotor thrust as function of the wind speed for the 5-MW turbine

2.2.5.2 Conclusions

The control system regulates the power production in high winds and optimizes the production in low winds, however the blade-pitch controller and the variable-speed controller have major impact on the wind turbine loads. The controller also prevents extreme loads and minimizes the fatigue damage by controlling repeated bending caused by the weight of the rotor and unsteady aerodynamics loads [17]. It is concluded that the variable-speed controller and blade-pitch controller of the wind turbine should be taken into account. Neglecting the control system gives unreliable loads and motion responses. However, the yaw controller has negligible effect on the loads and motions and can be neglected.

2.3 AERODYNAMIC LOAD

The aerodynamic loads are split in the aerodynamic loads on the tower and the wind turbine loads. The wind turbine loads are given in Figure 2-8 and the loads are computed by a momentum analyses. The wind turbine loads can be computed by an actuator disk, blade element theory (BET) or by computation fluid dynamics (CFD). Actuator disk is a one-dimensional momentum method, BET is a two-dimensional momentum method [32]. Both methods are explained in detail.

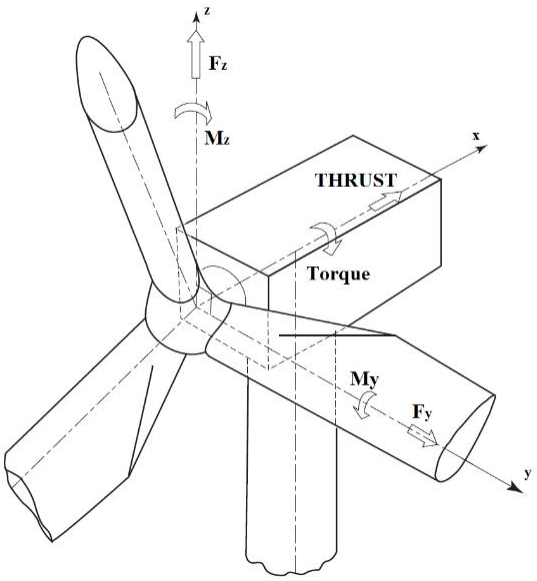

Figure 2-8: Global wind turbine loads

2.3.1 Actuator disk

If the actuator disk is used, then the wind turbine is simplified by assuming an infinite number of blades, meaning that the turbine has infinite number of lifting lines. The momentum theory assumes a steady incompressible flow and axisymmetric, the fluid is homogeneous and inviscid [32]. The Bernoulli equation can be used with the given assumptions.

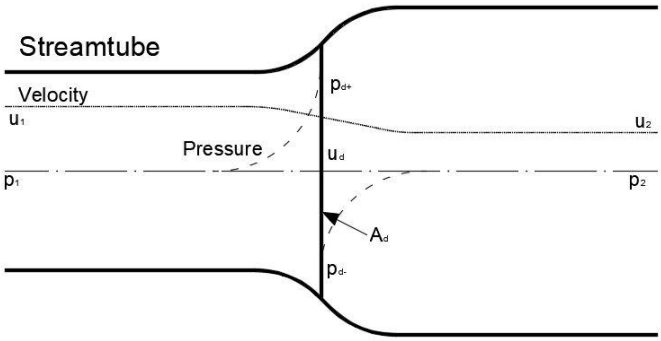

Figure 2-9: One-dimensional momentum analysis

The pressure drop at the rotor of wind turbine is uniform over the actuator disk. The flow is assumed to be in axial direction of the actuator disk. The Bernoulli equation for the control volumes 1 and 2((see Figure 2-10)) are given in equation (2-8) and equation (2-9) respectively, where the definitions are given in Figure 2-9.

$$p_1 + \frac{1}{2}\rho_{air}u_1^2 = p_{d+} + \frac{1}{2}\rho_{air}u_d^2 \quad (2\text{-}8)$$

$$p_{d-} + \frac{1}{2}\rho_{air}u_d^2 = p_2 + \frac{1}{2}\rho_{air}u_2^2 \quad (2\text{-}9)$$

p	pressure	u	Wind velocity
ρ_{air}	Density air		

The pressure at the start of the streamtube and the pressure far away are equal to the atmospheric pressure. The pressure drop at the actuator disk can then be expressed with equation (2-10).

$$\Delta p = p_1 - p_2 = \frac{1}{2}\rho_{air}(u_1^2 - u_2^2) \quad (2\text{-}10)$$

p	pressure	u	Wind velocity
ρ_{air}	Density air		

The trust force is equal to the pressure drop along the actuator disk, which is assumed to be constant. Substituting the function of the pressure drop in the function of the thrust force gives equation (2-11).

$$F_{thrust} = \mathrm{A_d}\Delta p = \frac{1}{2}\rho_{air}A_d(u_1^2 - u_2^2) \quad (2\text{-}11)$$

A_d	Area actuator disk	p	pressure
u	Wind velocity	ρ_{air}	Density air

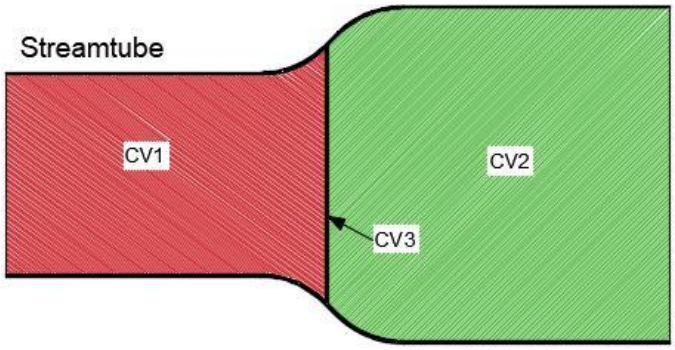

Figure 2-10: Control volume of the streamtube

The equations of power and forces can be rewritten with dimensionless coefficients, which results in derivations of the more common equations for power and force. Using the power and thrust coefficients of the wind turbine gives a reasonable and accurate result. The loads can be non-conservative.

$$P = \frac{1}{2}C_p\rho_{air}A_d u_1^3 \quad (2\text{-}12)$$

$$F_{thrust} = \frac{1}{2}C_t\rho_{air}A_d u_1^2 \quad (2\text{-}13)$$

A_d	Area actuator disk	p	pressure
u	velocity	ρ_{air}	Density air

Figure 2-8 gives global wind turbine forces and moments. The non-axial forces (F_y and F_z) cannot be calculated with the actuator disk, because only one-dimensional momentum is considered. Also the non-torsional moments (M_y and M_z) cannot be calculated, for a similar reason as the non-axial forces [20].

2.3.2 Blade element theory

Blade element theory (BET) is most commonly used in the wind turbine industry due to the high computational efficiency and high accuracy [33]. BET was first proposed by W. Froude in 1878 and later improved by D.W. Taylor and S. Drzewiecki [34]. BET calculates the load and the flow velocity around the blade assuming that the load on an arbitrary point at the blade can be computed independently from any other point. The loads can be computed with a dimensionless lift, drag and moment coefficient. The inflow angle of the wind with respect to the blade is known. The lifting-line theory is used. This theory yields states that lift distribution is depending on the blade geometry and the air flow conditions [32].

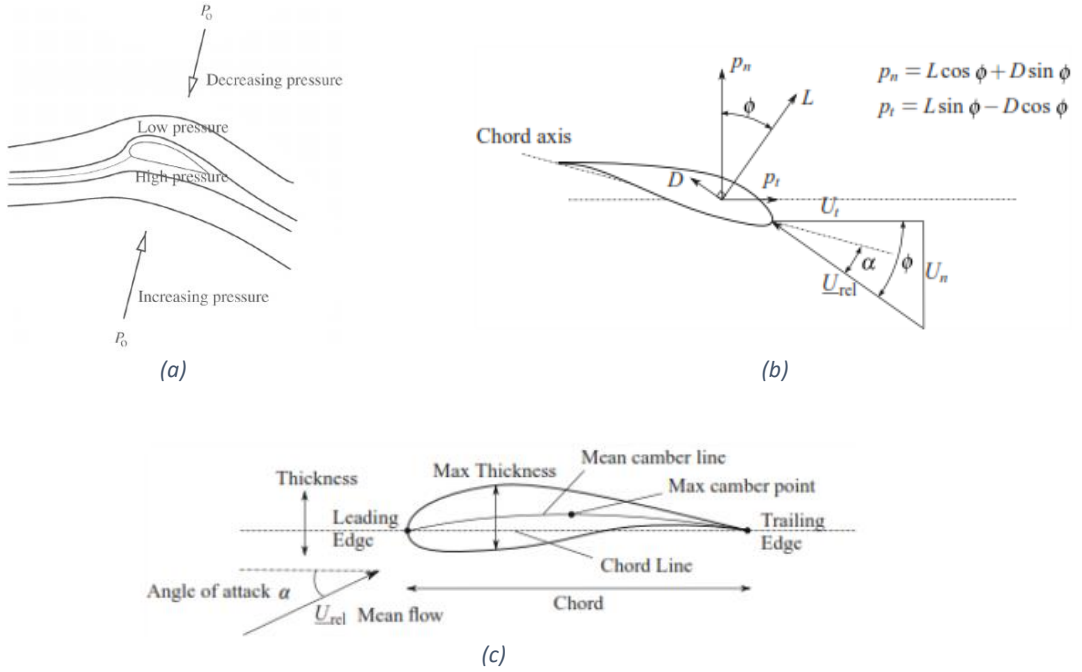

Figure 2-11: definitions of (a) pressure field [19] (b) forces on a blade [32] (c) geometrical parameter turbine blade [32]

The loads on the blade and the induced wind speed are calculated for a finite number of radial locations, called elements. For each element, with thickness dr (Figure 2-12 (a)), a steam tube is defined. If the wind speed V_0 at the location of an element and the angular frequency of the blades are known. The effective velocity can be computed by the vector sum of the velocity of the incoming flow and the velocity of that element. The induced velocity is the reaction of the incoming wind and angular velocity of the blade. The induced velocity needs to be determined by an iterative process. For the first iteration step an estimation of the induced velocity is required.

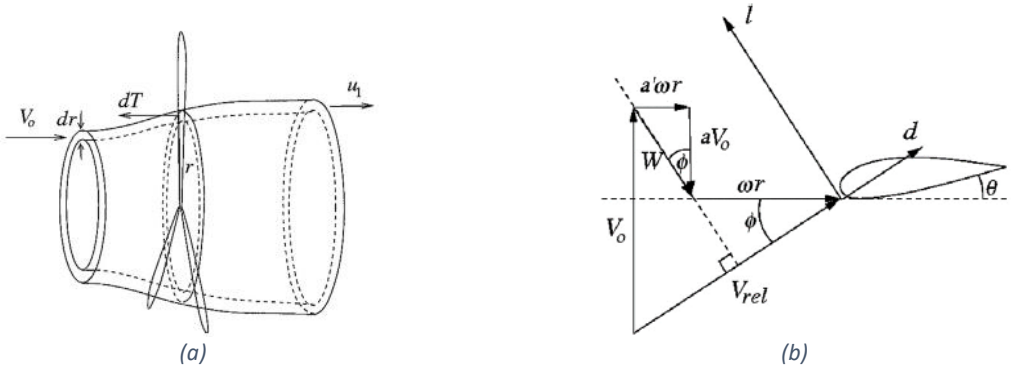

Figure 2-12: (a) Stream tube with de thickness dr cross the radial location r on the rotor plane [35]. (b) Velocities and forces on a blade element on the radial distance r.

Figure 2-12 (b) gives the velocity vectors on a blade. The axial velocity is perpendicular to the rotor plane and the tangential velocity is parallel to the rotor plane. The induced velocity W is parallel to the relative velocity. The axial and tangential velocity need to be computed using equation (2-14) and equation (2-15) respectively.

$$V_{axial} = V_0 - aV_0 = (1-a)V_0 \quad (2\text{-}14)$$

$$V_{tang} = \omega r + a'\omega r = (1+a')\omega r \quad (2\text{-}15)$$

V_0	Velocity incoming wind	a	Induction factor axial velocity
a'	Induction factor tangential velocity vector	ω	Angular velocity blade
r	Radius		

When the axial and tangential velocities are computed, the flow angle can be computed with equation (2-16) and the relative velocity with equation (2-17). The local angle of attack, angle between the rotor plane and the airfoil chord θ, can be computed with equation (2-18).

$$\tan(\phi) = \frac{(1-a)V_0}{(1+a')\omega r} \quad (2\text{-}16)$$

$$\alpha = \phi - \theta \quad (2\text{-}17)$$

$$V_{rel}^2 = (1-a)^2 V_0^2 + (1+a')^2(\omega r)^2 \quad (2\text{-}18)$$

ϕ	Angle of the relative velocity	V_0	Velocity incoming wind
a	Induction factor axial velocity	a'	Induction factor tangential velocity vector
ω	Angular velocity blade	r	Radius
θ	Airfoil chord	α	Angle of attack

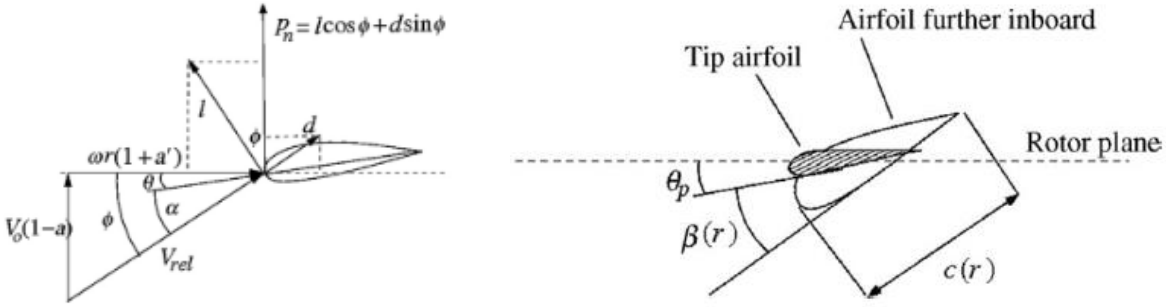

Figure 2-13: (a) Velocities and forces on a blade element on the radial distance r. (b) chord, the twist and pitch angle of the blade

The lift and drag force on a certain location of the blade are computed with equation (2-19) and the thrust of the stream tube can be calculated with equation (2-20). Where c is the length of the chord and N_e is the number of elements [35].

$$l = \frac{1}{2}\rho_{air} V_{rel}^2 c C_l(\alpha, Re)$$
$$d = \frac{1}{2}\rho_{air} V_{rel}^2 c C_d(\alpha, Re) \quad (2\text{-}19)$$

$$dT = N_e p_n dr \quad (2\text{-}20)$$
$$p_n = l\cos(\phi) + d\,sin(\phi)$$

l	Lift force element	d	Drag force element
ρ_{air}	Density air	V_{rel}	Relative velocity
c	Chord length	$C_l(\alpha, Re)$	Coefficient lift as function of angle of attack and Reynolds number
$C_d(\alpha, Re)$	Coefficient drag as function of angle of attack and Reynolds number	dT	Thrust element
N_e	Number of elements	ϕ	Angle of the relative velocity

By applying the conservation of angular momentum for the control volume of the stream tube, the relation between the non-dimensional tangential velocity reduction and the thrust can be found. Note that the angular upstream velocity is 0 and the angular velocity is the 2a'ωr in the wake [35].

$$dM = 4\pi r^3 \rho_{air} V_0 \omega a'(1-a)dr \tag{2-21}$$

$$dM = \frac{1}{2}\rho N_e \frac{V_0(1-a)\omega r(1+a')}{\sin(\phi)\cos(\phi)} r c c_t dr \tag{2-22}$$

$$c_t = C_l \sin(\phi) + C_d \cos(\phi)$$

$$p_n = l\cos(\phi) + d\, sin(\phi)$$

dM	Torque element	ρ_{air}	Density air
V_0	Incoming wind velocity	ω	Angular velocity blade
a	Induction factor axial velocity	a'	Induction factor tangential velocity vector
dr	Thickness	N_e	Number of elements
ϕ	Angle of incoming wind velocity	r	Radius
c	Chord length	C_l	Coefficient lift
C_d	Coefficient drag		

From equation (2-21) and equation (2-22) equation (2-23) can be derived to calculate a new tangential induction factor a'. If the error of a' is with the limits, the computation is stopped. The Prandtl tip loss factor can be applied to take the vortex behind the rotor into account. The iteration scheme of BEM is given in Figure 2-14, excluding Prandtl tip loss factor. The Prandtl tip loss factor is a correction of the tip-losses to a finite number of blades [32].

$$a' = \frac{1}{\frac{4\sin(\phi)\cos(\phi)}{\sigma c_t} - 1} \tag{2-23}$$

$$\sigma = \frac{N_e c}{2\pi r}$$

a'	Induction factor tangential velocity vector	ϕ	Angle of incoming wind velocity
c_t	Coefficient thrust force	N_e	Number of elements
r	Radius	c	Chord length

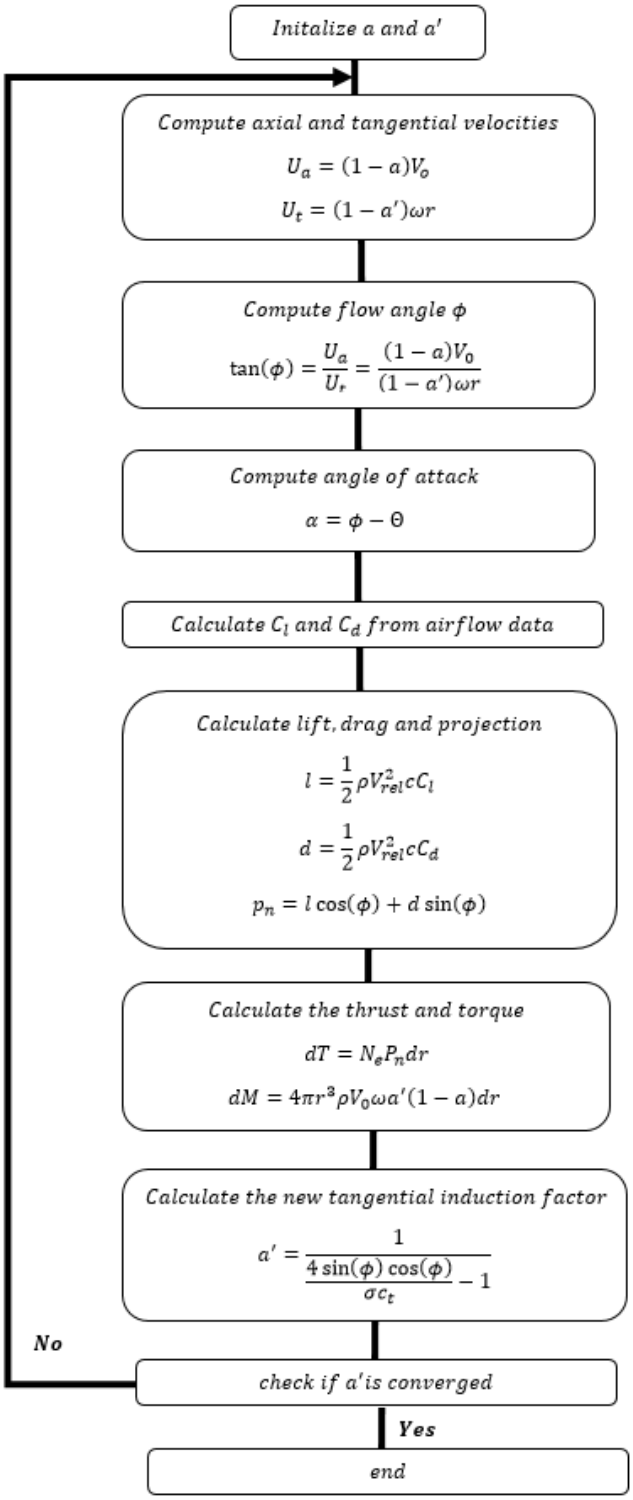

Figure 2-14: Flowchart of Blade Element Method

2.3.3 Conclusions

The flow field around a blade of a wind turbine is complex due to wind shear, turbulence, gust and yaw motion of the nacelle. For a floating offshore wind turbine the flow field is even more complex because of the relatively large motions of the platform [36]. For example, the yaw and pitch motions of the floating support structure are important to the performance of the wind turbine.

The global wind turbine loads can be computed by a momentum theory analyses, where the actuator disk is a one-dimensional momentum method and BET is a two-dimensional momentum methods. Both methods are explained in this paragraph. The actuator disk computes the thrust force and torque within an acceptable accuracy, however the method cannot compute the non-axial loads and the non-torsional loads. The non-torsional loads have a lower order, than the torque but the non-axial load F_y can be significant when the wind turbine is not properly aligned with the wind. Table 2-1, summarize the output of the momentum analysis and can be used as a look-up table to compare the momentum analysis methods.

Table 2-1: Summary momentum theory analysis

	Actuator disk	*BET*
Axial loads	+	+
Non-axial loads	-	+
Torque	+	+
Non-torsional loads	-	+
Computation time	+	-
Closed form	+	-
Blade responses	-	+
Wind shear	-	+

The actuator disk method has less computation time than the BET, however it cannot compute the non-axial loads and non-torsional moments, but the thrust and torque forces are computed within an acceptable accuracy. The developed model should compute the motions relatively fast, therefore the actuator disk assumption is used. The influences of the non-axial forces and non-torsional moments on the motions on the fatigue assessment should be investigated. However, this is outside the scope of the study.

2.4 HYDROMECHANICS LOADS

The hydromechanics loads can be separated into hydrostatic and hydrodynamic loads. The hydrostatic loads are the buoyancy forces and moments of the submerged part of the body in the fluid. The hydrodynamic loads are one of the most important loads affecting the fatigue lifetime of a floating support structure. The hydrodynamic models are investigated and explained. Finalized, with a conclusion which model is used in the study.

Hydrodynamic loads are the dynamic forces and moments due to the dynamic pressures of the fluid. These dynamic pressures are obtained by the time derivative of the potential. The potential can be split into the three parts (see equation (2-24)), wave potential, radiation potential and the diffracting potential [37]:

$$\Phi = \Phi_{diffraction} + \Phi_{wave} + \Phi_{radiation} \quad (2\text{-}24)$$

Φ Potential

The wave potential and the diffracting potential are related, namely the wave potential is the potential of undisturbed wave and the diffraction potential is the potential of the deflection of the incoming wave due to the presence of the body. The potentials are used to compute the pressures on the wetted surface, these pressures are the hydrodynamic loads. The hydrodynamic loads are the Froude-Krylov forces and the diffraction forces. The Froude-Krylov forces are caused by the pressure field of the undisturbed wave [38]. Due to the dynamic forces and moments acting on the body, the body will move. This forced motion generates waves in opposite direction of the incoming waves, these waves are radiated from the oscillating body. The hydrodynamic loads caused by the radiated waves are identified as the added mass of the body, damping and restoring forces and moments [38].

2.4.1 First order hydrodynamics

First-order hydrodynamic forces and moments only depend on the geometry of the structure and not on the motion responses. The first-order hydrodynamic forces have frequency depending added mass, frequency depending damping and frequency and directional depending hydrodynamic wave coefficient for diffraction. The radiation and diffraction potentials are solved using the panel method or strip method [37]. The radiation and diffraction potentials are solved without solving the equation of motion, because the potentials only depend on the geometry. Linear hydrodynamics are commonly used to design large floating structures for the oil and gas industry [39].

2.4.2 Second-order Hydrodynamics

First-order hydrodynamics superimpose the hydromechanics potentials. The radiation, diffraction and wave potential are solved separately. Superposition is only valid if the amplitudes of the motion are small with respect to the wave amplitudes and the rotations are small with respect to the wave slope. In second order hydrodynamics the wave-structure interaction is included as the quadratic terms of the potential flow [40]

The second-order hydrodynamics loads are superimposed with the first-order hydrodynamic loads. The second-order hydrodynamics can be derived with a Taylor expansion of the potential flow. The second-order loads are proportional to the square of the wave amplitude with frequencies equal to the sum of two frequencies or equal to the difference of two frequencies. The second-order loads have a small magnitude but the resonance effects can be high. Second-order loads are the mean-drift loads, the difference frequency loads, slow varying drift loads and sum-frequency loads [40].

Sum-frequencies forces are forces which are the sum of two frequencies, but have a small amplitude. The source is the same as for the difference-frequency forces, namely the interaction between waves with different frequencies. These forces have frequencies above and below the frequencies of the

first-order forces and are important for the TLPWT due to the high natural frequency in pitch, roll and heave, because they can excite the bending modes of the wind turbine tower [39]. The sum-frequency forces have the same magnitude of the first-order forces in heave direction, which are typically small. For surge, the difference-frequency forces are important because the natural frequency of surge is in the difference-frequency range. Due to the coupling between surge and pitch, the same effect is observed. By modelling the tower rigid, an overestimation of the natural frequency of pitch and roll are observed. Modelling the tower elastic and the natural frequency of the bending tower modes are in the sum-frequency region, which may cause large responses at these frequencies [41].

Drift forces are second-order hydrodynamic forces, calculated by of the square of the velocity term of the oscillating wetted part and the time varying potential of the oscillating wetted part. The drift forces are separated in mean drift forces and slow varying drift forces. The drift forces are small because the amplitudes are small but can cause large displacements of the floating wind turbine, resulting in large loads in the mooring lines of the TLP-concept. The drift forces can also excite large resonant surge motions. Slow varying drift forces are due to the interaction between waves with two different frequencies [39].

2.4.3 Third-order hydrodynamics

Third-order hydrodynamic effects are described with a third-order potential. Third-order hydrodynamic loads are important for structures where the wave-amplitudes and the cross-sectional dimensions have the same order. Ringing loads and responses are related to third or higher order wave loads. Ringing responses are observed in experiments and full-scale TLPs used in the oil and gas industry. Ringing is a transient structural deflection at the frequencies higher than the frequency of the incident wave. The ringing vibrations were first seen at the Heidun TLP and Draugen gravity based structure (GBS). Both structures needed to be reinforced to guaranty the safety during its life time.

Ringing occurs due to the impact of a steep wave slamming or resonance build-up. The impact load excites a wide-spectrum of structural modes. The study of Grue [42] showed that ringing can also occurs with a moderately steep wave. The higher-frequency loads will induce a build-up of resonance vibration during a time interval of one wave period. The secondary load cycle is a rapid and high frequency increase of the excitation force(Figure 2-15) and is important for the resonance build-up; the high load in-phase with the acceleration of the incoming wave. A secondary load cycle appears when the wave leaves the slender structure [43]. The rapidly appearance of the secondary cycle generates the resonate vibration of the structure. The second load cycle is observed in cases where the Keulegan-Carpenter number (KC-number) is in the range of 4-9 [42]. The vibrations have frequencies three to five times higher than the wave frequency, which means that ringing is at least a third-order effect.

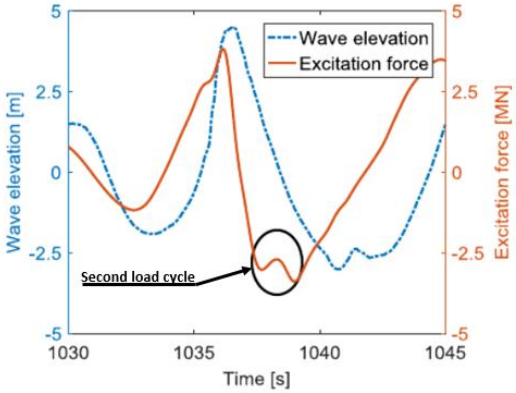

Figure 2-15: Occurrence of second load cycle [43]

As that ringing vibrations and responses are caused by third order wave effects, Faltinsen, Newman and Vinje [44] used a perturbation method to formulate the third-order wave loads. This perturbation method is applied to nonlinear free-surface boundary conditions, assuming a wave amplitude of the same order as cross-sectional dimensions. This formulation (equation (2-25)) is commonly used to incorporate third-order harmonic wave loads. The FNV-formulation consists of two terms, the horizontal force due to the first-order potential and horizontal force component due to the nonlinear potential.

$$F^{FNV} = F^{(1)} + F^{(2)} \tag{2-25}$$

$$F^{(1)} = 2\pi\rho_w g k D^2 \zeta \cos(2\pi f_w t)$$

$$F^{(2)} = \pi\rho_w g k^2 D^2 \zeta^3 (\cos(2\pi f_w t) - \cos(6\pi f_w t))$$

F	Force	ρ_w	Density water
g	Gravity acceleration	k	Wave-number
D	Diameter	ζ	Wave amplitude
f_w	Frequency wave		

Ringing for a column single-piercing the water surface occurs when linear diffraction is not significant contributing and wave amplitude and the cross-sectional dimensions have the same order. DNV [45] requires for the design of BFWT to evaluate ringing loads. The ringing effects should be investigated in time domain simulations with higher order wave loads effects. Ringing vibrations and responses are also observed in numerical simulations of a TLPWT, which was investigated by Bachynski and Moan [16]. The ringing forces influenced the pitch and roll motions primarily, which leads to higher tendon loads and increase loads at the base tower. The tendon loads increase between 12-30%, compared to the loads without ringing forces. Several negative tendon tensions were observed during the simulations. The ringing forces are most important for offshore structures that have a natural period between 3 and 4 seconds for pitch and roll motions.

2.4.4 Morison Equation

The Morison equation is a semi-empirical equation and takes the inertia and drag into account. It superposes a linear inertia force from potential flow and a quadratic drag force. The Morison equation is commonly used to model the hydrodynamic loads on offshore structures for the oil gas industry and the hydrodynamic loads on a fixed offshore wind turbine.

$$f_{morison}(t) = \rho_w A\dot{u} + \rho_w C_a A(\dot{u} - a) + \frac{1}{2}\rho_w C_d D\ (u - v)|u - v| \tag{2-26}$$

ρ_w	Density water	A	Area
u	Orbital velocity	$\dot{u}$	Orbital acceleration
a	Acceleration offshore structure	v	Velocity offshore structure
D	diameter	C_a	Coefficient added mass
C_d	Coefficient drag		

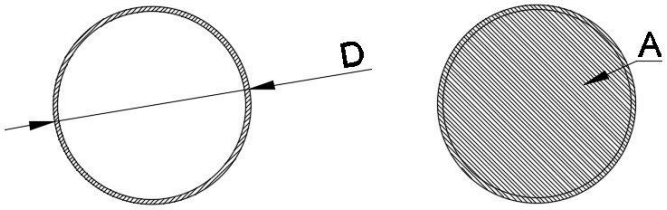

Figure 2-16: Definitions of the area and diameter

The Morison equation takes the Froude-Krylov force (first term of equation (2-26)), added mass (second term of equation (2-26)), and the viscous drag (third term of equation (2-26)) into account. The constants C_a and C_m are semi-empirical coefficients. Because diffraction is not taken into account, the Morison equation is only valid for slender structures. A slender structure is defined as a structure in which the cross-sectional dimensions are much smaller than the wavelength. The wavelength is computed by the dispersion relationship, given in equation (2-27).

$$f^2 = \frac{gk}{2\pi}\tanh(kd) \rightarrow \lambda = \frac{gT^2}{2\pi}\tanh\left(\frac{2\pi d}{\lambda}\right) \tag{2-27}$$

g	Gravity acceleration	k	Wave number
d	depth	λ	Wave length
T	Wave period	f	Frequency

The Morison equation has a few limitations. Firstly, it is not possible to include diffraction forces. Secondly, it is unclear how to separate currents and wave velocities. If the Morison equation is used in strip theory of floating structures, it assumes that viscous damping dominates the total damping and thus wave radiation damping can be neglected [46].

The study of Keulegan and Carpenter [47] determines for various diameters and flows the inertia and drag constants for the Morison equation and derive the period number, which is known as the Keulegan-Carpenter (KC) number. The KC-number is a non-dimensional number and gives the relation between drag and inertia forces on a slender structure.

$$KC = \frac{\pi\,\zeta_a}{D} \tag{2-28}$$

ζ_a	Wave amplitude	D	Diameter

Keulegan and Carpenter [47] concluded that for small KC-numbers (KC < 3) the inertia is dominant. For KC numbers between 3 and 15 a linearized drag term needs to be taken into account. For KC-numbers between 15 and 45, the full Morison equation should be taken into account. For KC-numbers higher than 45, only the drag force is sufficient.

2.4.5 Comparison of hydrodynamic modelling

The characteristics of the wave-structure interaction are depending on the geometry dimensions of the body, which are compared with the wave amplitude. The size of structure can be determined with Figure 2-17, with on the x-axis the diffraction parameter and on the y-axis the KC-number is displaced.

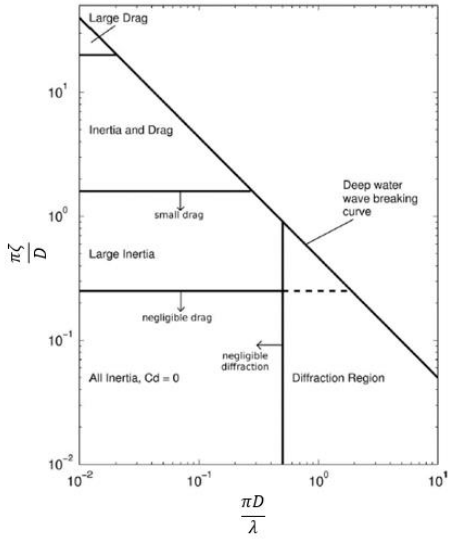

Figure 2-17: Classification of small versus large structures and their limits [48]

If the structure is inertia dominated, the inertia part of Morison equation is sufficient to calculate the hydrodynamic loads. The Morison equation is also sufficient in the large inertia and small drag area, inertia and drag area and the large drag area, see Figure 2-17. If the diffraction is dominant then a diffraction analysis should be performed. For the last area, the viscous drag and diffraction may be important. The viscous drag can be modelled using the drag part of the Morison equation [48]. Table 2-2, summarizes this paragraph and can be used as loop-up-table to compare the hydrodynamic models.

Table 2-2: Consideration included in hydrodynamic models [49]

	First order hydrodynamics	*Second order hydrodynamics*	*Third order hydrodynamics*	*Morison equation*
Added mass	Frequency dependent	Frequency dependent	Frequency dependent	Constant
Radiation damping	Frequency dependent	Frequency dependent	Frequency dependent	excluded
Quadratic damping	Excluded(1	Excluded(1	Excluded(1	Included
First order wave excitation	Radiation + diffraction	Radiation + diffraction	Radiation + diffraction	Inertia
Sum-frequencies	excluded	Direct method	Direct method	excluded
Difference frequencies	excluded	excluded	excluded	excluded
Mean wave drift force	Newman approximation	Newman approximation	Newman approximation	Viscous
Third-order wave	excluded	excluded	included	excluded

1) *Can included by the viscous part of the Morison equation*

2.4.6 Conclusions

Hydrodynamic loads are important for the fatigue lifetime of the TLPWT. Four hydrodynamic models are investigated, first order hydrodynamics, second-order hydrodynamics, third-order hydrodynamics and the Morison equation. Bachynski and Moan [49] investigated the influence of hydrodynamic model on the motions of a TLPWT. They investigate the motion responses in time domain with a first-order potential, second-order potential and the Morison Equation. The Morison equation gives good agreement with the potential flow in operational conditions, but for TLPWT with large diameters the Morison equations led to higher pitch moments than the second-order potential.

In the study of Bachynski and Moan [49] the third-order wave loads is not included, but third-order wave loads may be relevant when the cross-sectional dimensions and the wave-amplitude having the same order. This study focus on modelling the TLPWT for fatigue analyses. The wave-amplitudes have the same order of the cross-sectional dimensions of the TLPWT only occur in extreme environmental conditions (KC-number is in the range of 4-9). The hydrodynamics for this study will therefore be modelled with the Morison equation.

2.5 ENVIRONMENTAL MODELLING

The TLPWT will be installed to produce electricity in an environment with wind and waves. The environment needs to be modelled to get reliable results. The main source of environmental loads is the wind, waves and current. The wind and waves are assumed to stationary stochastic processes, which means that the mean and standard deviation are constant over time. Currents are assumed to be constant for the time frame.

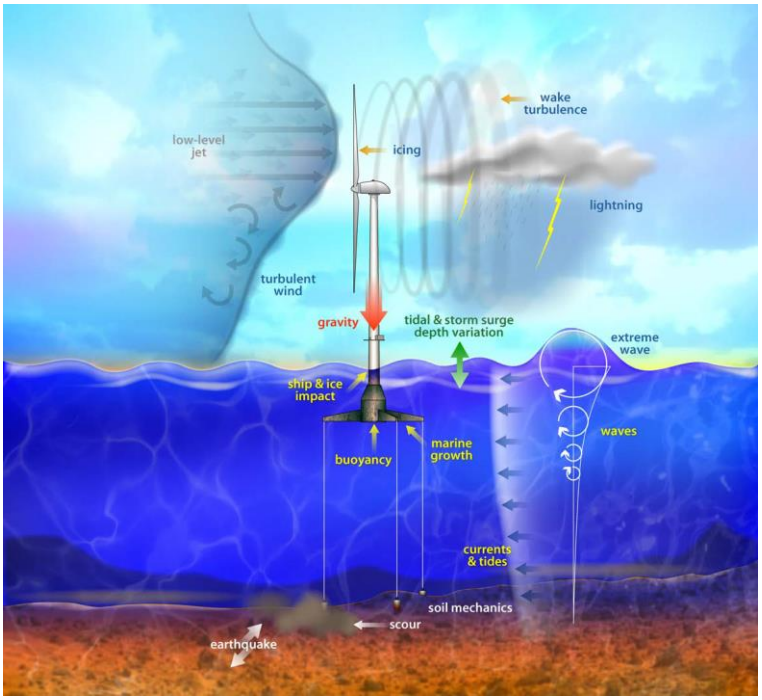

Figure 2-18: Load on a floating offshore wind turbine [1]

2.5.1 Wind

Wind has irregularities in the wind direction, wind speed and the vertical velocity components. This is called wind turbulence and can be treated as a time varying stochastic process of the wind speed. This assumption is correct if the time frame is less than 10-minutes. The loads of the wind can excite a natural frequency of a building or wind turbine. The turbulence of the wind can be described with a turbulence spectrum model, for example the model of Von Karman, Kaiman, Davenport and Hino [50].

The design regulations define several turbulence models and the normal turbulence model must be used for fatigue analysis of a wind turbine. The normal turbulence model represents the wind turbulence in terms of the 90% quantile of the standard deviation of the wind turbulence. For ultimate limit state (ULS) other turbulence models are required [45].

Shinozuka method and the Mann method apply the Taylor frozen turbulence hypothesis. The Taylor frozen turbulence hypothesis assumes that the wind eddies are frozen at the moment of passing the blades. This means that the wind field remains the same after passing an object. Thus, the local change within each eddy is ignored. This assumption is valid in situations where for example the wind field past the object once. The Taylor frozen turbulence hypothesis can be used to model the wind field passing a wind turbine but this hypothesis cannot be used to model a wind field passing a wind farm. Since the wind fields are identical for all wind turbines in line, apart from a delay of the wind field moving from a wind turbine to another wind turbine [51]. The Taylor frozen turbulence hypothesis relates time to space by assuming that the change in advection velocity of the turbulence

is magnitudes higher than the velocity scale of the turbulence himself. Meaning that the time can be replaced with a distance scaled by the mean velocity. The Shinozuka method and Mann method are generating a wind field in spatial domain moving with the mean wind velocity [52].

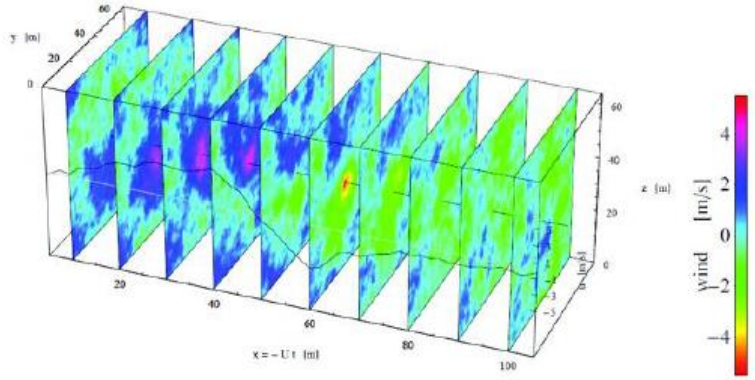

Figure 2-19: Wield turbulence in spatial domain [52]

The wind velocity is a function of time and the spatial coordinates. The wind velocity is separated in a static and a dynamic part (equation (2-29)). The wind shear profile defines the static wind velocity and the turbulence model defines the dynamic wind velocities:

$$u_{wind}(x,y,z,t) = u_m(z) + u_t(x,y,z,t) \tag{2-29}$$

u_{wind}	Wind velocity	u_m	Mean wind velocity
u_t	Turbulence wind		

The wind profile defines the variation in mean wind speed over the height. When the surface and the atmospheric stability are not complex, the wind profile can be represented by an idealized wind profile. The most commonly applied wind profiles are the logarithmic profile model (equation (2-30)), power law model (equation (2-31)) and the Froya model (equation (2-32)):

$$u_m(z) = \frac{u^*}{k_a}\ln\frac{z}{z_0} \tag{2-30}$$

$$u^* = \sqrt{\kappa}U_{10}$$

$$\kappa = \left(\frac{k_a}{\ln\frac{H}{z_0}}\right)^2$$

u_m	Mean wind velocity	z	z-coordinate
z_0	Roughness parameter	U_{10}	Reference velocity at z=10m
k_a	Von Karman's constant		

$$u_m(z) = u(H)\left(\frac{z}{H}\right)^{\alpha} \tag{2-31}$$

u_m	Mean wind velocity	z	z-coordinate
H	Reference height	α	Shear exponent

$$u_m(z) = u_0\left(1 + 5.73\cdot 10^{-2}\cdot\sqrt{1+0.148\cdot u_0}\ln\frac{z}{H}\right) \tag{2-32}$$

u_m	Mean wind velocity	z	z-coordinate
u_0	Reference wind velocity	U_{10}	Reference velocity at z=10m

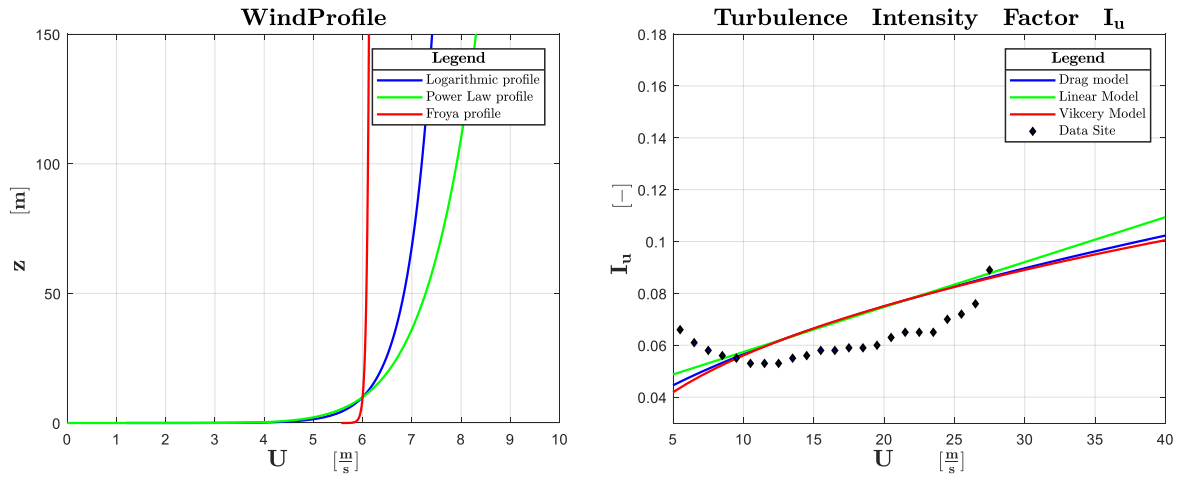

(a) *(b)*

Figure 2-20: (a) wind profile (b) turbulence intensity factor

The turbulence intensity factor expresses the amount of turbulence in a flow by dividing the standard deviation of the wind velocity by the mean wind velocity (equation (2-33)). For stable atmospheric layers the turbulence intensity factor can be computed with several expressions. The three most commonly used models are the modified Vickery model, the drag coefficient model and the linear model. Andersen and Lovseth [53] showed with their study that the linear model is conservative, as turbulence intensity factor increases if the height increases.

$$I_u = \frac{\sigma_u}{u_0} \tag{2-33}$$

I_u	Turbulence intensity factor	σ_u	Standard deviation wind
u_0	Mean wind velocity		

The design regulations and literature provide a large amount of theoretical wind spectra. The wind spectra are similar in the high frequency range, but large differences are found in the low frequency range (see Figure 2-21). The Davenport, Kaimal, and Von Karman spectra are spectrums for wind over land, and the Froya spectrum and Wills spectrum are spectra that are recommended for open-water conditions. The Froya spectrum (see equation (2-34)) is developed for neutral conditions over water in the Norwegian Sea. In areas where the atmospheric stability effects are more important, the Froya model is however not recommended [54].

$$S(f) = 320\frac{\left(\frac{u_0}{10}\right)^2\left(\frac{z}{10}\right)^{0.45}}{(1+f^n)^{\left(\frac{5}{3n}\right)}} \tag{2-34}$$

$$\tilde{f} = 172f\left(\frac{z}{10}\right)^{\frac{2}{3}}\left(\frac{u_0}{10}\right)^{-0.75}$$

$S(f)$	Spectrum	z	Height
n	Parameter	f	Frequency
u_0	Mean wind velocity		

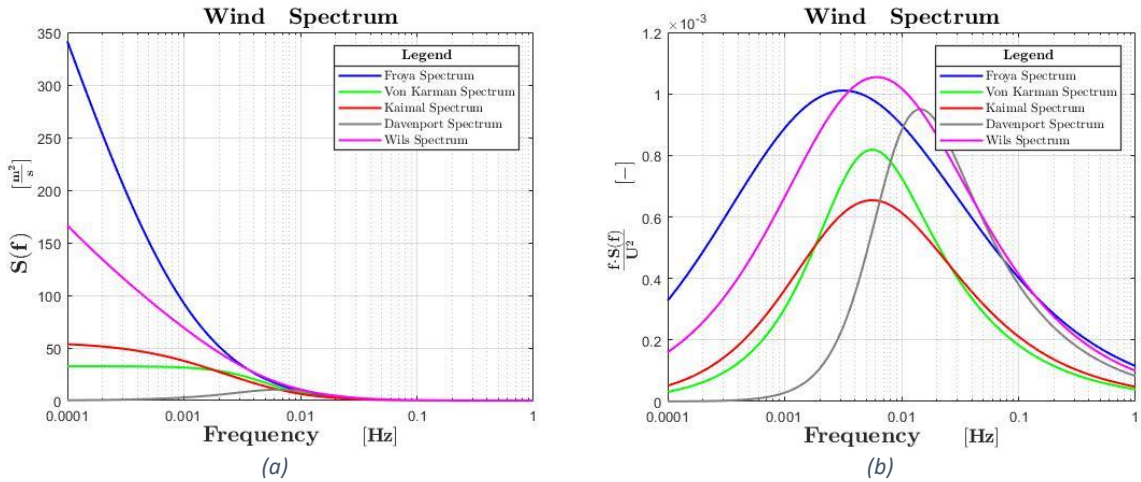

Figure 2-21: (a) Wind Spectrum. (b) Normalized Wind Spectrum

The Froya spectrum is a generalization of the Kaimal and Von Karman spectrum keeping the high frequency asymptote correct. In the low frequency range the Froya spectrum has however more energy. The Wills spectrum agrees better in the low frequency range for wind over water, but the turbulence intensity is underestimated high above the water [53].

A wind field cannot be extrapolated over the total area. It is unrealistic to assume constant wind velocities over a large area. Therefore a wind field need to be modelled, which means that the wind spectrum needs to be computed for many points in the wind field. The relation between two arbitrary points is given by the coherence spectrum. The coherence of two arbitrary points (point a and point b) is given in equation (2-35). The coherence spectrum for Froya coherence model is given in equation (2-36) [54].

$$coh(a,b) = \frac{(S_a(f)^2 + S_b(f)^2)}{\sigma_{u,a}^2 + \sigma_{u,b}^2} \tag{2-35}$$

σ_u	Standard deviation wind	f	Frequency

$$coh(f,\Delta) = e^{\left(-\frac{1}{u_0}\sqrt{A_y^2+A_z^2}\right)} \tag{2-36}$$

$$A_i = \alpha_i f^{r_i} \Delta_i^{q_i} z_g^{p^i}$$

Δ_i	Distance between point a and b in direction i	u_0	Reference velocity
α	Coefficient	f	Frequency
q	Coefficient	p	Coefficient
r	Coefficient	a	Point a in the wind field
b	Point b in the wind field		

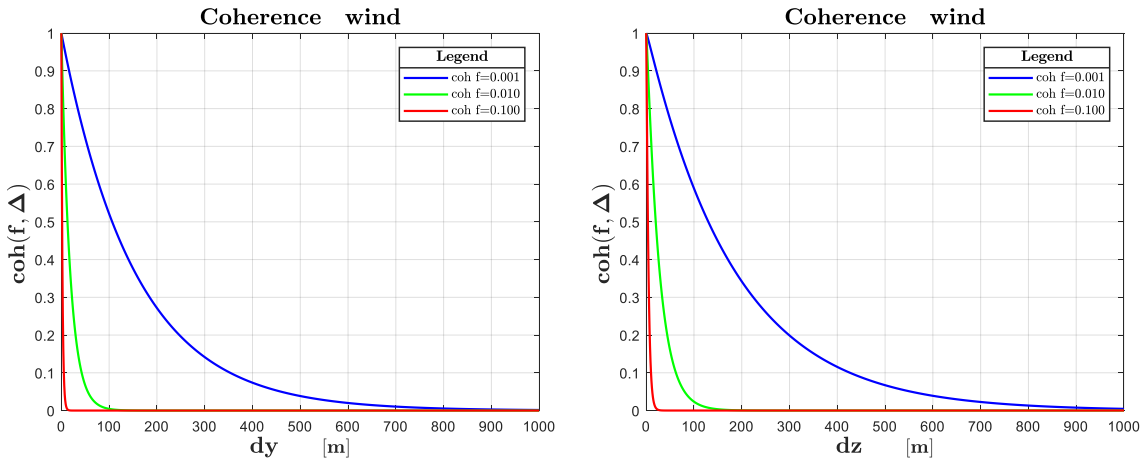

(a) *(b)*

Figure 2-22: (a) Coherence wind with varying dy. (b) Coherence wind with varying dz.

The spectrum of two points can be computed by equation (2-37). The spectrum S_{ab} needs to be computed for all possible combinations. The weights of the spectrum can be computed using Cholesky factorization method [55]. By applying an inverse Fourier transformation on the wind spectrum, the wind velocity field can be generated. The unidirectional wind field can be extended with the same method to generate a wind field with velocity components in the other two directions. The wind velocity is now a function of time and the spatial coordinates. Applying the Taylor frozen turbulence hypothesis, the wind velocity can be written as a function of only the spatial coordinates.

$$S_{a,b}(f) = coh(f,\Delta)\sqrt{S_a(f)S_b(f)} \tag{2-37}$$

$S_{a,b}$	Spectrum point a and b	f	Frequency
Δ	Distance between point a and b	coh	Coherence between point a and point b
S_a	Spectrum point a	S_b	Spectrum point b

2.5.2 Waves

The behavior of surface elevations of the ocean is chaotic, but commonly is assumed that the surface elevations are a summation of harmonic wave components. The statistical surface elevation can be described by just three parameters, namely the significant wave height, significant wave period and the energy spectral density of the harmonic wave components. Where significant wave height is defined as the mean wave height of one-third of the highest waves and significant wave period is defined as the mean of period of one-third of the highest waves [56].

2.5.2.1 Wave spectrum

The basic model to describe the ocean surface is with the random phase/amplitude model. This model uses two assumptions. The first assumption is a random phase between 0 and 2π and the second assumption is a constant amplitude for each frequency component. The phase of the wave components is uniformly distributed and wave heights are Rayleigh distributed [56]. The wave spectrum is defined by the assumption of an ideal situation, including a constant wind speed perpendicular to the coast, no impact by the seafloor and the coastline is infinite and straight. The parameters that affect the waves are the wind velocity, fetch, duration and the gravity acceleration [56].

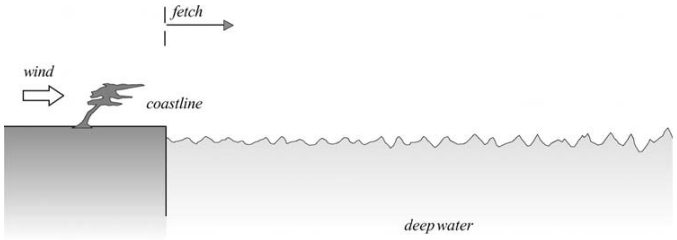

Figure 2-23: Ideal situation of waves [56]

Close to the shore the fetch is short and the waves are growing fast. The fetch is defined as the distance that the wind travels over open water. The growth of the waves slows down until it eventually stops, than the wave velocity of the longest wave is equally to the wind speed. Thus, no more energy is transferred from the wind to the waves. When no more energy is transferred then the waves are fully developed. The wave spectrum for a fully developed seas is described by the Pierson-Moskowitz wave spectrum [56].

$$E(f) = \alpha g^2 (2\pi)^{-4} f^{-5} e^{\left[-\frac{5}{4}\left(\frac{f}{f_{peak}}\right)^{-4}\right]} \tag{2-38}$$

$E(f)$	Energy spectrum	α	parameter
g	Acceleration frequency	f	Frequency
f_{peak}	Peak frequency		

The JONSWAP wave spectrum described a sea that is fetch limited, fetch limited seas are young seas. Fetch limited means that the wave energy is limited by the size of the wave generation area, the wave generation area is called the fetch. The JONSWAP wave spectrum can be applied for areas with storms and hurricanes but not for areas with swell, that are waves generated by distant weather systems. The steepness of swell waves is low and the quadrupled wave-wave interaction is very low or even absent [56]. If a peak enhancement parameter (γ) of 1 is used in the JONSWAP wave spectrum equation (2-39)), the JONSWAP spectrum becomes a Pierson-Moskowitz spectrum (fully developed sea).

$$E(f) = \alpha g^2 (2\pi)^{-4} f^{-5} e^{\left[-\frac{5}{4}\left(\frac{f}{f_{peak}}\right)^{-4}\right]} \gamma^{e^{\left[-\frac{1}{2}\left(\frac{\frac{f}{f_{peak}}-1}{\sigma}\right)^2\right]}} \tag{2-39}$$

$E(f)$	Energy spectrum	α	parameter
g	Acceleration frequency	f	Frequency
f_{peak}	Peak frequency	γ	Peak enhancement parameter
σ	parameter		

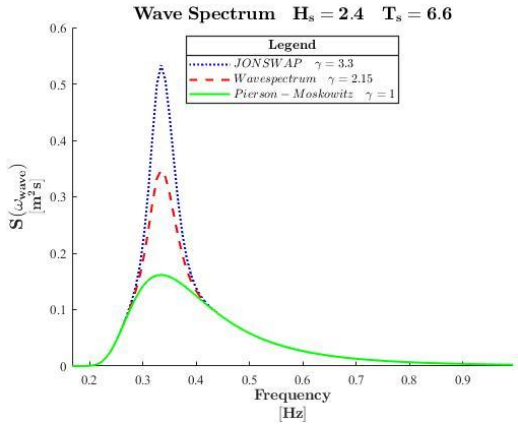

Figure 2-24: JONSWAP, Pierson-Moskowitz spectrum with Hs =2.4[m] and Ts = 6.6[s]

2.5.3 Tides and Current

The velocity vector of the current is the vector sum of the velocity vectors of all currents, which varies with the water depth. The current is represented by a current profile. The most common current profiles are the uniform current, shear current and the loop current [54].

$$u_c(z) = u_{c,tidal}(z) + u_{c,wind}(z) \tag{2-40}$$

u_c Velocity current
$u_{c,tidal}$ Velocity tidal
$u_{c,wind}$ Velocity wind

The tidal and wind currents are sufficient to model a representative current. Design regulations advice to use a simple power law profile for the tidal current and a linear profile for the wind current. The reference depth d_0 is typically 50 meters [54].

$$u_{c,tidal}(z) = u_{c,tide}(0)\left(\frac{d+z}{d}\right)^{\alpha} \tag{2-41}$$

$$u_{c,wind}(z) = u_{c,wind}(0)\left(\frac{d_0+z}{d_0}\right) \tag{2-42}$$

$u_{c,tidal}$ Velocity tidal
$u_{c,wind}$ Velocity wind
d Depth
α Parameter
d_0 Reference depth

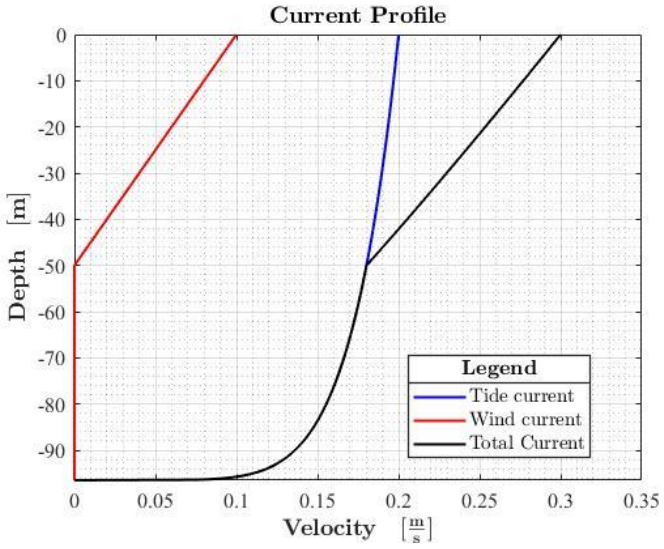

Figure 2-25: Current profile

2.6 MOORING SYSTEM

The mooring system consists of the tendons, anchoring and pontoon-tendon connection. The mooring system is essential for a TLP. The tendons limit the motions of the TLP and provide the TLP stability. The motions of the TLP are limited due to the inclination of the mooring lines. A displacement in the horizontal plane will also cause a displacement in the vertical direction. This typical nonlinear motion for a TLP is called set-down of centre of gravity (Figure 2-26) [57].

The TLP tendons are pre-tensioned due to the higher buoyance force than the weight of the TLP. During extreme events, with high waves and large tidal variations, the mooring lines may become slack. When the tension in the mooring lines is restored, the tendons experience a snap load. This high impact load can cause instant failure of the tendon or tendon-connection. If all tendons break in one pontoon of the TLPWT, the TLPWT will collapse. Therefore, snap load should in all cases be prevented [9].

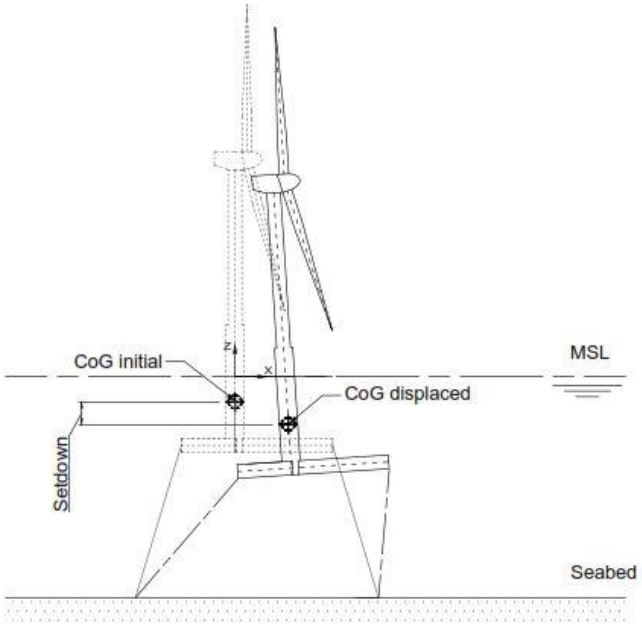

Figure 2-26: Large displacement causing a set-down

2.6.1 Modelling techniques

The tendons of a TLP can be modelled in three different ways, massless springs, elastic springs and tendon modelled with beam elements. The first method, massless springs, neglects the time varying tension in the tendon and neglects the hydrodynamic loads on the tendon. The second method, elastic spring, neglects the hydrodynamic loads. The last method, modelling the tendon with beam elements, takes the time varying tension and hydrodynamic loads into account [57]. The traditional way of modelling the tendons is with the massless springs or the elastic springs. Thus, the dynamics of the tendon and the dynamics of the TLP are uncoupled. Wang and Zou [58] concluded that the uncoupled system could produce inaccurate results. The uncoupled model neglects the hydrodynamic loads on the tendons and intrinsic dynamic of the system. Therefore, it is recommended by Wang and Zou to model the tendons with beam elements taking into account the hydrodynamic loads on the tendons and the varying tendon force.

2.6.2 Conclusion

The study of Wang and Zou [58] recommends to model the tendons with beam elements taking the hydrodynamic loads on the tensions and the varying tendon tension into account. Therefore, the model developed in this study models the tendons with beam elements.

2.7 NUMERICAL TIME INTEGRATION

The equation of motion is a differential equation with initial and boundary conditions. In most cases, an analytical solution cannot be achieved. Therefore, numerical methods are developed to approximate the solution. A numerical method solves the dynamic equilibrium at some discrete time points of interest. There are many numerical methods, but most of them are designed for first order differential equations. However, a higher order differential equation can be written into a first order system of differential equations [59].

There are two types of numerical time integration methods, an explicit method and an implicit method. The numerical method is explicit if this requires only information of the previous times steps to calculate the next time step, for example forward Euler method (equation (2-43)). The numerical method is implicit if it requires information of the next time step, for example backward Euler method (equation (2-44)). In general, explicit method in structural dynamics will be for wave propagation and implicit methods for structural response because the stability limit of time step size is approximately equal to the time step size needed to describe the wave propagation [60].

$$y_{n+1} = y_n + hf(t_n, y_n) \quad (2\text{-}43)$$

$$y_{n+1} = y_n + hf(t_{n+1}, y_{n+1}) \quad (2\text{-}44)$$

n Number of time step h Time step

The literature does not give a good definition of a stiff system. There are multiple criteria for stiff systems; two definitions are most commonly used in the literature. Firstly, stiff systems are systems for which explicit methods does not work. Secondly, the smallest eigenvalue of the system is much smaller than the largest eigenvalue of the system. In this work the last definition is used. The ratio between the largest and the smallest eigenvalue of the system is called the stiffness number [61].

The ideal numerical method for time integration for finite element methods should ideally follow six criteria [62].

1. At least second order accuracy
2. Unconditional stability for applications of linear problems
3. Controllable algorithmic damping of higher modes
4. No overshoot
5. Self-starting algorithm.
6. No more than one set of implicit equations to be solved each step

2.7.1 Numerical time methods

None of the numerical methods that are proposed in the literature meet the six criteria mentioned above. Therefore, three numerical methods have been investigated, the Newmark method, Houbolt method and Wilson method (see Appendix: Numerical time integration Methods). The Newmark method, Houbolt method and Wilson methods are three common implicit time integration methods used for finite element analysis. Implicit numerical time integration algorithms can have larger time steps in comparison with explicit methods. The use of large time steps, may causes numerical damping and the overshooting phenomena can occur. Note that, numerical damping is a nonphysical damping due to the algorithm [63].

2.7.1.1 Newmark method

The most used numerical time integration method is the Newmark method. Newmark [64] proposed an unconditionally stable method for linear elastic dynamic problems. The Newmark method is widely used because of its simplicity, computational cost and accuracy. The Newmark method assumes a linear acceleration between t and t+h. The velocity and displacement can be obtained by integrating the acceleration over the time step h. The integral is evaluated by a shape function. The numerical parameters γ and β can be used to control the stability and the amount of numerical damping.

$$v_{t+h} = v_t + a_t h + (a_{t+h} - a_t)\gamma h \tag{2-45}$$

$$x_{t+h} = x_t + v_t h + \left[\left(\frac{1}{2} - \beta\right) a_t + \beta a_{t+h}\right] h^2 \tag{2-46}$$

v	velocity	a	acceleration
x	Displacement	t	Time
h	Time step	γ	Numerical parameter
β	Numerical parameter		

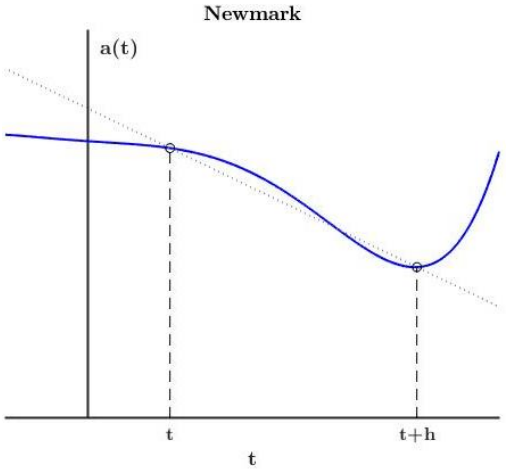

Figure 2-27: Newmark method

2.7.1.2 Houbolt method

John Houbolt [65] developed a systematic procedure in 1950 to calculate the structural response of an airplane subjected to dynamic loads. The Houbolt method uses a finite difference expression to approximate the velocity and acceleration. In contrast to the Newmark method, the Houbolt method is not self-starting. The Houbolt method requires information of the three previous time steps.

$$v_{t+h} = \frac{1}{6h}[11x_{t+h} - 18x_t + 9x_{t-h} - 2x_{t-2h}] \tag{2-47}$$

$$a_{t+h} = \frac{1}{h^2}[2x_{t+h} - 5x_t + 4x_{t-h} - x_{t-2h}] \tag{2-48}$$

v	velocity	a	acceleration
x	Displacement	t	Time
h	Time step		

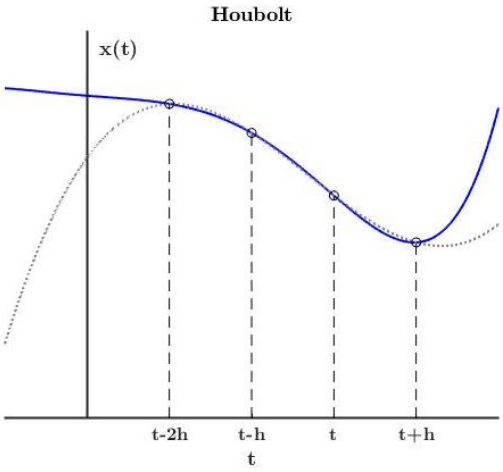

Figure 2-28: Houbolt method

2.7.1.3 Wilson Method

Wilson [66] proposed a general systematic procedure to compute the static and dynamic response of a nonlinear finite element analysis. The Wilson method is an extension of the linear acceleration method. The Wilson method assumes a linear acceleration between t and t+θh, where θ is a numerical parameter and can be used to control the stability and the amount of numerical damping. The numerical parameter θ is always bigger than one (θ ≥ 1.0). When θ =1.0, the Wilson method reduces to the linear acceleration method. The acceleration can be computed by the assumption of linear acceleration. The velocity and displacement can be obtained by integrating the acceleration over time. The numerical parameter θ can be used to control the stability and the amount of numerical damping.

$$a_{t+h} = \left(1 - \frac{1}{\theta}\right) a_t + \frac{1}{\theta} a_{t+\theta h} \tag{2-49}$$

$$v_{t+h} = v_t + \frac{h}{2}(a_t + a_{t+h}) \tag{2-50}$$

$$x_{t+h} = x_t + h v_t + \frac{h^2}{6}(a_{t+h} + 2a_t) \tag{2-51}$$

v	velocity	a	acceleration
x	Displacement	t	Time
h	Time step	θ	Numerical parameter, θ>1.0

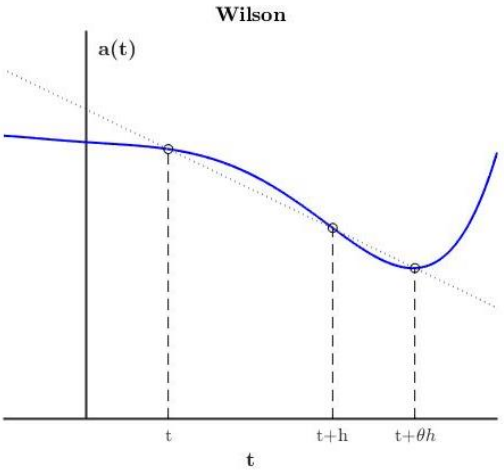

Figure 2-29: Wilson method

2.7.2 Stability

Stability of the numerical method is one of the most important properties of the numerical method. The numerical solution is stable if the error introduced at an arbitrary stage of the calculation is decreasing in subsequent steps of the method. In other words, the introduced error should not blow up the numerical method [67]. Investigation of the stability of the numerical method for dynamic problem is achieved by the amplification matrix A. An integration method is unconditional stable if the spectral radius (equation (2-52)) does not exceed the value of 1.0 for all time steps. Otherwise, the numerical method is conditionally stable [68].

$$\rho(\boldsymbol{A}) = \max|\lambda_i| \tag{2-52}$$

λ	eigenvalue	A	Amplification matrix

As it is well known, a numerical multistep method can be written in the form of equation (2-53), where L is the equivalent load vector and A the amplifications matrix of the numerical method. The amplification matrix A and the load operator vector L are depending on the numerical method and can be derived by using a test function. In this case the test function is a linear single degree of freedom mass-spring system including damping. The test function of time step t+h is given in equation (2-54) [68]. Changing the damping ratio ξ does not have much impact on the stability of the numerical method. Therefore, it is assumed that the damping ratio is zero.

$$\vec{X}_{n+1} = [\boldsymbol{A}]\vec{X}_n + \vec{L}f_n \tag{2-53}$$

$$a_{t+h} + 2\xi\omega v_{t+h} + \omega^2 x_{t+h} = \frac{f_{t+h}}{m} \tag{2-54}$$

$\vec{X}$	Dynamic state vector	$\boldsymbol{A}$	Amplification matrix
$\vec{L}$	Load operator vector	f_n	Load at time step n
a	Acceleration	ξ	Damping ratio
ω	Natural frequency	v	velocity
x	displacement	m	Mass

The eigenvalues problem of Amplification matrix A leads to a characteristic polynomial of the form given in equation (2-55). According the Routh-Hurwitz criteria (given in equation (2-56)), the numerical method is stable if it meets all five Routh-Hurwitz criteria. The characteristic polynomial meets the Rough-Horwitz criteria if the spectral radius is equal or smaller than 1 [69].

$$\det|\boldsymbol{A} - \boldsymbol{I}\lambda| = \lambda^3 - 2A_1\lambda^2 + A_2\lambda^2 - A_3 = 0 \tag{2-55}$$

$$1 - 2A_1 + A_2 - A_3 \geq 0 \tag{2-56}$$

$$3 - 2A_1 - A_2 + 3A_3 \geq 0$$

$$3 + 2A_1 - A_2 - 3A_3 \geq 0$$

$$1 + 2A_1 + A_2 + A_3 \geq 0$$

$$1 - A_2 + A_3 2(A_1 - A_3) \geq 0$$

The Houbolt method is always unconditional stable, the Newmark method is unconditional stable if $2\beta \geq \gamma \geq 0.5$ and the Wilson method is unconditional stable if $\theta \geq 1.37$. The spectral radius of the Newmark method, Houbolt method and Wilson method are shown in Figure 2-30.

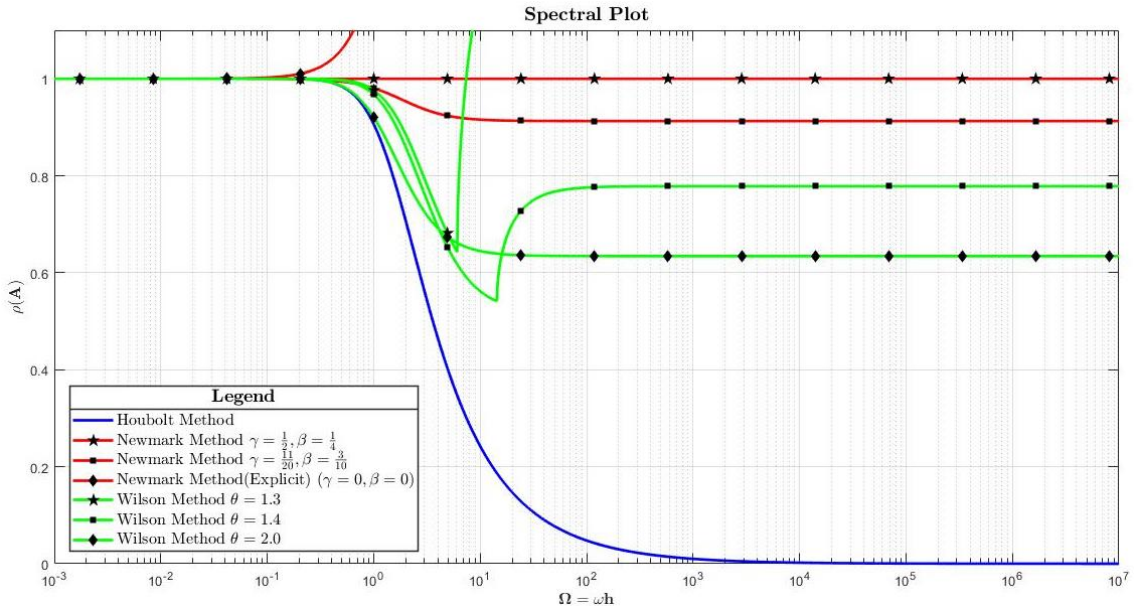

Figure 2-30: Spectral radius of Newmark, Houbolt and Wilson method

2.7.3 Accuracy

The accuracy is another important property of the numerical method. The order of accuracy from the truncation error is commonly used for first-order numerical time integration method. The order of accuracy quantifies the rate of convergences of a numerical time integration method. A numerical time integration method for structural dynamics should have at least second order accuracy. The rate of convergences is proportional to the step size to the n-th power [70].The local truncation error can be computed by the error equation (equation (2-57)). The order of accuracy can be found by a finite Taylor expansion of e(t+h) and e(t) around t+α.

$$\varepsilon(t+h) = \boldsymbol{A}\varepsilon(t) - h\tau(t) \tag{2-57}$$

$$|\tau(t)| = ch^k$$

ε	Error equation	h	Time step
$\boldsymbol{A}$	Amplification matrix	k	Order of accuracy
c	Constant	t	time

Hulbert and Hughes [71] proved that the Houbolt method always has second-order accuracy. The same study proves that order of accuracy of the Newmark method depends on the numerical parameters γ and β. The Newmark method has second-order accuracy for γ=1/2. The order accuracy of Wilson method is also depending on the numerical parameter θ.

It is well known that the order of accuracy for direct integration methods gives a rough estimate. A more accurate method for direct integration method is the relative period error and relative amplitude error. The relative period error (Figure 2-31 (a)) is defined as the period distortion and is the same as numerical dispersion. The relative amplitude error (Figure 2-31 (b)) is related to the numerical dissipation, also called algorithmic damping. The available measurement methods are determined only from the numerical solution itself [72]. The numerical damping and relative period error can be computed by equation (2-58) and equation (2-59).

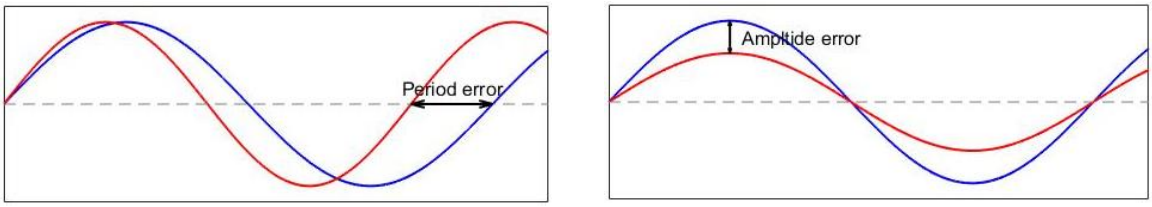

(a) *(b)*

Figure 2-31: (a) Amplitude error (b) period error

$$\bar{\xi} = -\frac{\ln(\rho((\boldsymbol{A})^2)}{2\bar{\Omega}} \tag{2-58}$$

$$\bar{\Omega} = \bar{\omega}h$$

$$\bar{\omega} = \tan^{-1}\left(\frac{Im(\lambda)}{Re(\lambda)}\right)$$

$$P = \frac{\bar{T} - T}{T} = \frac{\bar{\Omega}}{\Omega} - 1 \tag{2-59}$$

ξ	Damping ratio numerical	$\bar{\omega}$	Natural frequency numerical
$\boldsymbol{A}$	Amplification matrix	h	Order of accuracy
T	Natural period	$\bar{T}$	Natural period numerical
λ	Eigenvalue		

The numerical damping and relative period error are given in Figure 2-32 for the Newmark method, Houbolt method and Wilson method. This figure shows that, in general, all the numerical methods are accurate for very small step sizes, but the characteristics of the numerical methods are quite different for large step sizes. For example, Newmark method with numerical parameters β = ¼ and γ = ½ does not introduce numerical damping in the time domain simulations.

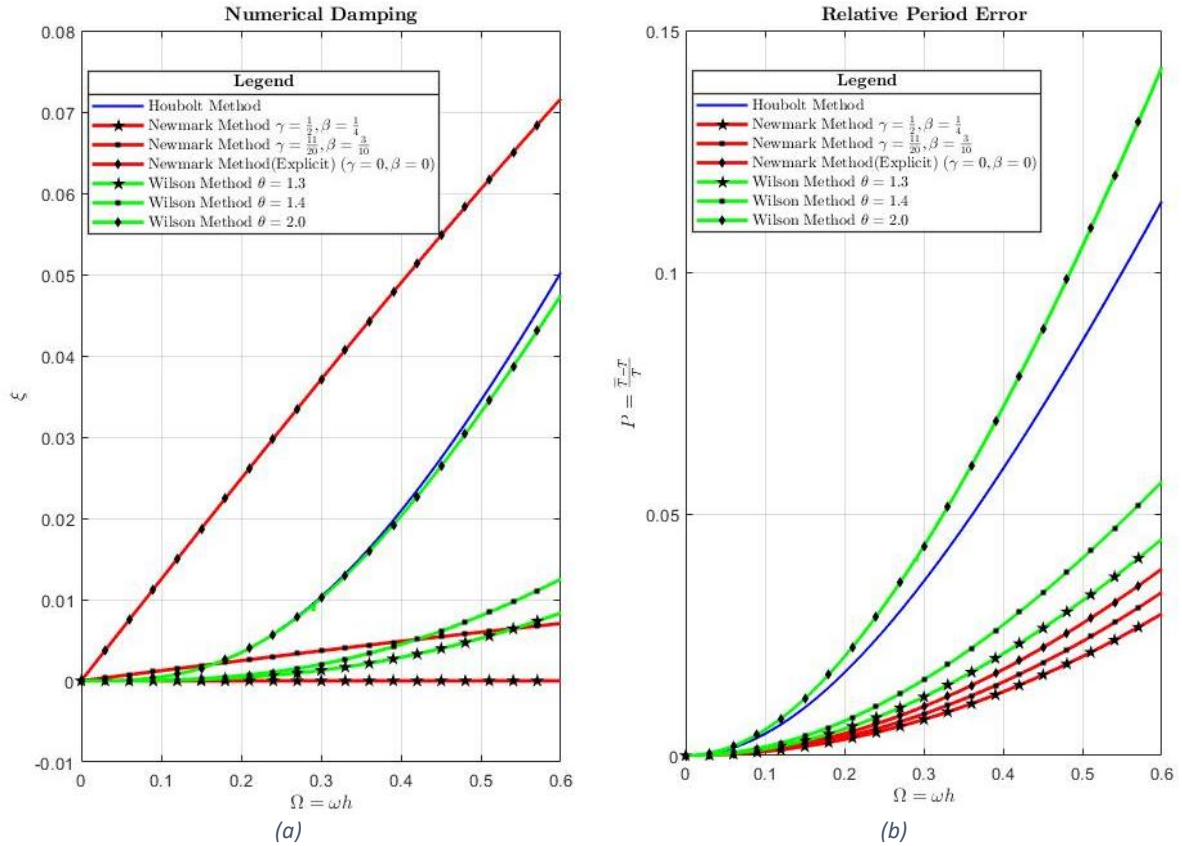

(a) *(b)*

Figure 2-32: (a) Numerical Damping. (b) Relative period error

2.7.4 Overshoot

Goudreau [73] discovered a very specific characteristic of the Wilson method. The Wilson method showed in numerical experiments a tendency to overshoot the exact solution significantly in the early response. Overshooting can be a property for unconditional stable numerical methods, which are applied to systems with large numbers of degrees of freedom. In large system large values of Ω ($\omega \cdot h$) are observed, which occur due to the high natural frequencies of the system. In the first few steps the overshooting phenomenon should be prevented.

The overshooting property is an important and independent property of the numerical method and should be evaluated. Hilber and Hughes [74] analyzed the overshooting property and concluded that the short-term behavior of the numerical method is governed by the norm of amplification matrix A. The long-term behavior is governed by the spectral properties of the amplification matrix A. The overshooting property is not analyzed for the Houbolt method, as analyzing the overshooting property of the multi-step method is depending on the starting procedure.

The overshooting phenomenon is evaluated at the end of the first time step, assuming a non-zero initial condition for the velocity and displacement. The overshooting phenomenon is investigated by taking the limit of $\Omega \rightarrow \infty$ and eliminate the acceleration term [74]. The results for the Wilson method (equation (2-60) and equation (2-61)) and the Newmark method (equation (2-62) and equation (2-63)) are given.

$$\lim_{\Omega\to\infty} v_1 \approx \left[\left(\frac{1}{4\theta} - 1\right)\Omega\right]\omega x + \left[\left(1 - \frac{1}{2\theta^2}\right)\right] v \tag{2-60}$$

$$\lim_{\Omega\to\infty} x_1 \approx \left[\left(-\frac{1}{2} + \frac{1}{2\theta}\right)\Omega^2\right] x + \left[h\left(1 - \frac{1}{\theta^2}\right)\right] v \tag{2-61}$$

$$\lim_{\Omega\to\infty} v_1 \approx \left(\frac{\gamma}{2\beta} - 1\right)\Omega\omega x - \left(1 - \frac{\gamma}{\beta}\right) v \tag{2-62}$$

$$\lim_{\Omega\to\infty} x_1 \approx \left(1 - \frac{1}{2\beta}\right) x \tag{2-63}$$

θ	Numerical parameter Wilson method	ω	Natural frequency
v	Velocity	x	Displacement
γ	Numerical parameter Newmark	β	Numerical parameter Newmark

The elimination of the acceleration terms and limiting $\Omega \rightarrow \infty$ for the displacement and velocity for the Wilson and Newmark methods show that in the Wilson method and Newmark method overshooting occur. The overshooting for the Wilson methods is in the displacement quadratic and for the velocity linear. The overshooting for the Newmark method is linear for the velocity, but no overshooting occurs for the displacement, which is illustrated by. Figure 2-33 shows the overshooting of the Newmark method and Wilson method for the displacement and velocities [74].

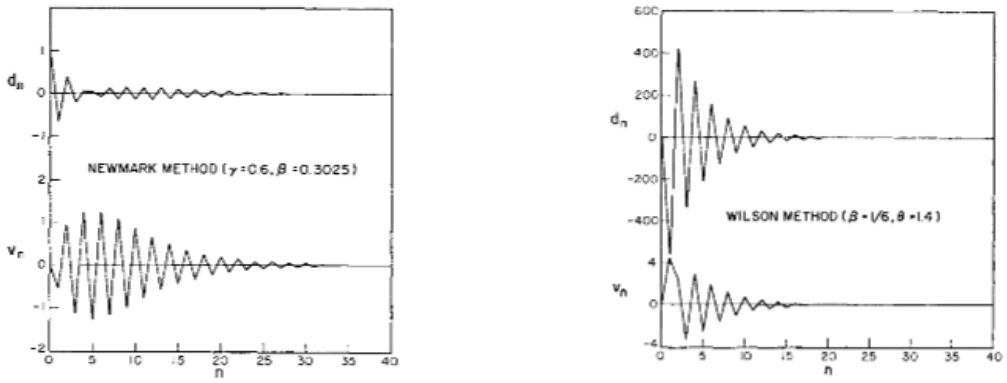

(a) *(b)*

Figure 2-33: Overshooting (a) Newmark [74] (b) Wilson [74]

2.7.5 Conclusion

Numerical time integration method solves the equation of motion for discrete time steps. The ideal numerical time integration method should have six properties. The Newmark method, Houbolt method and Wilson method are investigated in this study on the six properties. A summary of the three numerical methods is given in Table 2-3. The Newmark method and Wilson method are self-starting integration methods but the Houbolt method is not because it requires knowledges of x_{t-h} and x_{t-2h}. The algorithmic damping for the Newmark method and Wilson method is controllable because the algorithmic damping depends on the numerical parameters of the numerical method. The algorithmic damping is not controllable for the Houbolt method.

Table 2-3: Summary of numerical time integration method

	Newmark	*Houbolt*	*Wilson*
Order of accuracy	O(h)	$O(h^2)$	O(h)
Unconditional stable	$2\beta \geq \gamma \geq 0.5$	always	$\theta \geq 1.37$
Controllable algorithmic damping	+	-	+
Overshoot property	-	n/a	-
Self-starting	+	-	+
One set of implicit equations	+	+	+

The developed model solves the equation of motion of the TLPWT and the TLPWT is a stiff dynamic system due to the large mooring stiffness. Houbolt method computes the displacements and applies the finite difference equation to compute the velocities and accelerations. The Houbolt method uses less iteration to find dynamic equilibrium, therefore the Houbolt method is used. The step size is depending on the physical problem, which is the step size of the wind turbine. The Houbolt method has two disadvantages, it is not a self-starting method and has not a controllable algorithmic damping. However, a starting procedure of the wind turbine is required, otherwise nonphysical oscillations are introduced in the time simulation. Secondly, the required time step size will be small and therefore the algorithmic damping is small.

2.8 NATURAL FREQUENCIES AND MODAL SHAPES

In general, bodies with mass and a finite stiffness are able to vibrate. The vibrations exist due to the periodic change of potential and kinetic energy. The acceleration of the mass is related to the kinetic energy and the displacement of the stiffness related to the potential energy. The vibrations are classified into free vibrations, forced vibrations and self-excited vibrations. Free vibration is the vibration after a disturbance of the system equilibrium position, no external forces are acting on the system. The corresponding vibration is the free vibration and is calculated by the homogeneous solution of the equation of motion. The second class is forced vibration, which is the vibration due to an external force, the oscillation that occurs has the same frequency as the force frequency. The forced vibration is calculated by the particular solution of the equation of motion. The last class is the self-excited vibration, which are vibrations due to an external forces that sustains the motion. Thus, the external forces are depending on some parts of the motion itself [75].

Natural frequencies and mode shapes are an important characteristics of a dynamic system. The natural frequency is the frequency of vibration where the dynamic system oscillates without an external force after an initial displacement. The first natural frequency is sometimes called the fundamental frequency. Rigid body dynamic system with n degrees of freedom has n natural frequencies but a flexible body dynamic system always has infinite number of natural frequencies. The mode shape describes the pattern of motion in which all bodies in the dynamic system move with the same frequency and with the same fixed phase relation. Note, the configuration of a dynamical system does not change its shape during the motion [76].

The natural frequencies and mode shapes of a dynamic system can be found by solving an eigenvalue problem. The natural frequencies are the eigenvalues and the modes shapes are the eigenvectors of the eigenvalue problem. The eigenvalue problem of the equation of motion can be written as equation (2-64), which can be written as standard eigenvalue problem (equation (2-65)). The non-trivial solutions need to be found. Non-trivial solution in linear algebra has the property that the determinant is zero. The standard eigenvalue problem can be written into a characteristic equation (solution of equation (2-66)). For large dynamical system it is time consuming to solve the characteristic equation standard eigenvalue problem [76]. Several numerical methods have been developed to find the eigenvalues and eigenvectors, for example [77] and [78].

$$[\boldsymbol{K} - \omega^2 \boldsymbol{M}]\vec{\Psi} = \vec{0} \tag{2-64}$$

$$\omega^2[\boldsymbol{I}]\vec{\Psi} = [\boldsymbol{M}^{-1}\boldsymbol{K}]\vec{\Psi} \tag{2-65}$$

$$\det|\omega^2[\boldsymbol{I}] - [\boldsymbol{M}^{-1}\boldsymbol{K}]| = 0 \tag{2-66}$$

$\boldsymbol{K}$	Stiffness matrix	ω	Natural frequency
$\boldsymbol{M}$	Mass matrix	$\vec{\Psi}$	eigenvalue

2.8.1 Nonlinear resonance frequencies

For linear dynamics the principle of superposition holds. Mathematically, this means that the mass, stiffness and damping matrix are symmetrical and the forces are independent of the system's variables. However, the dynamic system of the TLPWT is nonlinear. For nonlinear dynamics the principle of superposition does not hold, but the analysis of nonlinear vibrations are wide, complex and still an important research field for engineers and researchers [76].

There are many sources of nonlinearities in mechanical systems, like geometric nonlinearities, material nonlinearities, structural nonlinearities, nonlinearities of constraints and nonlinearities due to damping. Nonlinear dynamic systems can be complex and have behaviors which linear dynamic systems dynamics have not, for example jumps, bifurcations, saturation, subharmonic, superharmonic, internal resonances, resonances captures, limit cycles, modal interactions and chaos [79].

Geometrical nonlinearity arises from the kinematics of the system. The assumption of small amplitudes with respect to the dimensional properties of the dynamical system around the equilibrium position no longer holds. The second nonlinearity in mechanical system is material nonlinearity, which arises from the material properties of the dynamic system. The stress-strain relation of the material may become nonlinear for large deformations. Structural nonlinearity is related to the stiffness of the mechanical system. The stiffness is not a linear property but the stiffness has higher order terms. When the stiffness increases the behavior is called hardening and when the stiffness decreases the behavior is called softening (see Figure 2-34). Nonlinearity of constraint is an abrupt change in the boundary conditions for example a pendulum moving close to a wall. Nonlinearity due to damping is related to the damping term in the equation of motions. Damping is a complex phenomenon and is related to the microscopic processes in the material, even the simplest damping models are typically highly nonlinear [79].

The linear and nonlinear responses of a TLP have been investigated many times, for example [80] and [81]. The primary nonlinearities in the dynamic system of a TLPWT are the geometric nonlinearities. The large displacement of the TLPWT causes a nonlinear restoring force. The restoring forces are part of the mooring stiffness and the mooring stiffness plays an important role in the dynamic behavior of the TLP. The mooring stiffness is nonlinear, because the tendon tension is not constant over time. A linear and a cubic spring often represent the mooring stiffness. Low [80] and Senjanovic [81] looked at the nonlinear mooring stiffness of a TLP. Both studies showed that the mooring stiffness is of the hardening type. In case of a nonlinear stiffness, the natural frequency is depending on the amplitude.

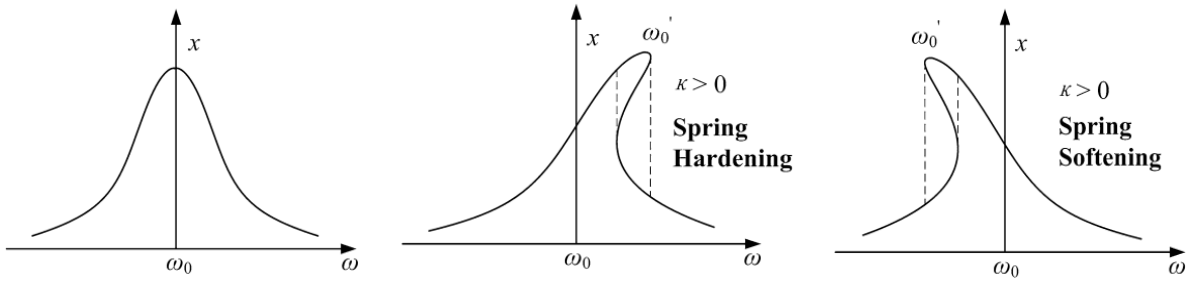

(a): Linear *(b): Nonlinear, hardening* *(c): Nonlinear, softening*

Figure 2-34: Frequency-amplitude relation for a nonlinear system [79]

2.8.2 Nonlinear modal analysis

The concept of linear modal analysis is known. As explained, a mode shape describes the pattern of motion with the same frequency and the same displacement ratio with respect to all other components. The mode shape has the orthogonally property. Which means that the equation of motion can be decoupled. The decoupled equation of motion is invariant. The final property is the property of modal superposition. Every motion can be written as a linear combination of the mode shapes.

The extension of linear modal analysis is nonlinear modal analysis. There are two definitions of nonlinear mode shapes, the Rosenberg definition and the Shaw Pierre definition. The Shaw and Pierre definition is used in this study, because this definition provides a direct extension to nonlinear modal analysis of damped dynamic systems. A Mode shape of a nonlinear system has a motion, which takes place on a two-dimensional invariant manifold in the system phase space. This manifold has the following properties: it passes through a stable equilibrium point of the system and, at that point, it is tangent to a plane which in an eigenspace of the system linearized about that equilibrium [82].

There are fundamental differences between linear mode shapes and nonlinear mode shapes. A nonlinear mode shape is not orthogonal to the other modes shapes, they are still mode shapes because the mode shapes are orthogonal to the surface of maximum potential energy. The other fundamental difference is that the nonlinear mode shapes are frequency-energy dependent and that the number of modes shape may be larger than the number of degrees of freedom. The last fundamental difference is that energy can be transferred from a mode shape to another mode shape. This phenomenon is known as mode interaction [82].

2.8.3 Sub- and super-harmonic response

The forced vibration behavior of a nonlinear system differs from a linear system. A nonlinear dynamic system that is excited by a force will vibrate in the force frequency but also a second resonance frequency will occur. This phenomenon is called sub- and super harmonic response. The sub- and super harmonic responses are observed in dynamical systems with small cubic stiffness. For super-harmonic response the secondary resonance frequency is higher than the force frequency, and for sub-harmonic response the secondary resonance frequency is lower than the force frequency [79].

$$f_{sub} = \frac{nf}{m}, \qquad (n, m = 1,2,3 \dots) \tag{2-67}$$

$$f_{super} = nf, \qquad (n = 1,2,3 \dots) \tag{2-68}$$

f Frequency

Sub-harmonic and super-harmonic oscillations may not be confused with second-order wave forces. Sub-harmonic and super-harmonic oscillations will also occur in waves with a single frequency and the resulting first-order hydrodynamic load. The frequency of the sub-harmonic or super-harmonic will however always be the exact fraction of the frequency. Second-order wave forces have the frequency of the difference or sum of two wave frequencies [83].

Ahmed [84] investigated the sub-harmonic and super-harmonic resonance of a TLP. Super-harmonic resonance and sub-harmonic resonance were visible in the spectrum of heave. Liaw [83] showed that sub-harmonic responses may occur but the presence of having subharmonic responses can be avoided with a good design. Structures with a large member size and low structural mass are the most vulnerable to subharmonic oscillations. Senjanovic [81] mentioned that neglecting the varying tendon tension and the coupling of motions may not be neglected. The design regulations recommend to consider the subharmonic and superharmonic resonance of the TLP.

2.9 CLOSURE

The focus of this chapter was on the wind turbine dynamics, computation methods the wind turbine loads, hydrodynamic models, model techniques of the environment, model techniques of the mooring system and the fundamentals of numerical time integration methods. Lastly, the analysis techniques of nonlinear and linear dynamics are explained. The following conclusions are made with regard to the developed model and the dynamics of a TLPWT:

- The passing blade frequencies are the main source of non-harmonic periodic processes and are caused due to tower shadow effect and wind shear effect, which are important for the fatigue lifetime of the wind turbine blades.
- The wind turbine blades are a rotating structure and this type of structure requires special care. For example, when a rotating structure experiences a rotation perpendicular to the plan of rotation, then the structure experiences a gyroscopic moment. The gyroscopic moments are negligible for BFWT, but can be large for a FWT due to the yaw and pitch motions. Therefore, the gyroscopic moments may be relevant.
- Every wind turbine has a control system. The control system maximizes the power production, prevents extreme loads and minimizes the fatigue damage. The control system is important for the motion responses of the wind turbine, therefore the control system should be implemented in the model.
- Two computational methods for the wind turbine loads are investigated. The actuator disk assumption is used in the model, because the thrust force and the aerodynamic torque dominate the motions of the FWT.
- The hydrodynamic loads are important for the fatigue lifetime of the TLPWT. The hydrodynamic loads are modelled with the Morison equation, which is commonly used in the offshore industry for slender structures like the TLPWT. The study of Backynski and Moan [49] showed that the Morison equation gives good agreement with the potential flow in operational conditions of the wind turbine.
- The mooring system of the TLPWT can be modelled as massless springs, elastic springs and with beam elements. The study of Wang and Zou [58] concluded that modelling the mooring system as massless springs or elastic springs produces inaccurate results. Therefore, the mooring system is modelled with beam elements in the model, taking the time varying tendon forces and the hydrodynamic loads on the tendon into account.
- A numerical time integration method solves the equation of motion of the TLPWT. The Houbolt method is implemented in the model, because the computation time is less with respect to the Newmark Method and Wilson Method. The Houbolt method is not a self-starting method and the numerical damping is not controllable, but the wind turbine requires a start-procedure and the time step size is small.
- The dynamic analyses techniques for linear and nonlinear dynamics are not the same. For example, the natural frequency of a nonlinear dynamics system depends on the amplitude of the motion. Other analyses techniques are needed, to analyse the nonlinear dynamic system of the TLPWT.

3 DEVELOPMENT OF AERO-HYDRO-ELASTIC-SERVO MODEL

3.1 INTRODUCTION

This chapter deals with the development of the aero-hydro-elastic-servo model. The Aero-Hydro-Elastic-Servo model takes the aerodynamics of the wind turbine, the hydrodynamics, the flexibility of the structures and the control system of the wind turbine into account. The conclusions of the previous chapter are used to make the model. The final step is the validation of the model, with Orcina Orcaflex which is a recognized commercial software packages.

3.2 MODEL DESCRIPTION

An adequate model is required to describe the complex dynamic system of the TLPWT. The model needs to meet the requirements of modelling the wind turbine dynamics, aerodynamics, hydrodynamics, flexibility of the total structure, structural damping and the environment. The TLPWT has a strong coupling between the aerodynamics, hydrodynamics, flexibility of the structure and the control system of the turbine. This coupling is called the aero-hydro-servo-elastic coupling [85], which means that the forces due to the wind have effect on the floater deformations and that the accelerations of the floater affect the turbine displacements.

The model is a finite element model (the fundamentals of a finite element method are explained in Appendix: Fundamentals of finite element method). A finite element analyses can be separated into three main steps, namely preprocessing, numerical computation and the postprocessing. The preprocessing requires the definitions of geometric properties and the material properties. In case of Aero-Hydro-Elastic-Servo model, the preprocessing also requires the definitions of environmental conditions, properties of the wind turbine, hydrodynamic coefficients and the boundary conditions of the model [86].

The numerical computation is the step where the software generates the matrices (mass matrix and stiffness matrix), these matrices describe the dynamic behavior of each element and represent the structure [86]. In this step is also the equation of motion solved by a numerical integration method. The Houbolt numerical time integration method is used, because the TLPWT is a very stiff system due to the mooring stiffness. The stiffness is directly related to the displacement and the Houbolt method applies a finite difference equation of the displacements to compute the velocities and accelerations. Therefore, the Houbolt method will use less iteration steps than the Newmark and Wilson Method. The numerical method computes the displacements, velocities, accelerations and the forces of discrete time steps.

The final step of the finite element analysis is the postprocessing. The postprocessing will plot the deformations, velocities and acceleration and forces. A Fast Fourier transformation (FTT) is performed to determine the response spectrum of the TLPWT.

The model is implemented in Matlab, a schematic overview of the Matlab model is given in Figure 3-1, with brief explanations on each component below.

- **Preprocessing**
  - ''Create TLPWT'' creates a structure array with line objects, with cross-sectional properties and material properties.
  - '''Meshing'' uses the structure array to discretize the TLPWT into elements and creates a structure array with elements.
  - ''Wave field generator'' and ''Wind field generator'' are algorithms that generate the stochastic wind velocity field and irregular waves, as explained in section 2.5.1 and 0 section.
- **Numerical computation**
  - ''Create K and M'' uses the structure array with elements to create the stiffness and mass matrix.
  - ''Solve static'' uses the mass and stiffness matric to solve the TLPWT hydrostatic to compute geometric stiffness of the TLPWT and computes the natural frequencies.
  - ''Structural damping'' uses the natural frequencies to compute the structural damping matrix and is explained in section 3.3.2.
  - ''ODE Solver'' solves the equation of motions for discrete time steps.
- **Postprocessing**
  - ''FFT'' uses the force, displacement, velocity and accelerations to transfer into a Fourier series.
  - ''Poincare'' uses the displacement and velocity to make a Poincare plot, which can be used to analyse the nonlinear behaviour.
  - ''Display output'' uses the forces, displacement, velocities and accelerations to create figures.

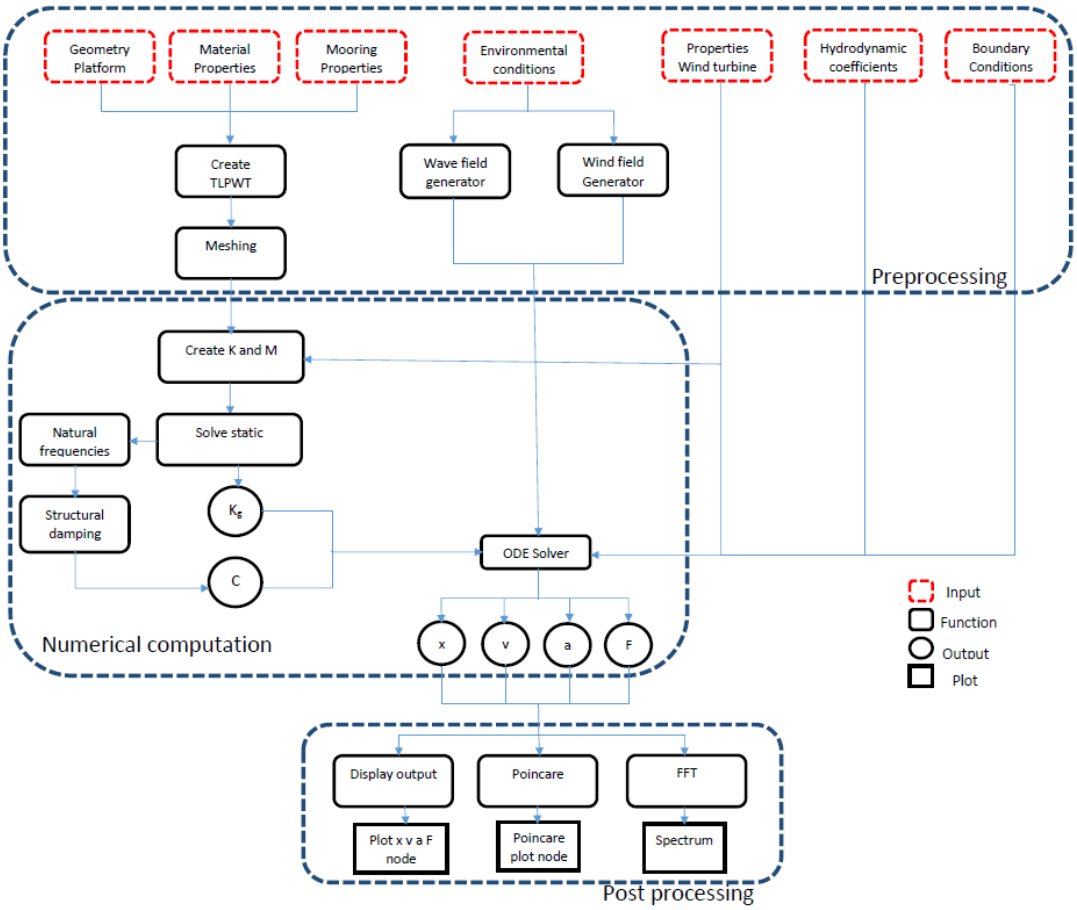

Figure 3-1: Arrangement of the model

3.3 STRUCTURAL MODEL

Modelling rigid bodies is fully understood by researches and engineers. Due to the developments of new technologies and lightweight materials, modelling flexibility of materials becomes important. Therefore, a shift from rigid body dynamics to deformable multi-body system is necessary. The TLPWT is a slender structure and the flexibility should be taken into account. The elasticity of the tower affects the natural frequency of the pitch motion of the platform; the natural frequency of the pitch motion decreases. This decrease can lead to resonance excitations of the wave frequencies or second-order sum-frequencies. Consequently, modelling the tower as a rigid body may lead to underestimation of the fatigue damage of the structure [87]. The magnitude of the pitch rotations and the amount of oscillations increase when taking the flexibility of the tower into account. The shift of the pitch natural period is caused by the coupling of the first bending mode of tower and the pitch natural frequency of the floater [88].

The TLPWT is mainly loaded laterally by the aerodynamic and hydrodynamic loading. The TLPWT consists of three pontoons, three tendons, a centre column and a tower. All elements are slender objects and mainly laterally loaded with respect to its axis. The tendons, pontoons and centre column and tower are modelled with the same one-dimensional beam element.

3.3.1 Beam element

A one-dimensional beam element is used to model all the objects of the TLPWT. There are two elementary beam theories, the Euler-Bernoulli beam theory [89] and the Timoshenko beam theory [90]. Timoshenko beam theory takes transverse shear deformation and rotational bending effect into account. The main assumption is that the cross section remain plane and the shear strain is constant over the length, with a length-height ratio of 10, the Timoshenko beam is an approximation of an Euler-Bernoulli beam [86].

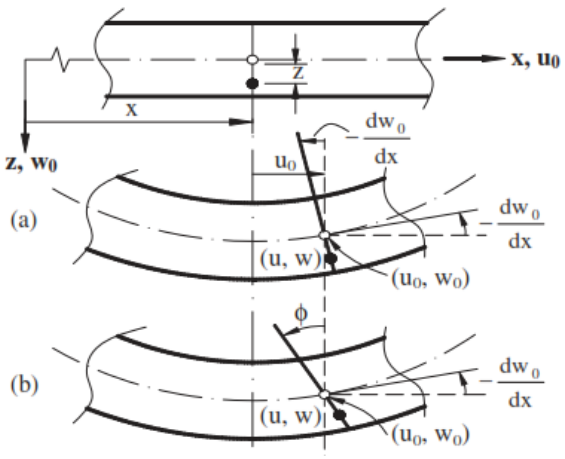

Figure 3-2: Cross-section displacement with (a) Euler-Bernoulli beam theory and (b) Timoshenko beam theory [91].

The one-dimensional beam element is a two node and six degrees of freedom per node beam element. There is no coupling between axial deformations, torsion and bending. A linear shape function is used for axial deformation and torsion and a cubic shape function is used for bending. The pontoons and the tower of the wind turbine have a linear tapering of the cross section over the length. The linear tapering is taken into account in the mass and stiffness matrix of the one-dimensional beam element. The derivation of the mass and stiffness matrix of the beam element are given in Appendix: One-dimensional finite element.

3.3.2 Structural damping

The damping matrix cannot be computed with the shape function like the element mass and element stiffness matrix. Therefore, the damping is taken into account by introducing an overall energy dissipation. Using the assumption that the total damping is the sum of the damping of the each individual mode, the damping can been written as equation (3-1). Where Ψ is the mode shape, f the natural frequency, ξ the damping ratio and δ the Kronecker delta function [68].

$$\Psi_i^T \boldsymbol{C} \Psi_j = 2\pi f_i \xi_i \delta_{ij} \tag{3-1}$$

$$\delta_{ij} = \begin{cases} 1, & i = j \\ 0, & i \neq j \end{cases}$$

$\boldsymbol{C}$	Damping matrix	Ψ	Mode shape
f	Frequency	ξ	Damping ratio
δ	Kronecker delta function		

Finite element models are large systems of coupled equations. Solving there system by modal superposition is not efficient for large systems. Assuming that the damping matrix can been written as a Caughey series [92, 93] (see equation (3-2)), the damping matrix becomes a series of the mass, stiffness matrix and the coefficients. The coefficients can be computed by solving the system of equations (3-3).

$$\boldsymbol{C} = \boldsymbol{M} \sum_{k=0}^{r} a_k \left[\boldsymbol{M^{-1}K}\right]^{\boldsymbol{k}} = a_0 \boldsymbol{M} + a_1 \boldsymbol{K} + a_2 \boldsymbol{M} \left[\boldsymbol{M^{-1}K}\right]^2 \ldots \tag{3-2}$$

$$\begin{bmatrix} 1 & \omega_1^2 & \omega_1^4 & \cdots & \omega_1^{2r-2} \\ 1 & \omega_2^2 & \omega_2^4 & \cdots & \omega_2^{2r-2} \\ \vdots & \vdots & \vdots & & \vdots \\ 1 & \omega_r^2 & \omega_r^4 & \cdots & \omega_r^{2r-2} \end{bmatrix} \begin{bmatrix} a_0 \\ a_1 \\ \vdots \\ a_{r-1} \end{bmatrix} = \begin{bmatrix} 2\omega_1\xi_1 \\ 2\omega_2\xi_2 \\ \vdots \\ 2\omega_r\xi_r \end{bmatrix} \tag{3-3}$$

$\boldsymbol{C}$	Damping matrix	$\boldsymbol{M}$	Mass matrix
$\boldsymbol{K}$	Stiffness matrix	a	Coefficient
ω	Natural frequency	ξ	Damping ratio

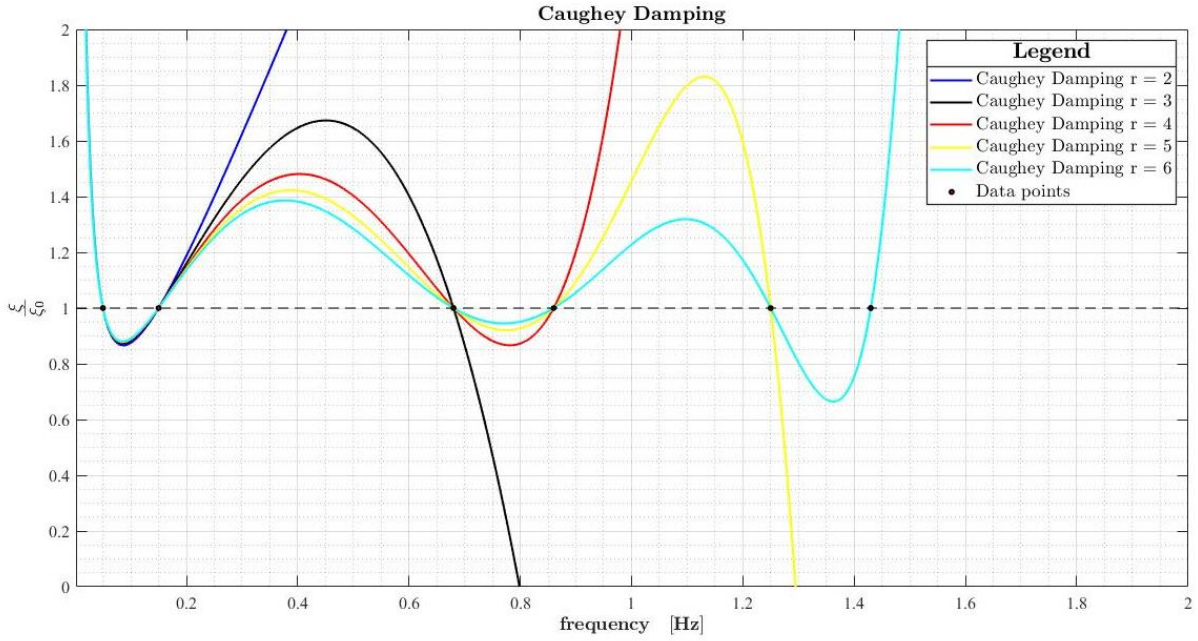

Figure 3-3: Damping ratio as function of the frequency

In practice a Caughey series of r = 2 is used [68], which means that the damping matrix is a linear combination of the mass and stiffness matrix of the structure. This is called proportional damping or Rayleigh damping [94]. Proportional damping has the advantaged that the computational cost is less, but the disadvantaged is that the damping is frequency dependent. The limit of the damping ratio goes to infinite for the lower frequencies and for the higher frequencies. It is important to determine the a_0 and a_1 coefficients well, to not overestimate the damping.

$$\boldsymbol{C} = a_0\boldsymbol{M} + a_1\boldsymbol{K} \tag{3-4}$$

$\boldsymbol{C}$	Damping matrix	$\boldsymbol{M}$	Mass matrix
$\boldsymbol{K}$	Stiffness matrix	a	Coefficient

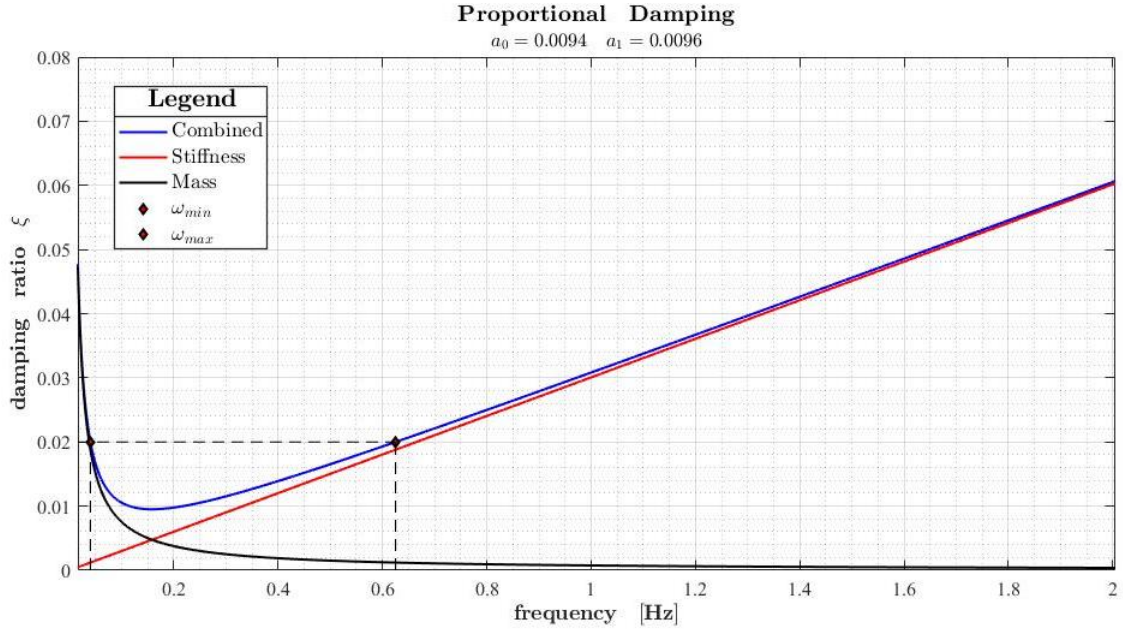

Figure 3-4: Damping ratio as function of the frequency

Proportional damping is used to take structural damping into account. The damping ratio prescribed by the design standards is between 1% and 5%, but for a fatigue assessment of wind turbine the design standards recommend a value between 1 and 2% [94]. The coefficients of the damping are computed with equation (3-5) and equation (3-9) [86]. Two frequencies are needed to compute the coefficients, the first frequency is the first natural frequency and the second frequency is the ninth natural frequency, because the higher modes are tendon modes or very high bending modes.

$$a_0 = \frac{2\omega_1\omega_2(\xi_1\omega_2 - \xi_2\omega_1)}{(\omega_2^2 - \omega_1^2)} \tag{3-5}$$

$$a_1 = \frac{2(\xi_2\omega_2 - \xi_1\omega_1)}{(\omega_2^2 - \omega_1^2)} \tag{3-6}$$

ω	Coefficient	ξ	Damping ratio

3.4 AERODYNAMIC MODEL

The aerodynamic forces are split into aerodynamic loads on the tower and wind turbine loads. The aerodynamic loads are depending on the wind conditions. This study makes use of the Froya wind model [53]. An unidirectional wind field is used in the model, an example of the turbulence and an example of the wind field is given Figure 3-5.

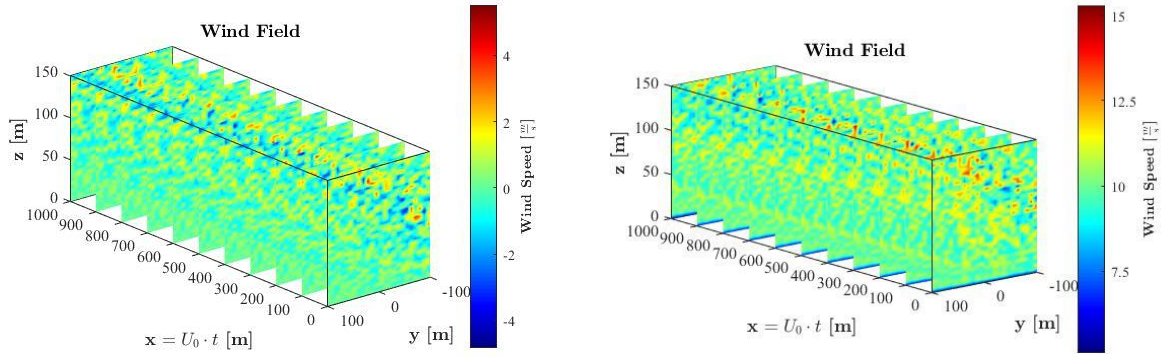

(a) (b)

Figure 3-5: (a) Wind field excluding shear profile (b) Wind field including shear profile

3.4.1 Aerodynamic loads on tower

The aerodynamic loads on the tower are distributed over the total length of the tower. The load per unit length can be computed with the drag part of the Morison equation (equation (3-7)).

$$f_{d_{wind}} = \frac{1}{2} C_d \rho_{air} (u_{wind} - v) |u_{wind} - v| D \tag{3-7}$$

C_d	Drag coefficient	ρ_{air}	Density air
u_{wind}	Velocity wind	v	Velocity TLPWT
D	Diameter		

3.4.2 Wind turbine loads

The wind turbine loads are split in a thrust force, aerodynamic torque and the gyroscopic moments. The wind turbine dynamics are modelled with the Bluewater wind turbine external function [20]. This external function models the wind turbine as an actuator disk and computes the thrust force, aerodynamic torque and the gyroscopic moments. The non-axial loads and non-torsional loads are not computed with the external functions. However, the non-torsional loads have a lower order, and the non-axial load F_y can be significant when the wind turbine is not properly aligned with the wind. Thus, the model can only been used for properly aligned wind [20].

3.4.2.1 Thrust force

The trust force can be computed with equation (3-8). The turbine trust force coefficients are known for the wind turbine, the properties of the wind turbine are confidential and are not published in this study.

$$F_{thrust} = \frac{1}{2} \rho_{air} A_{disk} C_t(\theta, TSR)(u_{wind} - v) |u_{wind} - v| \tag{3-8}$$

C_t	Thrust coefficient	θ	Pitch angle
u_{wind}	Velocity wind	v	Velocity TLPWT
A_{disk}	Area actuator disk	TSR	Tip-speed ratio

The turbine trust force coefficients are depending on the blade pitch angle, far-field wind velocity and the wind turbine rotational speed. The far-field wind velocity and the wind turbine rotational speed can be expressed by a dimensionless number tip-speed ratio (TSR). Wind turbines are designed to operate at optimal TSR and the turbine controller is designed to keep the turbine running at an optimal TSR until full power is reached.

$$TSR = \frac{\Omega R}{u_{wind}} \tag{3-9}$$

Ω Angular velocity disk R Radius rotor
u_{wind} Velocity wind

3.4.2.2 Passing blade frequencies

The thrust force variations are due to wind turbulence and non-harmonic periodic processes. These periodic processes are due to the tower shadow effect and wind shear effect. The passing blade frequencies are important for the blade fatigue, control system and the power output. The external function takes the tower shadow effect into account, but wind shear is omitted. Because the external function uses the velocity vector of the wind at the location of the RNA and assumes a constant velocity over the disk.

Tower shadow effect is taken into account by the external function. The force in x-direction is written as a superposition of the trust force and force due to the tower shadow effect (equation (3-10)). The tower shadow force is a non-harmonic periodic load and is written as a truncated Fourier series. A comprehensive study by DTU [95] on tower shadow effect is used to estimate the tower shadow effect. The Fourier series approximate the load by the third harmonic. Figure 3-6 gives the force spectrum of the external function for a constant wind velocity.

$$F_x = F_{thrust} + F_{shadow} \tag{3-10}$$

$$F_{shadow} = F_{thrust}\left(\sum_{j=1}^{3} C_j \sin(j\phi + 3\phi_j)\right)$$

F_{thrust} Thrust force C_j Coefficient

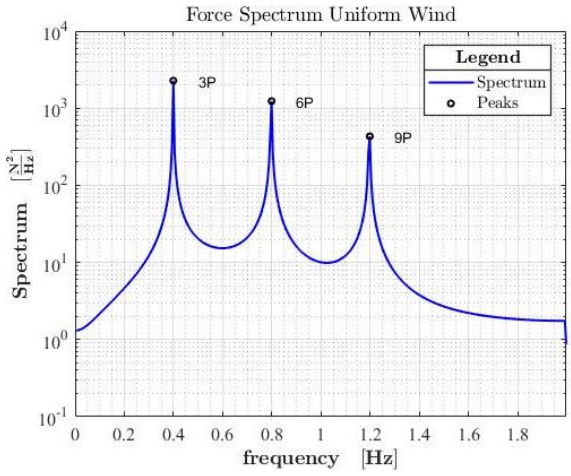

Figure 3-6: Thrust force spectrum with constant wind velocity

The external function takes tower shadow effect into account by means of an empirical formulation but excludes the wind shear effect. Meaning, that the tower shadow effect dominates the non-harmonic periodic thrust force variations. The influences of this limitation on the non-harmonic periodic thrust force variations are further investigated in this study in chapter 4 Dynamic analysis.

3.4.2.3 Gyroscopic moments

The gyroscopic moments are computed with the same wind turbine external function. The gyroscopic moments for bottom founded wind turbines can be neglected. For floating wind turbines the gyroscopic moments may be relevant. The rotations of the support structures are much larger with respect to the yaw motions of the nacelle. The gyroscopic moments are therefore included in the external functions. The gyroscopic moments are computed with equation (3-11).

$$M_{gyro} = \Omega_r \begin{bmatrix} 0 & 0 & 0 \\ 0 & 0 & I_p \\ 0 & -I_p & 0 \end{bmatrix} \begin{bmatrix} \dot{\theta}_x \\ \dot{\theta} y \\ \dot{\theta} z \end{bmatrix} \quad (3\text{-}11)$$

Ω_r Angular velocity wind turbine blades I_p Polar mass of inertia rotor
$\dot{\theta}_i$ Angular velocity in direction i

3.5 HYDROMECHANICS MODEL

The TLPWT is exposed to hydrostatic and hydrodynamic loads, which are together the hydromechanics loads. The hydrostatic load consists of the restoring forces and moments and the self-weight of the structure. The hydrodynamic loads are the loads due to the waves and currents.

3.5.1 Hydrostatic

The static loads consist the self-weight of the structure and the hydrostatic forces and moments. The hydrostatic forces and moments dependent on the shape of the submerged volume and the cross section area piercing the water line. The total hydrostatic force is equivalent to the integral of the hydrostatic pressure over the wetted surface, equation (3-12).

$$F_s = \iint_S p \cdot \vec{n}\, dS \tag{3-12}$$

F_s	Hydrostatic forces	p	pressure
$\vec{n}$	Normal vector	S	Wetted surface

The hydrostatic pressure is assumed to be constant. The diameter of the centre column is small with respect to the wave length, therefore the waterline area can be approximated by a constant waterline area. The motion of the TLPWT and the nonlinear boundary condition of the waterline, cause the submerged area to vary in time. The time varying part of the submerged body is small with respect the total submerged body of the TLPWT.

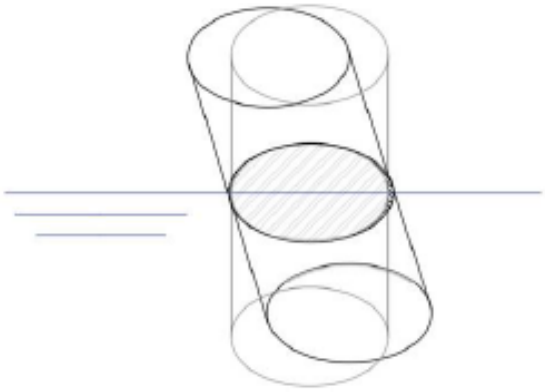

Figure 3-7: Changing water line area

The hydrostatic moments are described as an integral over the wetted surface of the hydrostatic pressures multiplied by the position vector, equation (3-13). In case of a non-zero pitch and roll rotation, the structure experience a restoring moment due to the unbalanced buoyancy forces. Another explanation is that the motion of the TLPWT and the nonlinear boundary condition, cause the underwater shape of the structure to change. The restoring moment is small with respect to the moment caused by the tendon tension of the TLPWT, therefore the hydrostatic moment is not included. The total static force per unit length can therefore be written as equation (3-14).

$$M_s = \iint_S p \cdot (r \times n)\, dS \tag{3-13}$$

$$f_s = \rho_w g A - \rho_m A_{cross} g \tag{3-14}$$

M_s	Hydrostatic moment	p	pressure
$\vec{n}$	Normal vector	S	Wetted surface
r	Radius	ρ_w	Density water
g	Gravity acceleration	ρ_s	Density material
A	Enclosed area	A_{cross}	Cross-sectional area

3.5.2 Wave theories

The JONSWAP wave spectrum is used to describe the surface elevations but tells nothing about the physics of waves. The choice of wave theory depends on three parameters, namely the wave height, wave period and water depth.

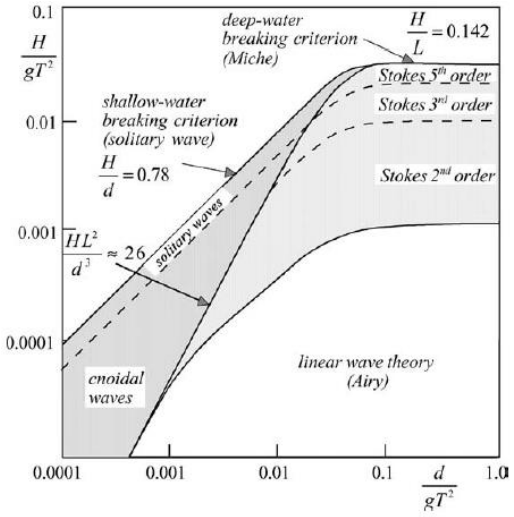

Figure 3-8: Range of applicability of wave theories [56]

In this study, Airy wave theory is used, which is mostly called linear wave theory. This linear wave theory assumes an ideal fluid, meaning that the fluid is incompressible, has a constant density, a continuous water body and has no viscosity. The first assumption is reasonable because the forces are small. If the forces are small, the compression due to the forces are also small. The second assumption of this theory is also reasonable because density differences occurs only over a large distance, but for this wave theory only a few wavelengths considered. The third assumption of a continuous water body is only valid if the wave are not too steep, that the wave breaks. If the wave breaks air bubbles come in the water. Therefore this wave theory cannot be used for very steep waves, see Figure 3-8. The last assumption is that the viscosity can be neglected, this is valid for the amount of wave length considered, because viscosity variations are usually to slow [37].

The boundary conditions of this theory are distinguished into kinematic boundary conditions and dynamic boundary conditions. The kinematic boundary conditions are related to motion of the water particles and the dynamic boundary conditions are related are related to the forces acting on the water particles. The kinematic boundary conditions are based on the water particles may not leave the surface and the water particles may not go into the sea floor. The dynamic boundary condition is based on the surface pressure is zero [56].

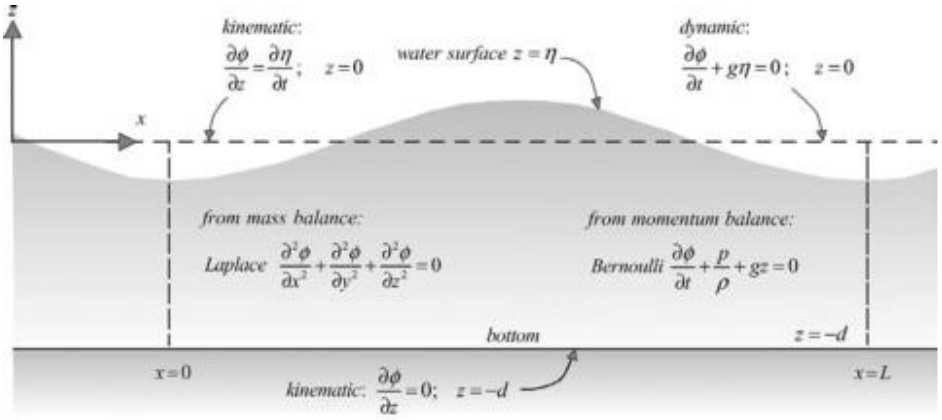

Figure 3-9: Boundary conditions for linear wave theory in terms of velocity potential [56]

Potential theory is applied and the velocity potential of the water particles can be derived with the given dynamic and kinematic boundary conditions. The derivation of the velocity potential of linear wave theory is not described in this study, but the derivation can be found in different books for example [56] and [37]. By definition of the velocity potential, the particle velocity is the partial derivative with respect to the direction of the velocity.

$$\Phi_{wave} = \frac{2\pi f\zeta}{k} \cdot \frac{\cosh[k(d+z)]}{\sinh(kd)} \cos(2\pi ft + kx) \tag{3-15}$$

$$k = \frac{2\pi}{\lambda}$$

Φ	Velocity potential	f	Wave frequency
ζ	Wave amplitude	k	Wave number
d	depth	z	z-coordinate

3.5.3 Particle kinematics

The ocean surface is irregular and has random wave heights, wave lengths and propagation velocities. The ocean can therefore be modelled using a random wave model. The random wave model is the sum of small linear wave components with different frequencies, amplitudes and phases. The JONSWAP spectrum is used to model the surface elevation. The waves are unidirectional and the direction of the waves can be chosen independently of the direction of the wind and current.

The model uses airy wave theory (linear wave theory). The wave kinematics in linear wave theory are derived from a velocity potential. The surface elevation is written in a summation of n-frequency components. The orbital velocity can therefore be written as a summation of the velocities. The particle velocities are written in equation (3-16) and equation (3-17). The particle accelerations are written in equation (3-18) and equation (3-19).

$$u_{w,x}(x,y,z,t) = 2\pi \sum_{i=1}^{n} f_i \zeta_i \frac{\cosh[k_i(d+z)]}{\sinh(k_i d)} \cos\left(2\pi f_i t - k_i\left(x\cos(\mu_{wave}) + y\sin(\mu_{wave})\right) + \phi_i\right) \quad (3\text{-}16)$$

$$u_{w,z}(x,y,z,t) = 2\pi \sum_{i=1}^{n} f_i \zeta_i \frac{\sinh[k_i(d+z)]}{\sinh(k_i d)} \sin\left(2\pi f_i t - k_i\left(x\cos(\mu_{wave}) + y\sin(\mu_{wave})\right) + \phi_i\right) \quad (3\text{-}17)$$

$$\dot{u}_{w,x}(x,y,z,t) = -4\pi^2 \sum_{i=1}^{n} f_i^2 \zeta_i \frac{\cosh[k_i(d+z)]}{\sinh(k_i d)} \sin\left(2\pi f_i t - k_i\left(x\cos(\mu_{wave}) + y\sin(\mu_{wave})\right) + \phi_i\right) \quad (3\text{-}18)$$

$$\dot{u}_{w,z}(x,y,z,t) = 4\pi^2 \sum_{i=1}^{n} f_i^2 \zeta_i \frac{\sinh[k_i(d+z)]}{\sinh(k_i d)} \cos\left(2\pi f_i t - k_i\left(x\cos(\mu_{wave}) + y\sin(\mu_{wave})\right) + \phi_i\right) \quad (3\text{-}19)$$

u	Orbital velocity	$\dot{u}$	Orbital acceleration
f	Wave frequency	k	Wave number
ζ	Wave amplitude	μ_{wave}	Wave direction
d	depth	ϕ_i	phase
x	x-coordinate	y	y-coordinate
z	z-coordinate	t	Time

3.5.4 Kinematic stretching

The wave kinematics described by the airy wave theory satisfies the nonlinear boundary conditions only at the mean water level, meaning that the theory is only valid for small wave heights. The consequences of this limitation are that the wave kinematics underestimate the wave kinematics at the wave through and overestimate the kinematics at the wave crest. To overcome this limitation, several methods can be used. The wheeler stretching method [54] is used to estimate the kinematics of the nonlinear boundary condition. The basic of this method is that the velocity components and acceleration components are stretched in case of a crest and compressed in case of a through.

$$z^w = d \cdot \frac{d+z}{d+\eta(x,y,t)} - d \quad (3\text{-}20)$$

d	depth	z	z-coordinate
η	Surface elevation		

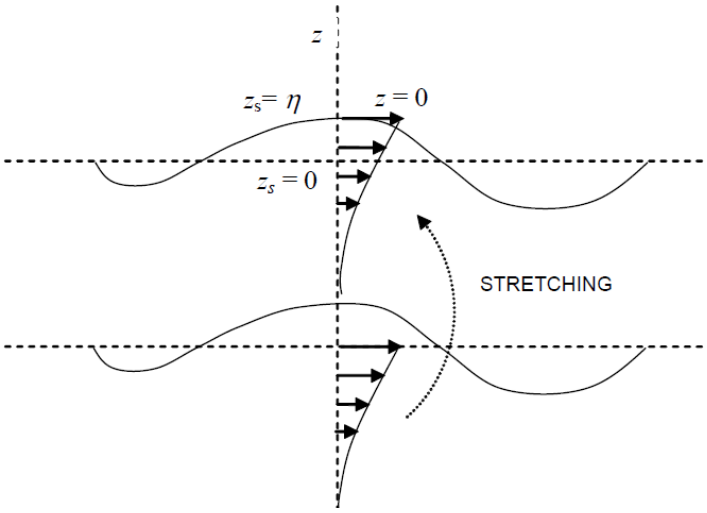

Figure 3-10: Stretching of the velocity profile [54]

3.5.5 Hydrodynamic load

Airy wave theory assumes that no current is present. In the model the current-wave interaction is therefore neglected. The velocity vector of fluid particles and current are summed as vectors quantity. The hydrodynamic loads are computed by the Morison equation. DNVGL [54] defines that the additional hydrodynamic damping should not be included, otherwise the damping is overestimated. The fluid particles velocities and accelerations in normal direction of the element are therefore neglected.

$$f_{morison}(t) = \rho_w A\dot{u} + \rho_w C_a A\,(\dot{u} - a) + \frac{1}{2}\rho_w C_d D\,(u - v)|u - v| \tag{3-21}$$

$$u_i = u_{w,i}(x, y, z, t) + u_{c,i}(x, y, t)$$

$$\dot{u}_i = \dot{u}_{w,i}(x, y, z, t)$$

A	Enclosed area	$\dot{u}$	Environmental acceleration
u	Environmental velocity	$u_{w,i}$	Orbital velocity
$u_{c,i}$	Current	$\dot{u}_{w,i}$	Orbital acceleration
ρ_w	Density water	C_a	Coefficient added mass
a	Acceleration TLP	C_d	Coefficient drag
v	Velocity TLPWT	D	Diameter

3.6 SERVO MODEL

National Renewable Energy Laboratory (NREL) developed a 5MW wind turbine for research purpose and the control system is public available. The NREL 5MW wind turbine and the wind turbine used at Bluewater are comparable, therefore the control system of the NREL 5MW is used in this study. The control system of the NREL 5MW wind turbine consists of a blade-pitch controller and a variable-torque controller. The nacelle-yaw control system is neglected because the response is slow enough that it will not contribute to large extreme loads or fatigue damage [96]. The variable-torque controller and the blade-pitch controller work independently for each other. Figure 3-11 gives a schematic overview of the NREL control system.

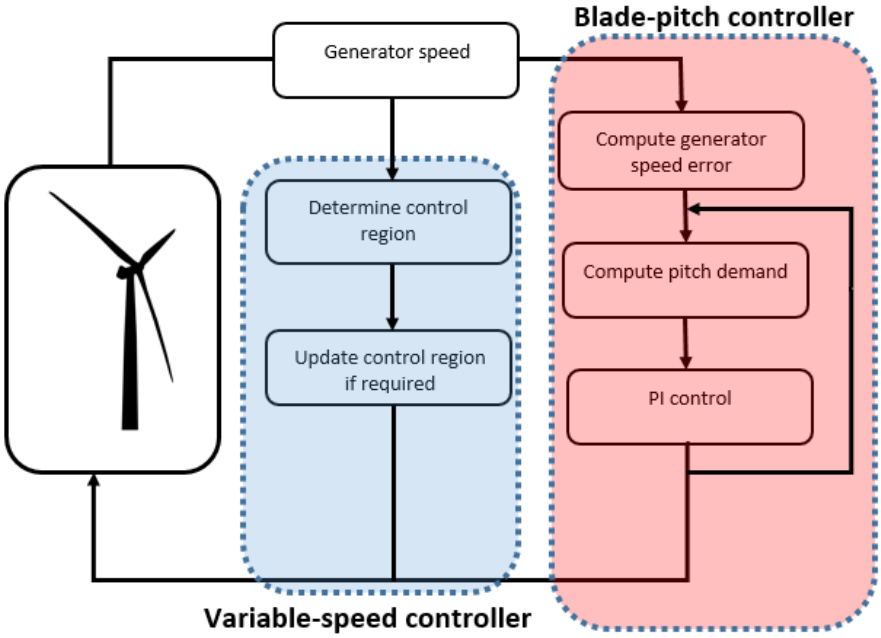

Figure 3-11: schematic overview NREL control system

3.6.1 Variable-speed controller

The variable-speed controller has the aim to optimize the aerodynamic efficiency, by applying quadratic relation between the rotational speed of the wind turbine blades and the generator torque [17].

$$M_{gen} = k_{gen}\Omega^2 \tag{3-22}$$

M_{gen} Generator torque k_{gen} Generator torque constant

Ω Rotational speed wind turbine

The control system includes 6 regions region 1, region 1.5, region 2, region 2.5, region 3 and region 4. However, region 4(cut-out region) is not implemented in the model, which means that the model cannot be used to model a shutdown of the wind turbine. Region 1 till region 3 are implemented in the model. Where region 1 is the wind turbine not producing power. Region 1.5 is the startup region. Region 2.0 is the control region to optimize the aerodynamic efficiency, the generator torque is than equal to equation (3-22). Region 2.5 is a transition region between region 2.0 and 3.0, is needed to reduce the noise emission at the rated power. Region 3 is the region where the power production is held constant, see Figure 3-12.

Table 3-1: Region wind turbine NREL [96]

Region	*[rad/s]*
Region 1.0	ω ≤ 0.7016
Region 1.5	0.7016 < ω ≤ 0.9394
Region 2.0	0.9394 < ω ≤ 1.2780
Region 2.5	1.2780 < ω ≤ 1.3090
Region 3.0	ω > 1.3090

3.6.2 Blade-pitch controller

The blade-pitch controller controls the generator speed and becomes active in region 3.0. The blade pitch controller is a proportional-integral (PI) control. A PI control is an algorithm which is widely used for controlling all kinds of processes and equipment. The control action is calculated as sum of two terms, one proportional to the control error and one proportional to the integral of the control error. The integral term ensures that in the steady state the error tends to zero, otherwise the control action would increase to infinity [17].

PI control of the blade-pitch controller is acting on the speed error (equation (3-23)) between the generator speed and the rated generator speed. The generator speed error is used to compute the pitch-angle demand (equation (3-24)), including the gain schedule, which compensates for the variable sensitivity of the blade loads to changes in pitch angle at different wind speeds.

$$\varepsilon_{gen} = \Omega_{gen} - \Omega_{rated} \tag{3-23}$$

$$\theta_{demand} = G_k\left[K_p\varepsilon_{gen} + K_I I_\varepsilon\right] \tag{3-24}$$

$$I_\varepsilon = \int_0^t \varepsilon_{gen}\, dt$$

ε_{gen}	Generator speed error	Ω_{gen}	Generator speed
Ω_{rated}	Rated generator speed	θ_{demand}	Pitch angle demand
G_k	Gain schedule	K_p	Proportional gain
K_I	Integral gain		

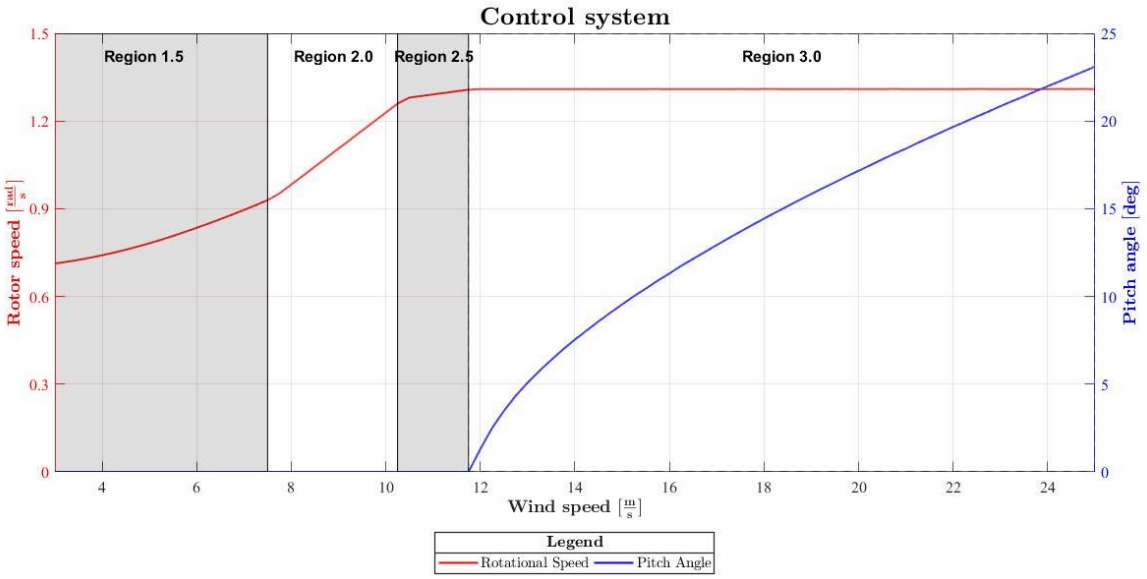

Figure 3-12: Operation a variable-speed, variable-pitch wind turbine

3.7 VALIDATION

The ‘’Matlab model’’ is validated. The software Orcaflex [13] is widely used in studies of FWT, for example [97], and here Orcaflex is used to validate the Matlab model. Salih [12] used Orcaflex to validate FWT model with model test performed by SBM Offshore [98]. He concluded that Orcaflex computes the motions and trends of the SBM TLP system well. Therefore, the Matlab model is validated by comparing the static responses, natural periods and motion responses. See, E Appendix: Validation of Model, a summary is given below.

3.7.1 Models

A Matlab model and Orcaflex model are developed to compare the results of both models. The models have the same geometric properties and the same constraints. The design of the TLPWT is based on a design that has been model tested of at MARIN [99].

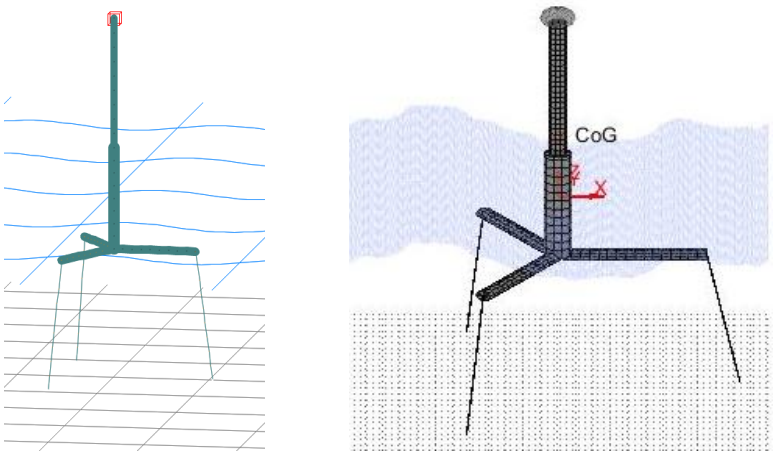

Figure 3-13: (a) Orcaflex Model; (b) Matlab model

Orcina ‘’OrcaFlex’’ is a commercial software package for dynamics analysis of marine systems. Orcaflex takes the flexibility of the tendons, pontoons and tower into account. Stiff springs are therefore used to model connections, like the pontoon-centre column connection and nacelle-tower connection. The nacelle and rotor are modelled using a buoy element with the mass and inertia properties of the nacelle and rotor.

3.7.2 Static

The hydrostatic forces are applied in all both models. Orcaflex is not be able to determine the mass of the structure but gives the mass per unit length of each object separately. Therefore, the mass of Orcaflex model is determined manually. The static results are given in Table 3-2, but normalized by dividing by the static properties of the Orcaflex model because these results are confidential. The Orcaflex model and the Matlab model have the same results. The mass of the TLPWT, pretension and the displacement at nacelle-tower connection and pontoon-centre column connection (PC) of both models are equal.

Table 3-2: Static Properties Models

	Orcaflex	*Matlab*	*Unit*
Total Mass	1.00	1.00	[-]
Platform Mass	1.00	1.00	[-]
Nacelle mass	1.00	1.00	[-]
Pretension tendon	1.00	1.00	[-]
Displacement z PC	1.00	1.01	[-]
Displacement z Nacelle	1.00	1.01	[-]

3.7.3 Natural period

The natural periods of the Matlab model and Orcaflex model take the added mass, mass and geometric stiffness into account, but the gyroscopic effect is excluded. Table 3-3 gives the natural periods of the Orcaflex model and Matlab models. The relative error is computed with equation (3-25) and also given in Table 3-3. The differences between the natural periods of the Orcaflex model and the Matlab Model are all below 0.01, which is negligible.

$$\epsilon = \frac{|T_{MAT} - T_{OF}|}{T_{OF}} \tag{3-25}$$

ϵ Error T Period

Table 3-3: Natural Periods Orcaflex and Matlab

	Orcaflex [s]	*Matlab [s]*	*Error [-]*
Surge	25.04	25.18	0.01
Sway	25.15	25.25	0.00
Heave	2.33	2.35	0.00
Roll	6.30	6.31	0.00
Pitch	7.23	7.22	0.00
Yaw	16.70	16.87	0.01

3.7.4 Response

The design of the TLPWT looks simple but the dynamics of the TLPWT is complex. The validation of the response is therefore separated into two steps. The first step is comparing the response of a bottom founded wind turbine (BFWT) with Orcaflex and the Matlab model. The second step is comparing the responses of the FWT. A regular wave with a misaligned current is used to compare the responses. The wind velocity is assumed to be zero, meaning that the wind turbine is off. Table 3-4 gives a summary of the environmental conditions.

Table 3-4: Environmental condition validation analysis

Parameter	*Symbol*	*Value*	*Unit*
Wave height	H_s	3.5	[m]
Wave Period	T_p	8.0	[s]
Wave direction	μ_{wave}	60	[°]
Current velocity wind	$u_{c,wind}$	0.0	[ms-1]
Current velocity tide	$u_{c,tide}$	0.0	[ms-1]
Current direction	μ_{curent}	90	[°]
Wind velocity	U_w	0	[ms-1]

3.7.4.1 Bottom founded wind turbine

The dynamic system of a bottom founded wind turbine (BFWT) is simpler than the TLPWT. The bottom founded wind turbine (BFWT) is modelled as a cantilever beam and the water depth is 96.5 meter. The cross-sectional dimensional properties of the BFWT are given in Table 3-5 and the definitions in Figure 3-14.

Table 3-5: Properties BFWT

Parameter	*Symbol*	*Value*	*Unit*
Diameter	D_t	10	[m]
Plate thickness	t_p	0.1	[m]
depth	D	96.5	[m]
Height	H_t	90.7	[m]

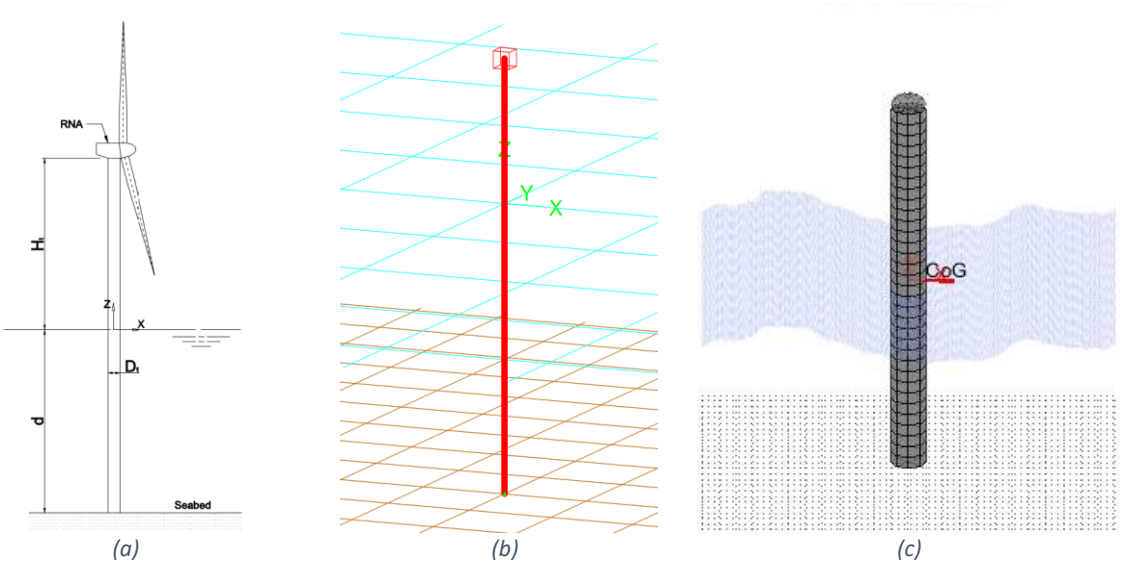

(a) *(b)* *(c)*

Figure 3-14: (a) Drawing; (b) Orcaflex model; (c) Matlab model

The responses of the nacelle of the Orcaflex model and Matlab model are compared. The natural period of the fore-aft and side-side for Orcaflex model and Matlab model are given in Table 3-5. The root mean square error (RMSE, see equation (3-26)) for the displacements, velocities and accelerations in x-direction and y-direction are all below the 0.036%, which is acceptable. Figure 3-15 gives the displacements, velocities and accelerations in global x-direction and global y-direction. From the figure, it can be seen that the Matlab model and the Orcaflex model show largely identical responses. Concluded is that the Matlab model can compute the responses of a BFWT satisfactory. The response spectrum is given Figure 3-15. The response spectrum show largely identical response. The first peak in the spectrum is the wave frequency. The second peak is the first natural frequencies of the BFWT.

$$RMSE = \sqrt{\frac{1}{n}\sum_{i=1}^{n}\left|x_{i,OF} - x_{i,MAT}\right|^2} \tag{3-26}$$

$RMSE$ Root mean square error
n Number of points
x Displacement

Table 3-6: Summary validation BFWT

	Natural period			RMSE		
	Matlab [s]	*Orcaflex [s]*	*Error [-]*	*x [m]*	*v [ms^{-1}]*	*a [ms^{-2}]*
Fore-aft	3.60	3.55	0.014	0.012	0.014	0.021
Side-side	3.25	3.45	0.05	0.021	0.025	0.036

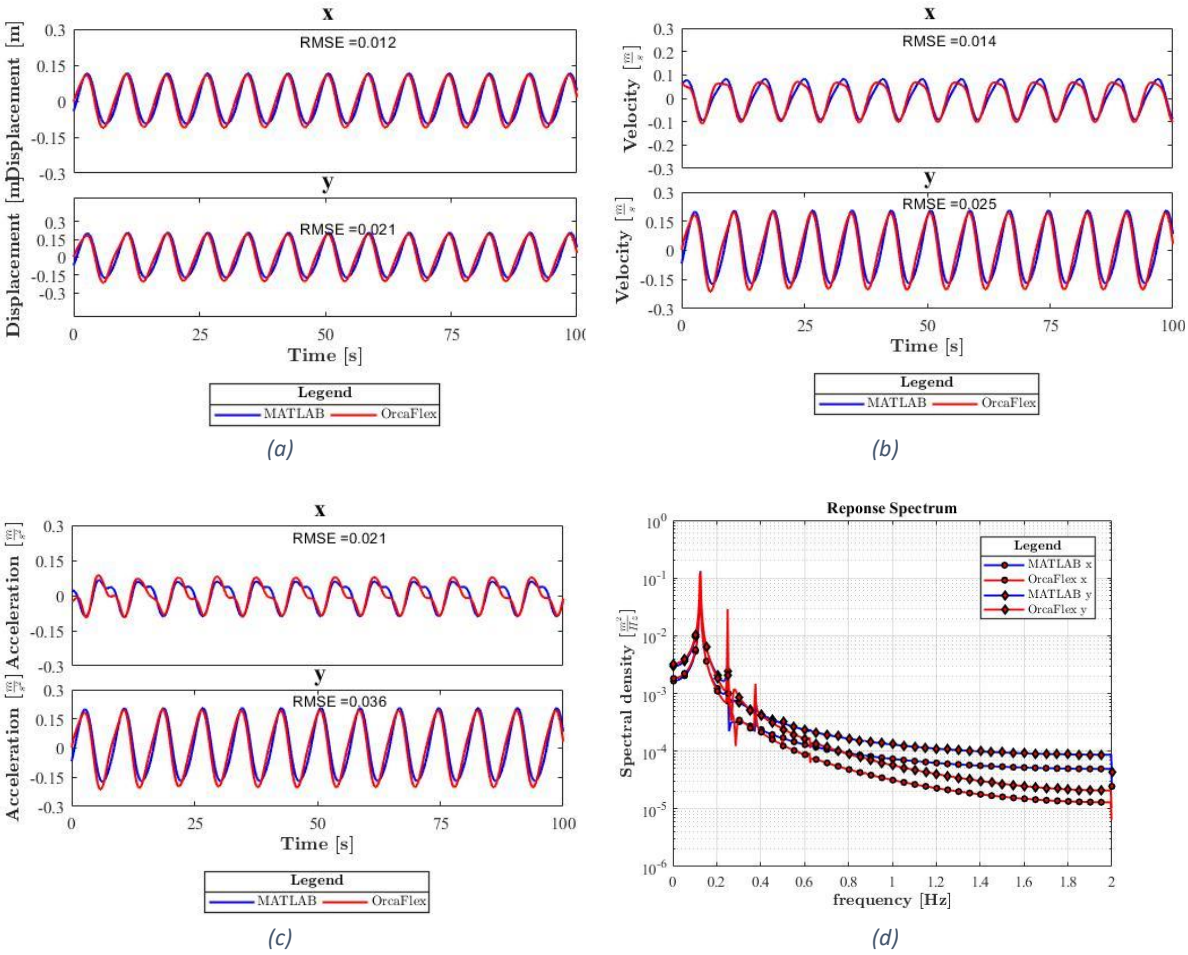

Figure 3-15: Responses of the BFWT of the Orcaflex and MATLAB model

3.7.4.2 Floating wind turbine

The properties of the TLPWT are given in Appendix: Properties TLPWT. The water depth is 96.5 meter and the same environmental conditions are used. A simulation of 100 seconds, excluding the starting procedure of the environment, is used to compare the motion responses of the Orcaflex model and the Matlab model. Figure 3-16 gives the displacements, velocities and accelerations in global x-direction and global y-direction at the pontoon-centre column connection. From the figure, it can be concluded that the Orcaflex model and Matlab model show comparable motion responses. The amplitudes of the motions are for the Orcaflex model and Matlab model approximately identical, however a small phase shift is visible in the figure. The RMSE-values of displacement, velocities and accelerations are below 0.1. The RMSE is dominated by the mean difference of the two time signals, a small phase shift causes a relatively high RMSE. Therefore, it is concluded that the Matlab model can compute the motions with an acceptable level of accuracy.

Table 3-7: Summary validation FWT

	RMSE		
	x [m]	*v* [ms^{-1}]	*a* [ms^{-2}]
x-direction	0.070	0.043	0.037
y-direction	0.096	0.062	0.056

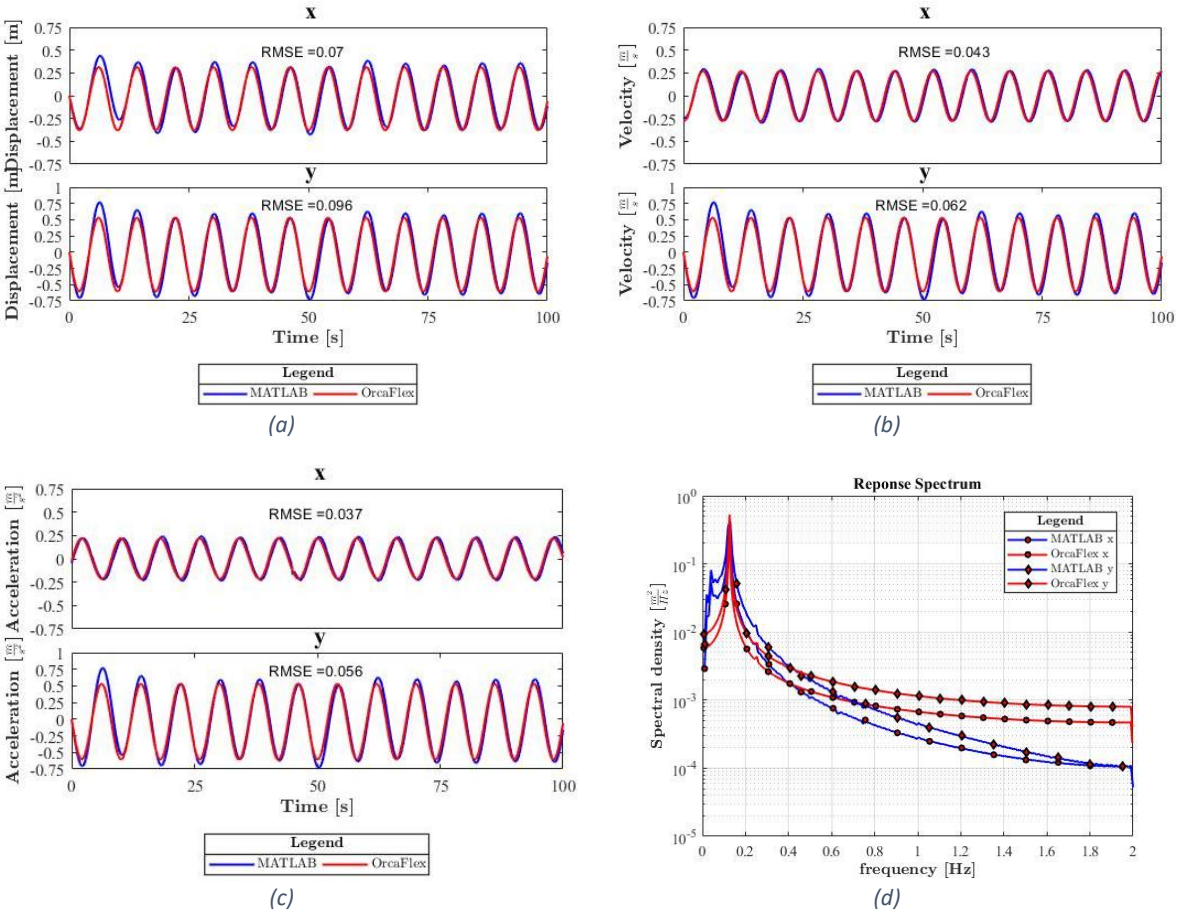

Figure 3-16: Responses of the FWT of the Orcaflex and MATLAB model

3.7.5 Conclusions

The validation of the Aero-Hydro-Elastic-Servo model was performed in multiple steps. Appendix: Validation of Model provides all the results. The first step compares the static response between the Matlab model and the Orcaflex model. Both model show similar static response. The next step compares the natural periods. The Matlab model computes the natural periods within less than 1% difference. The motion responses of the Matlab model are compared with the motion responses of the Orcaflex model. A BFWT and a FWT are used to compare the motion responses. The RMSE of the motions are below than 0.036 and the RMSE of the FWT are below 0.096 but still acceptable. This is acceptable because the amplitudes of the Orcaflex model and Matlab model are approximately identical, which is dominant by fatigue. Hence, the Matlab model is capable to compute the motion satisfactory.

The external wind turbine function itself should be validated for example with BEM-software. Within the time frame of this thesis, the validation of the external functions was limited. The control system is important for the dynamical response of the wind turbine. The NREL control system is used in the model.

4 DYNAMIC ANALYSIS

4.1 INTRODUCTION

The Matlab model that have been developed can compute natural frequencies, mode shapes and solves the EoM for a FWT correctly, see chapter 3. An advantage of the Matlab model with respect to the Orcaflex model is that the Matlab model is transparent. Orcaflex model cannot provide all the required output, for example the displacements of the nodes between the ends of an element. The Matlab model can provide all the output that the user needs.

In the second chapter (Theoretical review) of this report, some research questions are unanswered. The following research questions are listed below:

- What is the effect of the rotating rotor on the natural period and motions?
- What is the effect of the nonlinear mooring stiffness on the natural periods?
- What is the effect of neglecting the wind shear effect on the passing blade frequencies?
- What is the effect of the passing blade frequencies on the motions of the floating support structure?

4.2 NATURAL PERIODS

The natural periods of a dynamical system are important properties. The effects of the rotating rotor and the effect of the nonlinearities of the TLPWT on the natural periods are not known, therefore the gyroscopic effect and the nonlinear mooring stiffness are investigated.

4.2.1 Gyroscopic effect

The wind turbine blades are a rotating structure and this type of structure requires special care. The modal analysis performed in the validation of the Matlab model does not include the rotating blade impact. The EoM of a rotating system can been written as equation (4-1), where G is the gyroscopic matrix and H the circulatory stiffness matrix. The gyroscopic matrix G is transferring energy but not dissipating energy. The matrix G is a skew-symmetric matrix. A skew-symmetric matrix is a square matrix whose transpose equals its negatives. The circulatory stiffness matrix H couples the viscous damping of the rotating element to the displacement of the total system [100].

$$\boldsymbol{M}\vec{a}(t) + (\boldsymbol{C} + \Omega\boldsymbol{G})\vec{v}(t) + (\boldsymbol{K} + \Omega\boldsymbol{H})\vec{x}(t) = \vec{F}(t) \tag{4-1}$$

$\boldsymbol{M}$	Mass matrix	a	Accelerations vector
$\boldsymbol{C}$	Damping matrix	Ω	Rotation velocity disk
$\boldsymbol{G}$	Gyroscopic matrix	v	Velocity vector
t	time	$\boldsymbol{K}$	Stiffness matrix
$\boldsymbol{H}$	circulatory stiffness matrix	x	Displacement
F	Force		

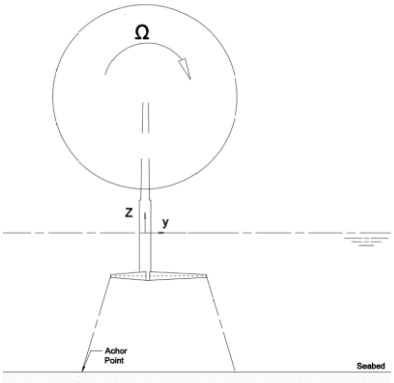

Figure 4-1: TLPWT including actuator disk

The rotor of the wind turbine of the TLPWT is modelled as a rigid actuator disk (see Figure 4-1), with the properties of the wind turbine used in this study. The structural damping of the TLPWT is neglected. The EoM of the TLPWT can be described by equation (4-2). The natural periods of the system now also depend on the rotational speed of the actuator disk. The influence of the rotational speed of the actuator disk is plotted in a Ω-T diagram, where Ω is the rotational speed of the wind turbine and T the natural period of natural frequency mode of interest. The Ω-T diagram of the TLPWT is shown in Figure 4-2.

$$[\boldsymbol{M}+\boldsymbol{A}]\vec{a}(t)+\Omega\boldsymbol{G}\vec{v}(t)+[\boldsymbol{K}+\boldsymbol{K}_m]\vec{x}(t)=\vec{F}(t) \tag{4-2}$$

$$\boldsymbol{G}=\begin{bmatrix}0 & \cdots & 0 & 0\\ \vdots & \ddots & \vdots & \vdots\\ 0 & \cdots & 0 & I_p\\ 0 & \cdots & -I_p & 0\end{bmatrix}$$

$$\vec{x}=[x_{n,1} \quad x_{n,2} \quad \cdots \quad x_{n,i}]^T$$

$$x_{n,i}=[u_{i,x} \quad u_{i.y} \quad u_{i,z} \quad \theta_{i,x} \quad \theta_{i,y} \quad \theta_{i,z}]$$

$\boldsymbol{M}$	Mass matrix	$\boldsymbol{A}$	Added mass matrix
a	Accelerations vector	$\boldsymbol{G}$	Gyroscopic matrix
Ω	Rotation velocity disk	I_p	Polar moment of inertia
v	Velocity vector	t	time
$\boldsymbol{K}$	Stiffness matrix	$\boldsymbol{K_m}$	Mooring stiffness
x	Displacement	F	Force
$x_{n,1}$	Displacement vector node 1	$\theta_{i,x}$	Rotation node i, around x-axis
$u_{i,x}$	Displacement node i x-direction		

The effect of the rotating rotor on the natural periods of the nine natural frequency modes (Figure 5-1) is analyzed. The natural periods are made dimensionless by dividing the natural periods with the natural frequencies when rotational speed of the rotor is zero. The dimensionless natural periods, are presented in Figure 4-2, as function of the rotational speed of the rotor. The dimensionless periods are straight lines for all modes, till approximately 3 rad/s. Concluded is that the natural period of the first nine modes are unaffected by the gyroscopic effect of the wind turbine.

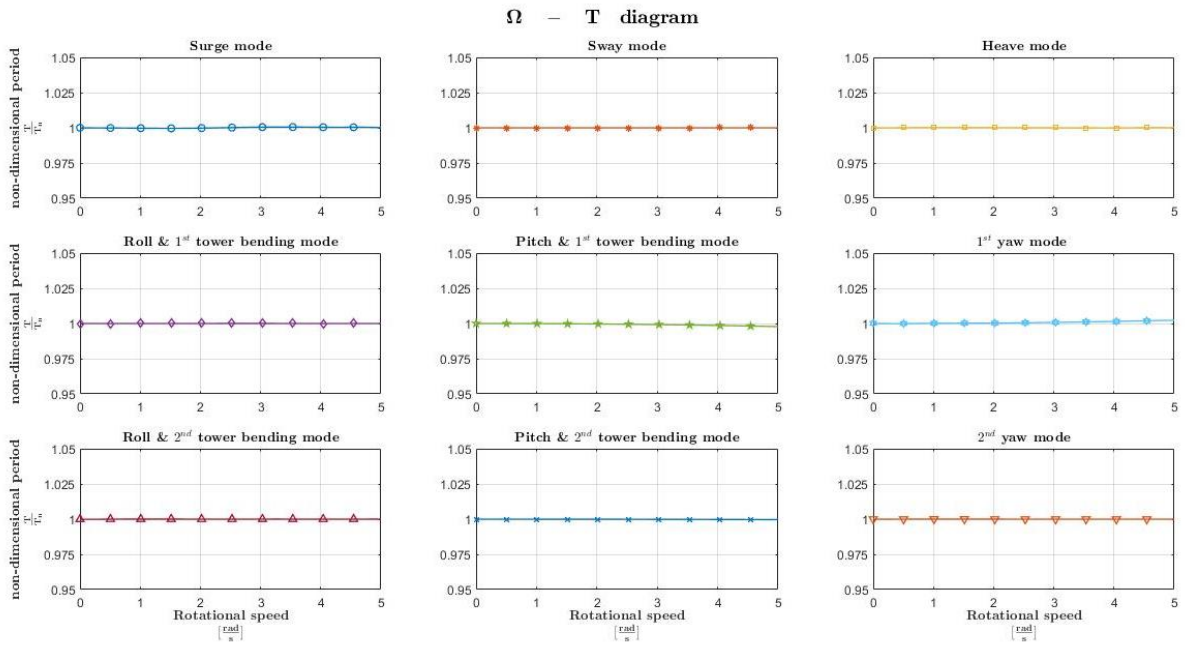

Figure 4-2: Ω-T diagram TLPWT

4.2.2 Nonlinear mooring stiffness

The TLPWT is a nonlinear system because the mooring stiffness depends on the displacements and rotations of the TLPWT. The effect on the nonlinear mooring stiffness on the natural periods is investigated. The TLPWT is displaced by a pulling force at the water line, to get more accurate results [99].

The effect of the nonlinear mooring stiffness on the natural periods is analyzed. Figure 4-3 gives the dimensionless natural periods as function of the displacement for all the nine natural frequency modes. The dimensionless natural period are made dimensionless by dividing the natural periods by the natural periods when the TLPWT is not displaced. The yaw mode shows small decrease in natural period for large displacement and the sway mode a small increase of natural period for large displacement, but not significant. The dimensionless periods of the other modes are straight lines, therefore the nonlinear mooring stiffness does not have significant effect on the natural periods of the TLPWT.

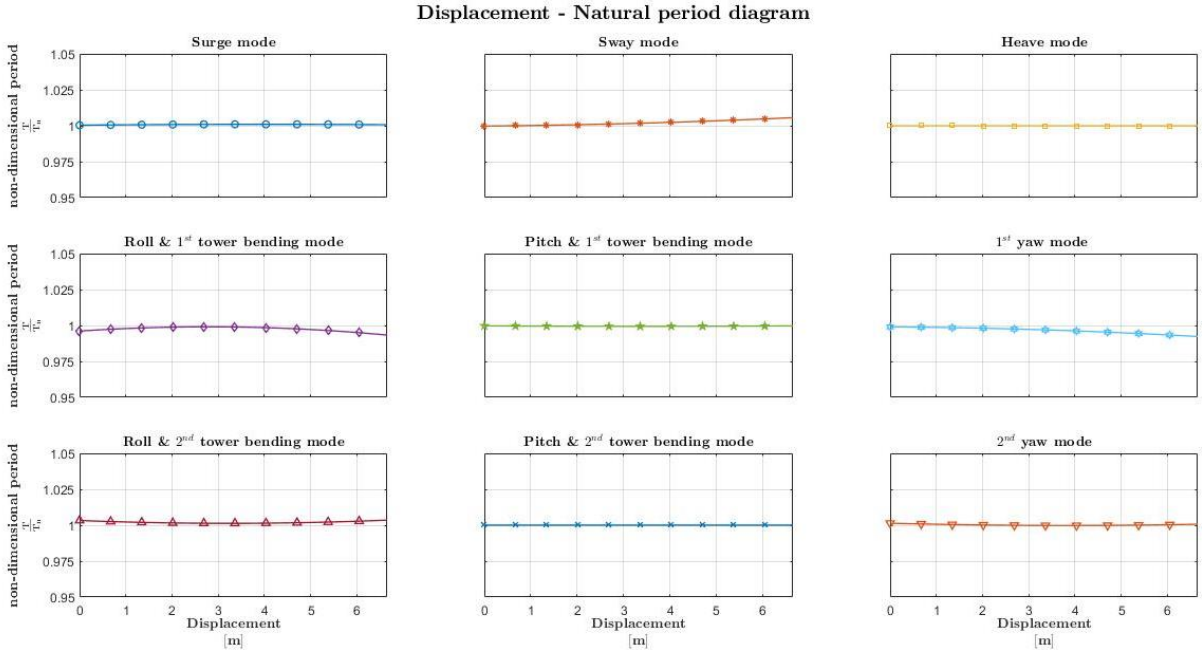

Figure 4-3: Non-dimensional period as function of the displacement

4.3 MOTION RESPONSE

The motion response of the TLPWT is complex, therefore the motion responses of the validation TLPWT (see Appendix: Properties TLPWT) are analyzed. The structural damping is assumed to be 2%, which is equal to the structural damping of the NREL 5MW wind turbine [96]. Two load cases are defined corresponding with moderate (LC 1 in Table 4-1) and extreme environmental condition (CL 2 in Table 4-1). The first load case has a significant wave height of 2.5m, wave peak period of 8s and a 10-minute average wind speed of 8 m/s. The second load case has a significant wave height of 5 meter, wave peak period of 10s and a 10-minute average wind speed of 12.5m/s. These load cases are used to investigate the effect of the gyroscopic moments on the motion and the effect of the passing blade frequencies.

Table 4-1: Environmental condition

Parameter	*Symbol*	*LC 1*	*LC 2*	*Unit*
Wave height	H_s	2.5	5	[m]
Wave Period	T_p	8	10	[s]
Wave direction	μ_{wave}	60	60	[°]
Current velocity wind	$u_{c,wind}$	0.0	0.0	[ms^{-1}]
Current velocity tide	$u_{c,tide}$	0.0	0.0	[ms^{-1}]
Current direction	μ_{curent}	90	90	[°]
Wind velocity	U_w	6.5	12.5	[ms^{-1}]
Structural damping ratio	ξ	0.02	0.02	[-]

4.3.1 Passing blade frequencies

The thrust force variations are caused by the wind turbulence and non-harmonic periodic processes, which are caused by tower shadow effect and wind shear effect, resulting in the fatigue loads of the wind turbine blades. The effect of the passing blade frequencies on the motion responses are investigated. The Bluewater wind turbine external function includes the tower shadow effect but does not take the wind shear effect into account, therefore FAST is used to investigate the wind shear effect. FAST [14] is an open-source software package for simulating coupled dynamic response of wind turbine.

4.3.1.1 Tower shadow effect

The thrust force oscillation due to the tower shadow effect for the wind speeds 6, 10, 17 and 24 m/s are given in Figure 4-4. The magnitude of the thrust force oscillations are significant. Concluded is that the tower shadow effect is important for the thrust force oscillations and should is to be taken into account. Figure 4-4 gives the thrust force with an active control system. The wind turbine control system controls the generator speed. The blade-pitch controller become active for high wind-speeds and will reduce the rotational speed of the blades.

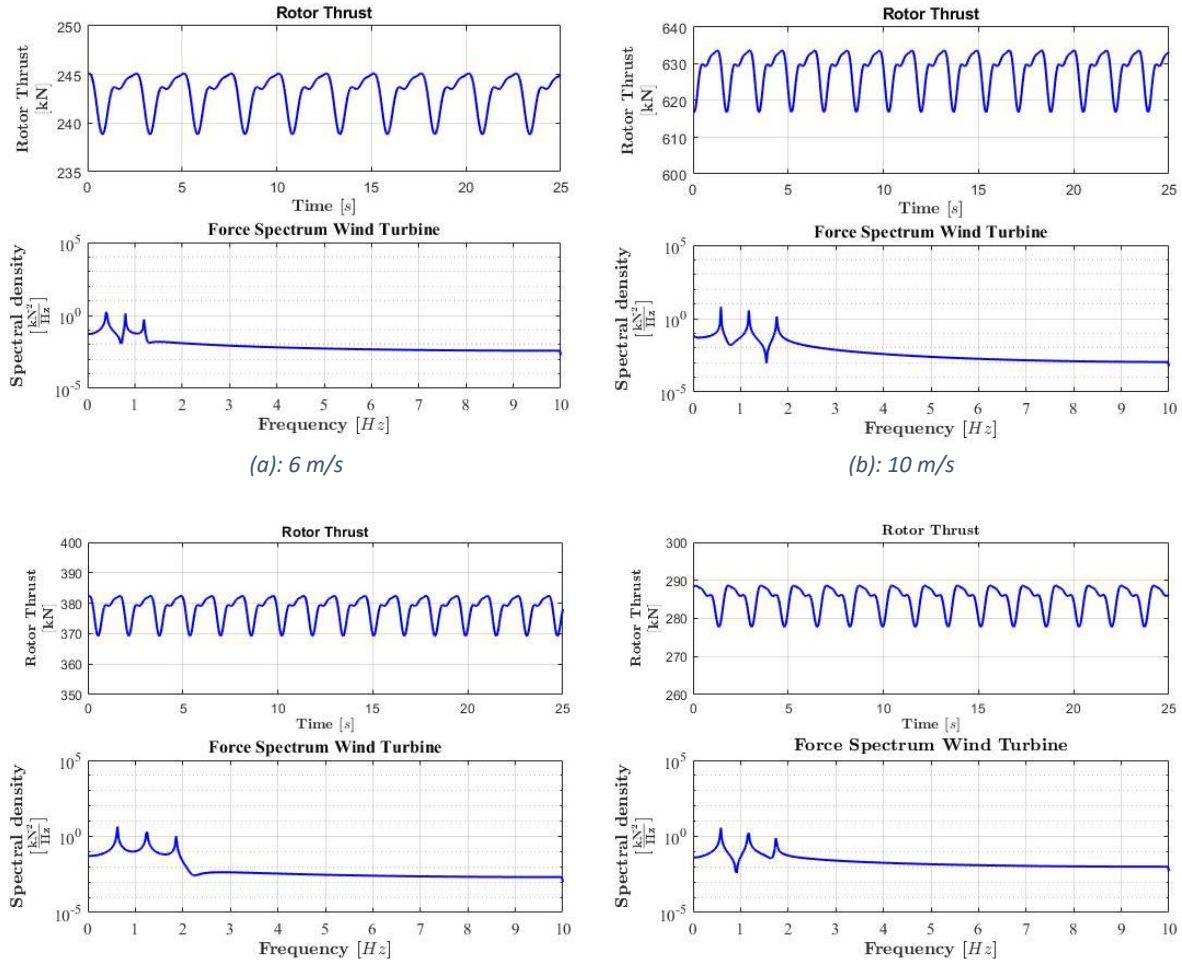

(a): 6 m/s *(b): 10 m/s*

(c): 17 m/s *(d): 24 m/s*

Figure 4-4: Thrust force oscillation due to tower shadow effect for several wind speeds

4.3.1.2 Wind Shear

The mean wind speed increases at higher elevations. The rotating blades of the wind turbine encounter difference wind speeds, an upwards rotating blade encounter a higher wind velocity than a downwards rotating blade. During a complete cycle, the thrust force is therefore oscillating with the same number of blades. The wind shear effect may be important for the wind turbine and is investigated.

The Bluewater wind turbine external function is used in the model, which does not take the wind shear into account, therefore FAST results from Bluewater are used to investigate the wind shear effect. The same wind turbine dimensions are used as the wind turbine of the external function, but the wind turbine is bottom fixed and not floating. Another difference is the wind shear model, FAST only allows the power law or the logarithmic wind shear model. The power law (equation (4-3)) wind shear model is used, which matches to the Froya wind (equation (4-4)) shear model. The wind shear effect is investigated for several wind speeds and the results are given in Figure 4-5.

$$u_m(z) = u(H)\left(\frac{z}{H}\right)^{\alpha} \tag{4-3}$$

u_m	Mean wind velocity	z	z-coordinate
H	Reference height	α	Shear exponent

$$u_m(z) = u_0\left(1 + 5.73 \cdot 10^{-2} \cdot \sqrt{1 + 0.148 \cdot u_0}\ln\frac{z}{H}\right) \tag{4-4}$$

u_m	Mean wind velocity	z	z-coordinate
u_0	Reference wind velocity	U_{10}	Reference velocity at z=10m

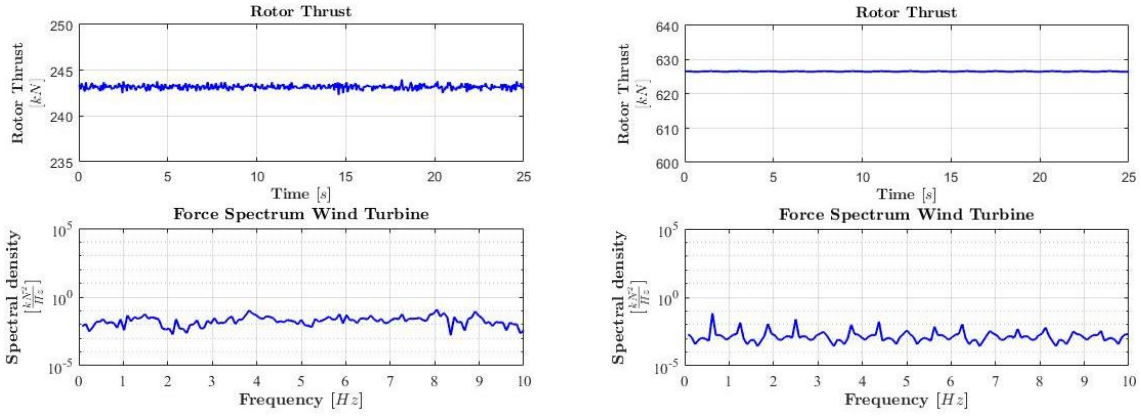

(a) 6 m/s

(b) 10 m/s

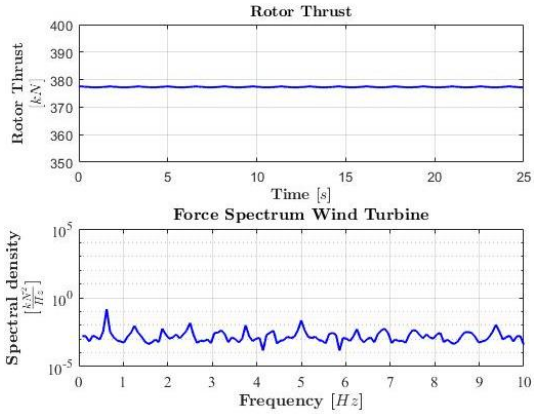

(c) 17m/s

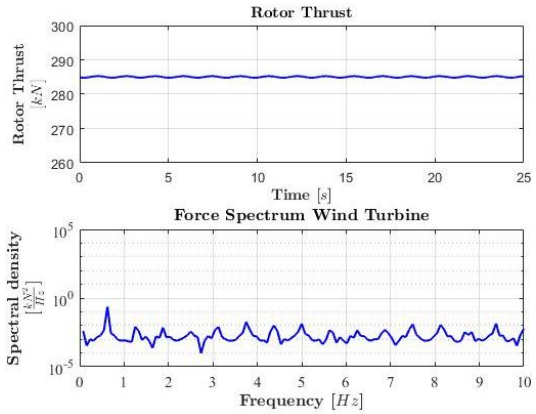

(d) 24 m/s

Figure 4-5: Thrust force for several wind speeds (a) 6 m/s (b) 10 m/s (c) 17 m/s (d) 24 m/s

The Froya wind shear model is used in the Matlab model, this model has the property of almost a constant mean wind speed over the height. The shear profile is site specific, therefore the wind shear effect is also investigated for several shear exponents (α in equation (4-3)) of the power law wind profile. A mean wind speed of 10 m/s is used and the results are given Figure 4-6.

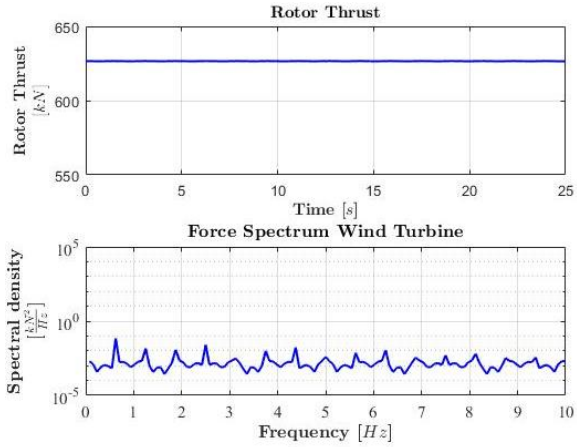

(a) α = 0.001

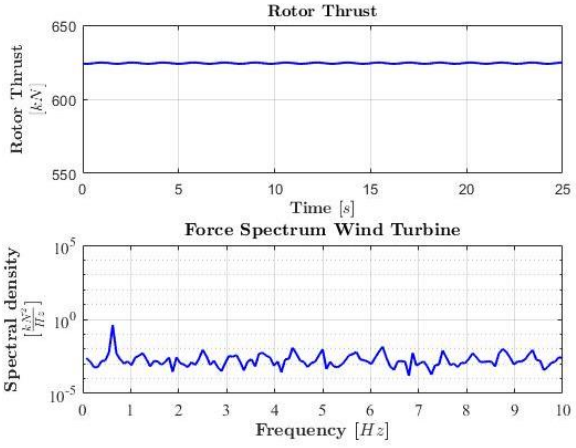

(b) α = 0.05

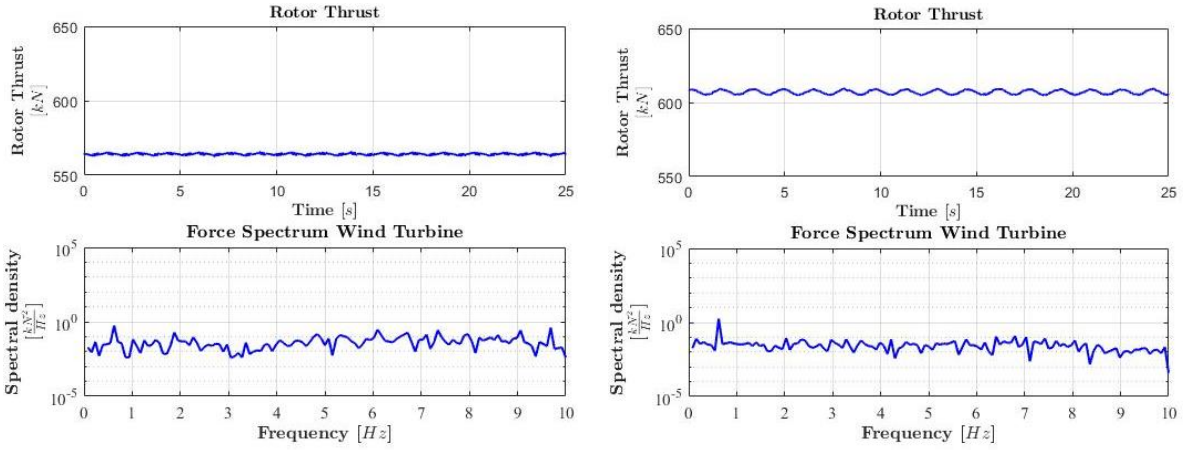

(c) α = 0.1 *(d) α = 0.2*

Figure 4-6: Thrust force for several shear exponents

The thrust force oscillations due to the wind shear effect is negligible. Concluded is that the wind shear effect can be neglected for the thrust force. The assumption that wind shear effect is negligible is valid, even for wind shear profiles with a higher wind gradient. The wind shear effect on the non-axial loads is not investigated, but is advised to investigate the shear effect with misalign wind.

4.3.1.3 Comparison tower shadow and wind shear effect

The tower shadow effect is dominant for the thrust force oscillations. For example, Figure 4-7 gives the thrust force oscillations for a wind speed of 10 m/s. The thrust force oscillations are made dimensionless by dividing the thrust force by the thrust force without the tower shadow and wind shear effect. From the figure, it can been seen that the thrust force oscillations due to wind shear are negligible. However, wind shear effect might be important for the non-axial loads. Concluded is that the tower shadow effect is dominant and the wind shear effect can be neglected on the thrust force oscillations. Not modelling the wind shear effect does not underestimate the thrust force oscillations.

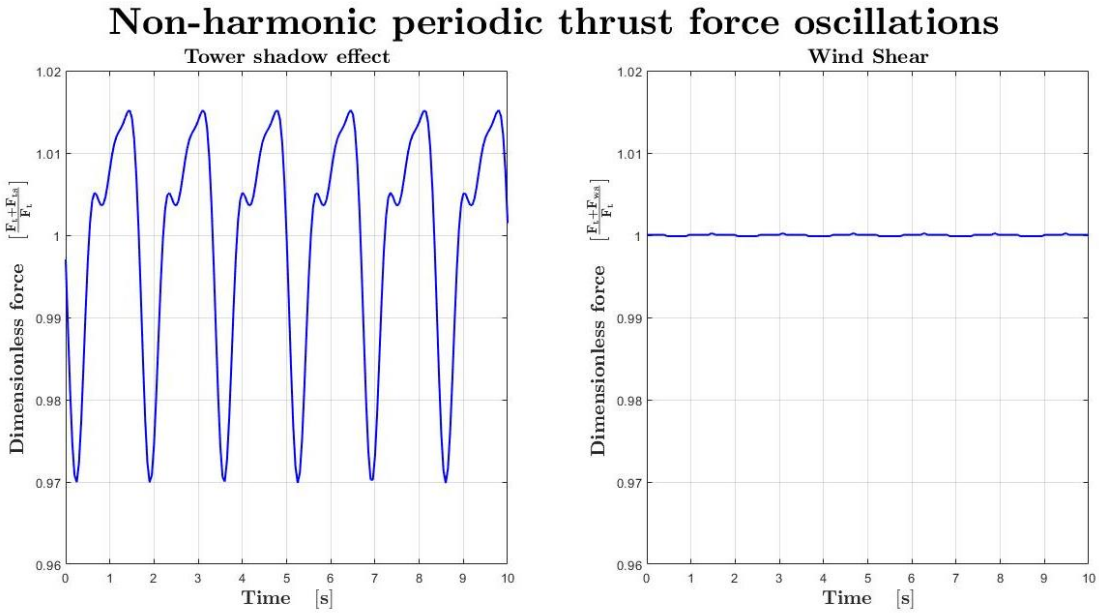

(a) *(b)*

Figure 4-7: Thrust force oscillations

4.3.1.4 Motion responses

The external function is used, which exclude the wind shear effect. However, the wind shear effect can be neglected (see 4.3.1.3 Comparison tower shadow and wind shear effect) on the thrust force oscillations with unidirectional wind. The effect of passing blade frequencies on the motions are investigated with the moderate and extreme environmental conditions. In case of the extreme environmental conditions lies the pitch/2nd tower bending mode in the 3P-frequency range.

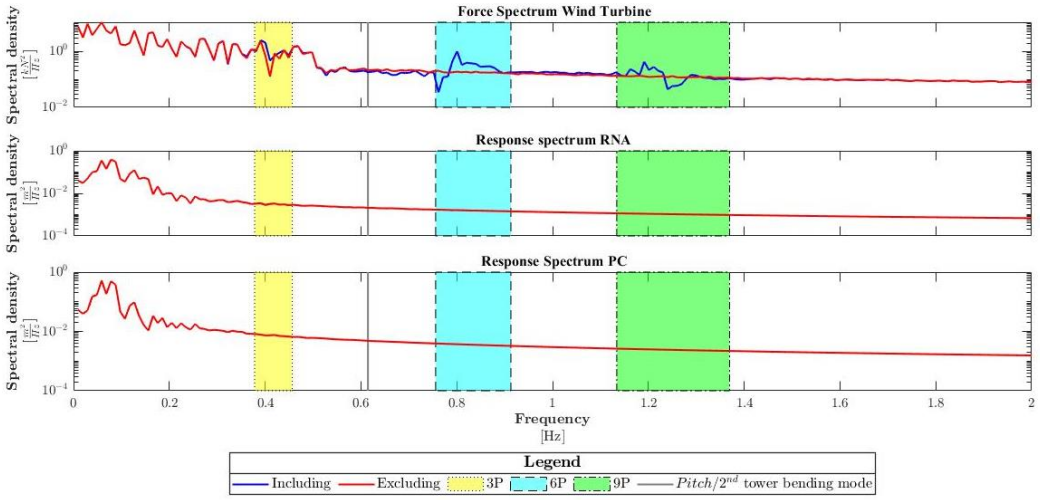

Figure 4-8: Response and force spectrum LC 1, including and excluding tower shadow effect

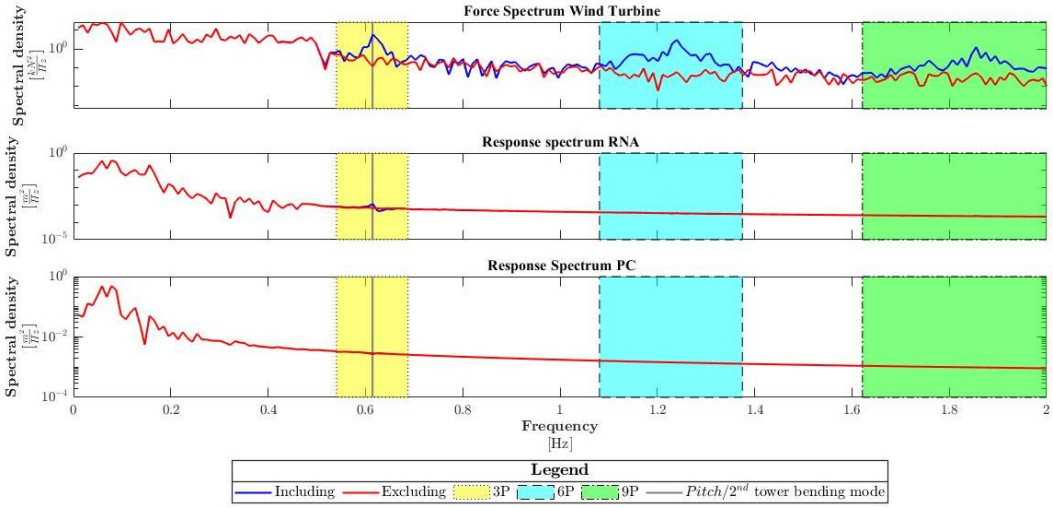

Figure 4-9: Response and force spectrum LC 2, including and excluding tower shadow effect

The motion response spectrum (x-direction) of the Nacelle-tower connection and pontoon-centre-column-connection and the force spectrum (x-direction) of the TLPWT are given in Figure 4-8 for the LC1 and Figure 4-9 for LC2. The figures show the response including and excluding the tower shadow effect. The force spectra between including and excluding the tower shadow effect show large difference in the colored areas, which is due to the non-harmonic period loading. In the colored area (yellow in Figure 4-8 and Figure 4-9) of 3P-frequency is a small difference noticed in the motion response spectra of the nacelle, but only if the pitch/2nd tower bending mode lies in the 3P-frequency range. The motion response spectra between including and excluding the tower shadow effect are identical. Concluded is that the tower shadow effect is important for the blades and RNA, but not for the floating support structure, because the large flexible tower works as a large damper.

4.3.1.5 Conclusions

The thrust force variations are due to the wind turbulence and non-harmonic periodic processes due to tower shadow effect and wind shear effect. Firstly, the tower shadow effect and the wind effect are investigated. The tower shadow effect is the dominant effect and the wind shear effect can be neglected on the thrust force oscillations, because the amplitude of these oscillations is small. However, the tower shadow effect must be taken into account.

The effect of the passing blade frequencies on the motions are investigated for two load cases. The spectrum of the thrust force and motions responses of the RNA and PC including and excluding the tower shadow effect are investigated. The passing blade frequencies are relevant for the wind turbine blades and RNA but not for the support structure. But it should be noticed that only the passing blade frequencies are important if a tower bending mode lies in the 3P frequency range. It is concluded that a tower bending mode should not be excited the tower bending mode, because large oscillations of the RNA may occur.

4.3.2 Gyroscopic moment

Figure 4-10 gives the forces and motion responses at the nacelle-tower connection of the moderate environmental conditions including the gyroscopic moments and excluding the gyroscopic moments. From the figure, it can be seen that the displacements and forces show identical responses. The rotations at the RNA show largely identical responses. The gyroscopic moments are small because the angular velocity of the rotor and the pitch and roll motions are relatively small. The motion responses of the TLP with gyroscopic moments and without gyroscopic moments show approximately identical responses. The gyroscopic moment can be neglected, but the gyroscopic effect is a self-excited vibration with little damping, which can become critical.

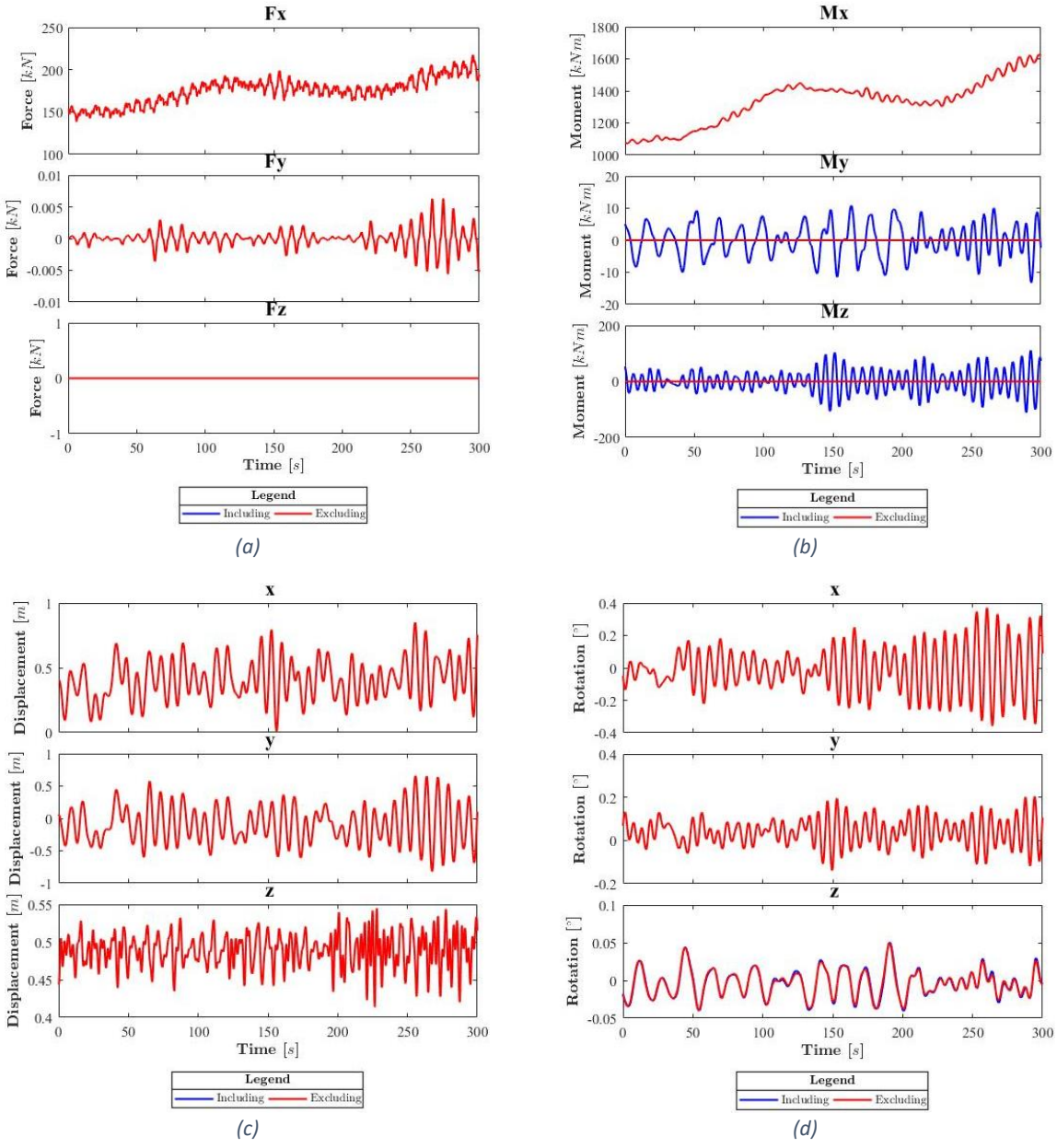

Figure 4-10: (a) Force (b) Moment (c) Displacement (d) Rotation of RNA including and excluding gyroscopic moments

4.4 CLOSURE

In the previous chapter the Matlab model is validated. The advantage of this model can provide all the output that the user wants. In the second chapter are some researches questions formulated and investigated in this chapter. The answers of the questions are given below.

- Rotating structures require special care, because this type of structures have properties which non-rotating structure have not, for example the gyroscopic effect. The influences of the gyroscopic effect on the natural period and motions are investigated. Concluded is that the gyroscopic effect can be neglected on the natural periods and the motions. The angular velocities of the blades are low and the angular velocities of the TLPWT too.
- The thrust force variations are due to wind turbulence and non-harmonic periodic processes. The main source of the non-harmonic processes are due to tower shadow effect and wind shear effect. Tower shadow effect is the dynamic interaction between the blades and the tower and wind shear effect is due to the main wind speed increases with the height. The thrust force oscillations due to tower shadow effect are compared with thrust force oscillations due to wind shear effect. Tower shadow effect is dominant and wind shear effect can be neglected. This assumption is made in the aerodynamic model.
- The passing blade frequencies are important for the fatigue life time of wind turbine blades. This effect on the motion responses of the nacelle-tower connection and PC-connection is investigated by comparing the response spectrum including and excluding the passing blade frequencies. Concluded is that the passing blade frequencies are important for the RNA, but only if the tower bending mode lies in this frequency range. The passing blade frequencies are not important for the PC-connection, because the large flexible tower works as a damper.

5 DEVELOPMENT AND APPLICATION OF THE METHOD

5.1 INTRODUCTION

The goal of this study is to develop and automate the design process to find a starting point to design a TLPWT. In the previous chapter the dynamic system of the TLPWT is investigated, the conclusions drawn in the previous chapter are used to find a good starting point.

5.2 METHOD DESCRIPTION

The TLPWT is exposed to aerodynamic and hydrodynamic loads, which may cause fatigue failure. Fatigue is stress driven and resonance drives stresses, therefore resonance of structural member should be avoided. The method finds a design with the natural frequencies outside the frequencies where wind and waves have energy and this method consists of two algorithms, mode tracking algorithm and selection algorithm. The following assumptions are made, with brief explanations on each assumption:

- **Linear dynamic system**
  The dynamic system of the TLPWT is a nonlinear dynamic system, due to the mooring stiffness and nonlinear setdown motion. However, the mooring stiffness becomes highly nonlinear for large amplitude motions, which only occurs during extreme environmental conditions. The natural periods of the TLPWT are approximately equal for small surge amplitudes, see section 4.2.2. Therefore, the TLPWT is assumed to be linear.
- **Forced vibrations**
  The vibrations due to the aerodynamic and hydrodynamic forces are self-excited vibrations, which are vibrations that sustains the motion. However, there is assumed that vibrations due to the aerodynamic and hydrodynamic forces are forced induced vibrations. This is a conservative assumption because the motion amplitudes of forced vibrations are larger in comparison of self-excited vibrations. However, there is one exception, which is the aerodynamic damping. The aerodynamic damping can become negative, which means that the aerodynamic forces increase, but negative aerodynamic damping can be solved with the control system of the wind turbine. Therefore, this can be excluded and is outside the scope.

Fatigue lifetime of the TLPWT is key dependent on the number of oscillations and the stress amplitudes. Forced vibrations have the same frequency as the forced frequencies, which are the wave, wind and passing blade frequencies. The wave and wind frequencies depend on the offshore size. However, the forced vibrations of nonlinear system differs form a linear system. A nonlinear dynamic system that is excited by a force will vibrate in the force frequency but also a second resonance frequency will occur. This is called sub- and superharmonic frequencies. However, this method assumes a linear dynamic system and sub- and superharmonic frequencies do not occur at linear dynamic systems.

This method can assist during the primarily design phase but is not acceptable as a fatigue assessment of the TLPWT. Design regulations, for example DNVGL [101], require a detailed fatigue analysis, which means time domain simulations to compute the stresses at the points of interest. The total required time for a lifetime fatigue assessment ranges from a few weeks to a few months.

5.3 MODES OF INTEREST

Resonance motions of a structure should always be prevented. Therefore, the natural frequencies of the TLPWT should be outside the load spectrum of the wind, waves and passing blade frequencies. There are many modes which can be excited but the only modes of interest are the rigid and elastic modes of the TLPWT. Thus the modes of the mooring system are excluded, because the mooring lines are outside the scope of this study. The mode shapes are given in Figure 5-1.

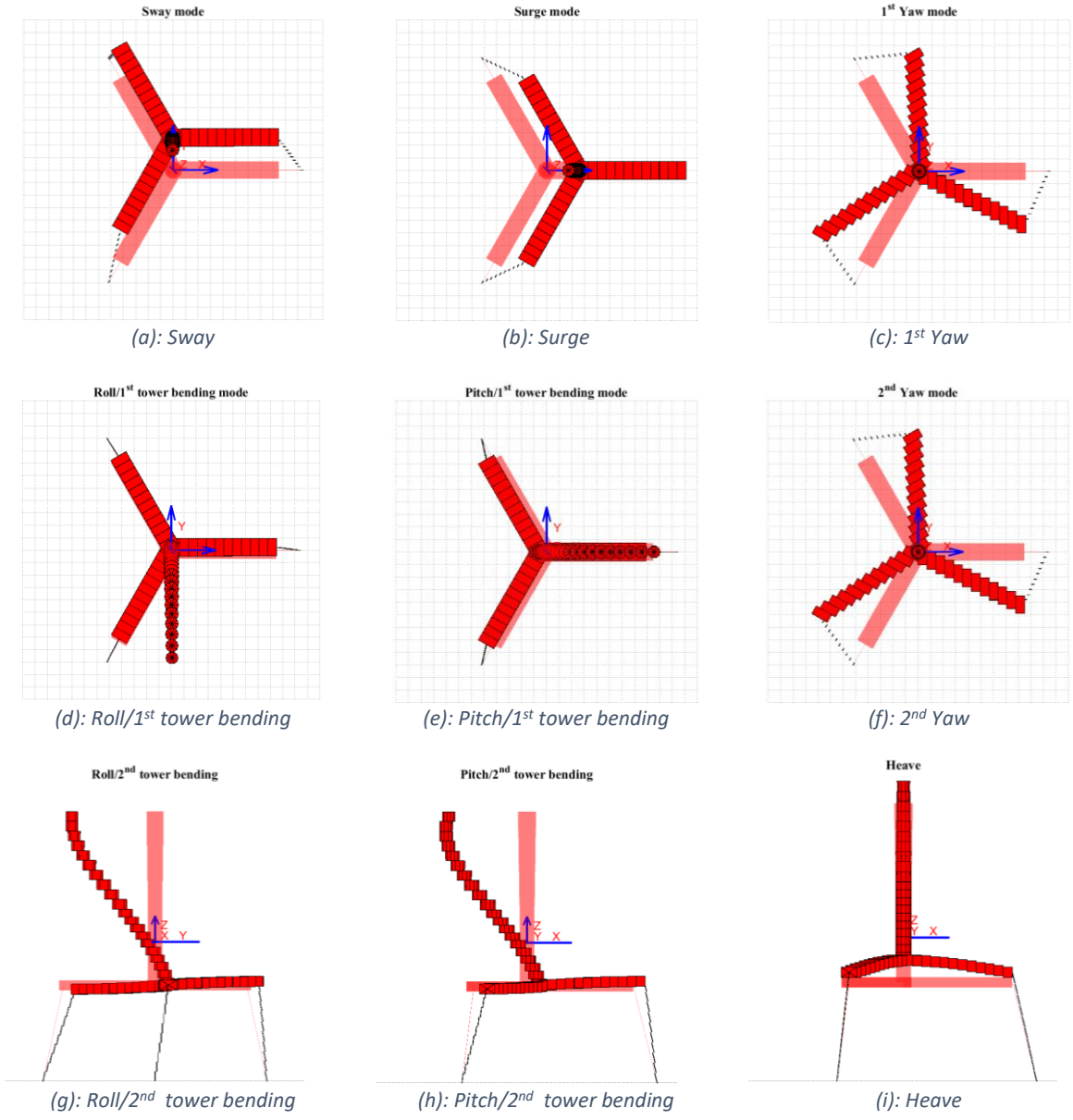

(a): Sway *(b): Surge* *(c): 1st Yaw*

(d): Roll/1st tower bending *(e): Pitch/1st tower bending* *(f): 2nd Yaw*

(g): Roll/2nd tower bending *(h): Pitch/2nd tower bending* *(i): Heave*

Figure 5-1: Reference modes shapes in order of natural frequency

5.4 MODE TRACKING ALGORITHM

The aim of this study is to investigate many design in a short time, therefore the parametric study is automated. When changing the design of the TLPWT, the natural frequencies and mode shapes are recalculated automatically. In some cases, the mode shapes may change from order in terms of the natural frequency. It is critical to track the rigid and elastic modes of the floating support structure accurately to ensure the correct natural frequency is matched to the natural frequency mode. Modal assurance criterion [101] (MAC) is used to track the modes. MAC (see equation (5-1)) computes the projection of a modes shape to the reference mode shape. MAC is originally used to match the experimental mode shape with a numerical mode shape. Nowadays, MAC is also used for model updating and parametric estimation consistency diagrams.

$$MAC = \frac{\left|\Psi_R^T \Psi_C\right|^2}{(\Psi_R^T \Psi_R^H)(\Psi_C^T \Psi_C^H)} \tag{5-1}$$

MAC	Modal assurance criterion	Ψ_C	Computed mode shape
Ψ_R	Reference mode shape		

The MAC gives a scalar value between 0 and 1. A MAC-value of 0 means that there is no consistent correspondence between the mode shape and the reference mode shape. MAC can take a value of 0 if the mode vectors are linearly unrelated, but also if the dynamic system is nonlinear. This occurs if the mode shapes are taken at different excitation levels. A MAC-value of 1 means a consistent correspondence between a mode shape and the reference mode shape. A MAC-value of 1 occurs if the mode shapes are the same modal vector [101]. The mode shapes are normalized therefore the modal vectors can have different scaling vectors.

5.4.1 Multiple natural frequencies

It is noticed that when two natural frequencies become close to each other, the eigenvectors computed with the Matlab eigensolver no longer matches with the reference modes. When two natural frequencies are going towards the same frequency, multiplicity of eigenvalues occur. The eigenvectors are linear dependent and the matrix becomes a defective matrix. The eigenvectors form a subspace and any combination of the eigenvector shows a solution of the eigenvalue problem. The Matlab eigensolver uses the QZ-algorithm. It is well documented that this algorithm is very sensitive to multiple and defective eigenvalues. Computing the eigenvalues and eigenvector of defective matrix remains a challenge. Optimization problems of natural frequencies or modes shapes the problem of multiple eigenvalues are well recognized, for example [102] and [103].

Figure 5-2 gives an example of multiple natural frequencies. The heave (Figure 5-2 (a)) and pitch/2nd tower bending mode (Figure 5-2 (b)) become closer and closer. Finally, both modes will have approximately the same natural frequencies and the modes become the same (Figure 5-2 (c)). A small change of the design of the TLPWT and the two modes can be tracked again (Figure 5-2 (d and e)).

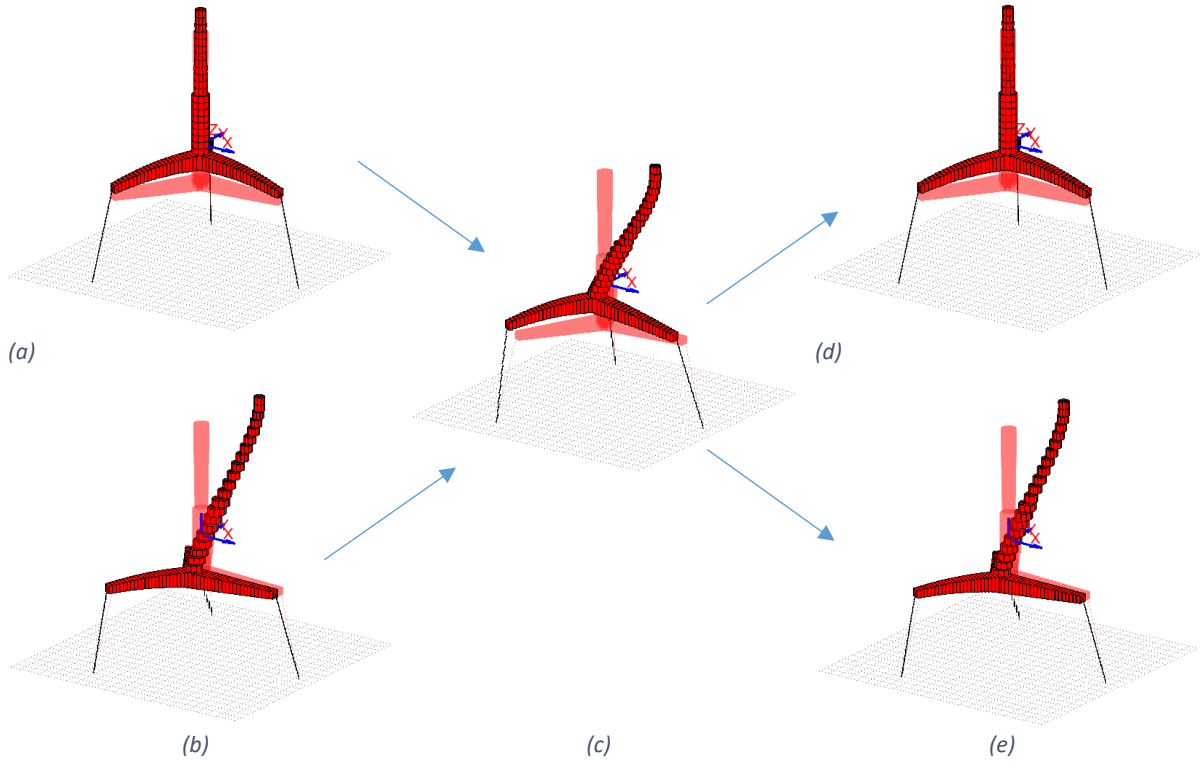

Figure 5-2: Example of multiple natural frequencies, heave and pitch\2nd tower bending mode

5.4.1.1 Solution

The presence of multiplicity of eigenvectors is observed in this study. It is not the aim of this study to solve this problem. So as long as the correct modes are tracked, the correct natural frequencies are found. If two natural frequencies switch the order in which they appear, the mode shapes are approximately identical and the QZ-algorithm is still be able to match the mode shapes. If the natural frequencies become closer and closer, the QZ-algorithm will not match with any mode shape. To overcome this problem of multiple eigenvalues, the design will be altered to allow the algorithm to match the correct mode shapes. Thus, the design of the TLPWT will change to avoid multiplicity of eigenvalues.

5.4.2 Algorithm

The parametric study will compute the natural frequencies and modes shapes for every combination of parameters. An algorithm is developed in this study to automate the parametric study and the algorithm is given in Figure 5-3. The first step is the initialization step and makes a combination of the design parameters. The second step is to create the TLPWT with the parameters. The third step is to solve the TLPWT hydrostatic. The tendon tension should be positive, otherwise the TLPWT will sink. If the TLPWT floats, a modal analysis is performed and the MAC criteria is used to find the correct natural frequencies.

The algorithm works properly, as long as the eigenvectors will not change significant. A mode is matched if the MAC-value is equal or higher than 0.30. This value is selected based on experimenting with the algorithm. If not all modes are found, than the pontoon height of the TLPWT will be increased by 0.01m and the same procedure is repeated. This step size is also based on experimenting with the algorithm. The algorithm will be able to calculate the natural frequencies, otherwise an error will be given. The final step is to save the dimensions, weight, tendon tension and the natural periods.

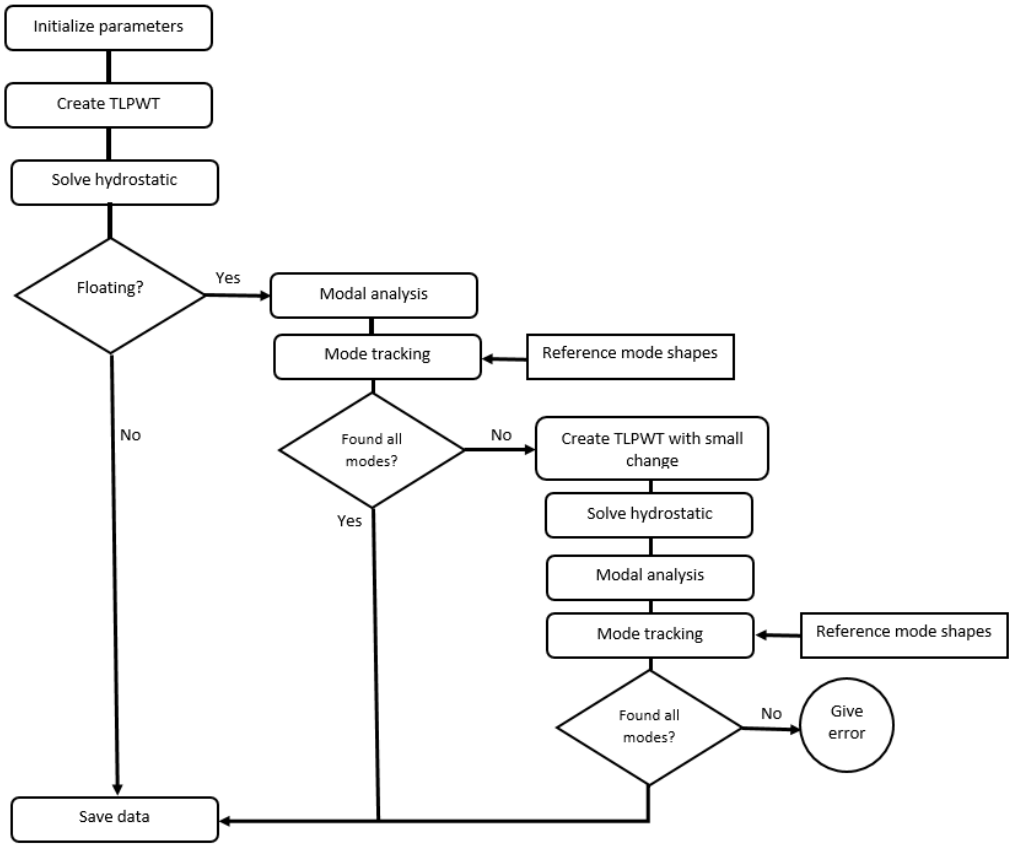

Figure 5-3: flow-chart algorithm

5.4.3 Discussions

The developed algorithm has been tested for the design parameters defined in 5.6.1 Design parameters, span a design space of approximately 6000 designs. The algorithm successfully track the modes in 99.98% of the cases. A match is considered successful if the algorithm is be able to track the mode, otherwise a value of -1 is given. Concluded is that the algorithm can successfully be used to track the natural periods in a short period of time for a large number of parameter variations.

5.5 SELECTION ALGORITHM

The developed mode tracking algorithm computes the mass, tendon tension and computes the natural periods in a short period of time, but does not identify the best design of the TLPWT. The aim of the selection algorithm is to investigate in a short period of time many designs and gives a good starting point for further variations.

5.5.1 Methodology

This method is based on the assumption that if the motion responses are low, resonance of the natural frequency modes of the TLPWT is avoided and the fatigue lifetime is relatively high. This method analyses the design space in a short amount of time. Frequency domain modelling is an efficient and effective method to analyse design and frequency domain modelling gives better understanding of the dynamic system [94]. However, there is no commonly accepted frequency domain modelling method for floating wind turbines, but for fixed offshore wind turbine many frequency domain methods are developed and proven to be effective and accurate, for example [94] and [104]. Frequency domain modelling requires to linearize the nonlinearities in aerodynamics, control system, hydrodynamics and the coupling.

The dynamic system of a TLPWT is nonlinear, for example the interaction between the wind turbine and the floating support structure. For a good starting point, there is assumed that the nonlinearities can be neglected. A linear system has the property that the output of the system only depends on the amplitude of the input and excitation frequency. The function, which relates the input and the output, is known as the transfer function and is explained in section 5.5.2.

The motion response spectrum is computed by equation (5-2). The area of the response spectrum is defined as the statistical variance or mean square value of zero mean process. The area can be computed with the equation (5-3). The area is multiplied with the probability of occurrence. It is known, that narrow banded spectrum are worse than a wide spectrum. Therefore the area is squared.

$$S_{\zeta;TLPWT} = \left|H_j(\mathrm{f})\right|^2 S_{force}(\mathrm{f}) \tag{5-2}$$

$S_{\zeta;TLPWT}$	Response spectrum TLPWT	H_j	Transfer function of mode j
f	Frequency	S_{force}	Spectrum force

$$\mu_0 = \int_0^\infty \left(S_{\zeta;TLPWT}(f)\right)^2 df \; (S_{w;w}) \tag{5-3}$$

μ_0	Total energy	n	Number
$S_{\zeta;TLPWT}$	Response spectrum TLPWT	f	Frequency
P	Probability of occurrence		

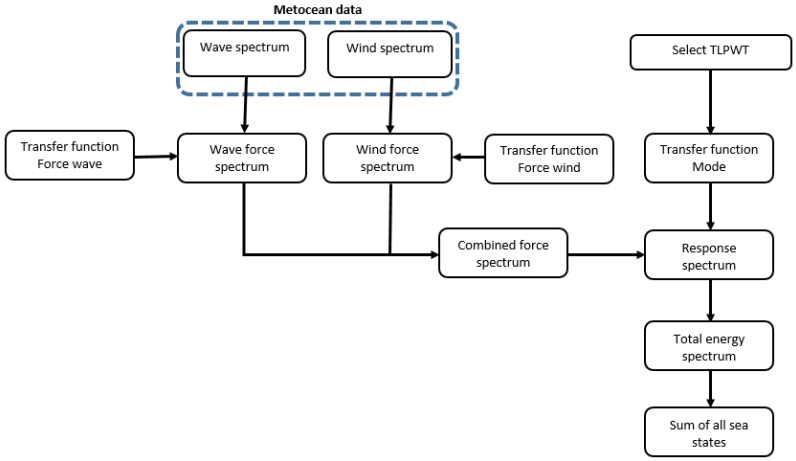

Figure 5-4: flow-chart algorithm

5.5.2 Transfer function definition

The transfer function can be visualized as a black box and gives the relation between the input and output as function of the frequency. The transfer function is defined as the ratio of the Laplace transform or Fourier transform of the output to that of the input. The concept of the transfer function is used in many engineering field, such as control, design, simulation and physical modelling [105]. The transfer function is based on the requirement of linearity of the system.

To calculate a transfer function of a linear system, the impulse response of the system is calculated. For a linear system, the response is calculated by the product of the input and the impulse response (see equation (5-4)).

$$y(t) = x(t) * h(t) \tag{5-4}$$

y	Output	x	input
h	Impulse responses	t	Time

Let the input be the sum of exponential function with a frequency (equation (5-5)). Since the system is linear, the output of the system is also the sum of exponential function with the same frequencies. Convolution theorem states that a Fourier transform of two signals is the pointwise product of their transforms. Thus, equation (5-4) can written in frequency domain as equation (5-6).

$$x(t) = \sum_{i-0}^{n} x_0 e^{2\pi f t} \tag{5-5}$$

$$Y(f) = H(f)X(f) \tag{5-6}$$

Y	Fourier transform of the output	X	Fourier transform of the input
H	Fourier transform of impulse response	f	Frequency

By definition, H(f) is the transfer function of the system, it is a characteristic property of the system. The transfer function is rational function, which means that the function is defined such that the numerator and the denominator are polynomials.

$$H(f) = \frac{Y(f)}{X(f)} \tag{5-7}$$

H	Transfer function	Y	Fourier transform of the output
X	Fourier transform of the input	f	Frequency

5.5.3 Transfer function modes

For a linear system, the motion can been written as a linear combination of the modes shapes. For each individual mode, the motion can be described by a single-degree-of-freedom damped mass-spring system. The transfer function of a damped mass-spring system is given in equation (5-8) and Figure 5-5 gives the transfer function for different damping ratios. This transfer function gives the relation between the force and the displacement.

$$H_x(\Omega) = \frac{x_{dynamic}}{x_{static}} = \frac{1}{\sqrt{(1-\Omega^2)^2 + (2\xi\Omega)^2}} \tag{5-8}$$

$$\Omega = \frac{f}{f_n}$$

H_j	Transfer function of mode j	f	Excitation frequency
f_n	Natural frequency	ξ	Damping ratio

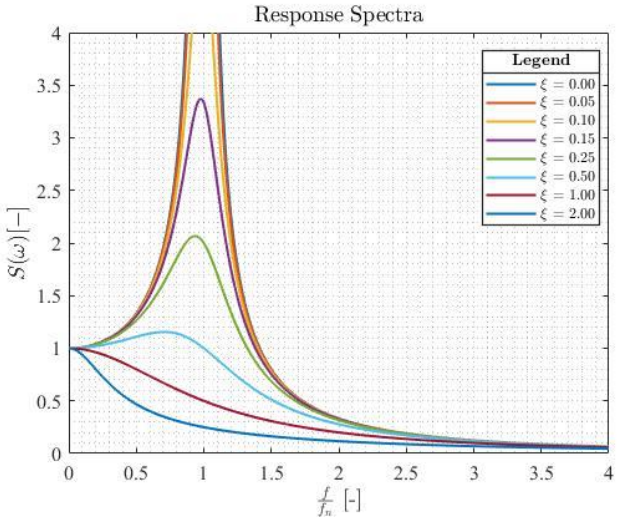

Figure 5-5: Transfer function mass-spring system for difference damping ratios

5.5.4 Transfer function waves

The hydrodynamic loads are modelled with the Morison equation and this equation includes a linear inertia and a quadratic drag. Morison equation is a nonlinear equation due to the quadratic drag force. However, the requirement of linearity of the transfer function is not fulfilled, therefore the quadratic drag force is linearized. The transfer function of the wave loads can therefore been written as a superposition of the linear inertia force and a linearized drag force.

$$\left|H_{f,wave}(f)\right|^2 = \left|H_{f,i}(f)\right|^2 + \left|H_{f,d}(f)\right|^2 \tag{5-9}$$

$H_{f,wave}$	Transfer function wave loads	$H_{f,i}$	Transfer function inertia loads
$H_{f,d}$	Transfer function drag loads	f	Frequency

With the assumption of deep water, the transfer function of the linear inertia force can be written as equation (5-10). The wave lengths are computed with the dispersion relation, which is for deep water equal to equation (5-11).

$$\left|H_{f,i}(f)\right| = \rho_w A(1 + C_a)\left|(2\pi f)^2 e^{kz}\right|^2 S_{wave}(f) \tag{5-10}$$

$$k = \frac{(2\pi f)^2}{g} \tag{5-11}$$

$H_{f,i}$	Transfer function inertia loads	f	frequency
ρ_w	Density water	A	Area
C_a	Coefficient added mass	k	Wave number
z	z-coordinate	S_{wave}	Wave spectrum

The drag term should be linearized. There are multiple methods to linearize the drag force of the Morison equation, for example Lorentz linearization, Taylor series linearization and stochastic linearization, which is also called equivalent linearization [12]. Up to the present, stochastic linearization is the most commonly used method for analysis of offshore structures, for example [106] and [107]. Therefore, stochastic linearization is adopted in this study.

Borgman [108] presents an accurate and simple approximation of the Morison equation and explains the proportionality between the spectral density of the Morison equation and the sea surface. He used the concept of stochastic linearization, which assumes that the quadratic velocity can be approximated as a multiplication of the velocity and a constant that is proportional to the standard deviation of the velocity. The constant is proportional to the expected value of the difference between the drag and linearized drag term. The transfer function of drag forces is given in equation (5-12).

$$\left|H_{f,d}(f)\right| = \frac{1}{2}\rho_w D C_d \left|\sigma_u^2 (2\pi f) e^{kz}\right|^2 S_{wave}(f) \quad (5\text{-}12)$$

$$\sigma_u^2 = \frac{8}{\pi} var(u)$$

$H_{f,d}$	Transfer function drag loads	f	frequency
ρ_w	Density water	D	Diameter
C_d	Coefficient drag	k	Wave number
z	z-coordinate	S_{wave}	Wave spectrum
σ_u^2	Variance non-Gaussian process		

The transfer function gives the relation between the wave spectrum and the wave loads per unit length. The hydrodynamic loads acting on the centre column are dominant and therefore only the hydrodynamic loads on the centre column are taken into account. The transfer function of the hydrodynamic loads is given in equation (5-13). Figure 5-6 gives the hydrodynamic force spectrum by the proposed method and the force spectrum of a time simulation of 600 seconds, which shows large identical spectra.

$$\left|H_{f,wave}(f)\right|^2 = \left|H_{f,i}(f)\right|^2 + \left|H_{f,d}(f)\right|^2 \quad (5\text{-}13)$$

$$\left|H_{f,i}(f)\right|^2 = \rho_w A (1 + C_a)(2\pi f)^2 \left(\frac{g}{2}\right)\left(1 - e^{-kz_d}\right)^2 S_{wave}(f)$$

$$\left|H_{f,d}(f)\right|^2 = \frac{1}{2}\rho_w D C_d \sigma_u^2 \left(\frac{g}{2}\right)\left(1 - e^{-kz_d}\right)^2 S_{wave}(f)$$

$$\sigma_u^2 = \frac{8}{\pi} var(u)$$

$H_{f,wave}$	Transfer function wave loads	$H_{f,i}$	Transfer function inertia loads
$H_{f,d}$	Transfer function drag loads	f	Frequency
ρ_w	Density water	A	Area
D	Diameter	C_a	Added mass coefficient
C_d	Drag coefficient	g	Gravity acceleration
z_d	Draught	S_{wave}	Wave spectrum

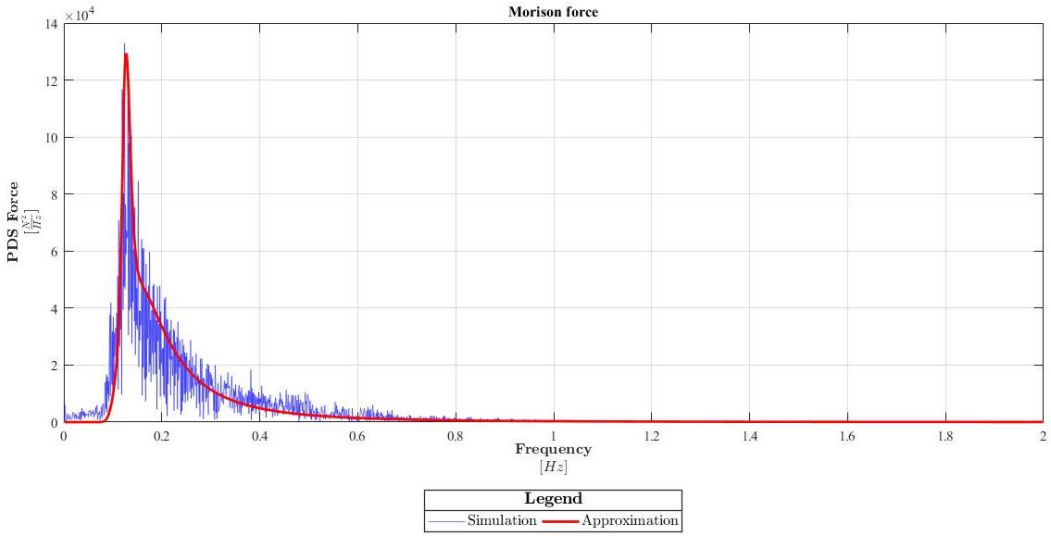

Figure 5-6: load spectra and transfer function of wind load

5.5.5 Transfer function wind

The wind loads on the tower are neglected and only the wind turbines loads are considered, because the wind loads acting on the tower are small with respect to the wind turbine loads. The wind turbine loads are highly nonlinear due to the tower shadow effect and the control system of the wind turbine. The nonlinearities of the wind turbine are hard to linearize. Van der Tempel [94] proposed a more pragmatic way to find the transfer function between the wind spectrum and the wind turbine loads.

The method proposed by Van der Tempel uses some form of time domain simulations to find the transfer function. The wind turbine loads are uncoupled from the structure, thus the behavior of the floating support structure is neglected. In case of the Matlab model, only the Bluewater wind turbine external function is used. The wind turbine loads are computed for several wind conditions, including tower shadow effect. By definition, the transfer function can be found by dividing the load spectra of the wind turbine loads by the wind spectrum (equation (5-14)). Note, aerodynamic damping is not included in this calculation. The same study showed that the aerodynamic damping is important for wind turbine responses of the bottom founded wind turbine. However, there is no commonly accepted method to take the aerodynamic damping into account for a FWT.

$$\left|H_{f,w}(f)\right|^2 = \frac{S_{Fx}(f)}{S_{wind}(f)} \tag{5-14}$$

$H_{f,w}$	Transfer function wind – turbine loads	S_{Fx}	wind turbine load spectrum
S_{wind}	Wind spectrum	f	Frequency

Figure 5-7 gives the force spectrum and the transfer function for several wind conditions. From the figure can be concluded that the transfer function is depending on the main wind speed. However, in the low frequency range the transfer function is approximately the constant. The transfer function is approximated by the build-in Matlab ‘’fit’’ function. The Gaussian model is used because this model is be able to fit the 3P peak in the transfer function. The approximated transfer function is given in Figure 5-8. For the wind speeds below the 15 m/s the transfer function approximation is acceptable, but the transfer function overestimate the wind turbine loads for wind speeds above the 15 m/s. However, these wind conditions are rare.

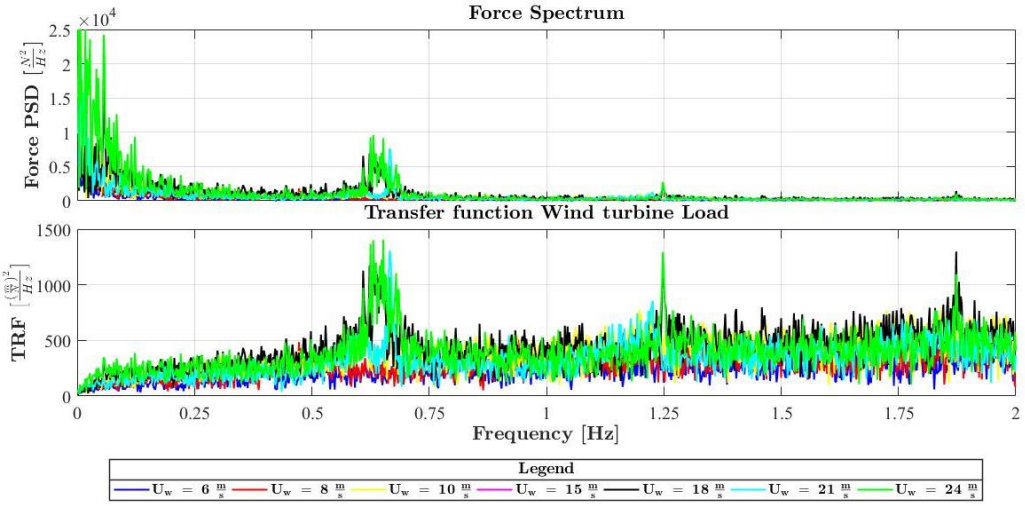

Figure 5-7: Force spectrum and transfer function for several wind conditions

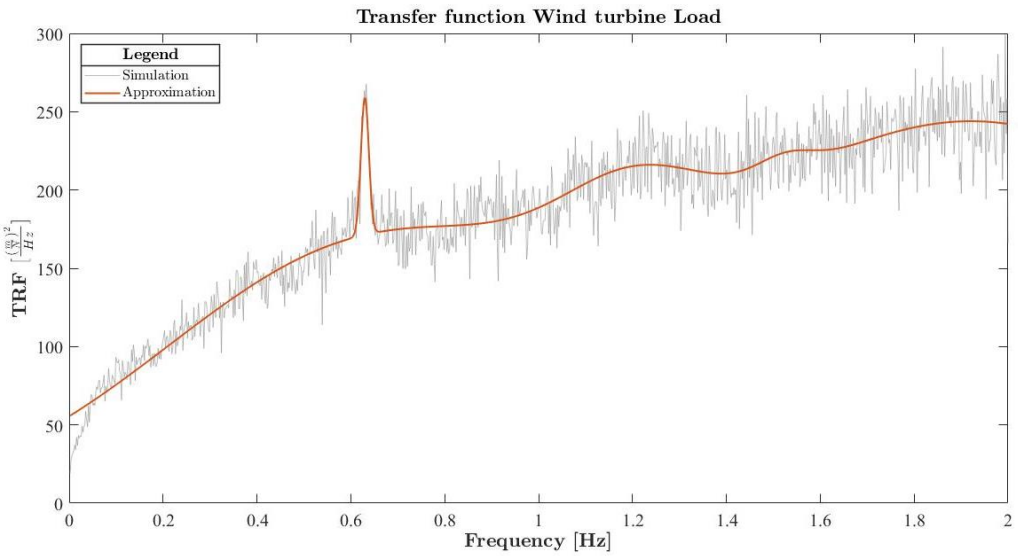

Figure 5-8: load spectra and transfer function of wind load

5.5.6 Transfer function waves & wind

The wave spectra and wind spectra are known from the metocean data. The wind load spectrum and wave load spectrum are computed by the transfer functions. However, an environmental load case is a combination of waves and wind. The load spectrum is a superposition of the wind load spectrum and the waves load spectrum. The DNV relation (equation (5-15)), between the significant wave height and the main wind speed, is used to combine the waves and wind.

$$u_{wind} = (25H_s)^{\frac{1}{1.64}} \tag{5-15}$$

u_{wind} Transfer function wind – turbine loads H_s wind turbine load spectrum

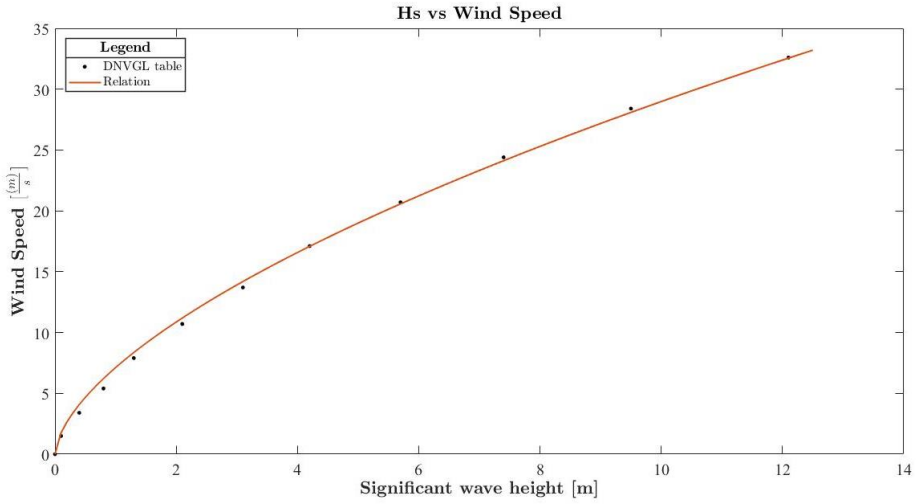

Figure 5-9: Relation significant wave height vs wind speed

5.6 DESIGN CASE

The mode tracking algorithm and the selection algorithm are be able to find a good starting point with the natural frequencies outside the wave and wind spectrums. The TLPWT is designed for North-Sea applications, which has a combination of high wind speeds, relatively high waves and strong current. The metocean data of the site is used in this study and Figure 5-10 gives the wind spectra and wave spectra.

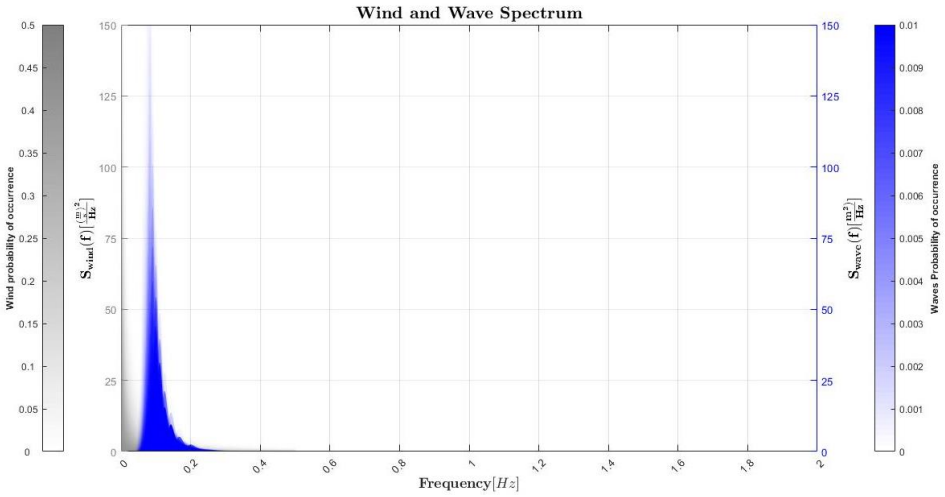

Figure 5-10: Environmental spectra of North-Sea site as functions of probability

5.6.1 Design parameters

The design of the TLPWT looks relatively simple but still there are many design parameters of the TLPWT. The tower is not part of the scope and therefore the design parameters of the tower are excluded. Which means that tower bending modes are approximately constant. The tower bending modes lie within the 3P-frequency range, therefore the design of the tower does not meets the requirements. The design of the tower should be modified.

Six design parameters are chosen to investigate the design space of the TLPWT. The design parameters are given in Table 5-1 and visualized in Figure 5-11. The parameter c is defined as the ratio between the pontoon height at the pontoon-centre column connection and the pontoon height at the pontoon-tendon connection (see equation (5-16)). The pontoon width is directly related to the pontoon height. The width is 0.65 of the height of the pontoon. The plate thickness of the pontoon and centre column are fixed.

$$c = \frac{h_{p.e}}{h_{p,s}} \tag{5-16}$$

c	Tapering of the pontoon	$h_{p.e}$	Pontoon height at pontoon-tendon connection
$h_{p,s}$	Pontoon height at pontoon-centre column connection		

Table 5-1: Design parameters

Parameter		*Symbol*	*Unit*	*Reference*	*Range*	*Step size*	*Total*
Pontoon	Length	L_p	[m]	42.5	35 - 50	5	4
	Height	h_p	[m]	7	4 - 13	3	4
	Tapering	c	[-]	0.5	0.4 - 0.6	0.05	5
Tendon	Angle	α_{tendon}	[degree]	8.5	5 - 15	3	5
Centre Column	Draught	d	[m]	30	24 - 36	3	5
	Diameter	D_{cc}	[m]	8	6 - 12	3	3

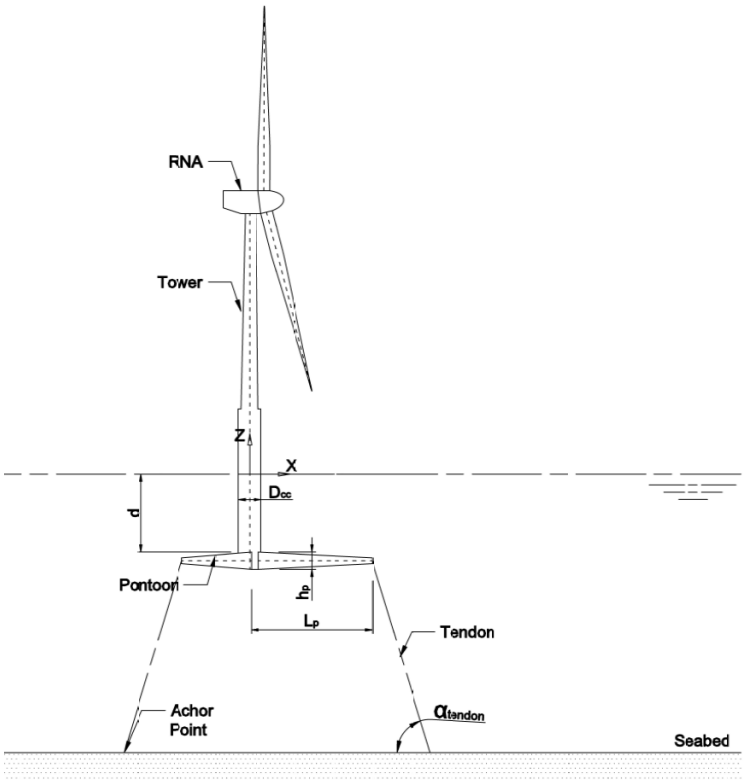

Figure 5-11: Location of Design parameter

5.6.2 Results

The mode tracking algorithm and selection algorithm are used for the design space defined in 5.6.1 Design parameters, which span a design space of approximately 6000 designs. Only the load cases are taken into account where the main wind speed is below 15 m/s, which means that 95% of the metocean data is covered. The damping ratios are determined with a decay test and the results are given in Appendix: Decay test and given in Table 5-2. The damping ratio for sway, pitch and roll are assumed to be equal to the damping ratio of surge. Table 5-3 gives the results and this design is called the improved TLPWT hereafter.

Table 5-2: Damping ratio

	Surge	*Heave*	*Yaw*
Damping ratio	0.22	0.11	0.22

Table 5-3: Design parameters of the reference and improved TLPWT

Parameter		*Symbol*	*Unit*	*Improved*
Pontoon	Length	L_p	[m]	35
	Height	h_p	[m]	8
	Tapering	c	[-]	0.5
Tendon	Angle	α_{tendon}	[degree]	12.5
Centre Column	Draught	d	[m]	27
	Diameter	D_{cc}	[m]	9

5.6.2.1 Comparison of reference TLPWT and improved TLPWT

The reference TLPWT (see Appendix: Properties TLPWT and Figure 5-12 (a)) is designed for the same locations, however the reference TLPWT is predominately designed to prevent slack tendons. The improved TLPWT (see Appendix: Properties TLPWT and Figure 5-12 (b)) is the design with the natural frequencies outside the wind and wave spectra, which is found after the use of mode matching and selection algorithm.

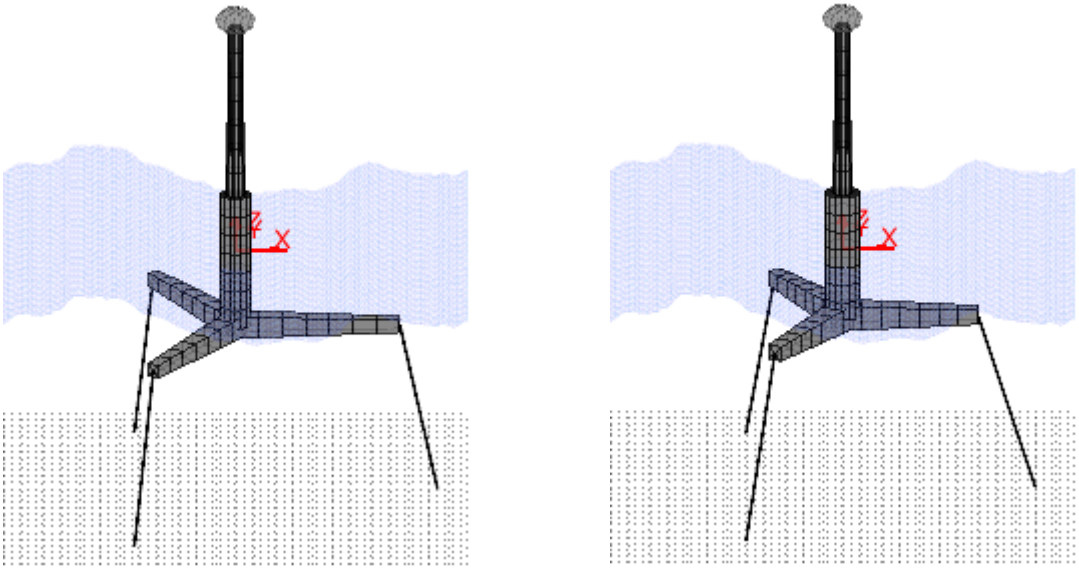

(a) *(b)*

Figure 5-12: (a) Reference TLPWT (b) Improved TLPWT

Table 5-4 gives the natural periods of the reference and improved design. The roll/1st tower bending mode of the reference TLPWT is close to the wave peak period of the site (see Figure 5-13), which is 8 seconds. The roll/1st tower bending mode of improved TLPWT has the natural period still in the wave spectra, but the amount of energy in these wave frequencies is below the 5% (see Figure 5-14) and in sea states where the loads are relatively low. Another large difference is the pitch/1st tower bending mode, but both natural periods are in the frequencies where the waves have less energy. The other natural periods are approximately the same.

Table 5-4: Natural periods of reference and improved TLPWT

Natural period	*Reference [s]*	*Improved [s]*
Sway mode	20.3	19.55
Surge mode	20.4	20.51
Heave mode	2.28	1.73
Roll/1st tower bending mode	7.97	6.12
Pitch/1st tower bending mode	6.00	5.27
1st yaw mode	13.86	13.98
Roll/2nd tower bending mode	2.35	2.00
Pitch/2nd tower bending mode	2.12	1.83
2nd yaw mode	2.64	2.10

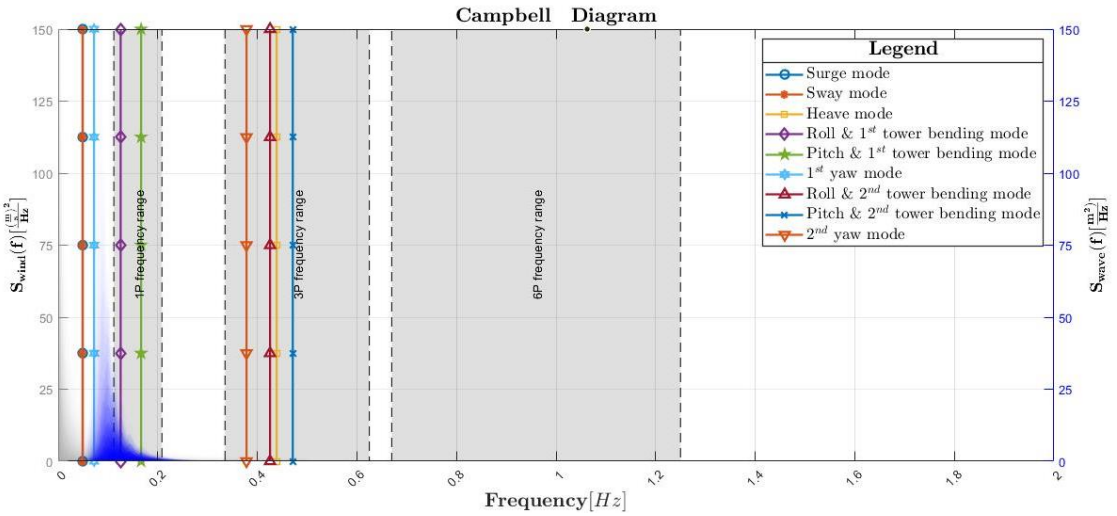

Figure 5-13: Campbell diagram reference TLP

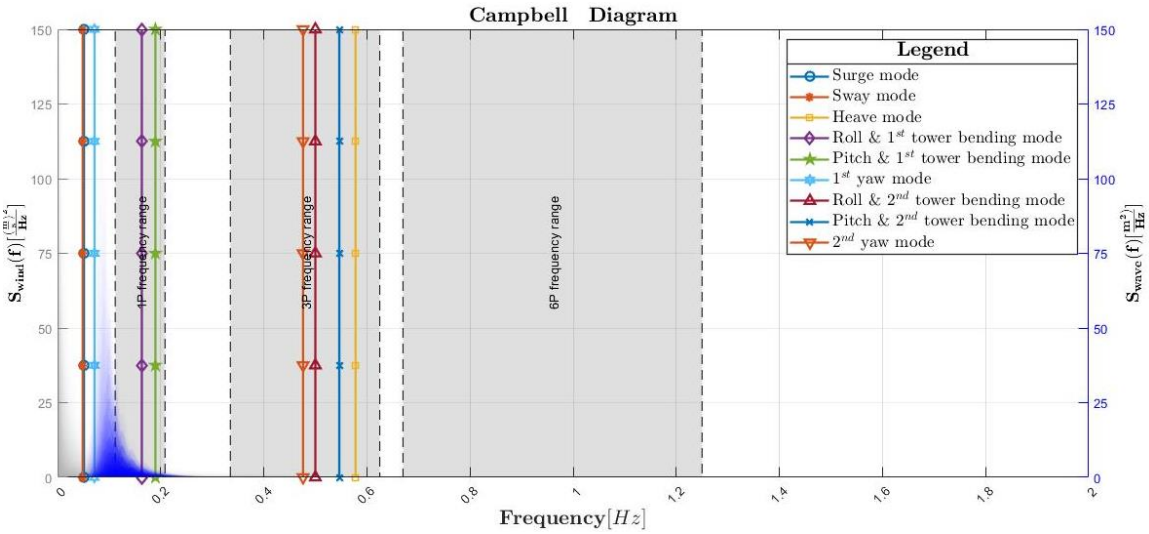

Figure 5-14: Campbell diagram Improved TLP

5.6.2.2 Design parameters

Table 5-5 gives the design parameters of the reference and improved TLPWT. The biggest difference between the reference TLPWT and the improved TLPWT is the pontoon length, which is 42.5m and 35m respectively. Another difference is the tendon angle, the tendon angle is much larger of the improved TLPWT than the reference TTLPWT. However, the sensitivity of the tendon angle on the natural periods is small, but the tendon angle is an important design parameter to prevent large accelerations in the nacelle. The other design parameters are approximately the same.

Table 5-5: Design parameters of the reference and improved TLPWT

		Symbol	*Unit*	*Reference*	*Improved*
Pontoon	Length	L_p	[m]	42.5	35
	Height	h_p	[m]	7	8
	Tapering	c	[-]	0.5	0.5
Tendon	Angle	α_{tendon}	[degree]	8.5	12.5
Centre Column	Draught	d	[m]	30	27
	Diameter	D_{cc}	[m]	8	9
Mass		M	[mT]	1.00	1.00
Tendon tension		T	[kN]	1.00	1.22

6 DISCUSSIONS

INTRODUCTION

In this study serval modelling decisions were made based on the trade-off between accuracy and the scope of this study. Many aspect were already discussed in the report, but several points that require additional discussion are discussed in this section.

DEVELOPMENT OF AERO-HYDRO-ELASTIC-SERVO MODEL

The developed aero-hydro-elastic-servo model uses an actuator disk to model the aerodynamics of the wind turbine. The actuator disk computes the thrust force and aerodynamic torque but the non-axial loads and non-torsional moments are not computed. The thrust force and aerodynamic torque are dominant, however the non-axial forces Fy can be significant when the wind turbine is not properly aligned but the yaw-controller keeps the wind turbine aligned. The non-torsional moments are also not computed, but the order of magnitude is lower and are not relevant for the substructure design.

The damping ratio of the structural damping of a wind turbine is between 1% and 5%, but for a fatigue assessment of a wind turbine a damping ratio between 1% of 2% is recommended. The damping ratio of 2% is used in the time domain simulations, which is the upper bound. However, the aerodynamic damping and hydrodynamic damping are dominant.

The control system is implemented in the Matlab model but the control system of a wind turbine is confidential. The wind turbine used at Bluewater and the NREL 5MW wind turbine are comparable, therefore the control system of the NREL 5MW wind turbine is used. However, the control system of the NREL 5MW may not be suitable for a TLPWT. More research is required to investigate the control system but this is outside the scope of this study.

DYNAMIC ANALYSIS

The gyroscopic effect is analyzed and can be neglected. The conclusions drawn are based on only one simulations with aligned wind and the rotor is assumed to rigid. However, the wind turbine blades are very flexible and misaligned wind might causes large rotations. Therefore, it is recommended to investigate the gyroscopic effect with flexible blades and misaligned wind.

The passing blade frequencies are caused by the tower shadow effect and the wind shear effect. The actuator disk assumes a constant wind velocity over the total surface, therefore wind shear effect is not included. The effect of wind shear on the thrust force is investigated. However, the effect on the non-axial forces and aerodynamics moments are not investigated. This should be investigated in further studies. The study of Wen [22] shows that aerodynamic torque fluctuation are dominated by the wind shear effect. However, FAST results of Bluewater shows that the aerodynamic torque fluctuation are negligible.

The effect of the passing blade frequencies on the motions are investigated and only the thrust force oscillations are included. However, the aerodynamic torque oscillations, non-axial load oscillations and the non-torsional oscillations are excluded. Therefore, the assumption that the other oscillations can be ignored should be validated.

DEVELOPMENT AND APPLICATIONS OF METHOD

Calculations with the Matlab model showed that the roll/1st tower bending mode and the pitch/1st tower bending mode of the reference TLPWT lie within the wave spectrum. The dimensional properties of the tower have large influence on these natural frequencies. However, the design parameters of the tower were not included in this study. Therefore, it is recommended to include the design parameters of the wind turbine tower but the aim of the algorithm was to find a design with the natural frequencies outside the frequencies where waves and wind have energy and the algorithm have shown to be successful.

A method has been presented which assumes that the TLPWT is a linear dynamic system, but the TLPWT is a nonlinear system. Nonlinear dynamic systems have behavior which linear dynamic systems have not. However, the linear and nonlinear responses of a TLP have been investigated many times. Assuming a linear TLP underestimate the responses of the TLP, but the presented method can only assist in the preliminary design phase of the TLPWT.

The presented method assumes that the number of oscillations are constant and are depending on the location. This assumptions is correct for forced vibrations of linear dynamic systems. However, not all vibrations are forced vibrations but self-excited vibrations are observed in time simulations. Also, the dynamic system of the TLPWT is nonlinear. Nonlinear dynamic system that is excited by a force will vibrate in the force frequency but also a second resonance frequency will occur. This phenomenon is called sub- and superharmonic response. However, the presence of sub- and harmonic responses is not investigated and should be investigated in further research.

The TLP-type floating wind turbine has the lowest weight of all floating wind turbine concepts and it is expected to result in a better cost-effective design but also the tendon tension is an important indicator for the total investment. The costs of the anchor system are proportional to the tendon tension [109] and the anchor system costs contribute significant to the total investment of the TLPWT. The mass of the reference TLPWT and the improved TLPWT are approximately equal. However, the tendon tension of the improved design is 22% higher, which means that the anchor system costs of the improved TLPWT is higher than the anchor system costs of the reference TLPWT.

The TLPWT has significant more risks than other support structures, the algorithms only deal with the risks of resonance of structural members but not the other risks of this TLP-concept. The following risks are not taken into account:

- **Slack tendons**
  The high impact loads, caused by large pitch motions, can cause instant failure on the tendon connection. If all tendons break in one pontoon, the TLPWT will collapse. Therefore, slack tendons should in all conditions be prevented.
- **High acceleration of the nacelle**
  Large motions of the nacelle reduce the efficiency of the wind turbine and high accelerations of the nacelle cause damage to the equipment in the nacelle, therefore the motions and accelerations of the nacelle should be limited.

Despite, these risks are outside the scope of this study.

7 CONCLUSIONS AND RECOMMENDATIONS

From the analysis of the results of this study, obtained with the developed aero-hydro-elastic-servo-model, some conclusions can be drawn, which will be presented in this chapter. In addition, some limitations of the current study will be mentioned, and will be basis for some recommendations and suggestions for further research.

7.1 CONCLUSIONS

The primary aim of this study is to improve the fatigue performance of TLPWT, although fatigue is not calculated. The fatigue performance is improved by reducing the stress amplitudes from the forced vibrations by shifting the natural frequencies of TLPWT. This has been achieved by two algorithms, the mode tracking algorithm and the selection algorithm. This approach has shown to be successful, although the algorithms can only be used in the preliminary design phase of a TLPWT for any given site.

The result of the algorithms is an improved TLPWT from resonance point of view. This design avoids resonance motions, however a design of the TLPWT should comply with many criteria such as prevent slack tendons. The reference TLPWT is predominately designed to avoid slack tendons, this design has a larger pontoon length with respect to the improved TLPWT (Table 7-1). The pitch/1st tower bending mode and roll/1st tower bending mode of the reference TLPWT will resonate because these natural periods are close to the wave peak periods. However, the pontoon length is an important design parameter to prevent slack tendon but also to avoid resonance, which means that there is a potential trade-off to be made between the two. Therefore, it is advised to reconsider the design parameters used in this study and include the design parameters of the wind turbine tower.

Table 7-1: Pontoon length of TLPWTs

		Unit	*Reference*	*Improved*
Pontoon	Length	[m]	42.5	35
	Height	[m]	7	8
	Tapering	[-]	0.5	0.5
Tendon	Angle	[degree]	8.5	12.5
Centre Column	Draught	[m]	30	27
	Diameter	[m]	8	9

The gyroscopic effect and the non-harmonic periodic thrust force oscillations are typical phenomena of the wind turbine. The influences of gyroscopic effect on the natural periods and motion responses are negligible. The non-harmonic periodic thrust force oscillations are due to wind shear and tower shadow effect. The wind shear effect can be neglected but tower shadow effect is relevant for motion responses of the nacelle-tower connection, but only if the tower bending mode is excited by the 3P-frequencies. Therefore, the tower bending mode should be outside the 3P-frequencies of the wind turbine.

7.2 RECOMMENDATIONS

The conclusions drawn in the previous section are based on the results of this study and made with the Matlab model. In this study some aspects are omitted which may be relevant for dynamical motion response of the TLPWT. Hence, the recommendations are:

- The fatigue assessment of the improved TLPWT and the reference TLPWT are outside the scope of this study. However, it is advised to analyse the fatigue performance of the reference TLPWT and improved TLPWT to validate this method.
- Ringing vibrations are observed in full scale TLP's used in the oil and gas industry. The cross-sectional dimensional are smaller for the TLPWT than for a TLP used in the oil and gas industry, increasing the risk of ringing vibrations. Ringing vibrations for TLPWT should be further investigated.
- The wave particle kinematics are described with linear wave theory. Linear wave theory is widely used to model the hydrodynamic loads, but this theory is not valid for steeps waves or shallow water waves. This assumption may has large influence on the fatigue damage for BFWT, the influence of this assumption on the fatigue damage for the TLPWT should be investigated. Linear wave theory omits the wave-current interaction. The wave-current interaction may be important for the mooring line dynamics and should be investigated.
- The selection algorithm approximates the motion response spectrum. It is recommended to improve the transfer functions and include the transfer functions between motion and stresses.
- The design of the tower has large influence on the natural frequencies of the dynamic system. Therefore, design parameters of the tower should be included in further studies.

The developed aero-hydro-elastic-servo model is implemented in Matlab and computes the natural frequencies, modes shapes and motion responses of a bottom founded wind turbine and floating wind turbine with an acceptable level of accuracy. Hence, the proposed improvements are:

- The numerical time integration method of the model uses a fixed time step. It is advantageous for the computation time to implement a numerical time integration method with a variable step size.
- The actuator disk computes the thrust force and the aerodynamic torque. The non-axial forces and non-torsional moments are relevant in case on misaligned wind. Therefore, it is recommend to implement a BEM model.

BIBLIOGRAPHY

[1] D. Matha, "Model Development and Loads Analysis of an Offshore Wind Turbine on a Tension Leg Platform, with a Comparison to other Floating Turbine Concepts," National Renewable Energy Laboratory, Golden, 2009.

[2] J. Azcona, D. Palacio, X. Munduate, L. Gonzalez and T. A. Nygaard, "Impact of mooring lines dynamics on the floating and ultimate loads of three offshore floating wind turbines computed with IEC 61400-3 guideline," *Wind Energy,* vol. 20, no. 5, pp. 797-813, 2017.

[3] Statoil, "World's frist floating wind farm has started production," 18 October 2017. [Online]. Available: https://www.statoil.com/en/news/worlds-first-floating-wind-farm-started-production.html.

[4] K. Thiagarajan and H. Dagher, "A Review of Floating Platform Concepts for Offshore Wind Energy Generation," *Journal of offshore mechanics and arctic engineering,* vol. 136, no. 2, 2014.

[5] A. Goupee, B. Koo, R. Kimball, K. Lambrakos and H. Dagher, "Experimental Comparison of Three Floating Wind Turbine Concepts," *Journal of Offshore Mechanics and Arctic Engineering,* vol. 136, no. 2, 2014.

[6] J. Jonkman and D. Matha, "Dynamics of Offshore Floating wind turbine - analysis of three concepts," *Wind energy,* vol. 14, no. 4, pp. 557-569, 2011.

[7] S. Kibbee, "TLP TECHNOLOGY SeaStar minimal platform for small deepwater reserves," Offshore magazine, 1996 01 06. [Online]. Available: http://www.offshore-mag.com/articles/print/volume-56/issue-6/news/general-interest/tlp-technology-seastar-minimal-platform-for-small-deepwater-reserves.html. [Accessed 03 03 2018].

[8] D. Tracy, Parametric Design of Floating Wind Turbines, Boston, MA.: Massachusetts Institute of Technology, Dept. of Mehcnaical Engineering, 2017.

[9] A. Henderson, C. M. and M. Masciola, "Overview of Floating Offshore Wind Technologies," in *Floating Offshore Wind Energy*, Cham, Germany, Springer, 2016, pp. 87-102.

[10] T. Lassen and R. Naman, Fatigue life analyses of Welded structures, London: ISTE, 2010.

[11] H. Kim, B. Jang, C. Park and Y. H. Bae, "Fatigue analysis of floating wind turbine support structure applying modified stress transfer function by artificial neural network," *Ocean Engineering,* vol. 149, pp. 113-126, 2018.

[12] R. Salih, "Influence of Nonlinear hydrodynamic reponse on the fatigue damage of a FOWT," U Delft Mechanical, Maritime and Materials Engineering; TU Delft Offshore and Dredging Engineering, Delft, 2018.

[13] Orcina, "Orcalfex Manual," Orcina Ltd. , Daltongate, Cumbria, 2016.

[14] J. Jonkman and M. Buhl, "FAST User's guide," National renwable energy laboratory, Golden, 2005.

[15] L. de Vries and R. Sint Jago, "AQWA Diffraction Model Result Review," Bluewater, Hoofddorp, 2018.

[16] E. Bachynski and T. Moan, "Ringing loads on Tension Leg Platform Wind Turbines," *Ocean Engineering,* vol. 84, pp. 237-248, 2014.

[17] T. Burton, N. Jenkins, D. Sharpe and E. Bossanyi, Wind Energy Handbook, John Wiley & Sons, 2011.

[18] E. Hau and H. von Renouard, Wind Turbines, Fundamentals technologies applications and economics, Springer: Berlin, 2006.

[19] M. Hansen , Aerodynamics of Wind Turbines, New York: Taylor and Francis, 2015.

[20] C. Casanovas, "Bluewater Orcaflex wind turbine external function," Bluewater Energy Solutions, Hoofddorp, 2018.

[21] D. Dolar and P. Lehn, "Simulation model of wind turbine 3P torque oscillations due to wind shear and tower shadow," *IEEE Transactions on Energy Conversion,* vol. 21, no. 3, pp. 717-724, 2006.

[22] B. Wen, S. Wei, K. Wei, W. Yang, Z. Peng and F. Chu, "Power fulctuation and power loss of wind turbines due to wind shear and tower shadow," *Frontiers of mechanical engieering,* vol. 12, no. 3, pp. 321-332, 2017.

[23] W. Hu, S. Thons, R. Rohrmann, S. Said and W. Rucker, "Vibration-based structural health monitoring of a wind turbine system. Part I: Resonance phenomenon," *Engineering structures,* vol. 89, pp. 260-272, 2015.

[24] H. Sintra, M. Mendes and R. Melico, "Modeling and Simulation of Wind Shear and Tower Shadow on Wind Turbines," *Procedia Technology,* vol. 17, no. 471-477, pp. 471-477, 2014.

[25] X. Shen and X. D. Z. Zhu, "Wind turbine aerodynamics and loads control in wind shear flow," *Energy,* vol. 36, no. 3, pp. 1424-1434, 2011.

[26] S. P.P., The gyroscope: its practical construction and application, treating of the physics and experimental mechanics of the gyroscope, and explaining the methods of its applications to the stabilization of monorailways, ships, aeroplanes and marine guns, London: E. & F.N. Spon, ltd, 1924.

[27] P. van der Male, K. van Dalen and A. Metrikine, "Aerodynamic Damping of Nonlinearily wind-excited wind turbine blades," in *Seminar on Wind Energy in Europe*, Gotland, Sweden, 2013.

[28] A. Velazquez and R. Swartz, "Damped gyroscopic effect and axial-flexural-torsional coupling using spinning finite elements for wind-turbine blades characterization," in *Conference on Sensors and Smart structures Technologies for Civil, Mechanical and Aerospace System*, San Diego, 2013.

[29] M. Shen, Z. Hu and G. Liu, "Dynamic response and viscous effect analysis of a TLP-type floating wind turbine using a coupled aero-hydro-mooring dynamic code," *Renewable Energy,* vol. 99, pp. 800-812, 2016.

[30] J. Aho, A. Buckspan, J. Laks, Y. Jeong, F. Dunne, L. Pao, P. Fleming, M. Churchfield and K. Johnson, "Tutorial of wind turbine control for supporting grid frequency through active power control," in *American Control Conference*, Montreal, 2012.

[31] T. Larsen and T. Hanson, "A method to avoid negative damped low frequent tower vibrations for a floating, pitch controlled wind turbine," in *The science of making torque from wind*, Bergen, 2017.

[32] E. Branlard, Wind turbine aerodynamics and vorticity-based methods : fundamentals and recent applications, Springer, 2017.

[33] Z. Ma, W. Li, N. Ren and J. Ou, "The typhoon effect on the aerodynamic performance of a floating offshore wind turbine," *Journal of Ocean Engineering and Science,* vol. 2, no. 4, pp. 279-287, 2017.

[34] "Blade element theory," Wikipedia, 21 07 2017. [Online]. Available: https://en.wikipedia.org/wiki/Blade_element_theory. [Accessed 26 02 2018].

[35] M. Hansen, "Aerodynamics and Design of Horizontal-Axis wind turbine," in *Aerodynamics of wind turbines*, London, Elsevier, 2015, pp. 161-184.

[36] T. Tran and D. Kim, "The platform pitching motion of floating offshore wind turbine: A preliminary unsteady aerodynamic analysis," *Journal of Wind Engineering and Industrial Aerodynamics,* vol. 142, pp. 65-81, 2015.

[37] J. Journee, W. Massie and R. Huijsmans, "Offshore Hydromechanics," Delft University of Technology, Delft, 2015.

[38] O. Faltinsen, Hydrodynamics of High-Speed Marine Vehicles, Cambridge: Cambridge university press, 2005.

[39] D. Martha, M. Schlipf, A. Cordle, R. Pereira and J. Jonkman, "Challenges in simulation of aerodynamics, hydrodynamics and mooring-line dynamics of floating offshore wind turbine," in *International offshore and polar engineering conference*, Maui, Hawaii, 2011.

[40] I. Bayati, J. Jonkman, R. A. and P. A., "The effects of second-order hydrodynamics on a semisubmerisble floating offshore wind turbine," in *The science of making torque from wind*, Copenhagen, 2014.

[41] L. Roald, J. Jonkman, A. Robertson and N. Chokani, "The effect of second-order hydrodynamics on floating offshore wind turbines," *Energy,* vol. 35, pp. 253-264, 2013.

[42] J. Grue and M. Huseby, "higher-harmonic wave forces and ringing of vertical cylinders," *Applied ocean research,* vol. 24, no. 4, pp. 203-214, 2002.

[43] L. Suja-Thauvin, J. Krokstad, E. Backynski and E. de Ridder, "Experimental results of a multimode monopile offshore wind turbine support strcture subjected to steep and breakng irregular waves," *Ocean Engineering,* vol. 146, pp. 339-351, 2017.

[44] O. Faltinsen, J. Newman and T. Vinje, "Nonlinear wave loads on a slender vertical cylinder," *Journal of fluid mechancis,* vol. 289, pp. 179-198, 1995.

[45] "DNVGL-OS-J101: Design of Offshore Wind Turbine Structures," DNVGL, Høvik, 2014.

[46] J. Jonkman, "Dynamics modeling and loads analysis of an offshore floating wind turbine," National Renewable Energy Laborary, Golden, 2007.

[47] G. Keulegan and C. L.H, "Forces on Cylinders and plates in a oscilating fluid," *Journal of Research of the National Bureau of Standards,* vol. 60, no. 5, pp. 423-440, 1958.

[48] M. Benitz, M. Lackner and D. Schmidt, "Hydrodynamics of offshore structures with specific focus on wind energy applications," *Renewable and sustainable energy reviews,* vol. 44, pp. 692-716, 2015.

[49] E. Bachynski and T. Moan, "Hydrodynamic modeling of tension leg platform wind turbines," in *International conference of Ocean, Offshore and Arctic engineering*, Nantes, 2013.

[50] L. Cochran, Wind Issues in the Design of Building, American Society of Civil Engineers, 2012.

[51] P. Sorensen, A. Hansen, P. Andre and P. Rosas, "Wind models for simulation of power fluctuations from wind farms," *Journal of Wind Engineering,* vol. 90, no. 12-15, pp. 1381-1402, 2002.

[52] R. Hill, "Corrections to Taylor's frozen turbulence approximation," *Atmospheric Research,* vol. 40, no. 2-4, pp. 153-175, 1996.

[53] O. Andersen and J. Lovseth, "The Froya database and maritime boundary layer wind description," *Marine Structures,* vol. 19, no. 2-3, pp. 173-192, 2006.

[54] "DNVGL-RP-C205: Environmental Conditions and Environmental Loads," DNVGL, Høvik, 2014.

[55] F. Chen, H. Liu and X. Zhang, "Comparison of simulation methods of spatially correlated wind speeds," in *International conference on electric utility deregulation and restructuring and power technologies*, Changsha, 2015.

[56] L. Holthuijsen, "Waves in Ocean and coastal waters," Cambridge University, 2010.

[57] B. Mekha, C. Johnson and J. Roesset, "Implication of tendon modeling on nonlinear response of TLP," *Journal of structural engineering,* vol. 122, no. 2, pp. 142-149, 1996.

[58] T. Wang and J. Zou, "Hydrodynamics in deepwater TLP tendon design," *Journal of hydrodynamics,* vol. 18, no. 3, pp. 386-393, 2016.

[59] C. Vuik, F. Vermolen, M. van Gijzen and M. Vuik, Numerical methods for ordinary differential equations, Delft: Delft Institute of Applied Mathematics, 2004.

[60] K. Subbaraj and M. Dokainish, "A survey of direct time-integration methods in computational structural dynamics - II Implicit methods," *Computers & Structures,* vol. 32, no. 6, pp. 1387-1401, 1988.

[61] D. Higham and L. Trefethen, "Stiffness of ODEs," *BIT Numerical Mathematics,* vol. 33, pp. 285-303, 1993.

[62] A. Tokic and I. Uglesic, "Elimination of overshooting effects and suppression of numerical oscillations in transformer transcient calculations," *IEEE Transaction on Power Delivery,* vol. 23, no. 1, pp. 243-251, 2008.

[63] Y. Kaiping, "A new family of generalized-alpha time integration algorithms without overshoot for structural dynamics," *Earthquake Engineering and Strcutural Dynamics,* vol. 37, no. 12, pp. 1389-1409, 2008.

[64] N. Newmark, "A method of computation for structural dynamics," *Journal of engineering mechanics,* vol. 85, no. 3, pp. 67-94, 1959.

[65] J. Houbolt, "A recurrence matrix solution for the dynamic response of aircraft," *Journal of the Aeronautical sciences,* vol. 17, no. 9, pp. 540-550, 1950.

[66] E. Wilson, I. Farhoomand and K. Bathe, "Nonlinear dynamic analysis of complex structures," *Earthquake dynamic analysis of complex structures,* vol. 1, pp. 241-252, 1973.

[67] M. Spijker, "Numerical Stability," University of Leiden, Leiden, 1998.

[68] K. Bathe, Finite Element Procedures, Watertown: Pearson Eduacation, 2014.

[69] C. Hoff and P. Phal, "Development of an implicit method with numerical dissipation from a generalized single-step algorithm for structural dynamics," *Computer Method in Applied Mechanics and Engineering,* vol. 67, no. 3, pp. 367-385, 1988.

[70] R. LeVeque, Finite difference methods for differential equations, Washington: University of Washington, 2006.

[71] G. Hulbert and T. Hughes, "An error analysis of truncated starting conditions in step-by-step time integration: Consequences for structural dynamics," *Earthquake engineering and structural dynamics,* vol. 15, no. 7, pp. 901-910, 1987.

[72] S. Chang, "Accuracy Evaluation of Newmark Method Referring to Theoretical Solutions," *Journal of Earthquake Engineering,* vol. 12, no. 1, pp. 1-16, 2008.

[73] G. Goudreau and R. Taylor, "Evaluation of numerical integration methods in elastodynamics," *Computer methods in applied mechanics and engineering,* vol. 2, no. 1, pp. 69-97, 1973.

[74] H. Hilber and T. Hughes, "Collocation, dissipation and overshoot for time integration schemes in structural dynamics," *Earthquake engineering and structural dynamics,* vol. 6, no. 1, pp. 99-117, 1978.

[75] T. Schmitz and K. Smith, Mechanical Vibrations: Modeling and Measurement, New York: Springer, 2012.

[76] S. Rao, Mechanical Vibration, Singapore: Pearson, 2011.

[77] J. Francis, "The QR transformation, part I," *The computer Journal,* vol. 4, no. 3, pp. 265-271, 1961.

[78] J. Francis, "The QR transformation, part II," *The computer Journal,* vol. 4, no. 4, pp. 332-345, 1962.

[79] A. Fidlin, Nonlinear Oscillations in Mechanical Engineering, Berlin: Springer, 2006.

[80] Y. Low, "Frequency domain analysis of a tension leg platform with statistical linearization of tendon restoring force," *Marine structures,* vol. 22, no. 3, pp. 480-503, 2009.

[81] I. Senjanovic, M. Tomic and N. Hadzic, "Formulation of consistent nonlinear restoring stiffness from dynamical analysis of tension leg platform and its influence on response," *Marine structures,* vol. 30, pp. 1-32, 2013.

[82] G. Kerschen, "Definition and fundamental Properties of Nonlinear Normal Modes," in *Modal Analysis of Nonlinear Mechanical Systems*, Wien, Springer-Verlag, 2014, pp. 1-46.

[83] C. Liaw, "Subharmonic response of offshore structures," *Journal of Engineering Mechanics,* vol. 113, no. 3, pp. 366-377, 1987.

[84] S. Ahmed, "Stochastic TLP response under long crested random sea," *Computer and Structures,* vol. 61, no. 6, pp. 975-993, 1996.

[85] J. Jonkman and W. Musial, "Offshore Code Comparison Collaboration (OC3) for IEA Task 23 Offshore Wind Technology and Deployment," National Renewable Energy Laboratory, Golden, Colorado, 2010.

[86] R. Cook, D. Malkus, M. Plesha and R. Witt, Concepts and Applications of Finite Element Analysis, New York: John Wiley & Sons, 2002.

[87] Y. Bae, M. Kim and S. Im, "Effects of Tower Elasticity and Aero-loading in Aero-Elastic-Control-Floater-Mooring coupled dynamic analysis for a TLP-type FOWT," in *International Offshore and Polar Engineering Conference*, Rhodes, 2012.

[88] S. Gueydon, P. Wuillaume, J. Jonkman, A. Robertson and P. A., "Comparison of second-order loads on a tension-leg platform for wind turbines," in *International Ocean and Polar Engineering Conference*, Kona, 2015.

[89] O. Bauchau and J. Craig, "Structural Analysis," in *Structural Analysis, Solid Mechanics and its Applications*, Dordrecht, Springer, 2009, pp. 172-221.

[90] S. Timoshenko, "On the correction factor for shear and differntial equation for transverse vibration of bars of uniform cross-section," *Philosophical magazin,* vol. 41, no. 245, pp. 744-756, 1921.

[91] Y. Yesilce, "DTM and DQEM for free vibration of axially loaded and semi-rigid-connected Reddy-Bickford beam," *International Journal for Numerical Methods in Biomedical Engineering,* vol. 27, no. 5, pp. 666-693, 2011.

[92] T. Caughey, "Classical Normal Modes in Damped Linear Dynamic Systems," *Journal of Applied Mechanics,* vol. 27, no. 2, pp. 269-271, 1960.

[93] T. Caughey and M. O'Kelly, "Classical Normal modes in Damped Linear Dynamic Systems," *Journal of Applied Mechanics,* vol. 32, no. 3, pp. 583-588, 1965.

[94] J. van der Tempel, Design of support structures for offshore wind turbines, Delft: TU Delft, Civil Engineering and Geosciences, 2006.

[95] F. Zahle, M. Aagaard and N. Niels, "Evaluation of tower shadow effects on various wind tubrine concepts," National Laboratory for Sustainable Energy, Roskilde, 2009.

[96] J. Jonkman, S. Butterfield, W. Musial and G. Scott, "Definition of a 5-MW Reference Wind Turbine for Offshore System Development," National Renewable Energy Laboratory, Golden, 2009.

[97] X. Xu and N. Srinil, "Dynamic response analysis of spar-type floating wind turbines and mooring lines with uncoupled vs coupled models," in *International conference on offshore mechanics and arctic engineering*, St. John's, 2015.

[98] R. Zamora-Rodriquez, P. Gomez-Alonso, J. Lopez, P. Dinoi, V. De-Diego-Martin, A. Simos and A. Iglesias, "Model scale analysis of a TLP floating wind turbine," in *International coference on Ocean, Offshore and Arctic Engineering*, San Francisco, 2014.

[99] S. van der Werff, "Orcaflex Model Calibration using Model Tests," Bluewater Energy Services, Hoofddorp, 2018.

[100] G. Genta, Dynamics of rotating systems, New york: Springer, 2005.

[101] DNVGL, "Design of Floating Wind Turbines," DNVGL, 2013.

[102] M. Pastor, M. Binda and T. Harcarik, "Modal Assurance Criterion," *Procedia Engineering,* vol. 48, pp. 543-548, 2012.

[103] A. Seiranyan, "Multiple eigenvalues in optimization problems," *Journal of applied mathematics and mechanics,* vol. 51, no. 2, pp. 272-275, 1987.

[104] M. Huigsloot, "Topology optimization involving constrained eigenfrequencies.," TU Delft Mechanical, Maritime and Materials Engineering, Delft, 2018.

[105] C. Tibaldi, L. Henriksen, M. Hansen and C. Bak, "Wind turbine fatigue damage evaluation based on a linear model and a spectral method," *Wind Energy,* vol. 19, pp. 1289-1306, 2015.

[106] R. Pintelon, Y. Rolain and W. Van der Moer, "Probability Density Function for Frequency Response Function Measurements Using Periodic Signals," *IEEE Transactions on intrumentation and measurement,* vol. 51, no. 1, pp. 61-68, 2003.

[107] Y. Liu and L. Bergdahl, "Influence of current and seabed friction on mooring cable response: comparison between time-domain and frequency-domain analysis," *Engineering structures,* vol. 19, no. 11, pp. 945-953, 1997.

[108] S. Benfratello and G. Falsone, "Non-guassian approach for stochastic analysis of offshore structures," *Journal of engineering mechanics,* vol. 121, no. 11, pp. 1173-1190, 1995.

[109] L. Borgman, "Ocean wave simulation for engineering design," *Journal of the Waterways and harbors division,* vol. 93, no. 2, pp. 129-156, 1967.

[110] E. Bachynski and T. Moan, "Design considerations for tension leg platform wind turbines," *Marine structures,* vol. 29, pp. 89-114, 2012.

[111] S. Oller, Nonlinear dynamics of Structures, Barcelona: International Center for Numerical Methods in Engineering, 2014.

[112] G. Liu and S. Quek, The Finite Element Method, Oxford: Butterworth-Heinemann, 2013.

[113] J. Vince, Rotation Transforms for Computer Graphics, London: Springer, 2011.

[114] J. Hutchinson, "Shear coefficients for Timoshenko beam theory," *Journal of Applied Mechanics,* vol. 68, no. 1, pp. 87-92, 2000.

[115] H. Hamdi, C. Mrad and R. Nasri, "Effects of gyroscopic coupling on the dynamics of a wind turbine blade with horizontal axis," in *Condition Monitoring of Machines in Non-stationary Operations*, Hammamet, 2012.

A APPENDIX: PROPERTIES TLPWT

Three TLPWT designs, Validation TLPWT, Reference TLPWT and Improved TLPWT, are used in this study. The first TLPWT design is used for the validation. The second TLPWT is the reference TLPWT and the third TLPWT is the result of the mode tracking and selection algorithm. This appendix gives the global and cross-dimensional properties of the TLPWT. The properties of the wind turbine are confidential, therefore the properties of the wind turbine are not published in this study.

A.1 VALIDATION TLP

A.1.1 Drawing

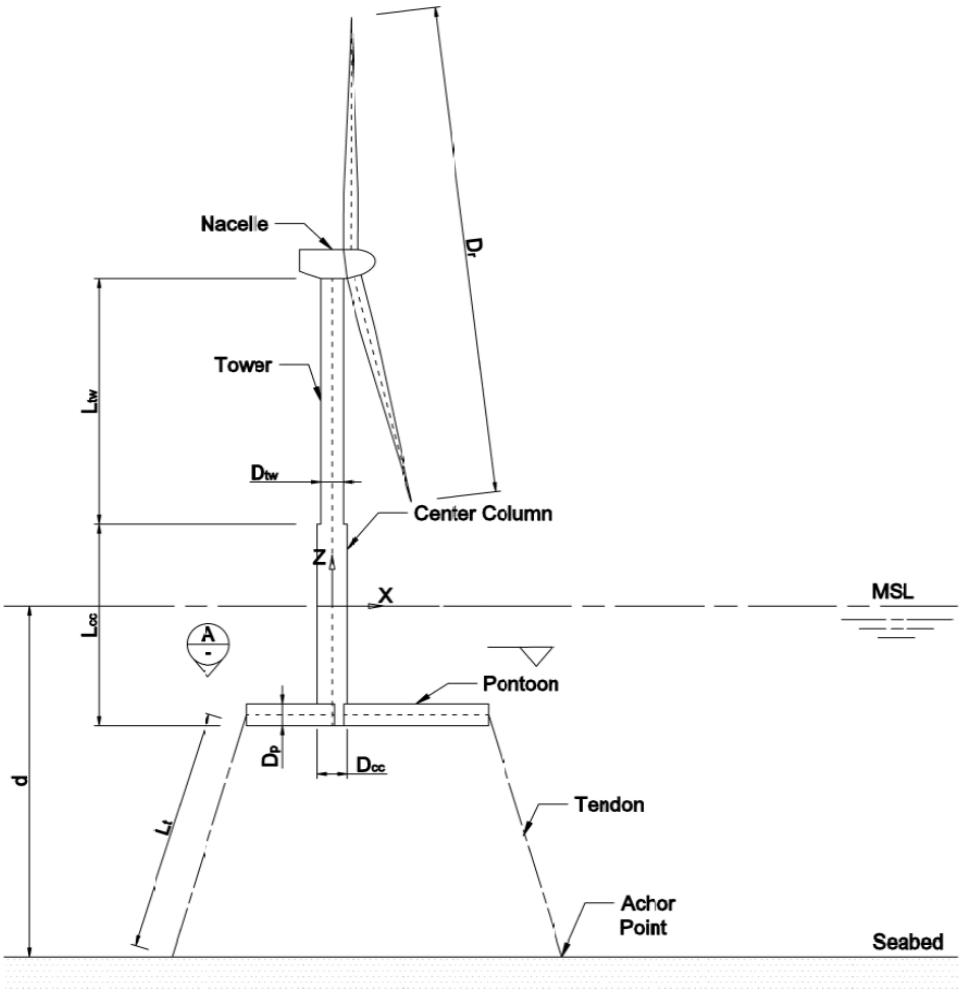

(a)

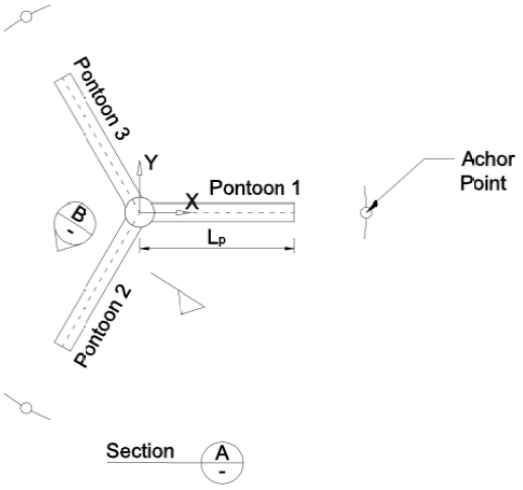

(b)

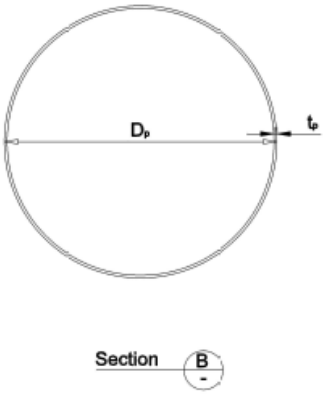

(c)

A.1.2 Material Properties

Parameter	Symbol	Unit	Value
Young modulus	E	[Nm^{-2}]	96.5
Density	ρ	[kgm^{-3}]	7785
Poisson ratio	ν	[-]	0.3

A.1.3 Platform specifications

Parameter	Symbol	Unit	Value
General			
Water depth	d	[m]	96.5
Mass	M	[mT]	[*]
Tower			
Length	L_{tw}	[m]	67.2
Diameter	D_{tw}	[m]	5.25
Plate thickness	t_{tw}	[m]	0.05
Added mass coefficient	C_a	[-]	[0.0 1.0 1.0]
Drag coefficient	C_d	[-]	[0.0 1.2 1.2]
Centre column			
Length	L_{cc}	[m]	55.6
Diameter	D_{cc}	[m]	8
Plate thickness	t_{cc}	[m]	0.05
Added mass coefficient	C_a	[-]	[0.0 1.0 1.0]
Drag coefficient	C_d	[-]	[0.0 1.2 1.2]
Pontoon			
Length	L_p	[m]	42.5
Diameter	D_p	[m]	4.75
Plate thickness	t_p	[m]	0.025
Added mass coefficient	C_a	[-]	[0.0 1.0 1.0]
Drag coefficient	C_d	[-]	[0.0 1.2 1.2]
Tendon			
Length	L_t	[m]	67.17
Diameter	D_t	[m]	0.15
Pretension	T	[kN]	[*]
Added mass coefficient	C_a	[-]	[0.0 1.0 1.0]
Drag coefficient	C_d	[-]	[0.0 1.2 1.2]

A.2 REFERENCE TLPWT

A.2.1 Drawing

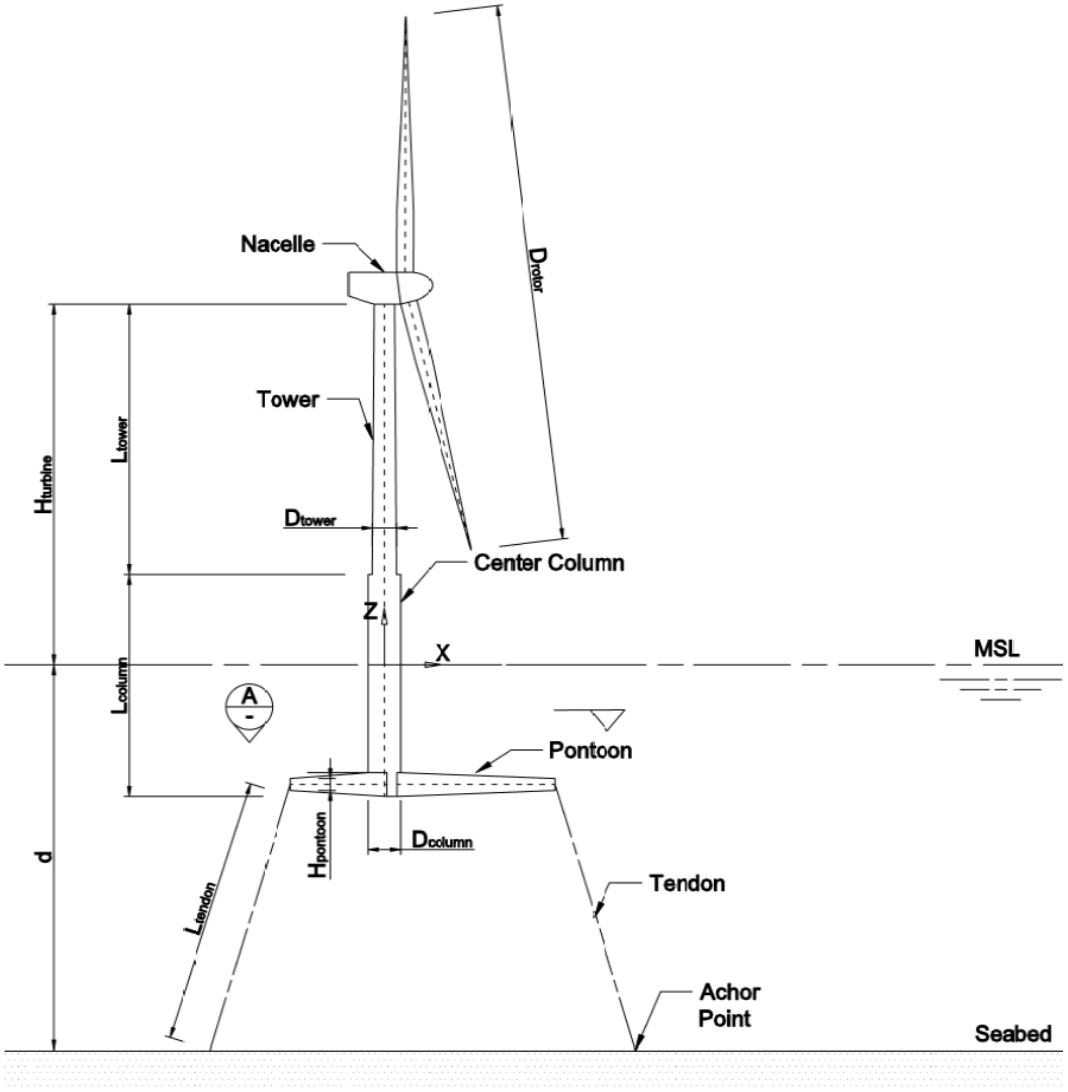

(a)

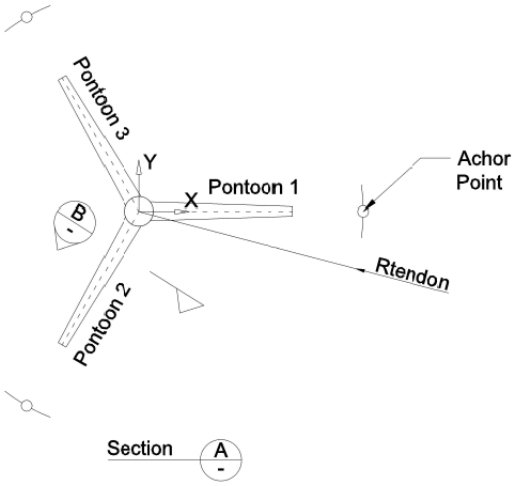

(b)

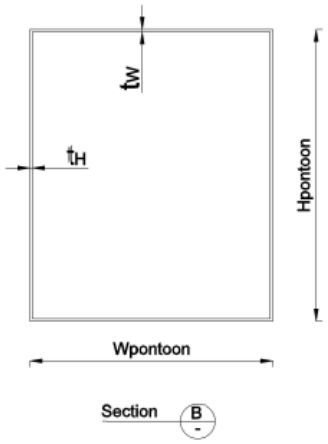

(c)

A.2.2 Material Properties

Parameter	Symbol	Unit	Value
Young modulus	E	[Nm^{-2}]	96.5
Density	ρ	[kgm^{-3}]	7785
Poisson ratio	ν	[-]	0.3

A.2.3 Platform specifications

Parameter	Symbol	Unit	Value
General			
Water depth	d	[m]	96.5
Mass	M	[mT]	[*]
Tower			
Length	L_{tw}	[m]	67.2
Diameter at centre column	D_{tw}	[m]	6
Diameter at RNA	D_{tw}	[m]	4.7
Plate thickness	t_{tw}	[m]	0.032
Added mass coefficient	C_a	[-]	[*]
Drag coefficient	C_d	[-]	[*]
Centre column			
Length	L_{cc}	[m]	55.6
Diameter	D_{cc}	[m]	8
Plate thickness	t_{cc}	[m]	0.05
Added mass coefficient	C_a	[-]	[*]
Drag coefficient	C_d	[-]	[*]
Pontoon			
Length	L_p	[m]	42.5
Height pontoon centre column connection	$H_{p,s}$	[m]	7
Width pontoon centre column connection	$W_{p,s}$	[m]	4.5
Height tendon pontoon connection	$H_{p,e}$	[m]	3.5
Width tendon pontoon connection	$W_{p,e}$	[m]	2.25
Flange thickness	t_h	[m]	0.05
Web thickness	t_w	[m]	0.025
Added mass coefficient	C_a	[-]	[*]
Drag coefficient	C_d	[-]	[*]
Tendon			
Length	L_t	[m]	67.17
Diameter	D_t	[m]	0.15
Pretension	T	[kN]	[*]
Added mass coefficient	C_a	[-]	[*]
Drag coefficient	C_d	[-]	[*]

* Confidential

A.3 IMPROVED DESIGN

A.3.1 Drawing

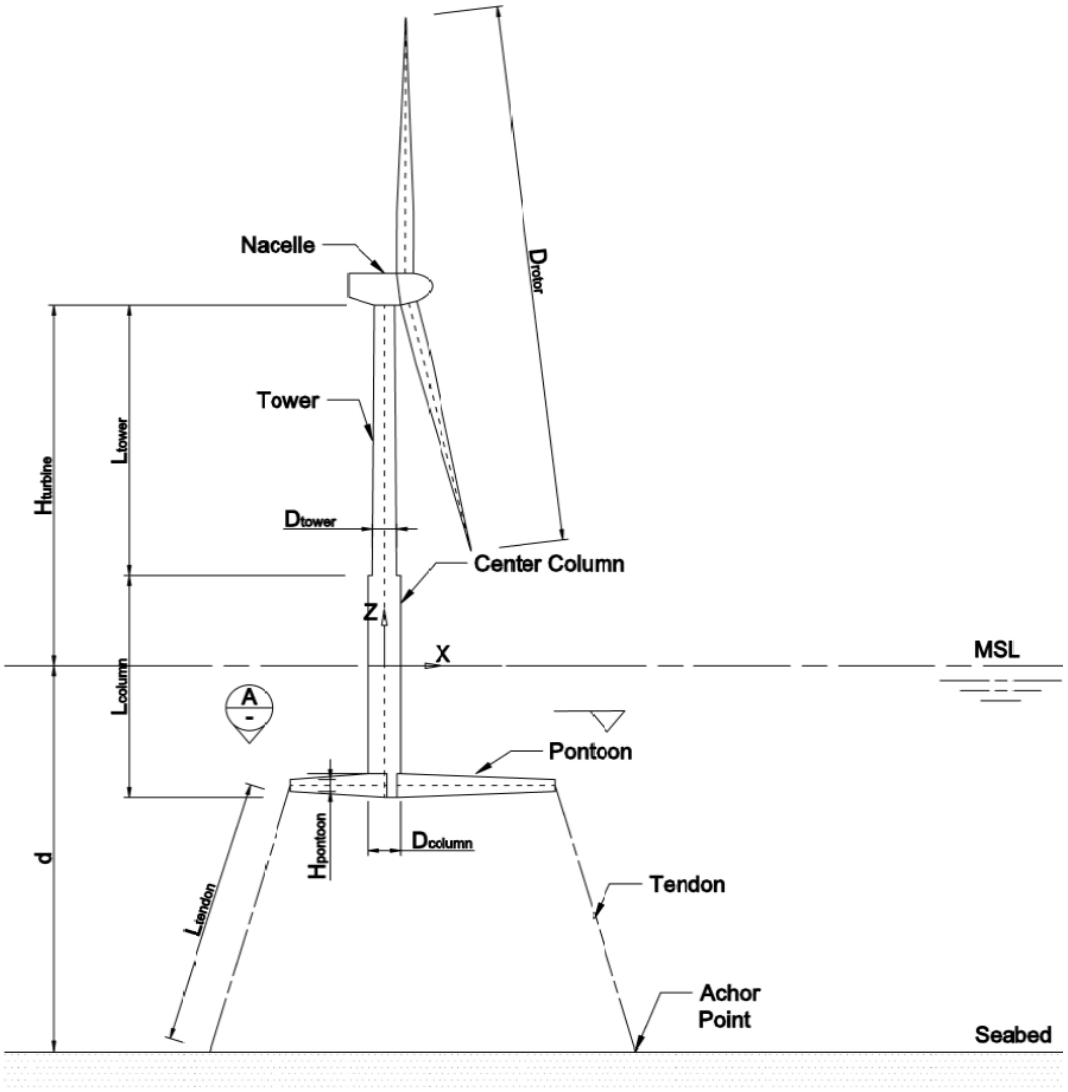

(a)

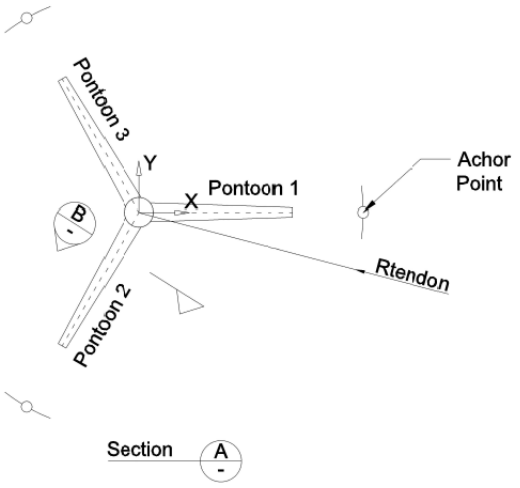

(b)

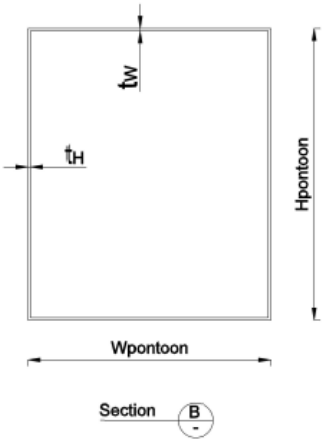

(c)

A.3.2 Material Properties

Parameter	Symbol	Unit	Value
Young modulus	E	[Nm^{-2}]	96.5
Density	ρ	[kgm^{-3}]	7785
Poisson ratio	ν	[-]	0.3

A.3.3 Platform specifications

Parameter	Symbol	Unit	Value
General			
Water depth	d	[m]	96.5
Mass	M	[mT]	[*]
Tower			
Length	L_{tw}	[m]	67.2
Diameter at centre column	D_{tw}	[m]	6
Diameter at RNA	D_{tw}	[m]	4.7
Plate thickness	t_{tw}	[m]	0.032
Added mass coefficient	C_a	[-]	[*]
Drag coefficient	C_d	[-]	[*]
Centre column			
Length	L_{cc}	[m]	52.6
Diameter	D_{cc}	[m]	9
Plate thickness	t_{cc}	[m]	0.05
Added mass coefficient	C_a	[-]	[*]
Drag coefficient	C_d	[-]	[*]
Pontoon			
Length	L_p	[m]	35
Height pontoon centre column connection	$H_{p,s}$	[m]	8
Width pontoon centre column connection	$W_{p,s}$	[m]	5.2
Height tendon pontoon connection	$H_{p,e}$	[m]	4.0
Width tendon pontoon connection	$W_{p,e}$	[m]	2.6
Flange thickness	t_h	[m]	0.05
Web thickness	t_w	[m]	0.025
Added mass coefficient	C_a	[-]	[*]
Drag coefficient	C_d	[-]	[*]
Tendon			
Length	L_t	[m]	67.17
Diameter	D_t	[m]	0.15
Pretension	T	[kN]	[*]
Added mass coefficient	C_a	[-]	[*]
Drag coefficient	C_d	[-]	[*]

* Confidential

B APPENDIX: NUMERICAL TIME INTEGRATION METHODS

Three numerical methods, Newmark method, Houbolt method and Wilson method are investigated. This appendix explains the numerical methods and derives the amplification matrix of the numerical methods. The spectral radius of the amplification matrix is used to investigate the stability and accuracy of the numerical method.

B.1 NUMERICAL TIME INTEGRATION METHODS

B.1.1 Newmark method

The Newmark family is a single step time integration method. Depending on the numerical parameters, this method is unconditional stable for linear dynamics. This method is mostly used numerical integration method in structural dynamics. The Newmark method computes the displacements and velocities by integration. This makes the method self-starting [110].

$$v_{t+h} = f(a_{t+h}, a_t, v_t, x_t) \tag{B-1}$$

$$x_{t+h} = f(a_{t+h}, a_t, v_t, x_t) \tag{B-2}$$

v	Velocity	x	Displacement
a	acceleration	t	Time
h	Time step		

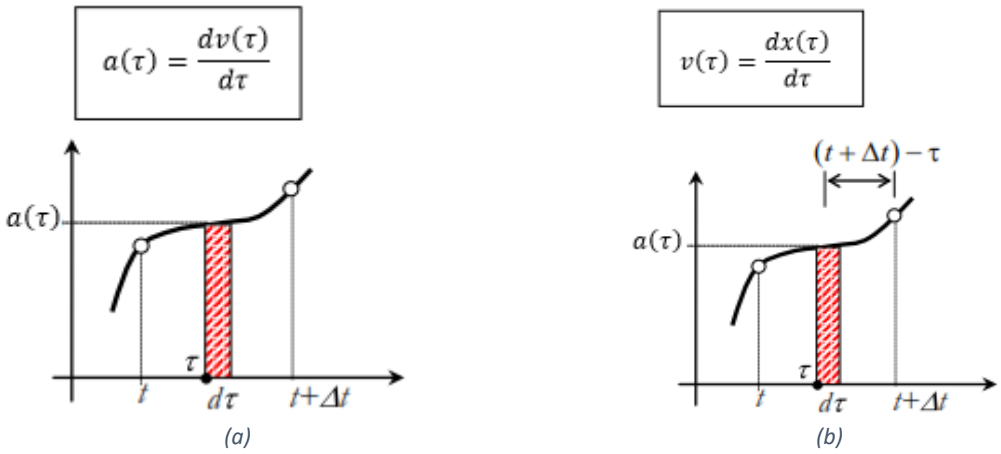

Figure B-1: (a) Velocity [110]. (b) Displacement [110]

The velocities, displacements and accelerations of the previous time step are known. The accelerations of the time step t+h are computed by an iterative process. The velocity and displacement can be obtained by integration of the acceleration. Substituting the expression of the velocity in the equation of displacement gives the final integral, where τ is the time and t the time at the time step and h the time step size. [110].

$$v_{t+h} = v_t + \int_t^{t+h} a(\tau)d\tau \tag{B-3}$$

$$x_{t+h} = x_t + \int_t^{t+h} v(\tau)d\tau \tag{B-4}$$

$$x_{t+h} = x_t + \int_t^{t+h} \left[v(\tau) + \int_0^{\tau} a(\tau)d\tau \right] d\tau = x_t + v_t h + \int_t^{t+h} \left[\int_0^{\tau} a(\tau)d\tau \right] d\tau$$

$$\int_t^{t+h}\left[\int_0^{\tau} a(\tau)d\tau\right]d\tau = \int_t^{t+h}[(t+h)-\tau]\,a(\tau)d\tau$$

$$x_{t+h} = x_t + v_t h + \int_t^{t+h}[(t+h)-\tau]\,a(\tau)d\tau$$

v	Velocity	x	Displacement
a	acceleration	t	Time
h	Time step	τ	Time t≤τ ≤t+h

The two equations can be solved by approximating the solution integrals. In the case of the Newmark method, the integrals are evaluated by linear variation of acceleration in time. Newmark method adopts a linear variation of acceleration in time of the following form (equation (B-5)), where f(τ) is the shape function [110]. The shape function gives the shape between t and t+h.

$$a(\tau) = a_t + f(\tau)(a_{t+h} - a_t) \tag{B-5}$$

a	acceleration	t	Time
h	Time step	τ	Time t≤τ ≤t+h

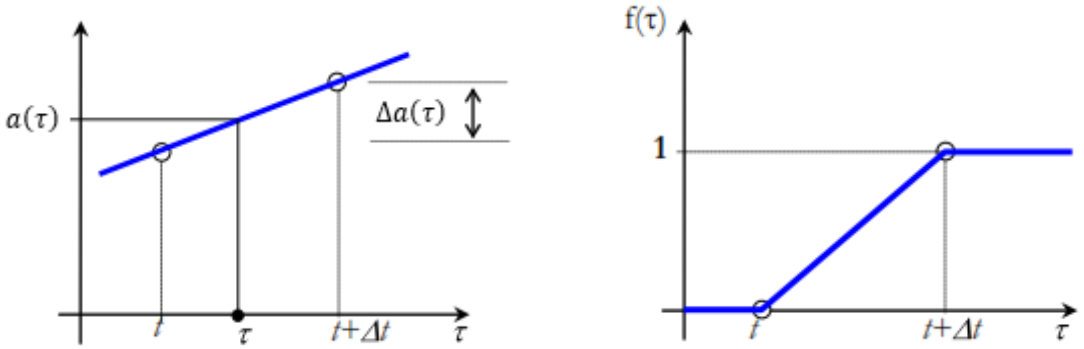

(a) *(b)*

Figure B-2: (a) linear acceleration in time [110]. (b) Shape function [110]

Both integral can be evaluated. The velocities and displacements can be obtained by equation (B-6) and equation (B-7). Figure B-4 shows the step-by-step procedure of the Newmark method [110]. Be aware that if the numerical parameters γ and β are equal to zero the implicit Newmark method become explicit.

$$v_{t+h} = v_t + a_t h + (a_{t+h} - a_t)\gamma h \tag{B-6}$$

$$\int_t^{t+h} f(\tau)d\tau = \gamma h$$

$$x_{t+h} = x_t + v_t h + a_t\frac{h^2}{2} + (a_{t+h} - a_t)\beta h^2 \tag{B-7}$$

$$\int_t^{t+h}\left[\int_0^{\tau} f(\tau)d\tau\right]d\tau = \beta h^2$$

v	Velocity	x	Displacement
a	acceleration	t	Time
h	Time step	τ	Time t≤τ ≤t+h
γ	Numerical parameter	β	Numerical parameter

The numerical parameter γ and β must be interpreted as the area of the of the shape function. Thus in case of Figure B-3 the numerical parameter γ is equal to 0.5.

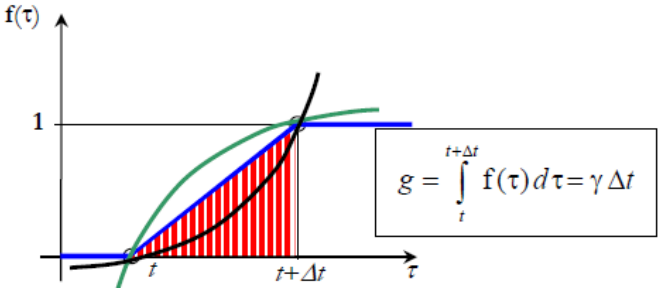

Figure B-3: Area of the shape function of the acceleration

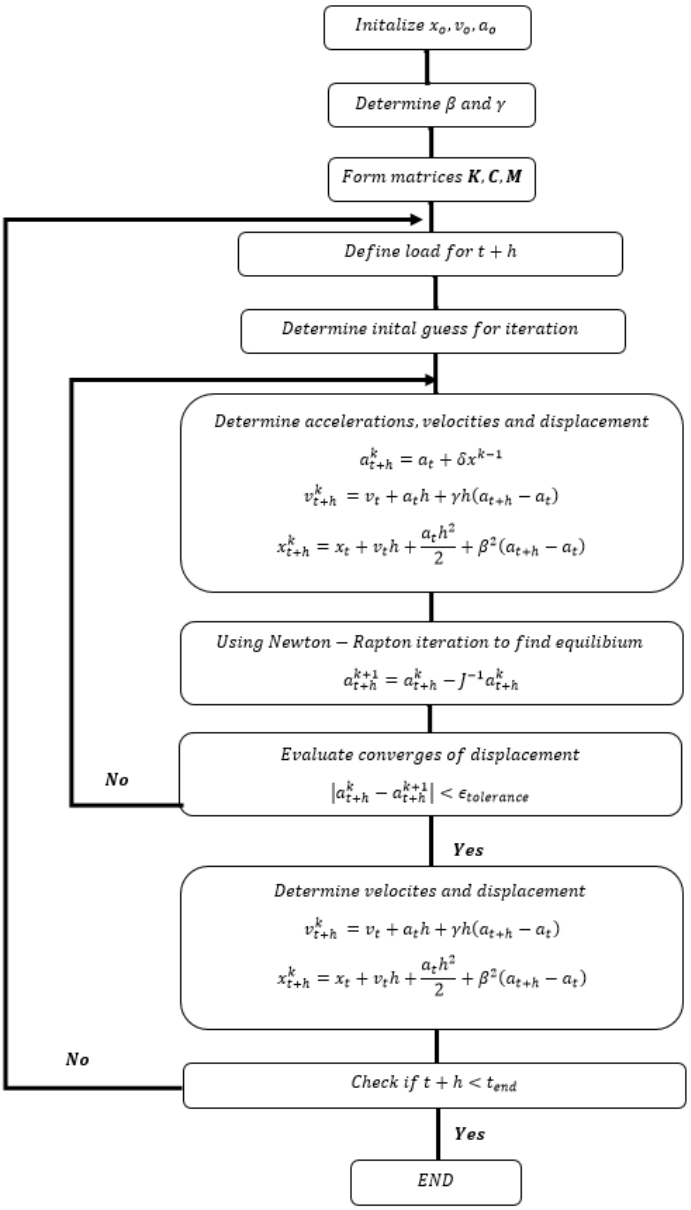

Figure B-4: Flowchart for Newmark step-by-step procedure

B.1.2 Houbolt method

The Houbolt method is a numerical time integration method for structural dynamics. The Houbolt method is a multistep method and uses four points. Is assumes a cubic polynomial function between those points. The general equation of a cubic shown in equation (B-8).

$$f(x) = ax^3 + bx^2 + cx + d \tag{B-8}$$

x	Variable	a	Constant
b	constant	c	Constant
d	Constant		

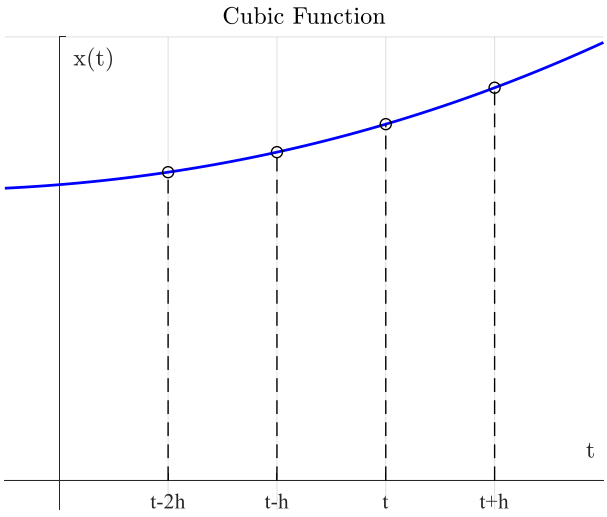

Figure B-5: Cubic Function

Every nth polynomic function can be written as difference equation. The general form is given in equation (B-9).The cubic function can then be written as equation (B-10). The definitions are given in Figure B-5 [65].

$$x(x) = x_i \prod_{k=1}^{n} \left(\frac{t}{h} - 1\right) \tag{B-9}$$

$$x(t) = -\frac{x_{t-2h}}{6}\left(\frac{t}{h}-1\right)\left(\frac{t}{h}-2\right)\left(\frac{t}{h}-3\right) + \frac{x_{t-h}}{2}\frac{t}{h}\left(\frac{t}{h}-2\right)\left(\frac{t}{h}-3\right) - \frac{x_t}{2}\frac{t}{h}\left(\frac{t}{h}-1\right)\left(\frac{t}{h}-3\right) + \frac{x_{t+h}}{6}\frac{t}{h}\left(\frac{t}{h}-1\right)\left(\frac{t}{h}-2\right) \tag{B-10}$$

x	Displacement	t	Time
h	Time step		

This method is more accurate than one-step method but requires more memory [110]. The accelerations and velocities at t+h can be found by the derivation of equation (B-10) at t+h. The velocities and accelerations can be computed by equation (B-11) and equation (B-12) respectively [65]. The standard backward difference formulation has an error of $(h)^2$ [60].

$$\left.\frac{dx}{dt}\right|_{x=t+h} = v_{t+h} = \frac{1}{6h}[11x_{t+h} - 18x_t + 9x_{t-h} - 2x_{t-2h}] \quad \text{(B-11)}$$

$$\left.\frac{dx^2}{dt^2}\right|_{x=t+h} a_{t+h} = \frac{1}{h^2}[2x_{t+h} - 5x_t + 4x_{t-h} - x_{t-2h}] \quad \text{(B-12)}$$

v	Velocity	x	Displacement
a	acceleration	t	Time
h	Time step		

The Houbolt method is an implicit method, the solution for t+h require knowledges of x_{t+h}, x_t, x_{t-h} and x_{t-2h}. Meaning that the Houbolt method is not a self-starting algorithm. The first three steps are computed with a starting procedure. It is common to compute the first three time steps with an explicit numerical method with a much smaller time step.

The Houbolt method is for linear dynamics unconditional stable. Meaning that there is no critical time step size. A much larger time size can be used than the time step size for an explicit method. Figure B-6 shows the step-by-step procedure. It can be seen that this method used the static analysis for time-dependent loads [60].

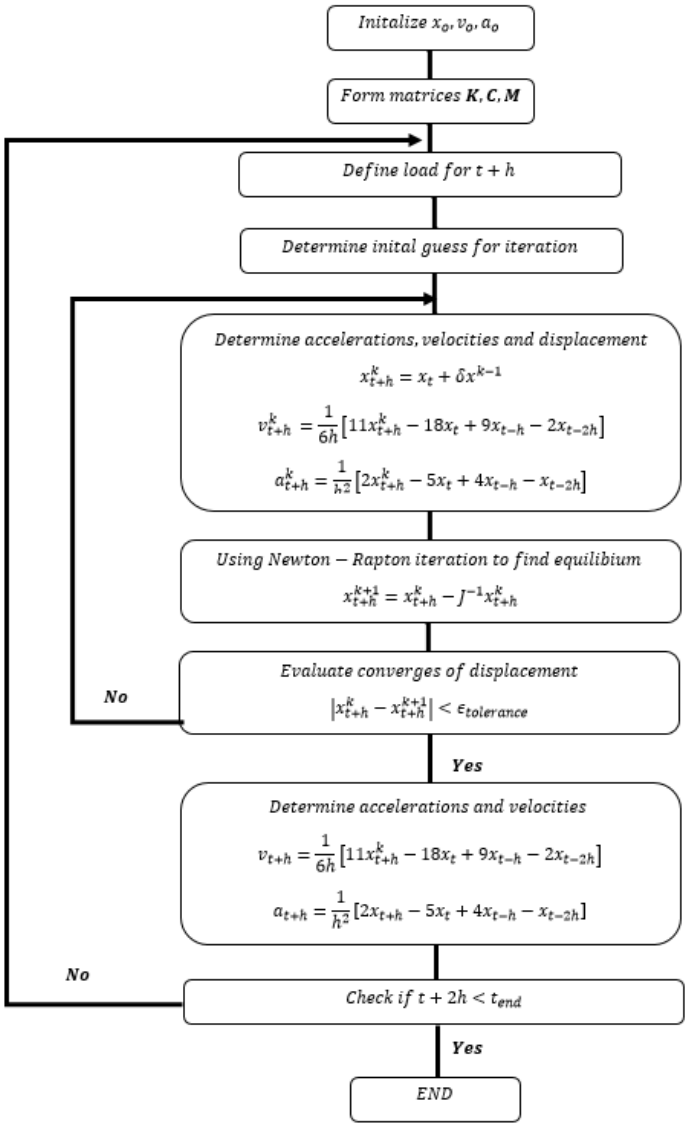

Figure B-6: Flowchart for Houbolt step-by-step procedure

B.1.3 Wilson method

The Wilson [66] method is an extension of the linear acceleration method. It assumes a linear acceleration between t and t+θh, where θ≥1.0. The Wilson method becomes unconditional stable for θ≥1.37. A value of 1.4 is typically used.

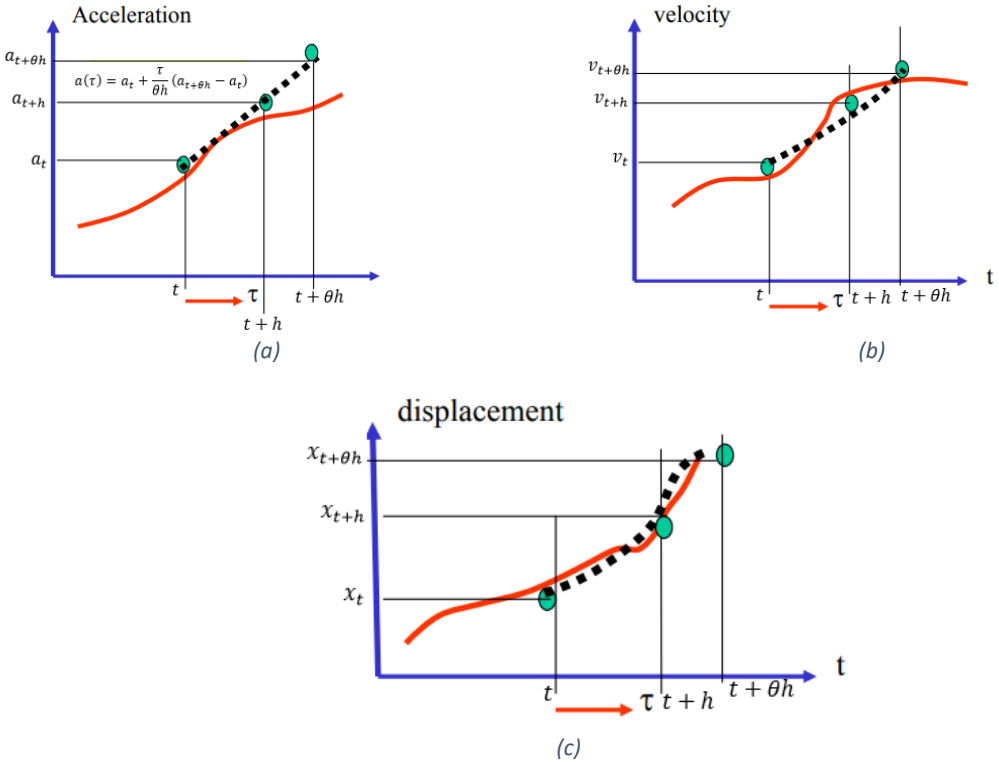

Figure B-7: Linear acceleration

The acceleration is linear between t and t+θh. The acceleration at t+h can be written for t≤τ≤t+θh as equation (B-13).

$$a_{t+\tau} = a_t + \frac{\tau}{\theta h}(a_{t+\theta h} - a_t) \tag{B-13}$$

a	acceleration	t	Time	
h	Time step	τ	Time	0≤τ≤θh
θ	Numerical parameter			

The velocities can be computed by integrating equation (B-13) once and the displacements by integrating equation (B-13) twice. The velocities and displacements of the previous time steps are known.

$$v_{t+\tau} = v_t + \int_t^{t+\tau} a(\tau)d\tau \tag{B-14}$$

$$v_{t+\tau} = v_t + \tau a_t + \frac{\tau^2}{2\theta h}(a_{t+\theta h} - a_t)$$

$$x_{t+\tau} = x_t + \int_t^{t+h} v(\tau)d\tau \tag{B-15}$$

$$x_{t+\tau} = x_t + \int_t^{t+\tau}\left[v(\tau) + \int_0^{\tau} a(\tau)d\tau\right]dt = x_t + \tau v_t + \int_t^{t+h}\left[\int_0^{\tau} a(\tau)d\tau\right]d\tau$$

$$\int_t^{t+h}\left[\int_0^{\tau} a(\tau)d\tau\right]d\tau = \frac{\tau^2}{2}a_t + \frac{\tau^3}{6\theta h}(a_{t+\theta h} - a_t)$$

a	acceleration	t	Time	
h	Time step	τ	Time	t≤τ≤t+θh
θ	Numerical parameter			

The accelerations, velocities and displacements for t+h can be obtained by substituting τ=h in equation (B-13), equation (B-14)and equation (B-15). The accelerations, velocities and displacements are given by the equation (B-16), equation (B-17) and equation (B-18) respectively. Figure B-8 gives the flowchart of the Wilson method.

$$a_{t+h} = \left(1 - \frac{1}{\theta}\right)a_t + \frac{1}{\theta}a_{t+\theta h} \tag{B-16}$$

$$\theta \geq 1.0$$

$$v_{t+h} = v_t + \frac{h}{2}(a_t + a_{t+h}) \tag{B-17}$$

$$x_{t+h} = x_t + hv_t + \frac{h^2}{6}(a_{t+h} + 2a_t) \tag{B-18}$$

a	acceleration	t	Time	
h	Time step	τ	Time	t≤τ≤t+θh
θ	Numerical parameter			

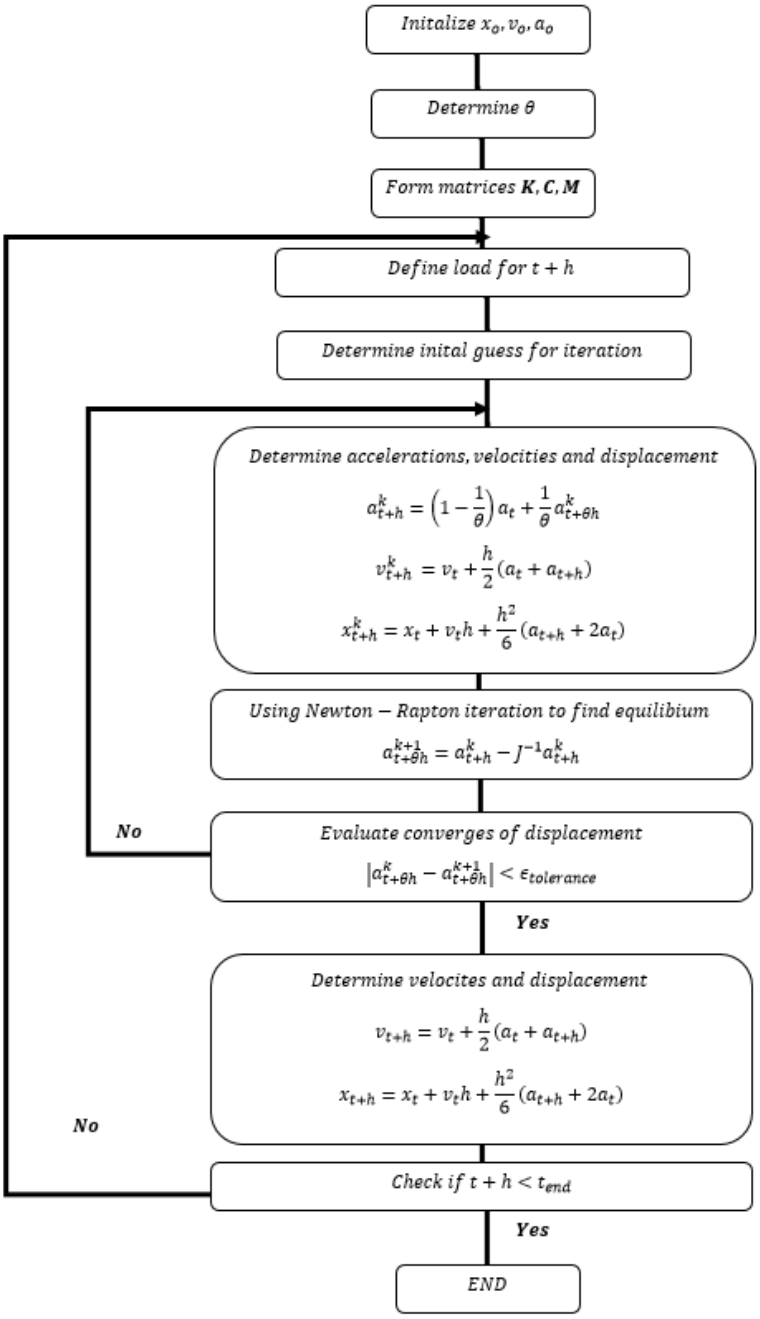

Figure B-8: Flowchart for Wilson step-by-step procedure

B.2 STABILITY

The stability of the Newmark method, Houbolt method and Wilson method are investigated by spectral matrix of the Amplifications matrix A of the numerical method. The numerical time integration method is stable if the spectral radius is between 0 and 1.0. The stability is checked with the test function of time step t+h, given in equation (B-19).

$$a_{t+h} + 2\xi\omega v_{t+h} + \omega^2 x_{t+h} = \frac{f_{t+h}}{m} \tag{B-19}$$

a	acceleration	ξ	Damping ratio
ω	Natural frequency	v	velocity
x	Displacement	t	Time
h	Time step	f	Force
m	Mass		

B.2.1 Newmark method

The equations of the velocities (equation (B-6)) and displacements (equation (B-7)) of the Newmark method are derived in B.1.1 Newmark method. Substituting the equations into the test function (equation (B-19)) and assuming a damping ratio ξ=0.0, then equation (B-20) is be obtained.

$$a_{t+h} + \omega^2\left(x_t + v_t h + \frac{a_t h^2}{2} + (a_{t+h} - a_t)\beta h^2\right) = \frac{f_{t+h}}{m} \tag{B-20}$$

$$a_{t+h}(1 + \beta\omega^2 h^2) = -\left(\frac{1}{2} - \beta\right)a_t - \frac{v_t}{h} + \frac{-x_t}{h^2}$$

$$v_{t+h} = v_t + \left((1-\gamma)a_t + \gamma\left(-\left(\frac{1}{2} - \beta\right)a_t - \frac{v_t}{h} + \frac{x_t}{h^2}\right)\right)h$$

$$x_{t+h} = x_t + hv_t + \left(\left(\frac{1}{2} - \beta\right)x_t + \beta\left(-\left(\frac{1}{2} - \beta\right)a_t - \frac{v_t}{h} + \frac{x_t}{h^2}\right)\right)h^2$$

a	acceleration	v	velocity
x	Displacement	ω	Natural frequency
t	Time	h	Time step
m	Mass	f	Force
β	Numerical parameter	γ	Numerical parameter

This equation can be written in the form of equation (2-53), which is given equation (B-21).

$$\begin{bmatrix} a_{t+h} \\ v_{t+h} \\ x_{t+h} \end{bmatrix} = \boldsymbol{A}\begin{bmatrix} a_t \\ v_t \\ x_t \end{bmatrix} + L\frac{f_{t+h}}{m} \tag{B-21}$$

$$\boldsymbol{A} = \begin{bmatrix} -\frac{1}{\delta}\left(\frac{1}{2} - \beta\right) & -\frac{1}{\delta h} & \frac{-1}{\delta h^2} \\ h\left((1-\gamma) - \frac{\gamma}{\delta}\left(\frac{1}{2} - \beta\right)\right) & 1 - \frac{\gamma}{\delta} & \frac{-\gamma}{\delta h} \\ h^2\left(\left(\frac{1}{2} - \beta\right) - \frac{\beta}{\delta}\left(\frac{1}{2} - \beta\right)\right) & h - \frac{\beta h}{\delta} & 1 - \frac{\beta}{\delta} \end{bmatrix} \qquad L = \begin{bmatrix} \frac{1}{\Omega^2\delta} \\ \frac{\gamma h}{\Omega^2\delta} \\ \frac{\beta h^2}{\Omega^2\delta} \end{bmatrix}$$

$$\delta = \left(\frac{1}{\Omega^2} + \beta\right)$$

$$\Omega = \omega \cdot h$$

The spectral radius can be found by the eigenvalues of A as function of the highest natural frequency.

$$\det|\boldsymbol{A} - \boldsymbol{I}\lambda| = 0 \tag{B-22}$$

$$\rho(A) = \frac{-2\delta\lambda^3 + 4\lambda^2\delta - 2\gamma\lambda^2 - 2\delta\lambda - \lambda^2 + \lambda}{2\delta}$$

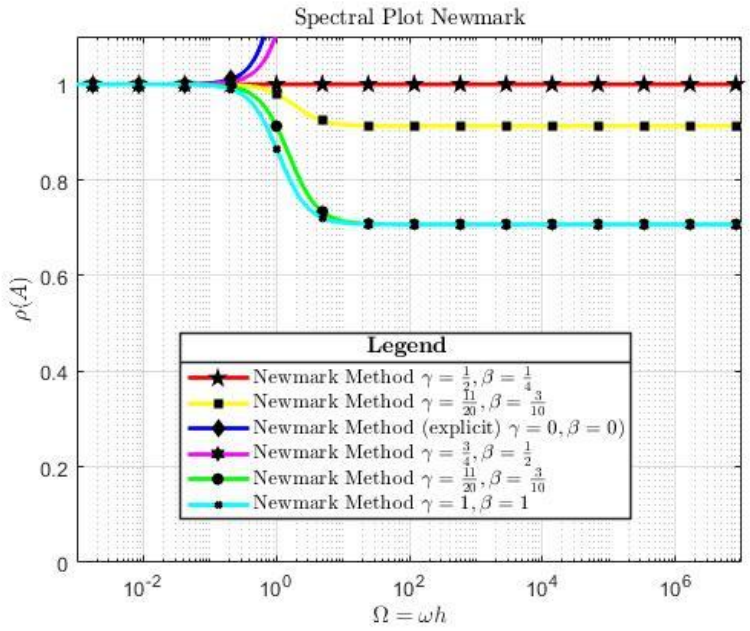

Figure B-9: Spectral plot Newmark

B.2.2 Houbolt method

The equation of the velocities (equation (B-11)) and accelerations (equation (B-12)) of the Houbolt method are derived in B.1.2 Houbolt method. Substituting the equations into the test function (equation (B-19)) and assuming a damping ratio ξ of 0.0, then equation has been obtained (B-23).

$$\frac{1}{h^2}(2x_{t+h} - 5x_t + 4x_{t-h} - x_{t-2h}) + \omega^2 x_{t+h} = \frac{f_{t+h}}{m} \tag{B-23}$$

$$x_{t+h}\left(\frac{2}{h^2} + \omega^2\right) = x_t\left(\frac{5}{h^2}\right) + x_{t-h}\left(-\frac{4}{h^2}\right) + x_{t-2h}\left(\frac{1}{h^2}\right) + \frac{f_{t+h}}{m}$$

x	Displacement	ω	Natural frequency
t	Time	h	Time step
m	Mass	f	Force

This equation can be written into the form of equation (2-53), which is given equation (B-24).

$$\begin{bmatrix} x_{t+h} \\ x_t \\ x_{t-h} \end{bmatrix} = \boldsymbol{A}\begin{bmatrix} x_t \\ x_{t-h} \\ x_{t-2h} \end{bmatrix} + \frac{L_{t+h}f_{t+h}}{m} \tag{B-24}$$

$$A = \begin{bmatrix} \frac{5}{\Omega^2\beta} & -\frac{4}{\Omega^2\beta} & \frac{1}{\Omega^2\beta} \\ 1 & 0 & 0 \\ 0 & 1 & 0 \end{bmatrix} \qquad L = \begin{bmatrix} \frac{1}{\omega^2\beta} \\ 0 \\ 0 \end{bmatrix}$$

$$\beta = \frac{2}{\Omega^2} + 1$$

$$\Omega = \omega h$$

The spectral radius can be found by the eigenvalues of A as function of the highest natural frequency.

$$\det|\boldsymbol{A} - \boldsymbol{I}\lambda| = 0 \tag{B-25}$$

$$\rho(A) = \left(\frac{5}{\Omega^2\beta} - \lambda\right)[\lambda^2 - 0] - \left(-\frac{4}{\Omega^2\beta}\right)[-\lambda - 0] + \left(\frac{1}{\Omega^2\beta}\right)[1 - 0]$$

$$\rho(\lambda) = \frac{\lambda^3\Omega^2\beta^2 + 5\lambda^2 - 4\lambda^2 + 1}{\Omega^2\beta^2}$$

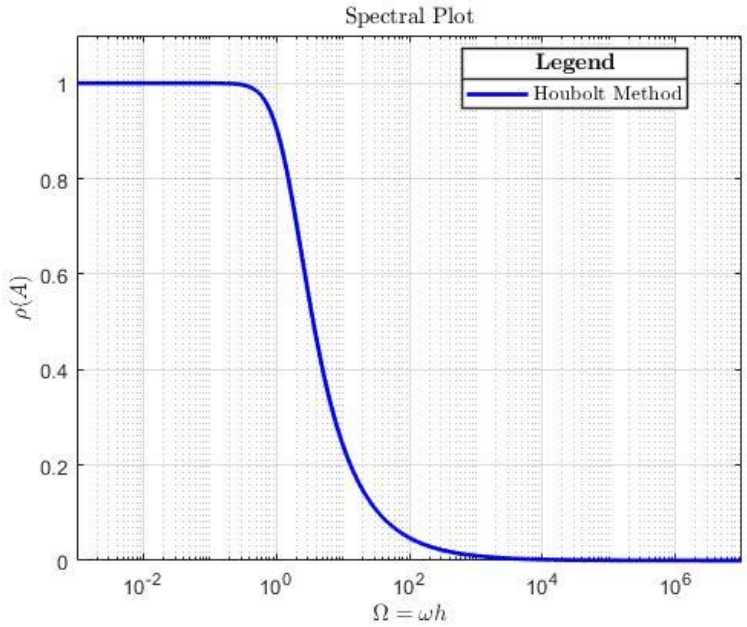

Figure B-10: Spectral plot Houbolt

B.2.3 Wilson method

The equation of the accelerations (equation (B-16)) velocities (equation (B-17)) and displacements (equation (B-18)) of the Wilson method derived in B.1.3 Wilson method. Substituting the equations into the test function (equation (B-19)) and assuming no damping (ξ=0), then equation (B-26) is derived.

$$\left(\left(1 - \frac{1}{\theta}\right)a_t + \frac{1}{\theta}a_{t+\theta h}\right) + \omega^2\left(x_t + hv_t + \frac{h^2}{6}(a_{t+h} + 2a_t)\right) = \frac{f_{t+h}}{m} \tag{B-26}$$

$$a_{t+h} = \left(1 - \frac{\theta}{3\beta} - \theta\right)a_t - \frac{1}{h}\left(\frac{\theta}{\beta}\right)v_t - \left(\frac{1}{h^2\beta}\right)x_t$$

$$\beta = \frac{\theta}{\Omega} + \frac{\theta^3}{6}$$

$$v_{t+h} = v_t + \frac{h}{2}a_t + \frac{h}{2}\left(\left(1 - \frac{\theta}{2\beta} - \theta\right)a_t - \frac{1}{h}\left(\frac{\theta}{\beta}\right)v_t - \left(\frac{1}{h^2\beta}\right)x_t\right)$$

$$x_{t+h} = x_t + hv_t + \frac{h^2}{6}\left(\left(1 - \frac{\theta}{6\beta} - \frac{1}{\theta}\right)a_t - \frac{1}{h}\left(\frac{\theta}{\beta}\right)v_t - \left(\frac{1}{h^2\beta}\right)x_t\right)$$

a	acceleration	v	velocity
x	Displacement	ω	Natural frequency
t	Time	h	Time step
m	Mass	f	Force
θ	Numerical parameter		

This equation can be written into the form of equation (2-53), which is given equation (B-27).

$$\begin{bmatrix} a_{t+h} \\ v_{t+h} \\ x_{t+h} \end{bmatrix} = \boldsymbol{A}\begin{bmatrix} a_t \\ v_t \\ x_t \end{bmatrix} + L\frac{f_{t+h}}{m} \tag{B-27}$$

$$\boldsymbol{A} = \begin{bmatrix} \left(1 - \frac{\theta^2}{3\beta} - \frac{1}{\theta}\right) & \frac{-\theta}{h\beta} & \frac{-1}{h^2\beta} \\ h\left(1 - \frac{1}{2\theta} - \frac{\theta^2}{6\beta}\right) & 1 - \frac{\theta}{2\beta} & \frac{-1}{h2\beta} \\ h^2\left(\frac{1}{2} - \frac{1}{6\theta} - \frac{\theta^2}{18\beta}\right) & h\left(1 - \frac{\theta}{6\beta}\right) & 1 - \frac{1}{\beta 6} \end{bmatrix} \qquad L = \begin{bmatrix} \frac{1}{\beta\Omega^2} \\ \frac{1}{2\omega\Omega\beta} \\ \frac{1}{6\omega^2\beta} \end{bmatrix}$$

$$\beta = \left(\frac{\theta}{\Omega^2} + \frac{\theta^3}{6}\right)$$

The spectral radius can be found by the eigenvalues of A as function of the highest natural frequency.

$$\det|\boldsymbol{A} - \boldsymbol{I}\lambda| = 0 \tag{B-28}$$

$$\rho(\lambda) = \frac{-18h(1+(\lambda-1)\theta)(\lambda-1)^2\beta^2 + \left((-6(\lambda-1)^2\theta^3 + (-9\lambda^2+9)\theta^2 + (-3\lambda^2-3\lambda-12)\theta - 3\lambda + 3)h + (-9\lambda+9)\theta + 3\lambda - 3\right)\beta - \theta^3(\lambda-1)(h-1)}{(18h\beta^2\theta)}$$

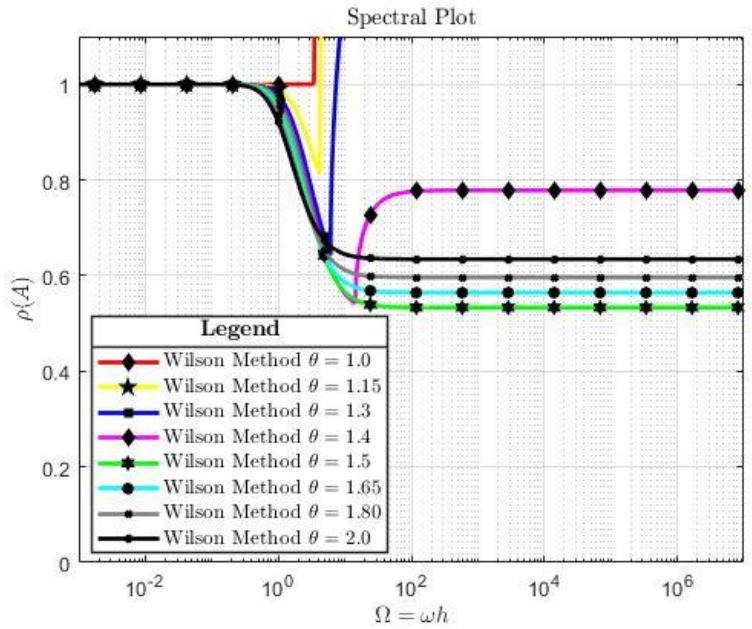

Figure B-11: Spectral plot Wilson

B.3 ACCURACY

The relative period error and the relative amplitude error are an accurate method to compare the accuracy of a numerical methods. The numerical damping is related to the relative amplitude error. The relative period error and the numerical damping for the Newmark method, Houbolt method and Wilson method are shown in the next figure.

Newmark method

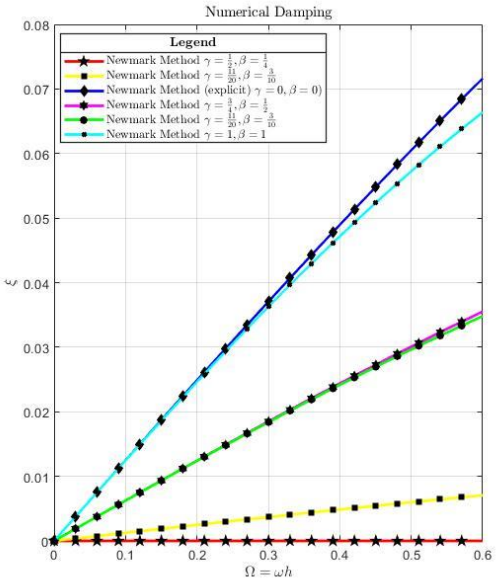

(a)

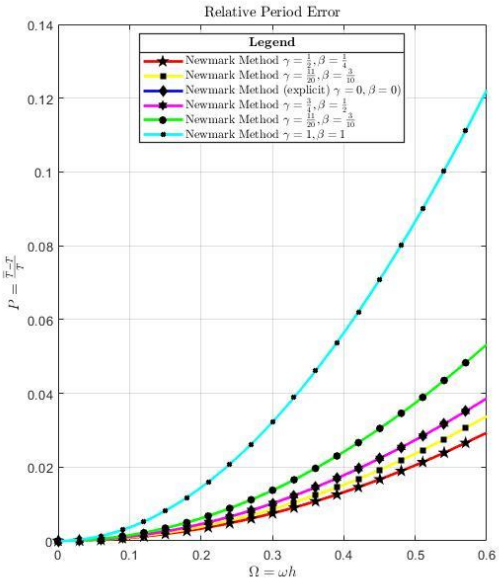

(b)

Houbolt method

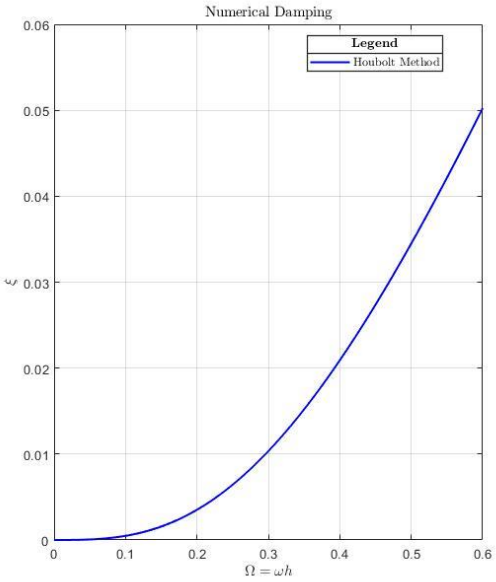

(c)

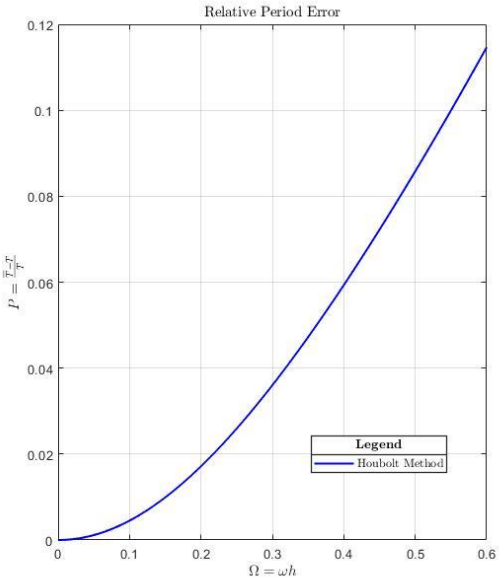

(d)

Wilson method

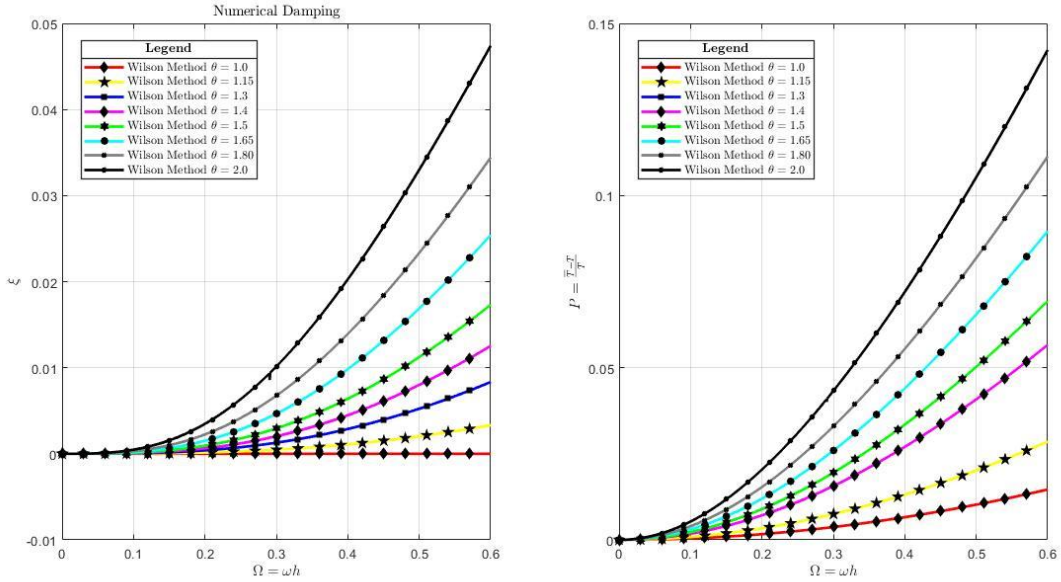

(e) *(f)*

Figure B-12: Accuracy numerical methods

C APPENDIX: FUNDAMENTALS OF FINITE ELEMENT METHOD

Finite element method (FEM) is a numerical method for field problems. A field problem requires that the spatial distribution of one or more variables need to be computed. Mathematically, the field problem is described by a differential equation. The spatial domain is discretized into a set of small elements. In the numerical solution, an element is a small piece of the structure. In each element, the pattern of the displacement is defined. Mathematically, the partial differential equation can after the spatial discretization written into a set ordinary differential equation for each element individually. The derivation of the element equations can be done on multiple ways, for dynamical problems the energy principle is mostly used [111].

Hamilton's principle can be used to derive discretized dynamic equations. The Hamilton's principle says that the displacement should be admissible. Meaning that the displacement is continuous in the problem domain, satisfies the boundary conditions and that it requires displacement history to satisfy the initial conditions [111]. Mathematically can this written as equation (C-1), where L is the Lagrangian functional. The Lagrangian function is given in equation (C-2).

$$\delta \int_{t_1}^{t_2} L \, dt = 0 \tag{C-1}$$

$$L = \Pi - T - W_f \tag{C-2}$$

δ	Delta function	L	Lagrangian
t	Time	Π	Potential energy
T	Kinetic energy	W_f	Work by external function

The domain is divided into elements with a set of nodes, which is called meshing. All the elements together are the total domain of the problem. It is possible to use more than one type of elements, as long it satisfy the first condition of the Hamilton's principle. The domain should be continuous. The size of mesh is depending on the accuracy of the problem and the computational resources available.

C.1 SHAPE FUNCTION

The displacement variations with respect to the coordinates are pre-defined by the shape functions of the element. Vector N are the shape functions of the element and has the form of equation (C-3). This approach is the displacement method [111].

$$N(x, y, z) = [N_1(x, y, z), N_2(x, y, z), \dots N_n(x, y, z)] \tag{C-3}$$

A standard procedure is developed to construct the shape functions for an elements. Considering an element with n_d nodes. The node has a one dimensional, two dimensional or three dimensional problem. The displacement is approximated in the form of linear combination of independent basis functions p.

$$u^h(x) = p^T(x)\alpha \tag{C-4}$$

$$\alpha^T = [\alpha_1 \quad \alpha_2 \quad \cdots \quad \alpha_{n_d}]$$

The form of the basis function depends on the dimensional domain and the order. A general rule of formulating the basis function is with the Pascal triangle. If higher order terms are needed, it is possible to allow higher order terms in the basis function.

$$p^T(x) = \{1 \quad x \quad x^2 \quad \cdots \quad x^p\} \tag{C-5}$$

$$p^T(x) = \{(x+y)^0 \quad (x+y)^1 \quad (x+y)^2 \quad \cdots \quad (x+y)^p\} \tag{C-6}$$

$$p^T(x) = \{(x+y+z)^0 \quad (x+y+z)^1 \quad (x+y+z)^2 \quad \cdots \quad (x+y+z)^p\} \tag{C-7}$$

The displacement in a node can be calculated by equation (C-8). An element has at least two nodes. The element displacement can therefore be written as (C-9). Where P is the moment matrix.

$$d_i = p^T(x_i)\alpha \tag{C-8}$$

$$d_e = \boldsymbol{P}\alpha \tag{C-9}$$

$$\boldsymbol{P} = \begin{bmatrix} p_1(x_1) & p_2(x_1) & \dots & p_{n_d}(x_1) \\ p_1(x_2) & p_2(x_2) & \dots & p_{n_d}(x_2) \\ \vdots & \vdots & \ddots & \vdots \\ p_1(x_{n_d}) & p_2(x_{n_d}) & \dots & p_{n_d}(x_{n_d}) \end{bmatrix}$$

Assuming that the moment matrix P is nonsingular, the vector α can be determined. A nonsingular matrix is an invertible matrix. Meaning that the determinant of the matrix is nonzero. Using equation (C-4) and equation (C-8) the approximated displacement can be written as equation (C-10). The vector N is the shape function matrix.

$$d_e = p^T\boldsymbol{P}^{-1}\alpha = N(x)\alpha \tag{C-10}$$

$$N(x) = p^T\boldsymbol{P}^{-1} = \left[P^T(x)P_1^{-1} \quad P^T(x)P_2^{-1} \quad \cdots \quad P^T(x)P_{n_d}^{-1}\right]$$

The shape functions should meet the five properties. The shape functions should have the reproduction property and the consistency property. The shape functions should be linear independent and have the delta function property. Also the shape function should have the partitions of unity property and should reproduce the linear field reproduction [111].

The first property of the shape function is reproduction and consistency property. The reproduction and consistency property say the displacement can be reproduced a long as the given field function includes the basis function to constructed the displacement. Thus, the displacement of the element is a function of the shape function.

$$u^h(x) = P^T(x)P^{-1}x_e = P^T(x)P^{-1}\alpha = P^T(x)\alpha = f(x) \tag{C-11}$$

The second property is the linear independency property shape functions. To ensure that the displacement of an element has one unique solution, the matrix P should be invertible. An invertible matrix has the property that the determinant of that matrix is nonzero. It can be proved that the determinant of the matrix A is zero if the matrix A is linear dependent.

The delta function property of the shape function implies that the shape function is defined for a specific node. Meaning that the shape function is everywhere zero, except at the specific node. This can be written as a delta function (equation (C-12)).

$$N_i(x_j) = \delta_{ij} = \begin{cases} 1, & i = j \\ 0, & i \neq j \end{cases} \tag{C-12}$$

The fourth property of the shape function is the partitions of unity property. Meaning that the sum of all the shape function should be equation to 1. The theory of partitions of unity is used to transform from the local coordinate system to the global coordinate system.

$$\sum_{i=1}^{n_d} N_i(x) = 1 \tag{C-13}$$

The last property of the shape function is the linear field reproduction property. This property is required to past the patch test. Passing the patch test means that the element is stable. Hence, that the FEM solution converge to a smooth displacement solution. Meaning that the displacements have a derivatives of all order everywhere in the domain.

C.2 ELEMENT

The mass matrix of the element can be derived from the kinetic energy term in the Langrangian function. The element stiffness matrix can be derived from the potential energy term in the Lagrangian function, assuming that the shape functions are known. The matrix c is the material matrix. For isotropic material this matrix is constant and not completely filled. For anisotropic materials, this is not constant and completely filled. The matrix L is the partial differential operator [111].

$$T = \frac{1}{2}\int_V \rho\, \boldsymbol{v^T v}\, dV = \frac{1}{2}\int_{V_e} \rho \boldsymbol{v_e^T N^T N v_e} dV = \frac{1}{2}\boldsymbol{v_e^T}\left(\int_{V_e} \rho \boldsymbol{N^T N} dV\right)\boldsymbol{v_e} \tag{C-14}$$

$$= \frac{1}{2} v_e^T \boldsymbol{M_e} v_e$$

$$\Pi = \frac{1}{2}\int_V \boldsymbol{\epsilon^T c \epsilon} dV = \frac{1}{2}\int_{V_e} \boldsymbol{x_e^T [LN]^T c [LN] x_e}\, dV = \frac{1}{2}\boldsymbol{x_e^T}\left(\int_{V_e} [\boldsymbol{B}]^{\boldsymbol{T}} \boldsymbol{c}\, [\boldsymbol{B}]\ dV\right)\boldsymbol{x_e} \tag{C-15}$$

$$= \frac{1}{2} x_e^T \boldsymbol{K_e} x_e$$

$$\boldsymbol{\epsilon = LN}$$

C.3 NODAL LOADS

The forces working on the elements need to be transferred to the nodal loads. The nodal load vector can be derived by finding the work equivalent loads. This means that the nodal force vector gives the same resulting force and moment around an arbitrary point as the applied load.

$$W_f = \boldsymbol{u^T r_e} = \int_V \boldsymbol{u^T F}\, dV = \int_V \boldsymbol{N^T}\, f_b + \int_{S_f} \boldsymbol{N^T}\, f_s\, dS_f \tag{C-16}$$

The two methods of nodal forces are the consistent and reduced loads. The consistent nodal loads include nodal moments but the reduced nodal loads consist only nodal forces. The accuracy of the method is depending on the field problem. The consistent nodal load leads to accurate displacement but approximate the bending moment at the nodes. The reduced nodal load leads to accurate bending moment but approximate the displacements. Both methods converge to the correct solution when the mesh is refined [86].

C.4 LOCAL COORDINATES TO GLOBAL COORDINATES

The element displacements and rotations are determine in the local coordinate system of the element. The orientation of the element in the global coordinate system is arbitrary. The element displacements and rotations need to be written into the global coordinate system. The transformation matrix gives the projection of the local coordinate system on the global coordinate system. The undamped equation of motion in global coordinate system can therefore written as equation (C-17).

$$\mathbf{K_e}\boldsymbol{T}\vec{x}_g + \boldsymbol{M_e}\boldsymbol{T}a_g = \boldsymbol{T}\vec{F_e} \tag{C-17}$$

$$\mathbf{T^{-1}K_e}\boldsymbol{T}\vec{x}_g + \boldsymbol{T^{-1}M_e}\boldsymbol{T}\vec{a}_g = \vec{F}_e$$

The transformation matrix has three important properties. The determinant of the transformation matrix is equal to 1.The transpose of matrix T is equal to the inverse of the matrix T. Meaning that matrix multiplication of matrix T and the transpose of matrix T is equal to the identity matrix. This proves that the transpose matrix is orthogonal which is off course true for an axis system.

$$\det[T] = 1 \tag{C-18}$$

$$\boldsymbol{T^T} = \boldsymbol{T^{-1}} \tag{C-19}$$

$$\boldsymbol{TT^T} = \boldsymbol{I} \tag{C-20}$$

A one-dimensional beam element with two nodes has six rotations and six displacements. The displacements and rotations of the element need to be transformed. It is therefore obvious that the transformation matrix has the same size as the element matrix. The transformation matrix is given into equation (C-21).

$$\boldsymbol{T} = \begin{bmatrix} \boldsymbol{R} & \mathbf{0} & \mathbf{0} & \mathbf{0} \\ \mathbf{0} & \boldsymbol{R} & \mathbf{0} & \mathbf{0} \\ \mathbf{0} & \mathbf{0} & \boldsymbol{R} & \mathbf{0} \\ \mathbf{0} & \mathbf{0} & \mathbf{0} & \boldsymbol{R} \end{bmatrix} \tag{C-21}$$

Two methods are generally used to form the transformation matrix, using the rotation matrix and the direction cosines method. The transformations matrix in a space around the origin can be written as a matrix multiplication of the rotations matrix around the x-axis, y-axis and z-axis. The rotations are the Euler rotations angles.

$$\boldsymbol{R} = \boldsymbol{R_x R_y R_z} \tag{C-22}$$

$$\boldsymbol{R_x} = \begin{bmatrix} 1 & 0 & 0 \\ 0 & \cos(\alpha) & -\sin(\alpha) \\ 0 & \sin(\alpha) & \cos(\alpha) \end{bmatrix} \qquad \boldsymbol{R_y} = \begin{bmatrix} \cos(\beta) & 0 & -\sin(\beta) \\ 0 & 1 & 0 \\ \sin(\beta) & 0 & \cos(\beta) \end{bmatrix} \qquad \boldsymbol{R_z} = \begin{bmatrix} \cos(\gamma) & -\sin(\gamma) & 0 \\ \sin(\gamma) & \cos(\gamma) & 0 \\ 0 & 0 & 1 \end{bmatrix}$$

$$\boldsymbol{R} = \begin{bmatrix} \cos(\beta)\cos(\gamma) & \cos(\beta)\sin(\gamma) & \sin(\beta) \\ -\sin(\alpha)\sin(\beta)\cos(\gamma) - \cos(\alpha)\sin(\gamma) & -\sin(\alpha)\sin(\beta)\sin(\gamma) + \cos(\alpha)\cos(\gamma) & \sin(\alpha)\sin(\beta) \\ -\cos(\alpha)\sin(\beta)\cos(\gamma) + \sin(\alpha)\sin(\gamma) & -\cos(\alpha)\sin(\beta)\sin(\gamma) - \sin(\alpha)\cos(\gamma) & \cos(\alpha)\cos(\beta) \end{bmatrix}$$

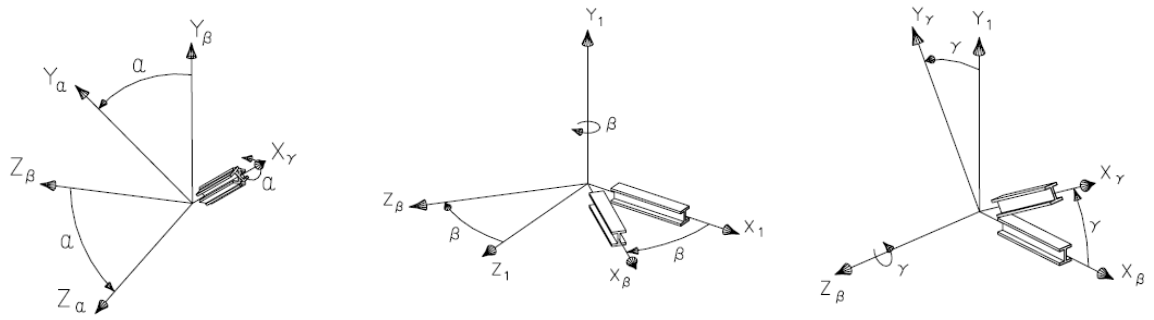

(a) *(b)* *(c)*

Figure C-1: (a) rotation x-axis [112] (b) rotation y-axis [112] (c) rotation z-axis [112]

The direction cosines method uses the unit vector of the projection of the local axis system on the global axis system. The unit vector of the projection of a vector local axis on the vector u can be determine with equation (C-23). The vector of the global axis are unit vector meaning that the norm of the vector is 1. Rewriting the equation gives the familiar form of the direction cosines method.

$$p = |\boldsymbol{v}|cos(u,v)\widehat{\boldsymbol{u}}\widehat{\boldsymbol{v}} = |\boldsymbol{v}|\left(\frac{\boldsymbol{u}\cdot\boldsymbol{v}}{|\boldsymbol{u}||\boldsymbol{v}|}\right)\left(\frac{1}{|\boldsymbol{u}|}\right)\boldsymbol{u}\left(\frac{1}{|\boldsymbol{v}|}\right)\boldsymbol{v} \tag{C-23}$$

$$p = \frac{\boldsymbol{u}\cdot\boldsymbol{v}}{|\boldsymbol{v}|} = \cos(\boldsymbol{u},\boldsymbol{v})$$

$$\boldsymbol{R} = \begin{bmatrix} \cos(x,X) & \cos(x,Y) & \cos(x,Z) \\ \cos(y,X) & \cos(y,Y) & \cos(y,Z) \\ \cos(z,Z) & \cos(z,Y) & \cos(z,Z) \end{bmatrix} \tag{C-24}$$

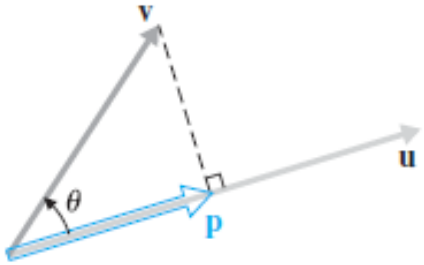

*Figure C-2: Projection of **v** onto **u***

D APPENDIX: ONE-DIMENSIONAL FINITE ELEMENT

The geometry of the TLPWT can be descripted three object types, tendon, pontoons and tower. The basics of the elements are basically the same. A beam element has two node element with at least two degree of freedom at each node and a maximum of 6 degrees of freedom per node. There are two elementary beam theories, the Euler-Bernoulli beam theory and the Timoshenko beam theory. The Timoshenko beam theory takes into account the transverse shear deformation and the rotational bending effect.

A Timoshenko beam assumes that the cross section remain straight. This element can be used for beams with higher length cross-sectional dimension ratio, therefore Timoshenko beam theory is used for a general 1D element. The element has nodal displacement in three directions and nodal rotations in three directions. The general beam element assumes no coupling between bending, torsional rotation and axial displacement. The matrix of the element can be obtain by superposition of the basic principles. A mass and stiffness matrix with the size of 12 by 12 is obtained.

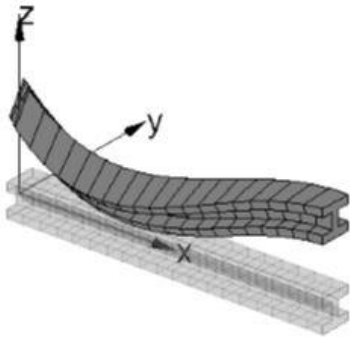

Figure D-1: Beam Element

$$\begin{bmatrix} N_{i,z} \\ Q_{i,z} \\ M_{i,y} \\ Q_{i,y} \\ M_{i,z} \\ M_{i,x} \\ N_{j,x} \\ Q_{j,z} \\ M_{j,y} \\ Q_{j,y} \\ M_{j,z} \\ M_{j,x} \end{bmatrix} = \begin{bmatrix} X & 0 & 0 & 0 & 0 & 0 & X & 0 & 0 & 0 & 0 & 0 \\ 0 & Y & 0 & 0 & 0 & Y & 0 & Y & 0 & 0 & 0 & Y \\ 0 & 0 & Z & 0 & Z & 0 & 0 & 0 & Z & 0 & Z & 0 \\ 0 & 0 & 0 & T & 0 & 0 & 0 & 0 & 0 & T & 0 & 0 \\ 0 & 0 & Z & 0 & Z & 0 & 0 & 0 & Z & 0 & Z & 0 \\ 0 & Y & 0 & 0 & 0 & Y & 0 & Y & 0 & 0 & 0 & Y \\ X & 0 & 0 & 0 & 0 & 0 & X & 0 & 0 & 0 & 0 & 0 \\ 0 & Y & 0 & 0 & 0 & Y & 0 & Y & 0 & 0 & 0 & Y \\ 0 & 0 & Z & 0 & Z & 0 & 0 & 0 & Z & 0 & Z & 0 \\ 0 & 0 & 0 & T & 0 & 0 & 0 & 0 & 0 & T & 0 & 0 \\ 0 & 0 & Z & 0 & Z & 0 & 0 & 0 & Z & 0 & Z & 0 \\ 0 & Y & 0 & 0 & 0 & Y & 0 & Y & 0 & 0 & 0 & Y \end{bmatrix} \begin{bmatrix} u_{i,x} \\ u_{i.y} \\ u_{i,z} \\ \theta_{i,x} \\ \theta_{i,y} \\ \theta_{i,z} \\ u_{j,x} \\ u_{j,y} \\ u_{j,z} \\ \theta_{j,x} \\ \theta_{j,y} \\ \theta_{j,z} \end{bmatrix} \quad \text{(D-1)}$$

D.1 SHAPE FUNCTIONS

Shape function estimates the displacement in a single node. The shape function is therefore also called approximation function. The general method to obtain a shape function is explained in Appendix: Fundamentals of finite element method. The shape function for axial displacement, torsion and bending are derived separately, because there is assumed that there is no coupling. The shape functions have the form of equation (D-2) where the basis function p is in one-dimensional domain.

$$N(x) = p^T P^{-1} \tag{D-2}$$

$$p^T = [1 \quad \xi \quad \xi^2 \quad \cdots \quad \xi^{n_d}]$$

$$P = \begin{bmatrix} p_1(x_1) & p_2(x_1) & \cdots & p_{n_d}(x_1) \\ p_1(x_2) & p_2(x_2) & \cdots & p_{n_d}(x_2) \\ \vdots & \vdots & \ddots & \vdots \\ p_1(x_{n_d}) & p_2(x_{n_d}) & \cdots & p_{n_d}(x_{n_d}) \end{bmatrix}$$

Axial displacement

One of the size degrees of freedom in a node of a beam element is the axial displacement. One shape function per node is required to describe the displacement field of the axial direction. The shape function for axial displacement in a node has a linear displacement.

(a) *(b)*

Figure D-2: Displacement in x-direction for node 1(a) and node 2(b)

The displacement in axial motion of node 1 and node 2 are shown in Figure D-2. There are two nodal displacement meaning that a linear basis function p is required (equation (D-3)). The basis function can be written as non-dimensional function with a domain from 0 to 1.

$$p^T(x) = [1 \; x] \begin{bmatrix} \alpha_1 \\ \alpha_2 \end{bmatrix} \tag{D-3}$$

$$p^T(\xi) = [1 \; \xi] \begin{bmatrix} \alpha_1 \\ \alpha_2 \end{bmatrix} \tag{D-4}$$

$$\xi = \frac{x}{L_e}$$

The boundary conditions are known at the nodes. The displacement of node in x-direction is equal to x_1 and the displacement of node 2 in x-direction is equal to x_2.

$$p(0) = x_1 \tag{D-5}$$

$$p(1) = x_2 \tag{D-6}$$

The shape function can be determine by (D-2). The shape function are shown in Figure D-3. The shape functions meet the properties a shape function.

$$N(\xi) = [N_1(\xi) \quad N_2(\xi)] = p^T P^{-1} = [1 \quad \xi] \begin{bmatrix} 1 & 0 \\ -1 & 1 \end{bmatrix} = [1 - \xi \quad \xi] \tag{D-7}$$

$$P = \begin{bmatrix} 1 & 0 \\ 1 & 1 \end{bmatrix}$$

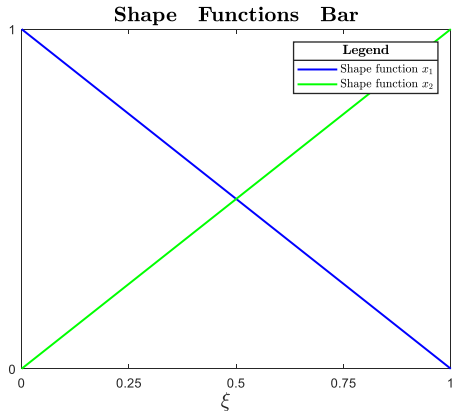

Figure D-3: Shape of axial displacement

D.1.1 Torsion

Rotation around the x-axis is one of the six degrees of freedom of a node. This phenomena is called torsion. The rotation is a two nodal rotation meaning that the basis function p is linear. The shape functions are equal to the shape functions of the axial displacement. The derivation can be found in the previous paragraph.

(a) *(b)*

Figure D-4: Rotation around the x-axis for node 1(a) and node 2(b)

D.1.2 Bending

The displacement in Z direction is coupled with the rotation around the y direction. Meaning that the basis function p is a cubic function. The displacement and rotation of node 1 and node 2 are shown in Figure D-5.

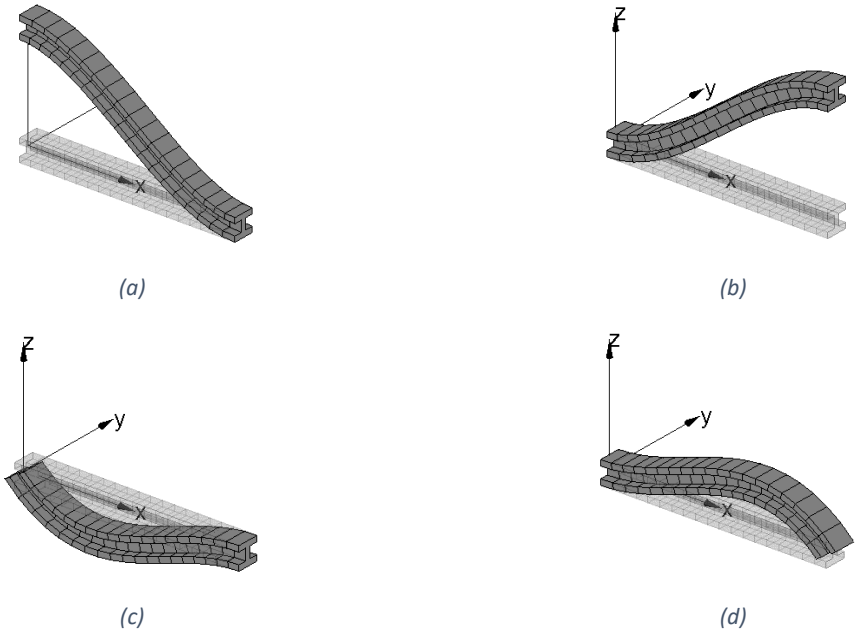

Figure D-5: (a) displacement in z-direction of node 1. (b) Displacement in z-direction of node 2. (c) Rotation of node 1. (d) Rotation of node 2

A Timoshenko beam is used because this theory includes shear deformation and rotational bending effect. Therefore, it is not necessary that the cross-sections are normal to the transverse axis. Which is assumed for the Euler-Bernoulli beam theory. The relation of the total slope consists two parts, due to the bending and due to the transverse shear. The relations are given in equation (D-8) and equation (D-9). Be aware that the axial displacement due to warping is ignored.

$$\frac{\partial v}{\partial x} = \frac{\partial v_b}{\partial x} + \frac{\partial v_s}{\partial x} = \theta_z + \gamma_{xy} \tag{D-8}$$

$$\frac{\partial v}{\partial x} = \frac{\partial v_b}{\partial x} + \frac{\partial v_s}{\partial x} = -\theta_y + \gamma_{xz} \tag{D-9}$$

The shear strain in the element is assumed to be constant. The relation between the moment and shear force is given in (D-10). The equation of the shear strain can be derived, where κ is the shear correction factor. The shear correction factor takes for the non-uniform distribution of the shear stress over the cross-section.

$$\frac{\partial M_z}{\partial x} - Q_y = 0 \tag{D-10}$$

$$M_z = -EI_{zz}\frac{\partial \theta_z}{\partial x}$$

$$Q_y = \kappa_y GA\gamma_{xy}$$

The basis function p for bending is a Hermitian polynomial of the third order and the shear deformation parameter, which takes into account the shear effect. The basis function p is given in equation (D-11). The spatial derivative of the basis function p can be computed with the chain rule, the derivative is given in equation (D-11).

$$p^T(\xi) = [\,1 \quad x \quad x^2 \quad x^3][\alpha_1 \quad \alpha_2 \quad \alpha_3 \quad \alpha_4]^T \tag{D-11}$$

$$\theta = \frac{\partial v_b}{\partial x} + \frac{\partial v_s}{\partial x} = \left(\frac{\partial p}{\partial x} - \gamma_0\right) = 0\alpha_1 + 1\alpha_2 + 2\xi\alpha_3 + 3\xi^2\alpha_4 - \gamma_0 \tag{D-12}$$

The shear strain can be computed with the relation of the moment-curvature (equation (D-13)) and the bending shear force relation (equation (D-14)).

$$\frac{\partial}{\partial x}\left(-EI\frac{\partial}{\partial x}(0\alpha_1 + 1\alpha_2 + 2\xi\alpha_3 + 3\xi^2\alpha_4 - \gamma_0)\right) - \kappa GA\gamma_0 = 0 \tag{D-13}$$

$$-6EI\alpha_4 - \kappa GA\gamma_0 = 0$$

$$\gamma_0 = -\frac{6EEI\alpha_4}{\kappa GA} \tag{D-14}$$

The four unknown can be determine by the boundary conditions. The boundary conditions at the nodes are known.

$$p^T(0) = z_1 \tag{D-15}$$

$$\left.\frac{\partial p}{\partial x}\right|_{x=0} = \theta_1$$

$$p^T(1) = z_2$$

$$\left.\frac{\partial p}{\partial x}\right|_{L_e=1} = \theta_2$$

Substitute the boundary conditions into the equations, than the matrix P can than formulated.

$$P = \begin{bmatrix} 1 & 0 & 0 & 0 \\ 0 & 1 & 0 & 6\Phi \\ 1 & L_e & L_e^2 & L_e^3 \\ 0 & 1 & 2L_e & 3L_e^2 + 6\Phi \end{bmatrix} \tag{D-16}$$

$$\Phi = \frac{12EI}{\kappa AGL_e}$$

The shape function can be determine by equation (D-2). The shape function is made dimensionless by dividing the matrix P by element length.

$$N(\xi) = p^T P^{-1} = [1 \quad \xi \quad \xi^2 \quad \xi^3]\, P^{-1} = [N_1 \quad N_2 \quad N_3 \quad N_4] \tag{D-17}$$

$$P^{-1} = \frac{1}{1+\Phi}\begin{bmatrix} 1+\Phi & 0 & 0 & 0 \\ -\Phi & 1+\frac{\Phi}{2} & \Phi & -\frac{\Phi}{2}L_e \\ -3 & -\left(2L_e + \frac{\Phi}{2}\right) & -2 & L_e\left(1+\frac{\Phi}{2}\right) \\ 2 & L_e & 3 & L_e \end{bmatrix}$$

$$\xi = \frac{x}{L_e}$$

$$\Phi = \frac{12EI}{\kappa GAL_e^2}$$

$$N_1 = \frac{1}{1+\Phi}(1 - 3\xi^2 + 2\xi^3 + \Phi(1-\xi))$$

$$N_2 = \frac{L_e}{1+\Phi}\left(\xi - 2\xi^2 + \xi^3 + \frac{\Phi}{2}(\xi - \xi^2)\right)$$

$$N_3 = \frac{1}{1+\Phi}(3\xi^2 - 2\xi^3 + \Phi\xi)$$

$$N_4 = \frac{L_e}{1+\Phi}\left(-\xi^2 + \xi^3 + \frac{\Phi}{2}(-\xi + \xi^2)\right)$$

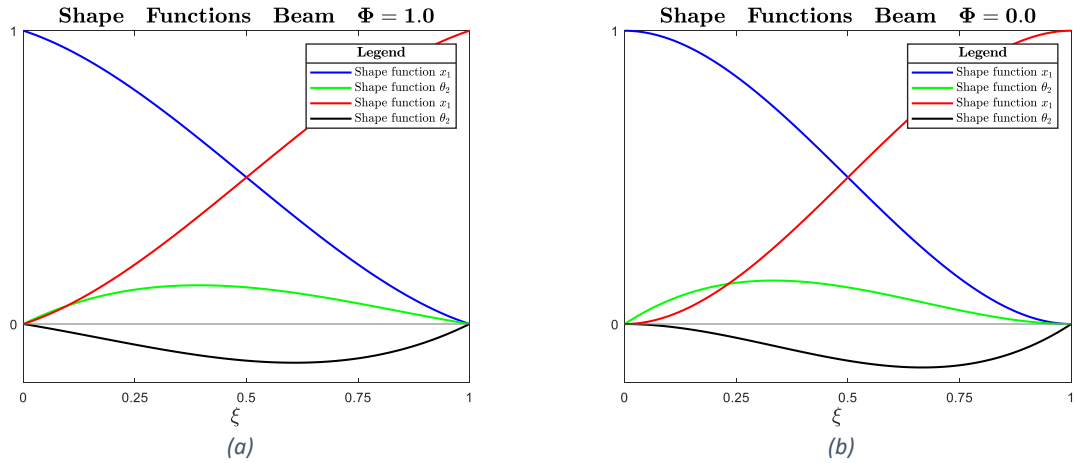

Figure D-6: Shape function (a) shear deformation parameter Φ=1.0, (b) shear deformation parameter Φ=0.0

D.2 CROSS SECTION PROPERTY FUNCTION

The cross-section properties are not required to be constant. For a non-uniform cross-sections, the cross-sectional dimensions are a function of x. For thin-walled linear tapered structures, the area, second moment of area and torsion constant can be approximated by equation (D-18), equation (D-19) and equation (D-20) respectively.

$$A(x) = A_0\left(1 + c\left(\frac{x}{L}\right)\right)^1 \quad \text{(D-18)}$$

$$I(x) = I_0\left(1 + c\left(\frac{x}{L}\right)\right)^3 \quad \text{(D-19)}$$

$$J(x) = J_0\left(1 + c\left(\frac{x}{L}\right)\right)^3 \quad \text{(D-20)}$$

$$c \triangleq \frac{d_j}{d_i} - 1$$

D.3 MASS MATRIX

The mass matrix can be derived by the equation (D-21). The mass matrix is computed for axial deformation, torsion and bending separately. The shape function matrix N is known. Assuming that the density of the element is uniform, the mass matrix can be computed.

$$M_e = \int_{V_e} \rho \boldsymbol{N^T N} dV \tag{D-21}$$

D.3.1 Axial deformation

The mass matrix displacement in x-direction is computed by equation (D-22).

$$M_e = \int_{V_e} \rho \boldsymbol{N^T N} dV = \rho L_e \int_0^1 A(\xi)\, N^T N\, d\xi = \frac{\rho A_0 L_e}{12} \begin{bmatrix} (c+4) & (c+2) \\ (c+2) & (3c+4) \end{bmatrix} \tag{D-22}$$

$$\int_0^1 A(\xi)\, N^T N\, d\xi = \int_0^1 A(\xi) \begin{bmatrix} \xi^2 - 2\xi + 1 & \xi - \xi^2 \\ \xi - \xi^2 & \xi^2 \end{bmatrix} d\xi = \begin{bmatrix} \frac{A_s(c+4)}{12} & \frac{A_s(c+2)}{12} \\ \frac{A_s(c+2)}{12} & \frac{A_s(3c+4)}{12} \end{bmatrix}$$

D.3.2 Axial rotation

The mass matrix of rotation around the x-axis is computed by (D-23).

$$M_e = \int_{V_e} \rho \boldsymbol{N^T N} dV = \rho \iint_A r\ dA \cdot L_e \int_0^1 N^T N\, d\xi \tag{D-23}$$

$$\iint_A r\, dA = I_p = I_x + I_y$$

$$\int_0^1 \left(I_y(x) + I_z(x)\right) \cdot N^T N\, d\xi = \int_0^1 \left(I_y(x) + I_z(x)\right) \begin{bmatrix} \xi^2 - 2\xi + 1 & \xi - \xi^2 \\ \xi - \xi^2 & \xi^2 \end{bmatrix} d\xi$$

$$\frac{(I_{ys} + I_{zs})}{60} \begin{bmatrix} c^3 + 6c^2 + 15c + 20 & 2c^3 + 9c^2 + 15c + 10 \\ 2c^3 + 9c^2 + 15c + 10 & 10c^3 + 36c^2 + 45c + 20 \end{bmatrix}$$

$$M_e = \rho L_e \frac{(I_{ys} + I_{zs})}{60} \begin{bmatrix} c^3 + 6c^2 + 15c + 20 & 2c^3 + 9c^2 + 15c + 10 \\ 2c^3 + 9c^2 + 15c + 10 & 10c^3 + 36c^2 + 45c + 20 \end{bmatrix}$$

D.3.3 Bending

The mass matrix of rotation around the x-axis is computed by (D-24).

$$M_e = \int_{V_e} \rho \boldsymbol{N^T N} dV = \iint_A \rho \, dA \cdot L_e \int_0^1 N^T N \; d\xi \tag{D-24}$$

$$\int_0^1 A(\xi) \cdot N^T N \, d\xi = \int_0^1 \begin{bmatrix} N_1N_1 & N_1N_2 & N_1N_3 & N_1N_4 \\ N_2N_1 & N_2N_2 & N_2N_3 & N_2N_2 \\ N_3N_1 & N_3N_2 & N_3N_3 & N_3N_3 \\ N_4N_1 & N_4N_2 & N_4N_3 & N_4N_4 \end{bmatrix} d\xi$$

$$\frac{\rho A_0}{1680 \cdot (1+\Phi)^2} \begin{bmatrix} M_{b11} & M_{b12} & M_{b13} & M_{b14} \\ M_{b22} & M_{b22} & M_{b23} & M_{b24} \\ M_{b31} & M_{b32} & M_{b33} & M_{b34} \\ M_{b41} & M_{b42} & M_{b43} & M_{b44} \end{bmatrix}$$

$$M_{b11} = (140c + 560)\Phi^2 + (280c + 1176)\Phi + 144c + 624$$

$$M_{b12} = 2L_e\big((14c + 35)\Phi^2 + (27c + 77)\Phi + 14c + 44\big)$$

$$M_{b13} = 4(c + 2)(35\Phi^2 + 63 + 27)$$

$$M_{b14} = -2L_e\big((14c + 35)\Phi^2 + (27c + 63)\Phi + 12c + 26\big)$$

$$M_{b21} = 2L_e\big((14c + 35)\Phi^2 + (27c + 77)\Phi + 14c + 44\big)$$

$$M_{b22} = 2L_e^2\big((7c + 14)\Phi^2 + (12c + 28)\Phi + 6c + 16\big)$$

$$M_{b23} = 2L_e\big((21c + 35)\Phi^2 + (36 + 63)\Phi + 14\mathrm{c} + 26\big)$$

$$M_{b24} = -7_e L_e^2\left((c + 2)\left(\Phi^2 + 2\Phi + \frac{6}{7}\right)\right)$$

$$M_{b31} = 4(c + 2)(35\Phi^2 + 63\Phi + 27)$$

$$M_{b32} = 2L_e\big((21c + 35)\Phi^2 + (36 + 63)\Phi + 14\mathrm{c} + 26\big)$$

$$M_{b33} = (420c + 560)\Phi^2 + (896c + 1176)\Phi + 480c + 624$$

$$M_{b34} = -2L_e\big((21c + 35)\Phi^2 + (50c + 77)\Phi + 30c + 44\big)$$

$$M_{b41} = -2L_e\big((14c + 35)\Phi^2 + (27c + 63)\Phi + 12c + 26\big)$$

$$M_{b42} = -7_e L_e^2\left((c + 2)\left(\Phi^2 + 2\Phi + \frac{6}{7}\right)\right)$$

$$M_{b43} = -2L_e\big((21c + 35)\Phi^2 + (50c + 77)\Phi + 30c + 44\big)$$

$$M_{b44} = L_e\big((7c + 14)\Phi^2 + (16c + 28)\Phi + 10c + 16\big)$$

D.3.4 Mass matrix of 1D general beam element

The general mass matrix of the beam element is given below.

$$M_e = \begin{bmatrix} X_{11} & 0 & 0 & 0 & 0 & 0 & X_{12} & 0 & 0 & 0 & 0 & 0 \\ 0 & Y_{11} & 0 & 0 & 0 & Y_{12} & 0 & Y_{13} & 0 & 0 & 0 & -Y_{14} \\ 0 & 0 & Z_{11} & 0 & -Z_{12} & 0 & 0 & 0 & Z_{13} & 0 & Z_{14} & 0 \\ 0 & 0 & 0 & T_{11} & 0 & 0 & 0 & 0 & 0 & T_{12} & 0 & 0 \\ 0 & 0 & -Z_{12} & 0 & Z_{22} & 0 & 0 & 0 & -Z_{23} & 0 & -Z_{24} & 0 \\ 0 & Y_{12} & 0 & 0 & 0 & Y_{22} & 0 & Y_{23} & 0 & 0 & 0 & -Y_{24} \\ X_{21} & 0 & 0 & 0 & 0 & 0 & X_{22} & 0 & 0 & 0 & 0 & 0 \\ 0 & Y_{13} & 0 & 0 & 0 & Y_{23} & 0 & Y_{33} & 0 & 0 & 0 & -Y_{34} \\ 0 & 0 & Z_{13} & 0 & -Z_{23} & 0 & 0 & 0 & Z_{33} & 0 & Z_{34} & 0 \\ 0 & 0 & 0 & T_{21} & 0 & 0 & 0 & 0 & 0 & T_{22} & 0 & 0 \\ 0 & 0 & Z_{14} & 0 & -Z_{24} & 0 & 0 & 0 & Z_{34} & 0 & Z_{44} & 0 \\ 0 & -Y_{14} & 0 & 0 & 0 & -Y_{24} & 0 & -Y_{34} & 0 & 0 & 0 & Y_{44} \end{bmatrix} \quad \text{(D-25)}$$

$$X_{11} = \frac{\rho A_i L_e}{12}(c+4) \qquad X_{12} = \frac{\rho A_i L_e}{12}(c+2)$$

$$X_{21} = \frac{\rho A_i L_e}{12}(c+2) \qquad X_{22} = \frac{\rho A_i L_e}{12}(c+4)$$

$$T_{11} = \rho L_e \frac{I_{iz}+I_{iy}}{60}(c^3+6c^2+15c+20) \qquad T_{12} = \rho L_e \frac{I_{ix}+I_{iy}}{60}(2c^3+9c^2+15c+10)$$

$$T_{21} = \rho L_e \frac{I_{ix}+I_{iy}}{60}(2c^3+9c^2+15c+10) \qquad T_{22} = \rho L_e \frac{I_{ix}+I_{iy}}{60}(10c^3+36c^2+145c+20)$$

$$\{Y,Z\}_{11} = \frac{\rho A_i L_e}{1680(1+\Phi_z)^2}\left((140c+560)\Phi^2+(280c+1176)\Phi+144c+624\right)$$
$$\{Y,Z\}_{12} = \frac{\rho A_i L_e}{1680(1+\Phi_z)^2}\left(2L_e\left((14c+35)\Phi^2+(27c+77)\Phi+14c+44\right)\right)$$
$$\{Y,Z\}_{13} = \frac{\rho A_i L_e}{1680(1+\Phi_z)^2}\left(4(c+2)(35\Phi^2+63+27)\right)$$
$$\{Y,Z\}_{14} = \frac{\rho A_i L_e}{1680(1+\Phi_z)^2}\left(2L_e\left((14c+35)\Phi^2+(27c+63)\Phi+12c+26\right)\right)$$
$$\{Y,Z\}_{22} = \frac{\rho A_i L_e}{1680(1+\Phi_z)^2}\left(2L_e^2\left((7c+14)\Phi^2+(12c+28)\Phi+6c+16\right)\right)$$
$$\{Y,Z\}_{23} = \frac{\rho A_i L_e}{1680(1+\Phi_z)^2}\left(2L_e\left((21c+35)\Phi^2+(36+63)\Phi+14c+26\right)\right)$$
$$\{Y,Z\}_{24} = \frac{\rho A_i L_e}{1680(1+\Phi_z)^2}\left(7_e L_e^2\left((c+2)\left(\Phi^2+2\Phi+\frac{6}{7}\right)\right)\right)$$
$$\{Y,Z\}_{33} = \frac{\rho A_i L_e}{1680(1+\Phi_z)^2}\left((420c+560)\Phi^2+(896c+1176)\Phi+480c+624\right)$$
$$\{Y,Z\}_{34} = \frac{\rho A_i L_e}{1680(1+\Phi)^2}\left(2L_e\left((21c+35)\Phi^2+(50c+77)\Phi+30c+44\right)\right)$$
$$\{Y,Z\}_{44} = \frac{\rho A_i L_e}{1680(1+\Phi)^2}\left(L_e\left((7c+14)\Phi^2+(16c+28)\Phi+10c+16\right)\right)$$

D.4 STIFFNESS MATRIX

The stiffness matrix is derived by the equation (D-26). The stiffness matrix will be compute for axial deformation, torsion and bending separately. The shape function matrix N is known. The derivatives of the shape function need to be determine and the material matrix c.

$$\boldsymbol{k_e} = \int_{V_e} [\boldsymbol{B}]^{\boldsymbol{T}} \boldsymbol{c}\, [\boldsymbol{B}]\ dV = \int_{V_e} [\boldsymbol{B}]^{\boldsymbol{T}} \boldsymbol{c}\, [\boldsymbol{B}]\ dV \tag{D-26}$$

$$\boldsymbol{B} = \left[\frac{\partial u}{\partial x} \quad \frac{\partial \varphi}{\partial x} \quad \frac{\partial v}{\partial y}\left(\frac{\partial v}{\partial y} + \frac{\partial u}{\partial x}\right) \quad \frac{\partial w}{\partial z}\left(\frac{\partial w}{\partial z} + \frac{\partial u}{\partial x}\right)\right]^T \boldsymbol{N}$$

D.4.1 Axial displacement

The strain and displacement relation of tension in a beam can be written as equation (D-27).

$$\epsilon = \frac{\partial u}{\partial x} \tag{D-27}$$

For one-dimensional problems the constitutive equation can be written as the Hook's Law. The young modules (E) of the material is known.

$$\sigma = E\epsilon = c\boldsymbol{LN} \tag{D-28}$$

The mass matrix displacement in x-direction is computed by equation (D-22).

$$K_e = \int_{V_e} [\boldsymbol{B}]^{\boldsymbol{T}} \boldsymbol{c}\, [\boldsymbol{B}]\ dV = \int_{V_e} \boldsymbol{N'}^{\boldsymbol{T}} \boldsymbol{E}\, \boldsymbol{N'}\ dV = \int_A dA\, \frac{E}{L_e} \int_0^1 \boldsymbol{N'}^T \boldsymbol{N'}\, d\xi \tag{D-29}$$

$$\int_0^1 A(\xi)\, \boldsymbol{N'}^T \boldsymbol{N'} d\xi = \int_0^1 A(\xi) \begin{bmatrix} 1 & -1 \\ -1 & 1 \end{bmatrix} d\xi = A_s \begin{bmatrix} \frac{c}{2}c + 1 & -\frac{c}{2} - 1 \\ -\frac{c}{2} - 1 & \frac{c}{2} + 1 \end{bmatrix}$$

$$\boldsymbol{N'} = \frac{d\boldsymbol{N}}{d\xi}\frac{d\xi}{dx} = \frac{1}{L_e}\frac{d\boldsymbol{N}}{d\xi}$$

$$K_e = \frac{EA_s}{L_e} \begin{bmatrix} \frac{c}{2}c + 1 & -\frac{c}{2} - 1 \\ -\frac{c}{2} - 1 & \frac{c}{2} + 1 \end{bmatrix}$$

D.4.2 Axial rotation

The strain and displacement relation of tension in a beam can be written as equation (D-30).

$$\epsilon = \frac{\partial \varphi}{\partial x} \tag{D-30}$$

For torsion the material matrix is equal to the shear modulus of the material.

$$\sigma = G\epsilon = c\boldsymbol{LN} \tag{D-31}$$

The mass matrix displacement in x-direction is computed by equation (D-32).

$$K_e = \int_{V_e} [\boldsymbol{B}]^{\boldsymbol{T}} \boldsymbol{c}\, [\boldsymbol{B}]\ dV = \int_{V_e} \boldsymbol{N'^T E\, N'}\ dV = \int_A r^2\, dA\, \frac{G}{L_e} \int_0^1 \boldsymbol{N'^T N'}\, d\xi \tag{D-32}$$

$$\int_0^1 \boldsymbol{N'^T} N' d\xi = \int_0^1 \begin{bmatrix} 1 & -1 \\ -1 & 1 \end{bmatrix} d\xi$$

$$\boldsymbol{N'} = \frac{d\boldsymbol{N}}{d\xi}\frac{d\xi}{dx} = \frac{1}{L_e}\frac{d\boldsymbol{N}}{d\xi}$$

$$K_e = \frac{GJ_s}{4L_e}\begin{bmatrix} (c+2)(c^2+2c+2) & -(c+2)(c^2+2c+2) \\ -(c+2)(c^2+2c+2) & (c+2)(c^2+2c+2) \end{bmatrix}$$

D.4.3 Bending

The relation between strain and deflection can be written as equation (D-33), where the first term is the strain due to the bending and the second term is the strain due to the axial forces, which allow the beam to buckle.

$$\epsilon = \frac{\partial v}{\partial y}\left(\frac{\partial v}{\partial y} + \frac{\partial u}{\partial x}\right) = \frac{\partial^2 v}{\partial y^2} + \frac{\partial u}{\partial x}\frac{\partial v}{\partial y} \tag{D-33}$$

For one-dimensional problems the constitutive equation can be written as the Hook's Law. The young modules E of the material is known.

$$\sigma = E\epsilon = c\boldsymbol{LN} \tag{D-34}$$

The stiffness matrix displacement in x-direction is computed by equation (D-22).

$$K = \int_{V_e} [\boldsymbol{B}]^{\boldsymbol{T}} \boldsymbol{c}\, [\boldsymbol{B}]\ dV = \int_{V_e} [\boldsymbol{LN}]^{\boldsymbol{T}} E\, [\boldsymbol{LN}]\ dV = \tag{D-35}$$

$$\boldsymbol{K_e} = E \int_0^{L_e} \int_A^{y(x)^2} \boldsymbol{N''^T N''}\, dA\, dx = E \int_0^{L_e} I(\xi) \boldsymbol{N''^T N''}\, dx$$

$$\boldsymbol{K_g} = E\frac{du}{dx} \int_0^{L_e} \int_A^{y(x)^2} \boldsymbol{N'^T N'}\, dA\, dx = E\frac{du}{dx} \int_0^{L_e} A(\xi)\, \boldsymbol{N'^T N'}\, dx$$

The element stiffness of the beam can be compute with (D-36).

$$\boldsymbol{K_e} = E\int_0^{L_e} I(x)\boldsymbol{N''^T N''}\,dx \tag{D-36}$$

$$\int_0^{Le} I(x)N''^T N''dx = \frac{L_e}{L_e^4}\int_0^1 I(\xi)\begin{bmatrix} N''_1N''_1 & N''_1N''_2 & N''_1N''_3 & N''_1N''_1 \\ N''_2N''_1 & N''_2N''_2 & N''_2N''_3 & N''_2N''_2 \\ N''_3N''_1 & N''_3N''_2 & N''_3N''_3 & N''_3N''_3 \\ N''_4N''_1 & N''_4N''_2 & N''_4N''_3 & N''_4N''_4 \end{bmatrix} d\xi$$

$$N'' = \frac{d^2N}{d\xi^2}\left(\frac{d\xi}{dx}\right)^2 + \frac{dN}{d\xi}\frac{d^2\xi}{dx^2} = \frac{1}{L_e^2}\left(\frac{d^2N}{d\xi^2}\right)$$

$$dx = L_e d\xi$$

$$= \frac{I_{ys}}{20\cdot(1+\Phi)^2}\begin{bmatrix} K_{b11} & K_{b12} & K_{b13} & K_{b14} \\ K_{b22} & K_{b22} & K_{b23} & K_{b24} \\ K_{b31} & K_{b32} & K_{b33} & K_{b34} \\ K_{b41} & K_{b42} & K_{b43} & K_{b44} \end{bmatrix}$$

$$K_{b11} = 84c^3 + 288c^2 + 360c + 240$$

$$K_{b12} = 6L_e\left(20 - 20c - 14c^2 - 4c^3 - \Phi(3c^3 + 10c^2 + 10c)\right)$$

$$K_{b13} = -(84c^3 + 288c^2 + 360c + 240)$$

$$K_{b14} = 6L_e\left(20 + 40c + 34c^2 + 10c^3 + \Phi(3c^3 + 10c^2 + 10c)\right)$$

$$K_{b21} = 6L_e\left(20 - 20c - 14c^2 - 4c^3 - \Phi(3c^3 + 10c^2 + 10c)\right)$$

$$K_{b22} = 5L_e^2\left(\left(\Phi^2 - \frac{8}{5}\Phi + \frac{8}{5}\right)c^3 + \left(4\Phi^2 - 4\Phi + \frac{32}{5}\right)c^2 + (6\Phi^2 + 12)c + 4\Phi^2 + 8\Phi + 16\right)$$

$$K_{b23} = 6L_e\left(-20 - 20c - 14c^2 - 4c^3 + \Phi(3c^3 + 10c^2 + 10c)\right)$$

$$K_{b24} = -5L_e^2\left(\left(\Phi^2 + 2\Phi - \frac{16}{5}\right)c^2 + (2\Phi^2 + 4\Phi - 4)c + 2\Phi^2 + 4\Phi - 4\right)(c+2)$$

$$K_{b31} = -(84c^3 + 288c^2 - 360c - 240)$$

$$K_{b32} = 6L_e\left(-20 - 20c - 14c^2 - 4c^3 + \Phi(3c^3 + 10c^2 + 10c)\right)$$

$$K_{b33} = 84c^3 + 288c^2 + 360c + 240$$

$$K_{b34} = -6L_e\left(20 + 40c + 34c^2 + 10c^3 + \Phi(3c^3 + 10c^2 + 10c)\right)$$

$$K_{b41} = 6L_e\left(20 + 40c + 34c^2 + 10c^3 + \Phi(3c^3 + 10c^2 + 10c)\right)$$

$$K_{b42} = -5L_e\left(\left(\Phi^2 + 2\Phi - \frac{16}{5}\right)c^2 + (2\Phi^2 + 4\Phi - 4)c + 2\Phi^2 + 4\Phi - 4\right)(c+2)$$

$$K_{b43} = -6L_e\left(20 + 40c + 34c^2 + 10c^3 + \Phi(3c^3 + 10c^2 + 10c)\right)$$

$$K_{b44} = 5L_e^2\left(\left(\Phi^2 - \frac{28}{5}\Phi + \frac{44}{5}\right)c^3 + \left(4\Phi^2 + 20\Phi + \frac{152}{5}\right)c^2 + (6\Phi^2 + 24\Phi + 36)c + 4\Phi^2 + 8\Phi + 16\right)$$

$$K_e = \frac{EI_s}{20L_e^3(1+\Phi)^2}\begin{bmatrix} K_{b11} & K_{b12} & K_{b13} & K_{b14} \\ K_{b22} & K_{b22} & K_{b23} & K_{b24} \\ K_{b31} & K_{b32} & K_{b33} & K_{b34} \\ K_{b41} & K_{b42} & K_{b43} & K_{b44} \end{bmatrix}$$

The geometric stiffness of the beam can be compute with equation (D-37).

$$\boldsymbol{K_g} = E\frac{du}{dx}\int_0^{L_e} A(\xi)\boldsymbol{N'^T N'}\, dx \tag{D-37}$$

$$\int_0^{Le} A(\xi)\boldsymbol{N''^T N''} dx = \frac{L_e}{L_e^2}\int_0^1 \begin{bmatrix} N'_1N'_1 & N'_1N'_2 & N'_1N'_3 & N'_1N'_1 \\ N'_2N'_1 & N'_2N'_2 & N'_2N'_3 & N'_2N'_2 \\ N'_3N'_1 & N'_3N'_2 & N'_3N'_3 & N'_3N'_3 \\ N'_4N'_1 & N'_4N'_2 & N'_4N'_3 & N'_4N'_4 \end{bmatrix} d\xi$$

$$\boldsymbol{N'} = \frac{d\boldsymbol{N}}{d\xi}\frac{d\xi}{dx} = \frac{1}{L_e}$$

$$dx = L_e d\xi$$

$$= \frac{A_s}{120(1+\Phi)^2}\begin{bmatrix} K_{g11} & K_{g12} & K_{g13} & K_{g14} \\ K_{g22} & K_{g22} & K_{g23} & K_{g24} \\ K_{g31} & K_{g32} & K_{g33} & K_{g34} \\ K_{g41} & K_{g42} & K_{g43} & K_{g44} \end{bmatrix}$$

$$K_{g11} = 12(c+2)(5\Phi^2 + 10\Phi + 6)$$

$$K_{g12} = 2L_e(5\Phi^2 c + 8\Phi c + 6c + 6)$$

$$K_{g13} = -60(c+2)\left(\Phi^2 + 2\Phi + \frac{6}{5}\right)$$

$$K_{g14} = -2L_e(5\Phi^2 c + 8\Phi c - 6)$$

$$K_{g21} = 2L_e(5\Phi^2 c + 8\Phi c + 6c + 6)$$

$$K_{g22} = L_e^2(5\Phi^2 c + 10\Phi^2 + 6\Phi c + 20\Phi + 4c + 16)$$

$$K_{g23} = -2L_e(5\Phi^2 c + 8\Phi c + 6c + 6)$$

$$K_{g24} = -5L_e^2\left(\Phi^2 + 2\Phi + \frac{2}{5}\right)(c+2)$$

$$K_{g31} = -60(c+2)\left(\Phi^2 + 2\Phi + \frac{6}{5}\right)$$

$$K_{g32} = -2L^2(5\Phi^2 c + 8\Phi z + 6c + 6)$$

$$K_{g33} = 12(c+2)(5\Phi^2 + 10\Phi + 6)$$

$$K_{g34} = 2L_e(5\Phi c + 8\Phi c - 6)$$

$$K_{g41} = -2L_e(5\Phi^2 c + 8\Phi c - 6)$$

$$K_{g42} = -5L_e\left(\Phi^2 + 2\Phi + \frac{2}{5}\right)(c+2)$$

$$K_{g43} = 2L_e(5\Phi^2 c + 8\Phi c - 6)$$

$$K_{g44} = L_e^2\left(5\Phi^2 c + 10\Phi^2 + 14\Phi c + 20\Phi + 4c + 16\right)$$

$$K_e = \frac{T_s}{120 \cdot L_e(1+\Phi)^2}\begin{bmatrix} K_{g11} & K_{g12} & K_{g13} & K_{g14} \\ K_{g22} & K_{g22} & K_{g23} & K_{g24} \\ K_{g31} & K_{g32} & K_{g33} & K_{g34} \\ K_{g41} & K_{g42} & K_{g43} & K_{g44} \end{bmatrix}$$

D.4.4 Stiffness matrix of 1D general beam element

The general stiffness matrix of the beam element is given below.

$$K_e = \begin{bmatrix} X & 0 & 0 & 0 & 0 & 0 & \mathrm{X} & 0 & 0 & 0 & 0 & 0 \\ 0 & Y_{11} & 0 & 0 & 0 & Y_{12} & 0 & -Y_{13} & 0 & 0 & 0 & Y_{14} \\ 0 & 0 & Z_{11} & 0 & -Z_{12} & 0 & 0 & 0 & -Z_{13} & 0 & -Z_{14} & 0 \\ 0 & 0 & 0 & T & 0 & 0 & 0 & 0 & 0 & -T & 0 & 0 \\ 0 & 0 & -Z_{21} & 0 & Z_{22} & 0 & 0 & 0 & Z_{23} & 0 & Z_{24} & 0 \\ 0 & Y_{12} & 0 & 0 & 0 & Y_{22} & 0 & -Y_{23} & 0 & 0 & 0 & Y_{24} \\ \mathrm{X} & 0 & 0 & 0 & 0 & 0 & X & 0 & 0 & 0 & 0 & 0 \\ 0 & -Y_{13} & 0 & 0 & 0 & -Y_{23} & 0 & Y_{33} & 0 & 0 & 0 & -Y_{34} \\ 0 & 0 & Z_{13} & 0 & Z_{23} & 0 & 0 & 0 & Z_{33} & 0 & Z_{34} & 0 \\ 0 & 0 & 0 & -T & 0 & 0 & 0 & 0 & 0 & T & 0 & 0 \\ 0 & 0 & -Z_{14} & 0 & Z_{24} & 0 & 0 & 0 & Z_{34} & 0 & Z_{44} & 0 \\ 0 & Y_{14} & 0 & 0 & 0 & Y_{24} & 0 & -Y_{34} & 0 & 0 & 0 & Y_{44} \end{bmatrix} \quad \text{(D-38)}$$

$$X = \frac{EA_i}{2L_e}(c+2) \qquad T = \frac{GJ_i}{4L_e}(c+2)(c^2+2c+2)$$

$$\{Y,Z\}_{11} = \frac{EI_i}{20L_e^3(1+\Phi)^2}(84c^2 + 288c^2 + 360c + 240)$$

$$\{Y,Z\}_{12} = \frac{EI_i}{20L_e^3(1+\Phi)^2}\left(6L_e\left(20 - 20c - 14c^2 - 4c^3 - \Phi(3c^3 + 10c^2 + 10c)\right)\right)$$

$$\{Y,Z\}_{13} = \frac{EI_i}{20L_e^3(1+\Phi)^2}\left(-(84c^2 + 288c^2 + 360c + 240)\right)$$

$$\{Y,Z\}_{14} = \frac{EI_i}{20L_e^3(1+\Phi)^2}\left(6L_e\left(20 + 40c + 34c^2 + 10c^3 + \Phi(3c^3 + 10c^2 + 10c)\right)\right)$$

$$\{Y,Z\}_{22} = \frac{EI_i}{20L_e^3(1+\Phi)^2}\left(5L_e^2\left(\left(\Phi^2 - \frac{8}{5}\Phi + \frac{8}{5}\right)c^3 + \left(4\Phi^2 - 4\Phi + \frac{32}{5}\right)c^2 + (6\Phi^2 + 12)c + 4\Phi^2 + 8\Phi + 16\right)\right)$$

$$\{Y,Z\}_{23} = \frac{EI_i}{20L_e^3(1+\Phi)^2}\left(6L_e\left(-20 - 20c - 14c^2 - 4c^3 + \Phi(3c^3 + 10c^2 + 10c)\right)\right)$$

$$\{Y,Z\}_{24} = \frac{EI_i}{20L_e^3(1+\Phi)^2}\left(-5L_e^2\left(\left(\Phi^2 + 2\Phi - \frac{16}{5}\right)c^2 + (2\Phi^2 + 4\Phi - 4)c + 2\Phi^2 + 4\Phi - 4\right)(c+2)\right)$$

$$\{Y,Z\}_{33} = \frac{EI_i}{20L_e^3(1+\Phi)^2}(84c^3 + 288c^2 + 360c + 240\ )$$

$$\{Y,Z\}_{34} = \frac{EI_i}{20L_e^3(1+\Phi)^2}\left(-6L_e\left(20 + 40c + 34c^2 + 10c^3 + \Phi(3c^3 + 10c^2 + 10c)\right)\right)$$

$$\{Y,Z\}_{44} = \frac{EI_i}{20L_e^3(1+\Phi)^2}\left(5L_e^2\left(\left(\Phi^2 - \frac{28}{5}\Phi + \frac{44}{5}\right)c^3 + \left(4\Phi^2 + 20\Phi + \frac{152}{5}\right)c^2 + (6\Phi^2 + 24\Phi + 36)c + 4\Phi^2 + 8\Phi + 16\right)\right)$$

$$K_g = \begin{bmatrix} 0 & 0 & 0 & 0 & 0 & 0 & 0 & 0 & 0 & 0 & 0 & 0 \\ 0 & Y_{11} & 0 & 0 & 0 & Y_{12} & 0 & -Y_{13} & 0 & 0 & 0 & Y_{14} \\ 0 & 0 & Z_{11} & 0 & -Z_{12} & 0 & 0 & 0 & -Z_{13} & 0 & -Z_{14} & 0 \\ 0 & 0 & 0 & 0 & 0 & 0 & 0 & 0 & 0 & 0 & 0 & 0 \\ 0 & 0 & -Z_{21} & 0 & Z_{22} & 0 & 0 & 0 & Z_{23} & 0 & Z_{24} & 0 \\ 0 & Y_{12} & 0 & 0 & 0 & -Y_{22} & 0 & -Y_{23} & 0 & 0 & 0 & Y_{24} \\ 0 & 0 & 0 & 0 & 0 & 0 & 0 & 0 & 0 & 0 & 0 & 0 \\ 0 & -Y_{13} & 0 & 0 & 0 & -Y_{23} & 0 & Y_{33} & 0 & 0 & 0 & -Y_{34} \\ 0 & 0 & Z_{13} & 0 & Z_{23} & 0 & 0 & 0 & Z_{33} & 0 & Z_{34} & 0 \\ 0 & 0 & 0 & 0 & 0 & 0 & 0 & 0 & 0 & 0 & 0 & 0 \\ 0 & 0 & -Z_{14} & 0 & Z_{24} & 0 & 0 & 0 & Z_{34} & 0 & Z_{44} & 0 \\ 0 & Y_{14} & 0 & 0 & 0 & Y_{24} & 0 & -Y_{34} & 0 & 0 & 0 & Y_{44} \end{bmatrix} \quad \text{(D-39)}$$

$$\{Y,Z\}_{11} = \frac{T_s}{120 \cdot L_e(1+\Phi)^2}\left(12(c+2)(5\Phi^2+10\Phi+6)\right)$$

$$\{Y,Z\}_{12} = \frac{T_s}{120 \cdot L_e(1+\Phi)^2}\left(2L_e(5\Phi^2 c+8\Phi c+6c+6)\right)$$

$$\{Y,Z\}_{13} = \frac{T_s}{120 \cdot L_e(1+\Phi)^2}\left(-60(c+2)\left(\Phi^2+2\Phi+\frac{6}{5}\right)\right)$$

$$\{Y,Z\}_{14} = \frac{T_s}{120 \cdot L_e(1+\Phi)^2}\left(2L_e(5\Phi^2 c+8\Phi c-6)\right)$$

$$\{Y,Z\}_{22} = \frac{T_s}{120 \cdot L_e(1+\Phi)^2}\left(L_e^2\left(5\Phi^2 c+10\Phi^2+6\Phi c+20\Phi+4c+16\right)\right)$$

$$\{Y,Z\}_{23} = \frac{T_s}{120 \cdot L_e(1+\Phi)^2}\left(-2L_e(5\Phi^2 c+8\Phi c+6c+6)\right)$$

$$\{Y,Z\}_{24} = \frac{T_s}{120 \cdot L_e(1+\Phi)^2}\left(-5L_e^2\left(\Phi^2+2\Phi+\frac{2}{5}\right)(c+2)\right)$$

$$\{Y,Z\}_{33} = \frac{T_s}{120 \cdot L_e(1+\Phi)^2}\left(12(c+2)(5\Phi^2+10\Phi+6)\right)$$

$$\{Y,Z\}_{34} = \frac{T_s}{120 \cdot L_e(1+\Phi)^2}\left(2L_e(5\Phi c+8\Phi c-6)\right)$$

$$\{Y,Z\}_{44} = \frac{T_s}{120 \cdot L_e(1+\Phi)^2}\left(L_e^2(5\Phi^2 c+10\Phi^2+14\Phi c+20\Phi+4c+16)\right)$$

D.5 SHEAR CORRECTION FACTOR

The shear correction factor is introduced to take the shear rotation into account. Timoshenko beam theory defines the shear correction factor as the ratio of the average strain of a section to the shear strain at the centroid. The shear correction factor is depending on the shape of the cross section and can be determine with a free-vibration test or balance of energy. The shear coefficient κ for a circular cross-section can be determine with equation (D-40) [113]. The shear coefficient κ for a thin walled structure is given in equation (D-40).

$$\kappa = \frac{6\left(r_i^2+r_o^2\right)^2(1+\nu)^2 0}{7r_i^4+34r_i^2r_o^2+7r_o^4+\nu\left(12r_i^4+48r_i^2r_o^2+12r_o^4\right)+\nu^2\left(4r_i^4+16r_i^2r_o^2+4r_o^4\right)} \quad \text{(D-40)}$$

$$\kappa = \frac{10(1+\nu)(1+3m)^2}{(12+72m+150m^2+90m^3)+\nu(11+66m+135m^2+90m^3)+10n^2\left((3+\nu)m+3m^2\right)} \quad \text{(D-41)}$$

$$m = \frac{bt_1}{ht}$$

$$n = \frac{b}{h}$$

D.6 TRANSFORMATION MATRIX

The orientation of an element is arbitrary. The stiffness and mass matrix are derived with respect to a local coordinate system that is arbitrary oriented with respect to the global coordinate system. The stiffness and mass matrix should be transformed. The transformation matrix transform the local coordinates of the element into global coordinate system. The transform matrix has the form of equation (D-42). Matrix R is a three-dimensional rotation matrix. The direction cosines method is used. The local coordinate system need first be determined.

$$\boldsymbol{T} = \begin{bmatrix} \boldsymbol{R} & \boldsymbol{0} & \boldsymbol{0} & \boldsymbol{0} \\ \boldsymbol{0} & \boldsymbol{R} & \boldsymbol{0} & \boldsymbol{0} \\ \boldsymbol{0} & \boldsymbol{0} & \boldsymbol{R} & \boldsymbol{0} \\ \boldsymbol{0} & \boldsymbol{0} & \boldsymbol{0} & \boldsymbol{R} \end{bmatrix} \tag{D-42}$$

$$\boldsymbol{R} = \begin{bmatrix} \cos(x,X) & \cos(x,Y) & \cos(x,Z) \\ \cos(y,X) & \cos(y,Y) & \cos(y,Z) \\ \cos(z,Z) & \cos(z,Y) & \cos(z,Z) \end{bmatrix}$$

For the beam element two coordinates are known, meaning that only the x-axis is defined by the vector between those coordinates. The y-axis and z-axis are orthogonal to the x-axis and there are infinite vectors orthogonal to x-axis. The elements have a right-handed coordinate system. The local coordinate system can be found by finding the rotation angles.

$$\boldsymbol{L} = [\boldsymbol{x}\ \boldsymbol{y}\ \boldsymbol{z}] \tag{D-43}$$

$$\boldsymbol{L} = r_z(\gamma) r_y(\beta) r_x(\alpha)$$

$$\boldsymbol{r_x} = \begin{bmatrix} 1 & 0 & 0 \\ 0 & \cos(\alpha) & -\sin(\alpha) \\ 0 & \sin(\alpha) & \cos(\alpha) \end{bmatrix}$$

$$\boldsymbol{r_y} = \begin{bmatrix} \cos(\beta) & 0 & \sin(\beta) \\ 0 & 1 & 0 \\ -\sin(\beta) & 0 & \cos(\beta) \end{bmatrix}$$

$$\boldsymbol{r_z} = \begin{bmatrix} \cos(\gamma) & -\sin(\gamma) & 0 \\ \sin(\gamma) & \cos(\gamma) & 0 \\ 0 & 0 & 1 \end{bmatrix}$$

The rotation γ and β can be found by the (D-44) equation and (D-45). There is assumed that the rotation around the x-axis is zero and the rotations are independent.

$$\gamma = \cos^{-1}\left(\frac{\boldsymbol{u}\cdot\boldsymbol{v}}{|\boldsymbol{u}||\boldsymbol{v}|}\right) \tag{D-44}$$

$$\boldsymbol{u} = \begin{bmatrix} x_1 \\ x_2 \end{bmatrix} \qquad \boldsymbol{v} = \begin{bmatrix} 1 \\ 0 \end{bmatrix}$$

$$\beta = \cos^{-1}\left(\frac{\boldsymbol{u}\cdot\boldsymbol{v}}{|\boldsymbol{u}||\boldsymbol{v}|}\right) \tag{D-45}$$

$$\boldsymbol{u} = \begin{bmatrix} x_1 \\ x_3 \end{bmatrix} \qquad \boldsymbol{v} = \begin{bmatrix} 1 \\ 0 \end{bmatrix}$$

D.7 NODAL FORCES

The acting on the elements need to be written into nodal forces. The loads working on a one-dimensional beam element are forces, moments and distributed loads. The nodal forces vector for a beam element can be computed by equation (D-46). Be aware the f_s is a surface load and f_b is a body load. The surface loads can directly applied on the nodes. The body loads need to be transferred to nodal loads.

$$f_e = \int_V \boldsymbol{N^T} f_b \, dV + \int_{S_f} \boldsymbol{N^T} f_s \, dS_f \tag{D-46}$$

There is assumed that there is no coupling between deformations in a particular direction. The load need to be transfer to nodal loads. There is assumed that the load between two nodes are linear. The linear distributed load can be divided into a uniform distributed load and distributed load with a linear decay.

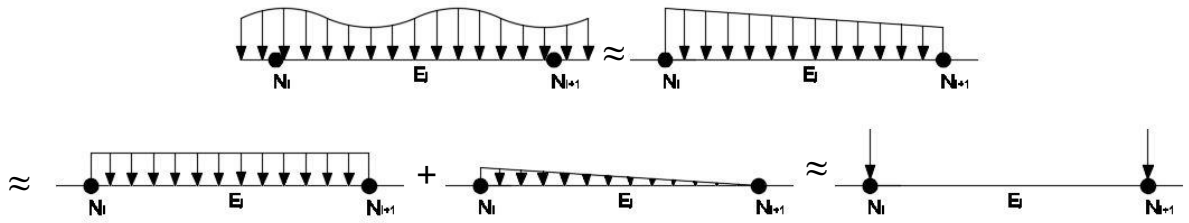

Axial

$$f_e = \int_V \boldsymbol{N^T} f_b = \int_V \boldsymbol{N^T} f_u + \int_V \boldsymbol{N^T} f_t \tag{D-47}$$

$$\int_V \boldsymbol{N^T} f_2 = A f_u \int_0^1 \begin{bmatrix} \boldsymbol{\xi} \\ \mathbf{1} - \boldsymbol{\xi} \end{bmatrix} = \begin{bmatrix} \frac{1}{2} f_{x,u} \\ \frac{1}{2} f_{x,u} \end{bmatrix}$$

$$\int_V \boldsymbol{N^T} f_2 = A f_t \int_0^1 \begin{bmatrix} \boldsymbol{\xi} \\ \mathbf{1} - \boldsymbol{\xi} \end{bmatrix} = \begin{bmatrix} \frac{2}{3} f_{x,t} \\ \frac{1}{3} f_{x,t} \end{bmatrix}$$

Bending

$$f_e = \int_V \boldsymbol{N^T} f_b = \int_V \boldsymbol{N^T} f_u + \int_V \boldsymbol{N^T} f_t \tag{D-48}$$

$$\int_V \boldsymbol{N^T} f_b = A f_u \int_0^1 \begin{bmatrix} \frac{1}{1+\Phi}(1-3\xi^2+2\xi^3+\Phi(1-\xi)) \\ \frac{L_e}{1+\Phi}\left(\xi-2\xi^2+\xi^3+\frac{\Phi}{2}(\xi-\xi^2)\right) \\ \frac{1}{1+\Phi}(3\xi^2-2\xi^3+\Phi\xi) \\ \frac{L_e}{1+\Phi}\left(-\xi^2+\xi^3+\frac{\Phi}{2}(-\xi+\xi^2)\right) \end{bmatrix} = \begin{bmatrix} \frac{1+\Phi_z}{2+2\Phi_z}L_e f_y \\ \frac{(1+\Phi_z)L_e^2 f_y}{12+12\Phi_z} \\ \frac{1+\Phi_z}{2+2\Phi_z}L_e f_y \\ -\frac{(1+\Phi_z)L_e^2 f_y}{12+12\Phi_z} \end{bmatrix}$$

$$\int_V \boldsymbol{N^T} f_b = A f_t \int_0^1 \begin{bmatrix} \frac{1}{1+\Phi}(1-3\xi^2+2\xi^3+\Phi(1-\xi)) \\ \frac{L_e}{1+\Phi}\left(\xi-2\xi^2+\xi^3+\frac{\Phi}{2}(\xi-\xi^2)\right) \\ \frac{1}{1+\Phi}(3\xi^2-2\xi^3+\Phi\xi) \\ \frac{L_e}{1+\Phi}\left(-\xi^2+\xi^3+\frac{\Phi}{2}(-\xi+\xi^2)\right) \end{bmatrix} = \begin{bmatrix} \frac{7+\Phi_z}{20+20\Phi_z}L_e f_y \\ \frac{(1+\Phi_z)L_e^2 f_y}{20+20\Phi_z} \\ \frac{3+\Phi_z}{20+20\Phi_z}L_e f_y \\ -\frac{(1+\Phi_z)L_e^2 f_y}{30+30\Phi_z} \end{bmatrix}$$

The reduced nodal force method is used. The nodal moments are omitted. The nodal moments are of the same approximate same order. For nodes connected to two elements, the nodal forces converge to zero. The nodal forces can therefore disregarded.

$$f_e = \int_V \boldsymbol{N^T} f_b = \int_V \boldsymbol{N^T} f_u + \int_V \boldsymbol{N^T} f_t \tag{D-49}$$

$$\int_V \boldsymbol{N^T} f_b = A f_u \int_0^1 \begin{bmatrix} \frac{1}{1+\Phi}(1-3\xi^2+2\xi^3+\Phi(1-\xi)) \\ \mathbf{0} \\ \frac{1}{1+\Phi}(3\xi^2-2\xi^3+\Phi\xi) \\ 0 \end{bmatrix} = \begin{bmatrix} \frac{1+\Phi_z}{2+2\Phi_z}L_e f_y \\ 0 \\ \frac{1+\Phi_z}{2+2\Phi_z}L_e f_y \\ 0 \end{bmatrix}$$

$$\int_V \boldsymbol{N^T} f_b = A f_t \int_0^1 \begin{bmatrix} \frac{1}{1+\Phi}(1-3\xi^2+2\xi^3+\Phi(1-\xi)) \\ 0 \\ \frac{1}{1+\Phi}(3\xi^2-2\xi^3+\Phi\xi) \\ 0 \end{bmatrix} = \begin{bmatrix} \frac{7+\Phi_z}{20+20\Phi_z}L_e f_y \\ 0 \\ \frac{3+\Phi_z}{20+20\Phi_z}L_e f_y \\ 0 \end{bmatrix}$$

E APPENDIX: VALIDATION OF MODEL

The Aero-Hydro-Elastic-Servo model (Matlab model) must be validated. This appendix provides all the results of the validation. The model is validated in multiple steps, the first step is the validation of the Beam element. The final step is validation of the natural period and the response motions of a bottom founded wind turbine and the floating wind turbine.

E.1 ELEMENT

The element derived in Appendix: One-dimensional finite element must be validated. The validation of the element is split in three parts. Firstly, the cantilever without a tension force is validated. The natural frequencies of the element are compared with a cantilever beam in Ansys and analytical equation of the cantilever beam. Secondly, the natural frequencies of a tensioned cantilever beam are compared. The final step is comparing the natural frequencies of a tensioned cantilever beam with a linear tapering. The cross-dimensional properties of the cantilever beam are given Table E-6, which are the dimensional properties of a pontoon. The relative error is determine with equation (E-1).

The natural periods are depending on the mass and stiffness matrix. The natural periods of the one-dimensional element is compared with the ANSYS BEAM188 element. This element is suitable for slender to moderately thick beamed structures. The element is based on the Timoshenko beam theory and is well-suited for linear and nonlinear applications. The one-dimensional beam element derived in Appendix: One-dimensional finite element is also a Timoshenko beam element including a linear tapering.

$$\epsilon = \frac{|T_{MATLAB} - T_{ANSYS}|}{T_{ANSYS}} \tag{E-1}$$

$$\epsilon = \frac{|T_{analytical} - T_{ANSYS}|}{T_{analytical}} \tag{E-2}$$

Table E-1: Validation element

Parameter	*Symbol*	*Value*	*Unit*
Length	L	42.5 m	m
Diameter	D	4.7 m	m
Plate thickness	T_p	0.025 m	m
Tapering factor	c	0.5	[-]
Tension force	F_t	500.000	kN

E.1.1 Cantilever beam

The analytical equation of the natural frequencies (see equation (E-3)) of a cantilever beam are multiple times derived and not presented in this appendix. The analytical natural frequencies of the cantilever beam are compared with the natural frequencies of the beam element. Table E-2 gives the analytical natural frequencies, the Matlab natural frequencies and the relative error. The relative errors are approximately 0.002, which are still within the acceptable limits.

$$f_n = \left(\frac{\beta}{L}\right)^2 \sqrt{\frac{EI}{\rho A}} \tag{E-3}$$

$\beta = 1.875, 4.694, 7.854, 10.996, 14.137, 17.279 \ldots$

Table E-2: Natural frequencies analytical, ANSYS and MATLAB

	Analytical [Hz]	*Ansys [Hz]*	*Matlab [Hz]*	*Error* Analytical - Matlab	*Error* Ansys - Matlab
First bending mode	2.672	2.614	2.642	0.01	0.02
Second bending mode	16.75	14.67	16.55	0.01	0.05
First axial mode	30.70	30.69	30.70	0.00	0.00
First torsion mode	19.09	19.04	19.10	0.00	0.00

E.1.2 Tensioned cantilever beam

A stiffness of a beam increases when the tension in the beam increased. The cantilever beam is loaded at the top with a force of 500.000kN. The geometric stiffness of the element is than dominant. The natural frequencies of the tensioned cantilever beam are given in Table E-3, only the bending modes are given because the stiffness of the bending changed. The natural frequency of the second bending mode has the largest relative error. The natural frequency of second bending mode of Ansys compared with the analytical natural frequency showed also large difference. Concluded is that the geometric stiffness is correct.

Table E-3: Natural frequencies ANSYS and MATLAB

	ANSYS [Hz]	*MATLAB [Hz]*	*Error*
First bending mode	4.14	4.09	0.012
Second bending mode	16.86	18.74	0.100

E.1.3 Tapered cantilever beam

The one-dimensional beam element has a linear tapering. The final step is comparing the natural frequencies of a tapered beam. Table E-4 gives the natural frequencies of the tapered cantilever beam of the Ansys and the Matlab model. The maximum relative error is 0.059, but the natural frequency of second bending mode of Ansys compared with the analytical natural frequency showed also large difference. Concluded is that the tapered cantilever beam model is correct.

Table E-4: Natural frequencies ANSYS and MATLAB

	ANSYS [Hz]	*MATLAB [Hz]*	*Error*
First bending mode	2.874	2.873	0.000
Second bending mode	12.99	13.70	0.059
First axial mode	27.77	27.78	0.000
First torsion mode	35.72	34.48	0.035

E.1.4 Discussions

The element is validated with Ansys. Ansys is a commercial finite element analysis software package to simulate engineering problems. The software has the property to model a one-dimensional beam element including a linear tapering. A cantilever beam with the dimensions of the pontoon is used to validate the element. The dimensional properties and the forces are shown in Table E-1. The validation is performed in three steps, a cantilever beam, tensioned cantilever beam and a tapered cantilever beam. The second-bending mode of the Matlab model compared with the Ansys model show a large difference, but the natural frequency of the second bending mode of the Ansys model compared with the analytical model showed also a large difference. Concluded is that the tapered cantilever beam model is correct.

E.2 BOTTOM FOUNDED WIND TURBINE

The dynamic system of the bottom founded wind turbine is simpler than the TLPWT. The bottom founded wind turbine is modelled in the aero-hydro-elastic-servo model implemented in Matlab and in Orcina Orcaflex. Orcaflex is a commercial software package for dynamic analysis of marine systems [13]. The wind turbine is modelled as a cantilever beam. The RNA is modelled with a mass element in Matlab and a buoy element in Orcaflex. Figure E-1 shows the models and a drawing of the wind turbine. The cross-dimensional properties are given in Table E-5.

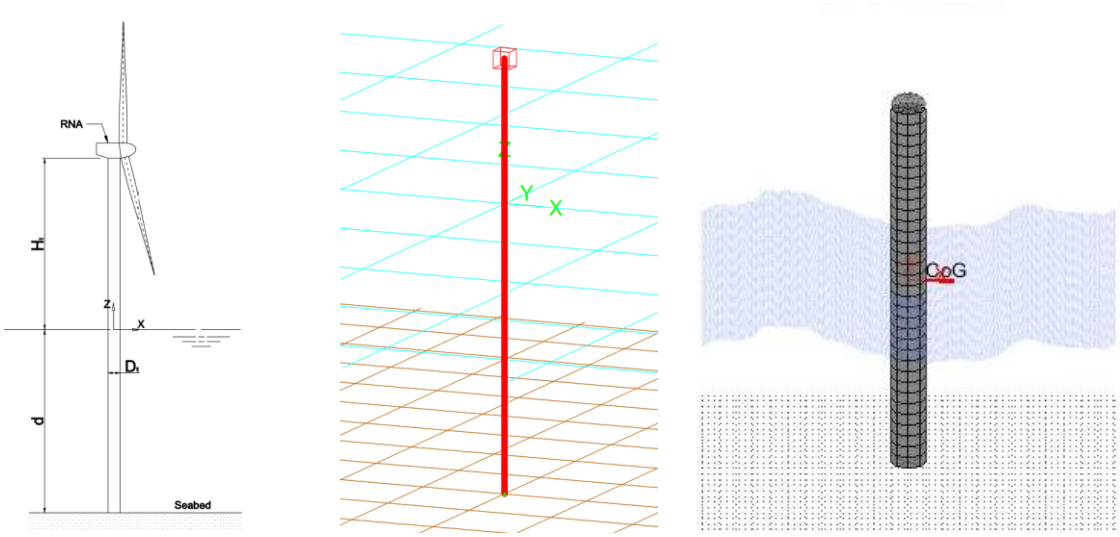

(a) (b) (c)

Figure E-1: (a) Drawing; (b) Orcaflex model; (c) Matlab model

Table E-5: Dimensional properties BFWT

Parameter	*Symbol*	*Value*	*Unit*
Diameter	D	10	[m]
Plate thickness	t_p	0.1	[m]
depth	d	96.5	[m]
height	H	90.7	[m]

E.2.1 Natural period

The natural periods in static position of the BFWT for all both models are given in Table E-6. The added mass is taken into account. The relative error of the natural period is computed using equation (E-4). The largest relative error is 0.081 which is still within an acceptable limit.

$$\epsilon = \frac{\left|T_{MATLAB} - T_{Orcaflex}\right|}{T_{orcaflex}} \quad \text{(E-4)}$$

Table E-6: Natural Periods BFWT

	Orcaflex [s]	*MATLAB [s]*	*Error [-]*
Fore-aft 1st	4.47	4.55	0.015
Side-side 1st	4.63	4.72	0.019
Fore-aft 2nd	1.22	1.12	0.081
Side-side 2nd	1.44	1.34	0.069
Torsion	1.65	1.63	0.012

E.2.2 Hydrodynamic response

The hydrodynamic motion responses of the BTWT of the Orcaflex model and the Matlab model are compared. A regular wave with a wave height of 3.5m and a wave peak period of 8 seconds is used. The wind velocity is assumed to be zero, meaning that the wind turbine is off. A summary of the environmental conditions are given Table E-7.

Table E-7: one year extreme wave

Parameter	*Symbol*	*Value*	*Unit*
Wave height	H_s	3.5	[m]
Wave Period	T_p	8.0	[s]
Wave direction	μ_{wave}	60	[°]
Current velocity wind	$u_{c,wind}$	0.0	[ms-1]
Current velocity tide	$u_{c,tide}$	0.0	[ms-1]
Current direction	μ_{curent}	90	[°]
Wind velocity	U_w	0	[ms-1]

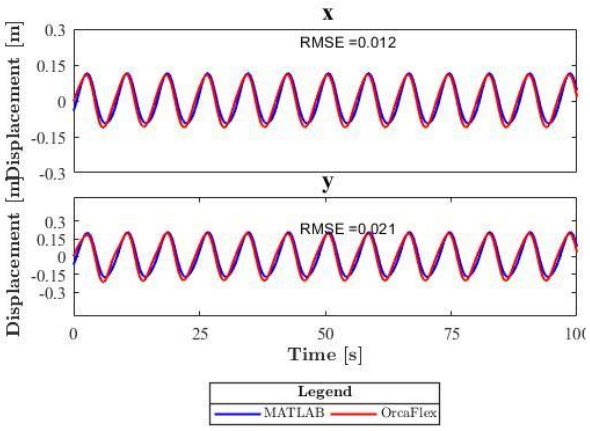

(a)

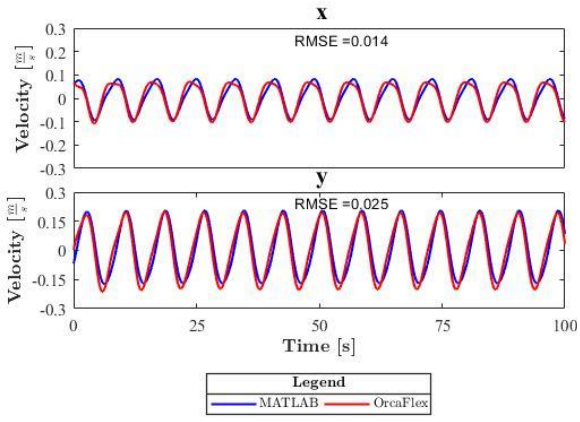

(b)

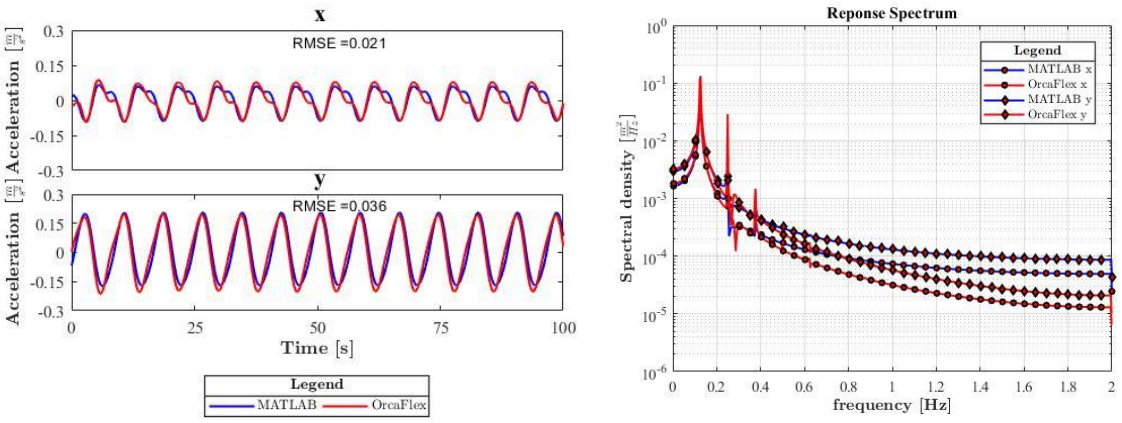

(c) (d)

Figure E-2: Responses of the BFWT of the Orcaflex and MATLAB model

E.3 FLOATING TLP-TYPE WIND TURBINE

A Matlab model, Orcaflex model and Ansys model are made to compare the static and dynamic results. The models have the same geometric properties and the same constraints. The design of the TLPWT is based on the design used to perform the model test of the TLPWT at MARIN. In the design of the TLPWT, the pontoon has rectangular shaped pontoons. The TLPWT used for the model test has circular shaped pontoons.

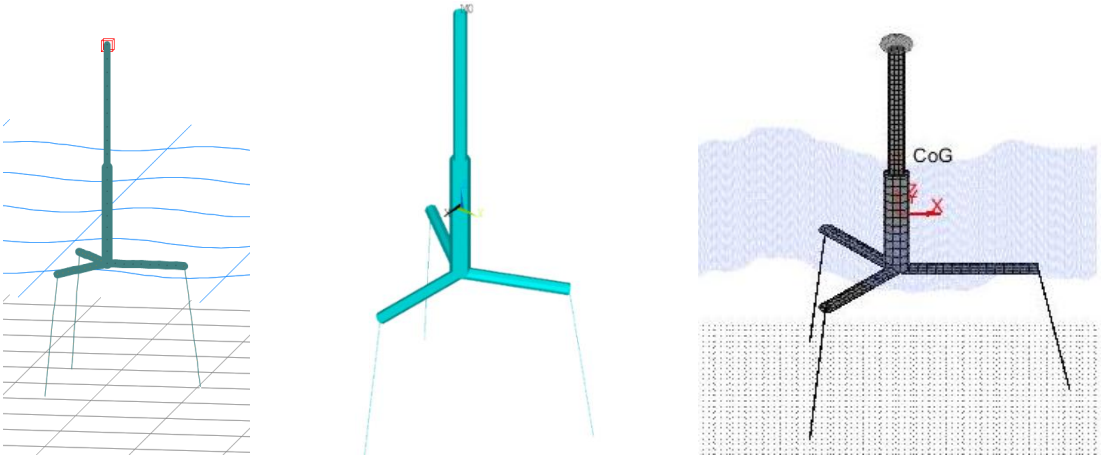

(a) (b) (c)

Figure E-3: (a) Orcaflex Model; (b) ANSYS model; (c) MATLAB model

Orcina Orcaflex is a commercial software package for dynamics analysis of marine systems. The FAST-Orcaflex coupling is many times used in studies of FWT. Orcaflex takes the flexibility of the tendons, pontoons and tower into account. Orcaflex software uses the lumped mass approximation. It is not possible to model the nacelle fixed to the end of the tower. Stiff springs are therefore used to model the tower-nacelle connection. The nacelle is modelled using a buoy element with the mass and inertia properties of the nacelle and rotor blades. Ansys is a commercial finite element analysis software package to simulate engineering problems. The tendons, pontoons and tower are modelled using the BEAM188 element. The Nacelle is modelled using a MASS21 element with the mass and inertia properties of the nacelle and rotor blades. The Matlab model is explained in chapter 3 Development of aero-hydro-elastic-servo model. The tendon, pontoon and tower are modelled with the same element. The nacelle is modelled with a mass element. The mass element has the mass and inertia properties of the nacelle and rotor.

E.3.1 Static

The hydrostatic forces and weights are applied in all three models. Orcaflex is not be able to determine the mass of the structure. Orcaflex gives the mass per unit length of each element separately. The mass of Orcaflex model is determine manually. Ansys model and Matlab model are be able to compute the mass of the TLP. The static results are given in Table E-8. The Orcaflex model and the Matlab model have approximate the same results. The Ansys model has slightly higher pretension, but difference is negligible

Table E-8: Static Properties Models

	Orcaflex	*ANSYS*	*MATLAB*	*Unit*
Total Mass	1.00	1.00	1.00	mT
Platform Mass	1.00	1.00	1.00	mT
Nacelle mass	[*]	[*]	[*]	mT
Pretension tendon	1.00	1.03	1.00	kN
Displacement z TP	0.503	0.515	0.497	m
Displacement z Nacelle	0.499	0.512	0.494	m

* Confidential

E.3.2 Natural period

The natural periods in static position of the TLPWT for all three models are given in equation (E-5). The added mass is not taken into account, because the Ansys model does not include the added mass. The relative error of the natural periods are computed using equation (E-5). The natural periods between Orcaflex and the Matlab modal are approximately the same. The surge and sway natural periods between Ansys and the Matlab are different but the tendon tension is higher which affect the surge and sway natural periods.

$$\epsilon = \frac{\left|T_{MATLAB} - T_{Orcaflex}\right|}{T_{orcaflex}} \tag{E-5}$$

Table E-9: Natural Periods excluding added mass

	Orcaflex [s]	*ANSYS [s]*	*MATLAB [s]*	*Error [-]*
Surge	15.80	13.38	15.47	0.02
Sway	15.46	13.36	15.30	0.01
Heave	1.82	1.85	1.83	0.00
Roll	5.74	5.56	5.68	0.01
Pitch	6.90	6.73	6.70	0.03
Yaw	13.55	13.35	13.56	0.00

The Ansys model is the added mass is not taken into account. The Matlab model and the Orcaflex model take the added mass into account. The added mass should cannot be neglected by a computing the natural periods. Table E-10 gives the natural frequencies of the Orcaflex and Matlab model. The relative error is computed with equation (E-6) and also given in Table E-10. The difference between the natural frequencies of the Orcaflex model and the Matlab model are negligible. Concluded is that the Matlab model is capable to determine the natural period of the TLPWT correctly.

$$\epsilon = \frac{|T_{MATLAB} - T_{ORCAFLEX}|}{T_{ORCAFLEX}} \quad \text{(E-6)}$$

Table E-10: Natural Periods including added mass

	Orcaflex [s]	*MATLAB [s]*	*Error [-]*
Surge	25.04	25.18	0.01
Sway	25.15	25.25	0.00
Heave	2.33	2.35	0.00
Roll	6.30	6.31	0.00
Pitch	7.23	7.22	0.00
Yaw	16.70	16.87	0.01

E.3.3 Hydrodynamic response

The motion responses of the Orcaflex and the Matlab model are compared for two environmental conditions. The one year extreme wave conditions and the 10 year extreme wave condition.

E.3.3.1 1 year extreme wave condition

A regular wave with no current and no wind velocity is used to compare the responses. Table E-11 gives a summary of the environmental conditions. Figure E-4 gives the displacements, velocities and accelerations of the TLPWT. A simulation 100 second is used, excluding the starting procedure, and the root mean square error is used to compare the motion responses (RMSE). The RMSE are within the below the 0.1. Expected is that the RMSE converges to approximate zero if the length of the simulation increase.

Table E-11: Environmental condition validation analysis

Parameter	*Symbol*	*Value*	*Unit*
Wave height	H_s	3.5	[m]
Wave Period	T_p	8.0	[s]
Wave direction	μ_{wave}	60	[°]
Current velocity wind	$u_{c,wind}$	0.0	[ms-1]
Current velocity tide	$u_{c,tide}$	0.0	[ms-1]
Current direction	μ_{curent}	90	[°]
Wind velocity	U_w	0	[ms-1]
Static thrust force	F_t	0	[kN]

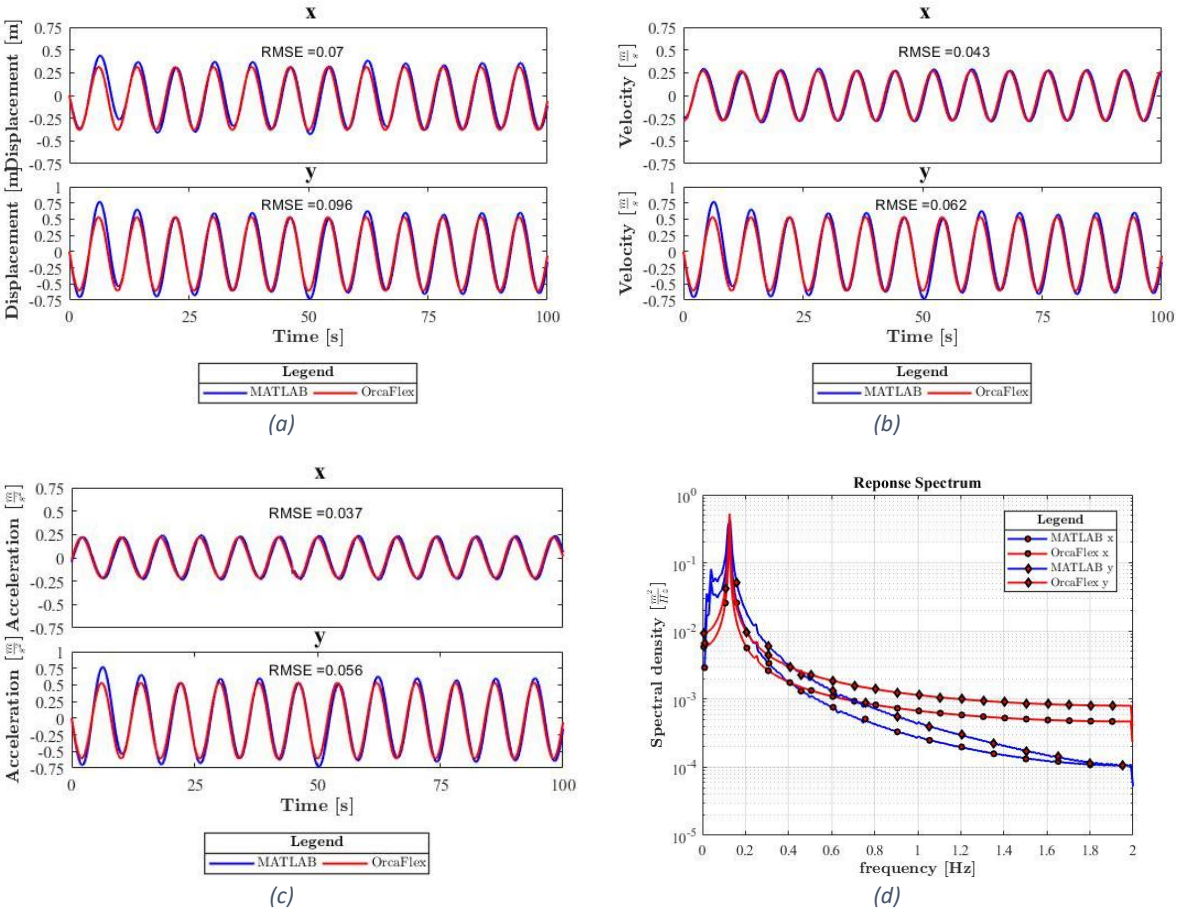

Figure E-4: Responses of the TLPWT of the Orcaflex and MATLAB model

E.3.3.2 10 year extreme wave condition

The motion responses of the 1 year extreme wave condition are small. To validate the model for an extreme environmental condition is the 10 year extreme wave condition used. The 10 year extreme wave condition is a regular wave without current, wind and static thrust force.

Table E-12: Environmental condition validation analysis

Parameter	*Symbol*	*Value*	*Unit*
Wave height	H_s	10	[m]
Wave Period	T_p	15.8	[s]
Wave direction	μ_{wave}	60	[°]
Current velocity wind	$u_{c,wind}$	0.0	[ms-1]
Current velocity tide	$u_{c,tide}$	0.0	[ms-1]
Current direction	μ_{curent}	90	[°]
Wind velocity	U_w	0	[ms-1]
Static thrust force	F_t	0	[kN]

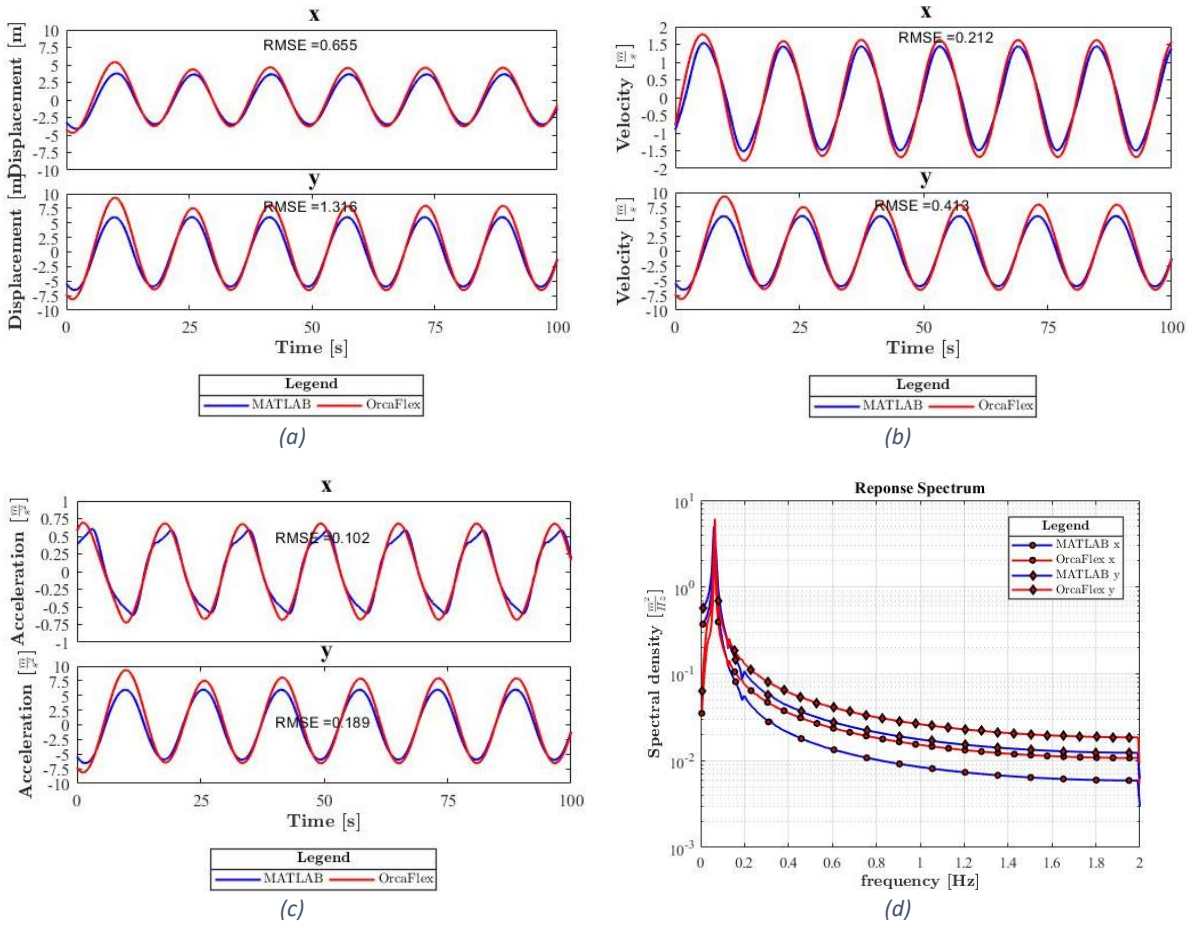

Figure E-5: Responses of the TLPWT of the Orcaflex and MATLAB model

E.4 CONCLUSION

The validation of the Aero-Hydro-Elastic-Servo model was performed in multiple steps. The first step compares the static response between the Matlab model, Ansys model and the Orcaflex model. All models show similar static response. The next step compares the natural periods and the Matlab model computes the natural periods within less than 1% difference compared with the Orcaflex model. The motion responses of the Matlab model are compared with the motion responses of the Orcaflex model. A BFWT and a FWT are used to compare the motion responses. The BFWT has simpler dynamical system with respect to the FWT. The BFWT is modelled as a cantilever beam. The RMSE of the motions are below than 0.036 and the RMSE of the FWT are below 0.096 but still acceptable. This is acceptable because the amplitudes of the Orcaflex model and Matlab model are approximately identical, which is dominant by fatigue. Hence, the Matlab model is capable to compute the motion correctly.

The Orcaflex model and the Matlab model use the same wind turbine external function. This function itself should be validated with a BEM-software. Within the time frame of this thesis, it is not possible to validate the external function. The external wind function is therefore not validated. The control system is important for the dynamical response of the wind turbine. The NREL control system is used in the model.

F APPENDIX: DECAY TEST

The natural frequency is the frequency of vibration without an external force after an initial displacement. Due to the damping of the system, the TLPWT stops to oscillate. The damping of the system and the fundamental frequencies can been investigated with a free vibration test. The free vibration test of surge, heave and yaw are shown in Figure F-1 and Figure F-2. The damping ratios are determine with equation (F-1) and are shown Table F-1.

$$x(t) = x_0 e^{-\xi 2\pi f_n t} \quad \text{(F-1)}$$

Table F-1: Damping ratio

	Surge	*Heave*	*Yaw*
Damping ratio	0.22	0.11	0.22

Surge

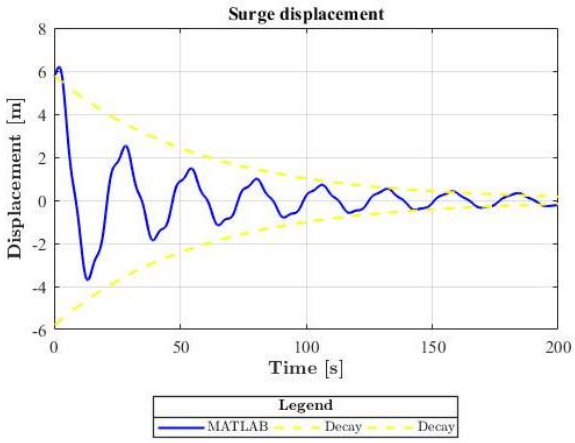

(a)

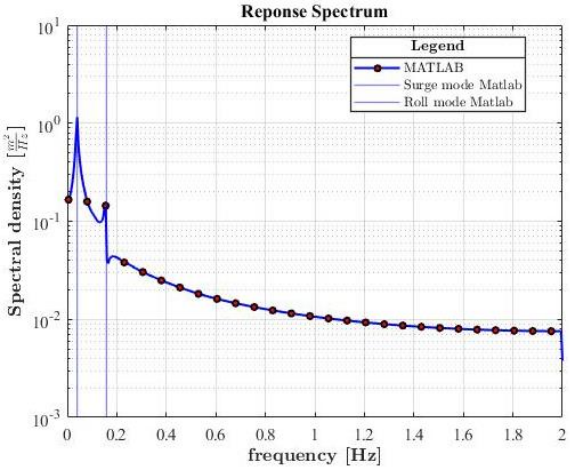

(b)

Figure F-1: Free vibration test surge

heave

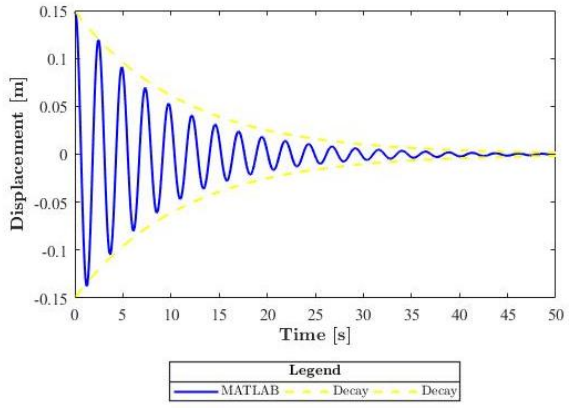

(a)

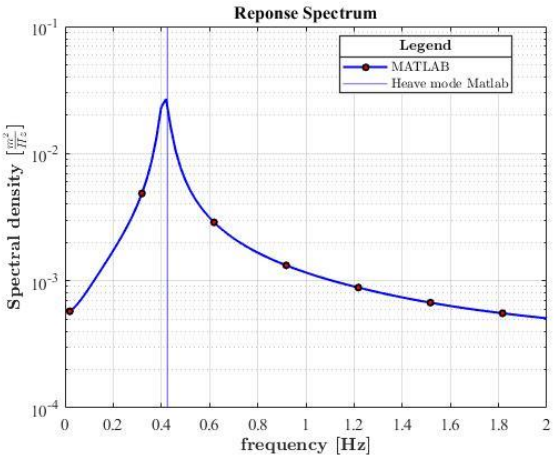

(b)

Figure F-2: Free vibration test heave

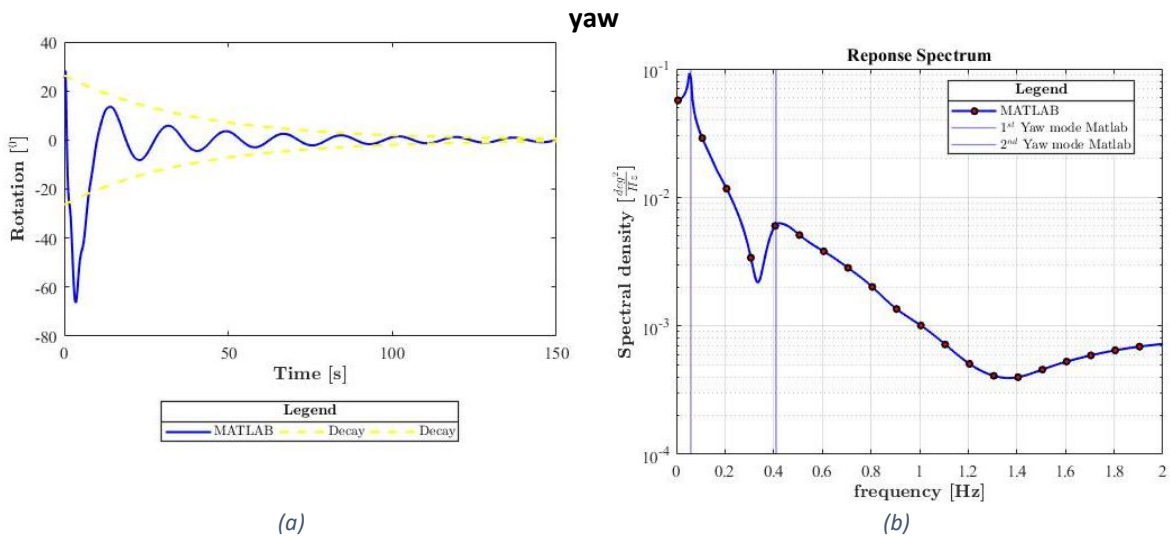

(a) *(b)*

Figure F-3: Free vibration test yaw